Gesellschaft für Anlagen- und Reaktorsicherheit (GRS) mbH

Thermal Effects on the Opalinus Clay

A Joint Heating Experiment of ANDRA and GRS at the Mont Terri URL (HE-D Project)

Final Report

GRS - 224

Gesellschaft für Anlagen- und Reaktorsicherheit (GRS) mbH

Thermal Effects on the Opalinus Clay

A Joint Heating Experiment of ANDRA and GRS at the Mont Terri URL (HE-D Project)

Final Report

Chun-Liang Zhang
Tilmann Rothfuchs
Norbert Jockwer
Klaus Wieczorek
Jürgen Dittrich
Jürgen Müller
Lothar Hartwig
Michael Komischke

March 2007

Remark:

This report was prepared under contract No. 02 E 9773 with the German Bundesministerium für Wirtschaft und Arbeit (BMWA).

The work was conducted by the Gesellschaft für Anlagen- und Reaktorsicherheit (GRS) mbH.

The authors are responsible for the content of this report.

Also available as report TR2007-02 of the Mont-Terri-project.

GRS - 224
ISBN 978-3-931995-98-0

Deskriptoren:

Bohrung, Bruchmechanik, Deformation, Dehnung, Dichtigkeit, Elastisch-Plastische Verformung, Endlagerung, Endlager, Experiment, Festigkeit, Forschung, Gas, Geomechanik, Gestein, Messauswertung, Wärmeleitung

Foreword

From October 2003 to December 2005, a joint heating experiment (HE-D) was performed at the Mont Terri Rock Laboratory by ANDRA and GRS to investigate thermal effects on clay formations hosting a repository for high level radioactive waste. GRS participated in this experiment with in-situ measurements, laboratory experiments, and numerical modelling.

In the HE-D experiment the Opalinus clay was heated up to 100 °C by a heater of 6 m length installed in a horizontal borehole of 300 mm diameter and 14 m length. Two heating phases with power inputs of 650 and 1950 Watts were conducted and followed by a cooling phase. Responses of the clay rock to the thermal loading were investigated by monitoring the temperature, pore-water pressure, gas migration, and deformation in the surrounding rock with 110 instruments installed in 24 boreholes. Detailed information is given about the layout of the field test, the instrumentation, and the measurement results.

The very complex thermo-hydro-mechanical processes occurring in the clay rock during the experiment were numerically simulated and analyzed. For the validation of the coupled THM models used, the modelling results were compared with the measured data. The parameters associated with the models were established on basis of various laboratory tests performed on normally-sized samples and confirmed by back-calculations of muck-up heating tests on large-scale samples taken from the HE-D test field.

The GRS work was funded by the German Federal Ministry of Economics and Technology (BMWi) under contract No. 02 E 9773.

The most important results of GRS's work achieved in this joint project are summarized in this report.

Table of Contents

1 Introduction

Clay formations are being considered worldwide as host medium for the disposal of radioactive waste. In order to prove the feasibility of the disposal concepts proposed by the countries like for instance France, Switzerland, and Belgium, a number of underground research laboratories (URL) are in operation in different clay formations, such as the over-consolidated Opalinus clay at Mont Terri in Switzerland, the Callovo-Oxfordian argillite at the Meuse/Haute-Marne site Bure in France, and the plastic Boom clay at Mol in Belgium. In these URLs, a large number of full-scale in-situ experiments haven been performed and are currently planned to be conducted in the future. In the recent years, basic research on clay formations has also been initiated in Germany, in accordance with the R+D programme defined by the German Federal Ministry of Economics and Technology (BMWi). The German research work is characterized by participation in international research projects being conducted in the above mentioned URLs.

Effects of heat output from high level radioactive waste (HLW) on geological and engineered barriers are of primary importance with regard to the long-term safety of the repository. The thermal loading induces complex thermo-hydro-mechanical (THM) processes in the multi-barrier system, which influence the performance of the system significantly. In order to enhance the knowledge about the THM processes in argillaceous rocks, the in-situ heating experiment HE-D was performed in the Opalinus clay at the Mont Terri Rock Laboratory in Switzerland from October 2003 to December 2005. The HE-D experiment was conducted by the French Agence Nationale Pour la Gestion de Déchets Radioactifs (ANDRA) in cooperation with the Mont Terri consortium partner Gesellschaft für Anlagen- und Reaktorsicherheit (GRS) mbH. Additionally, there were several other research institutes contributing to the project under contracts with ANDRA: e.g., CEA, GEXTER, LAEGO and LML of France, DBE Technology of Germany, SOLEXPERTS and Geotechnical Institute (GI) of Switzerland, and UPC/CIMNE of Spain.

The concept of the in-situ heating experiment was developed to heat the clay formation in an undisturbed zone by using an electric heater equipment installed in a horizontal borehole. The main objective was to investigate responses of the clay rock to thermal loading by monitoring temperature, pore-water pressure, gas migration, and deformation in the clay rock around the heater. The field observations were analysed

by the support of numerical simulations which were performed by the project partners. The models were to be validated by the field measurement data.

The project was supported by GRS with the following work packages:

- In-situ measurements of temperature, pore-water pressure and gas migration in the clay rock around the heater before, during and after the heating phases with use of mini- and multi-packer-systems, and determination of gas entry / breakthrough pressure and permeability of the clay rock;
- Laboratory investigations on normally-sized and large-scale samples from the HE-D test field to characterise the THM behaviour of the clay rock and thus to provide a database for identification of material parameters;
- Numerical simulations of laboratory mock-up heating tests for calibration of key parameters, for design of the in-situ experiment, for interpretation of the THM processes in the test field, and for model validation by comparison of the modelling results and measurement data.

The GRS programme was performed under contract number 02E9773 with BMWi, the Projektträger Karlsruhe des BMWi und BMFT für Wassertechnologie und Entsorgung (PK/WTE), between August 2003 and December 2006.

In Chapter 2, a general description of the HE-D in-situ heating experiment is given in terms of objectives, geological conditions of the test field, details on the installation of the heater equipment and the instruments, conduction of the experiment with heating and cooling phases. Results of the GRS's measurements of temperature, pore-water pressure, gas entry / breakthrough pressure, and permeability to gas and water are presented. The deformation measurements performed by DBE-TEC and SOLEXPERTS are given, too.

GRS's laboratory experiments on samples taken from the HE-D test field provided a fundamental database about the THM behaviour of the clay rock. The tests on normally-sized samples and the mock-up heating tests on large-scale samples are presented in Chapter 3.

Results of the GRS's modelling work, including general description of the THM coupling theories applied, determination of parameters, simulations of the laboratory

mock-up tests, pre-operational and interpretative calculations of the in-situ experiment, as well as comparisons between calculations and measurements are presented in Chapter 4.

Finally, achievements and conclusions based on GRS's investigations are summarized in Chapter 5.

2 In-situ Heating Experiment

2.1 Background and Objectives

The HE-D heating experiment was originally proposed by ANDRA at the beginning of 2003 as a mock-up test for the support of a similar heating experiment named TER to be conducted at a later time in the Callovo-Oxfordian argillite at the Meuse/Haute-Marne Underground Research Laboratory (MHM-URL) in France /WIL 03/. The basic concept of the TER experiment is to heat the clay rock by means of a heater equipment without any filling material between the heater and the rock. In order to test a prototype of the heater equipment, the HE-D experiment was designed and started in October 2003 in the Opalinus clay at the Mont Terri Rock Laboratory (MTRL) in Switzerland.

The main objectives of the HE-D experiment were as follows:

- To test the capability of a prototype heater equipment to reach a maximum temperature of 100 °C at the heater / rock interface for a period of 1 year under a inflated packer pressure of 1 MPa and eventually of 150 °C, depending on the results of the previous heating history;
- To develop and test measuring instruments and techniques specially suitable for monitoring temperature, pore-water pressure, gas migration, and deformation in argillaceous rocks which have particular properties of very low permeability and free water content;
- To observe and investigate responses of the Opalinus clay to heating and cooling during the in-situ experiment;
- To characterize THM properties of the Opalinus clay in laboratory tests on samples taken from the test field and to determine parameters associated with the constitutive models to be applied;
- To model THM processes taking place in the rock around the heater and to compare the modelling results with the field measurements for validation of the models.

2.2 Geological Conditions

The Mont Terri Rock Laboratory (MTRL) has been excavated beside the security gallery of the Mont Terri motorway tunnel in the north-western part of Switzerland and implemented on the south-western slope of the Mont Terri anticline (Figure 2-1). It is located in the Opalinus clay formation consisting of three main facies: clay-schist facies, clay-sand facies and clay-sand facies rich in carbonates, as shown in Figure 2-2. More details about the different lithologies can be found in /THU 99/. The bedding planes plunge towards the southeast (SE) with an azimuth of 140 – 150°. The apparent thickness is about 160 m. Its current overlay varies between 250 and 320 m, while it is estimated to have reached at least 1000 m in the past. The pores in the clay rock are saturated with water, but water circulations are practically negligible due to its very low permeability and pressure gradient. The pore-water pressure in the far regions from the openings in the MTRL amounts to about 2.1 MPa and the rock temperature to 15 °C.

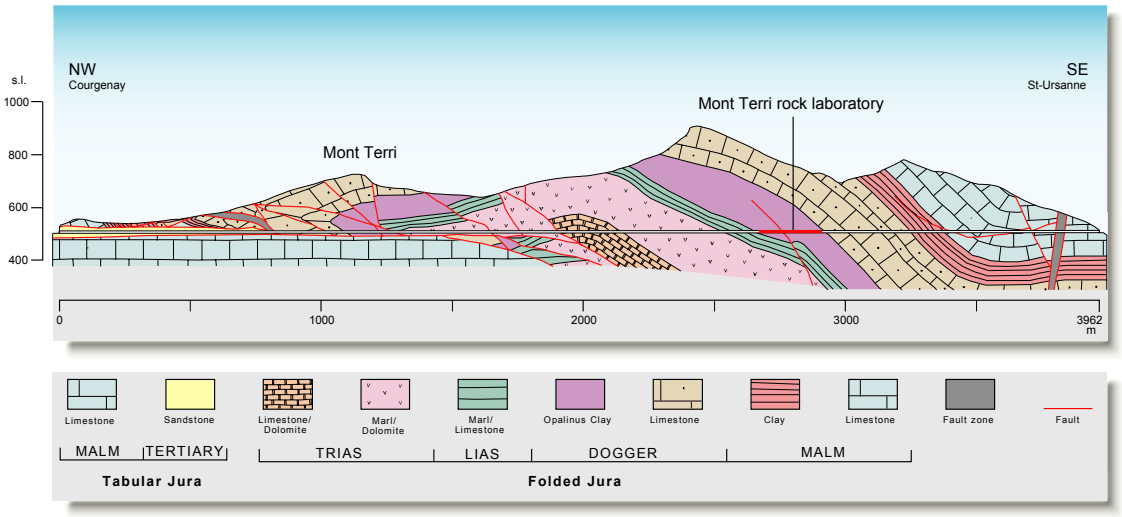

Figure 2-1 Geological profile along the motorway tunnel showing the location of the Mont Terri Rock Laboratory

The state of stress at the MTRL is estimated according to /BOS 03/:

- the maximum principal stress σ_1 with a magnitude range of 6 - 7 MPa and a sub-vertical direction of 210° azimuth and 70° dip,
- the intermediate principal stress σ_2 with a magnitude range of 4 - 5 MPa and a sub-horizontal direction of 320° azimuth and 10° dip (sub-parallel to the motorway tunnel and the security gallery), and

- the minimum principal stress σ_3 with a magnitude range of 2 - 3 MPa and a sub-horizontal direction of 50° azimuth and 20° dip (more or less normal to the motorway tunnel and the security gallery).

The HE-D test field is located in the clay-rich shaly facies near the main gallery Ga98 and the MI niche (Figure 2-2). Immediately after the excavation of the HE-D niche from the main gallery in October 2003, a geological survey was conducted by the Geotechnical Institute of Bern /NUS 04a; 04b/, /WIL 05/. The results indicated that this region seems to be homogeneous, weakly disturbed (relatively low fracture frequency) and located outside of fault zones and not intersected by significant thrusts.

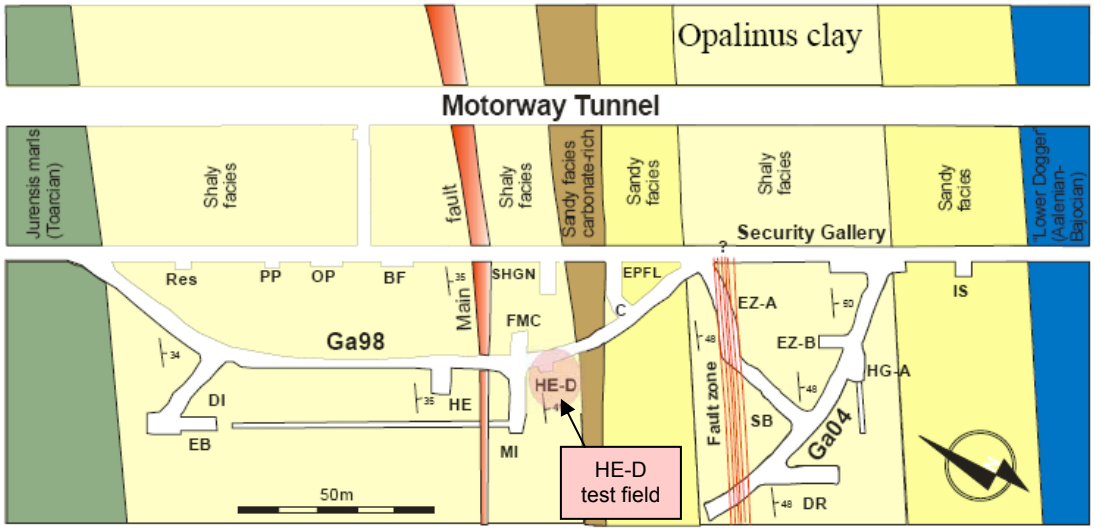

Figure 2-2 Horizontal cross section of the Mont Terri Rock Laboratory showing the location of the HE-D test field

Figure 2-3 shows the front of the HE-D niche with the mapping mesh, from which the fault planes and the bedding planes can be identified. The fault planes plunge towards the SE with angles between 30° and 65° and are sub-parallel to the bedding planes. The fault and bedding planes lead to anisotropic properties of the rock mass. Additionally, the excavation of the main gallery Ga98 and the MI niche have also created damaged and disturbed zones (EDZ) in the surrounding rock, which usually extend up to 1 m to 2 m from the opening walls, depending on opening dimension, stress state and mechanical properties of the rock mass /ALH 04/. Figure 2-4 shows the geological map of the HE-D niche surface. The interconnected fracture network composed of open joints and shear fractures extends to about 60 cm behind the shotcrete of the gallery Ga98 and some discrete fractures to 1.3 m /NUS 04a/.

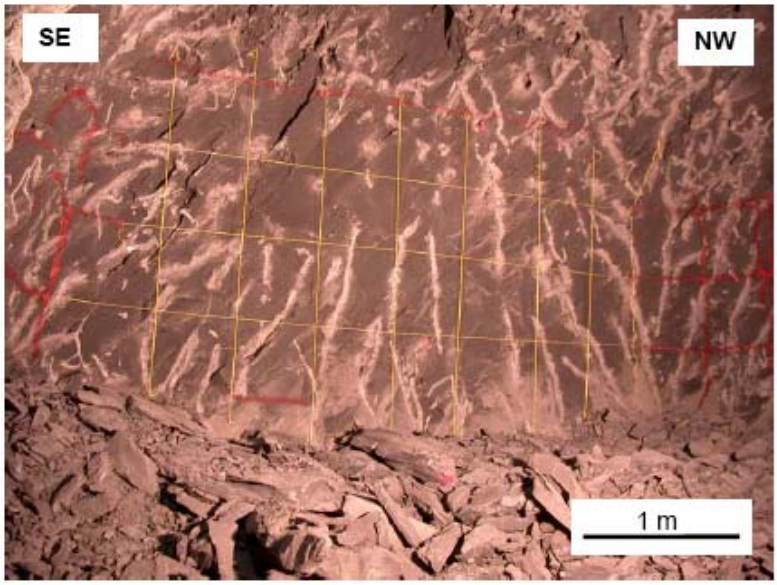

Figure 2-3 Structural map of the front of the HE-D niche

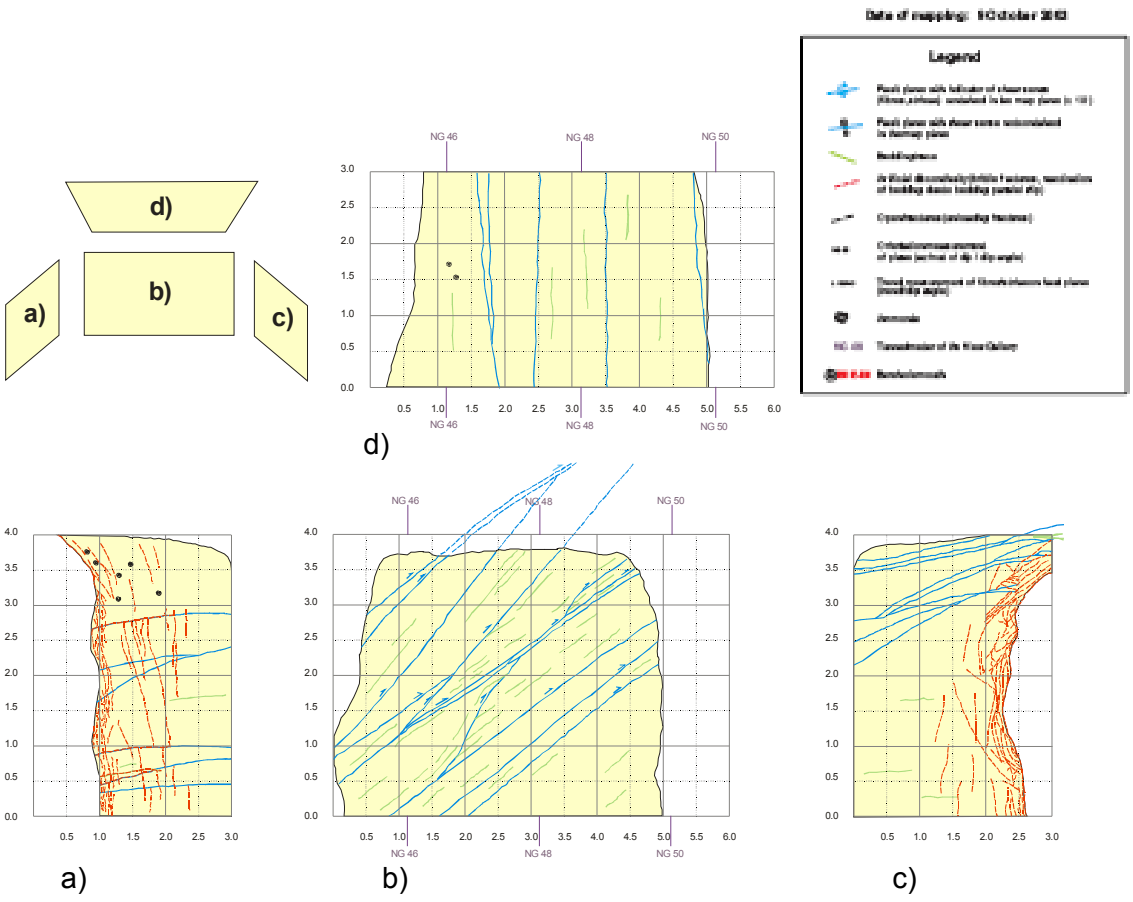

Figure 2-4 Geological and structural maps of the HE-D niche

2.3 Test Layout

The HE-D experiment was designed to heat the Opalinus clay in an undisturbed zone and to investigate its responses to heating and cooling by monitoring temperature, pore-water pressure, gas migration, and deformation at different locations within the test field. In order to enable an easy transfer of the test results to the TER experiment which would be later conducted in the Callovo-Oxfordian argillite at the main level of the MHM-URL, the very similar clay-rich shaly facies of the Opalinus clay was selected for the HE-D experiment. The test field is located near the main gallery Ga98 and the MI niche, which were excavated in 1998. Figure 2-5 illustrates the test layout with the heater borehole BHE-D0 and 24 other boreholes drilled for different measurements.

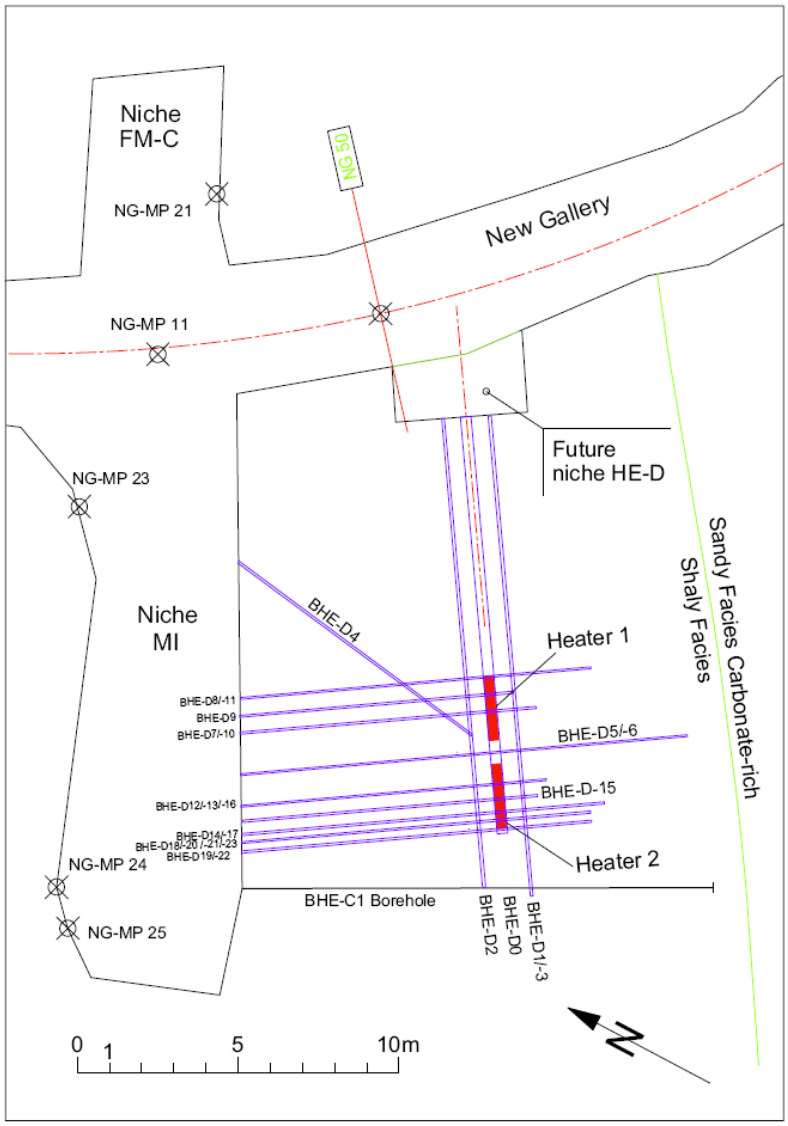

Figure 2-5 Layout of the HE-D experiment with heater and measuring boreholes

2.4 Installation of Heater

The HE-D experiment was started in October 2003 with excavation of the HE-D niche from the main gallery. In March 2004, the 300 mm wide heater borehole BHE-D0 was drilled by the company COREIS with compressed air horizontally from the HE-D niche to a depth of 14 m parallel to the bedding plane 8 m distant to the MI niche. Figure 2-6 shows a photo of the borehole drilling and coring actions. The drilled cores of 260 mm diameter and 1.0 - 2.5 m lengths exhibited visually a very compact and relative homogeneous quality, as can be seen in Figure 2-7. The big cores were used for the envisaged large-scale laboratory heating tests (section 3.5).

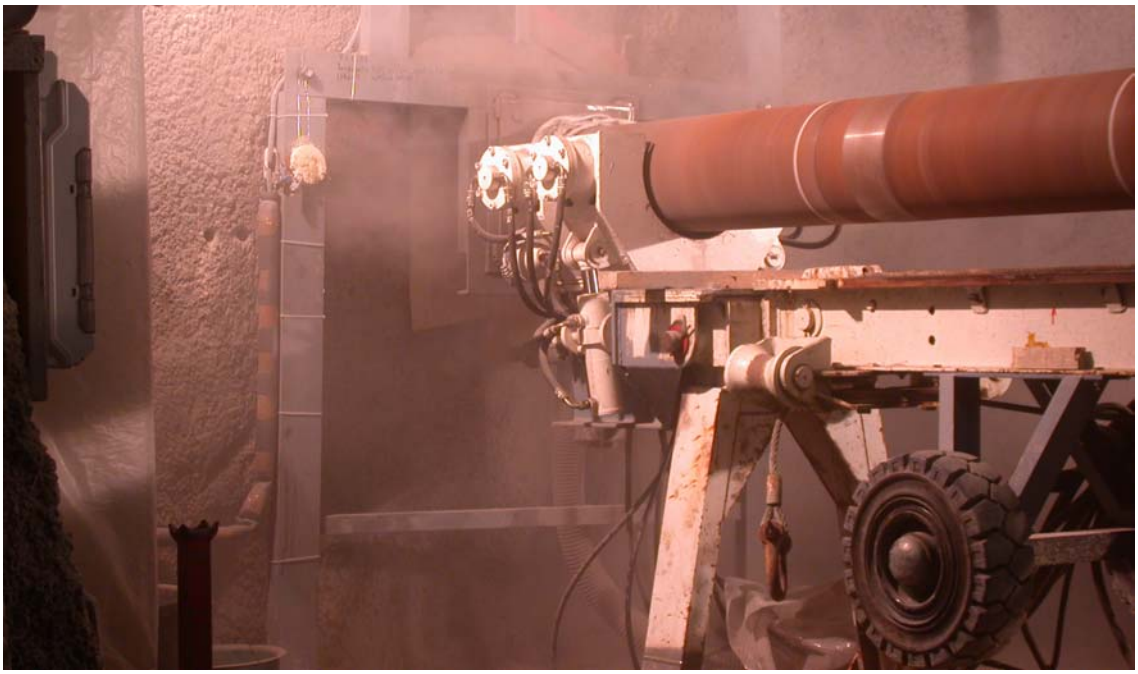

Figure 2-6 Drilling and coring of the HE-D heater borehole

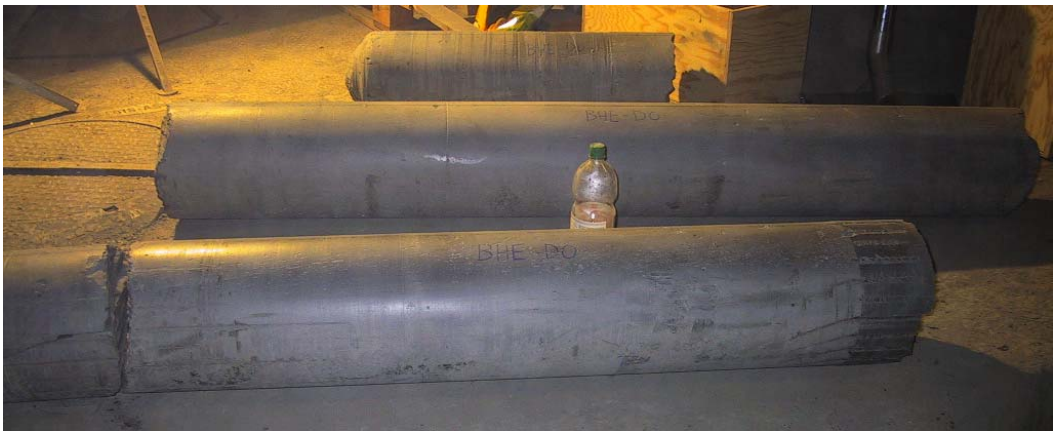

Figure 2-7 Drilled cores (D=260 mm, L=1–2.5 m) from the HE-D heater borehole

The first part of the borehole from 0 to 6.5 m was enlarged to a diameter of 335 mm and equipped with a metal tube with an inner diameter of 310 mm. In the deep part of the borehole from 6.5 m to 14 m, the electric heater equipment was installed. Figure 2-8 shows the layout of the heater borehole.

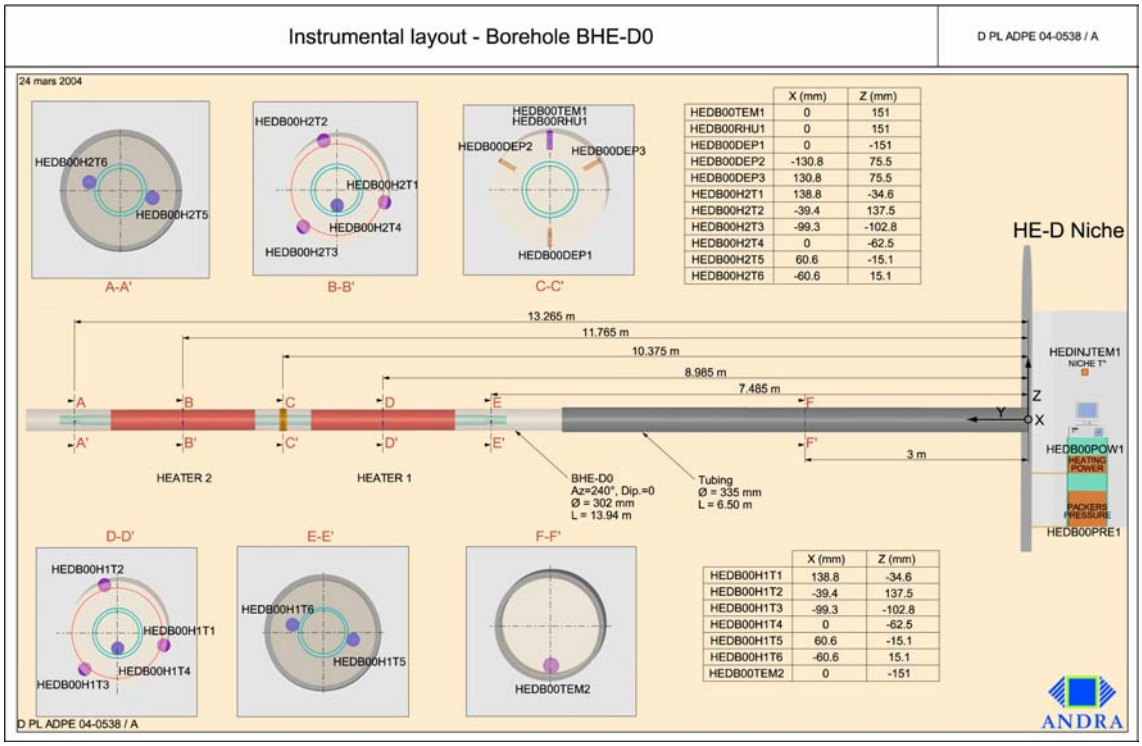

	X (mm)	Z (mm)
HEDB00TEM1	0	151
HEDB00RHU1	0	151
HEDB00DEP1	0	-151
HEDB00DEP2	-130.8	75.5
HEDB00DEP3	130.8	75.5
HEDB00H2T1	138.8	-34.6
HEDB00H2T2	-39.4	137.5
HEDB00H2T3	-99.3	-102.8
HEDB00H2T4	0	-62.5
HEDB00H2T5	60.6	-15.1
HEDB00H2T6	-60.6	15.1

	X (mm)	Z (mm)
HEDB00H1T1	138.8	-34.6
HEDB00H1T2	-39.4	137.5
HEDB00H1T3	-99.3	-102.8
HEDB00H1T4	0	-62.5
HEDB00H1T5	60.6	-15.1
HEDB00H1T6	-60.6	15.1
HEDB00TEM2	0	-151

Figure 2-8 Layout of the HE-D heater borehole with two heaters and measuring instruments

The heater equipment consists of two electric heaters and a link connecting them. Both heaters have the same dimensions. Figure 2-9 shows the details of one of them. Each heater has an effective heating element with an inflatable packer of 2 m length and two end caps. The total length of each heater is 3 m and the outer diameter is 286 mm. The heating element consisting of electric resistors is inserted into an internal metal tube. The effective heating length of both heaters is 2 x 2.58 m = 5.16 m, while the total length is 6.2 m. The heaters were designed for a maximum temperature of 150 °C at the outer surface and a maximum inflation pressure of 10 MPa in the packers. The thermal power and/or temperature as well as the pressure of the heater packers are regulated by an integral-proportional-derivative (IPD) regulator positioned in the HE-D niche. At several cross sections of the heater equipment, temperature sensors were installed to monitor and control the temperature distribution. One of the sensors serves as the reference for regulating the heating system. In the link (C-C' section in Figure

2-8), three displacement sensors, a temperature sensor and a thermohygrometer were mounted for the measurement of the borehole convergence, the temperature and the relative humidity during the test. The connection of the heaters and the instruments in the link are shown in Figure 2-10. The design, installation and operation of the heater equipment were performed by the French company GEXTER /WIL 03; 05/.

Figure 2-9 Photo and dimension of a HE-D heater

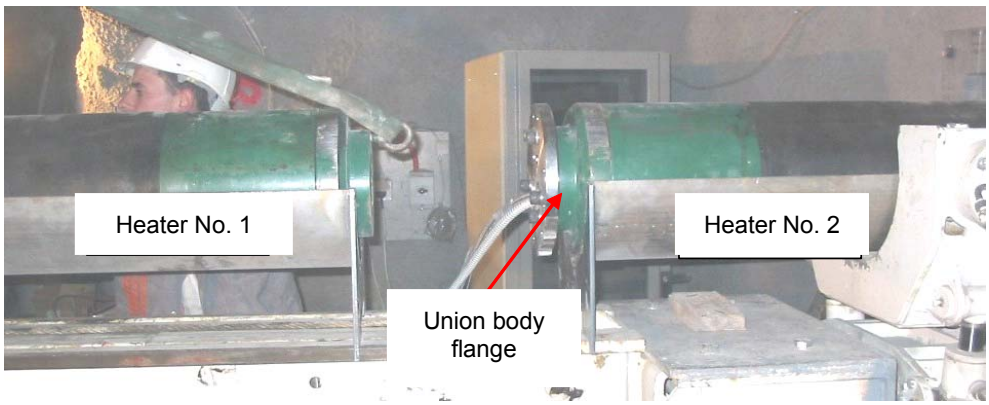

a. Link between both heaters

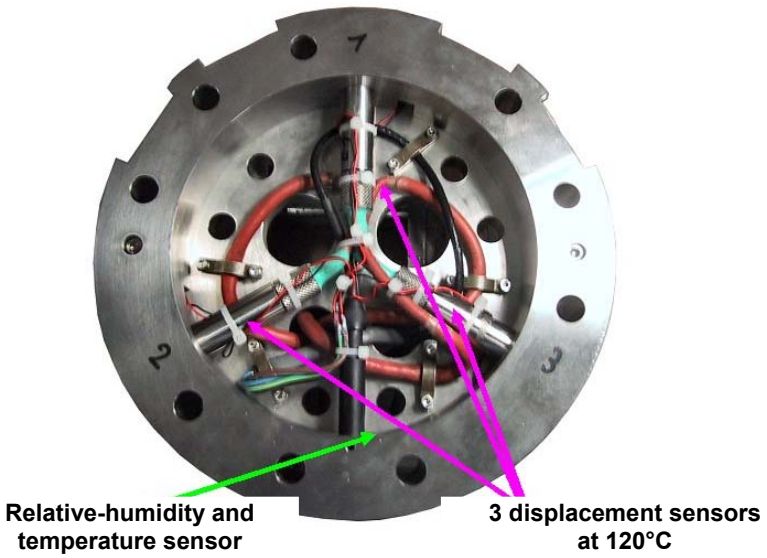

b. Instrumentation in the link

Figure 2-10 Instrumentation in the link connecting both heaters

2.5 Instrumentation

The installation of all sensors for monitoring temperature, pore-water pressure, gas migration and deformation in the clay rock around the heater equipment was performed between November 2003 and January 2004, 2 to 5 months before the drilling and installation of the heater borehole BHE-D0. The sensors were inserted in 24 measuring boreholes of different diameters between 20 and 101 mm, which were drilled with compressed air from the HE-D niche and the MI niche to the measuring positions (Figure 2-5). The drilled cores were provided to several laboratories (GRS, LAEGO, DBE-TEC and others) for characterisation of the clay rock and for determination of material parameters.

2.5.1 Temperature Measurement Arrangement

In 17 boreholes, BHE-D0 to D3, D6 to D17 and BHE-D24, temperature sensors were installed at 45 positions which are more concentrated near the heater borehole. Most temperature sensors installed by GEXTER in BHE-D0 to D3 are of PT100 type. In borehole BHE-D1, another type of optical-fibre sensors (CFO) which had been applied in the previous HE-C heating experiment were also placed by CEA in five positions

close to the PT100 sensors in order to compare the results of the different sensors. Figure 2-11 shows photos of the two types of sensors close to each other and the installation in the borehole. During the installation, each sensor was pressed against the wall of the borehole with a metallic arm activated by a micro-jack /WIL 03; 05/. After the installation, the boreholes were sealed with resin.

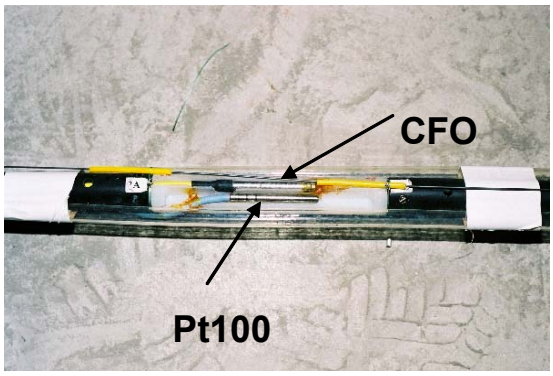

a. two types of sensors

b. insertion of the sensors

Figure 2-11 Temperature sensors used by GEXTER and CEA

The positions of the temperature sensors in boreholes BHE-D1 / D2 of 56 mm diameter and BHE–D24 of 20 mm diameter are illustrated in Figure 2-12 with names like HEDB01TEM0x, HEDB02TEM0x and HEDB24TEM0x. The other temperature sensors were installed in combination with sensors for monitoring deformation (BHE-D6) and pore-water pressure (BHE-D3, D7 to D17), respectively (see the following sections).

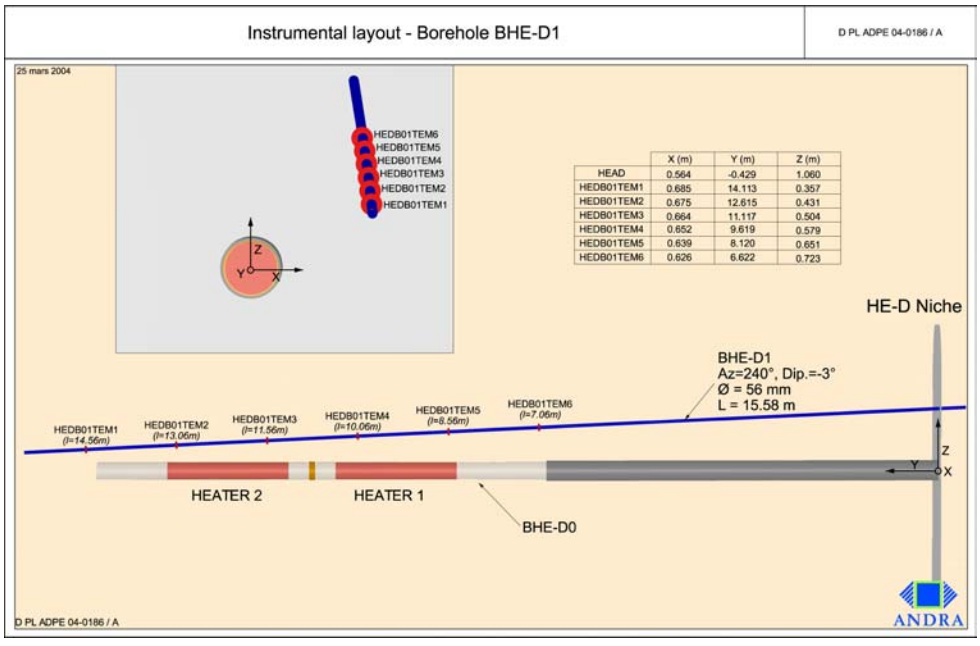

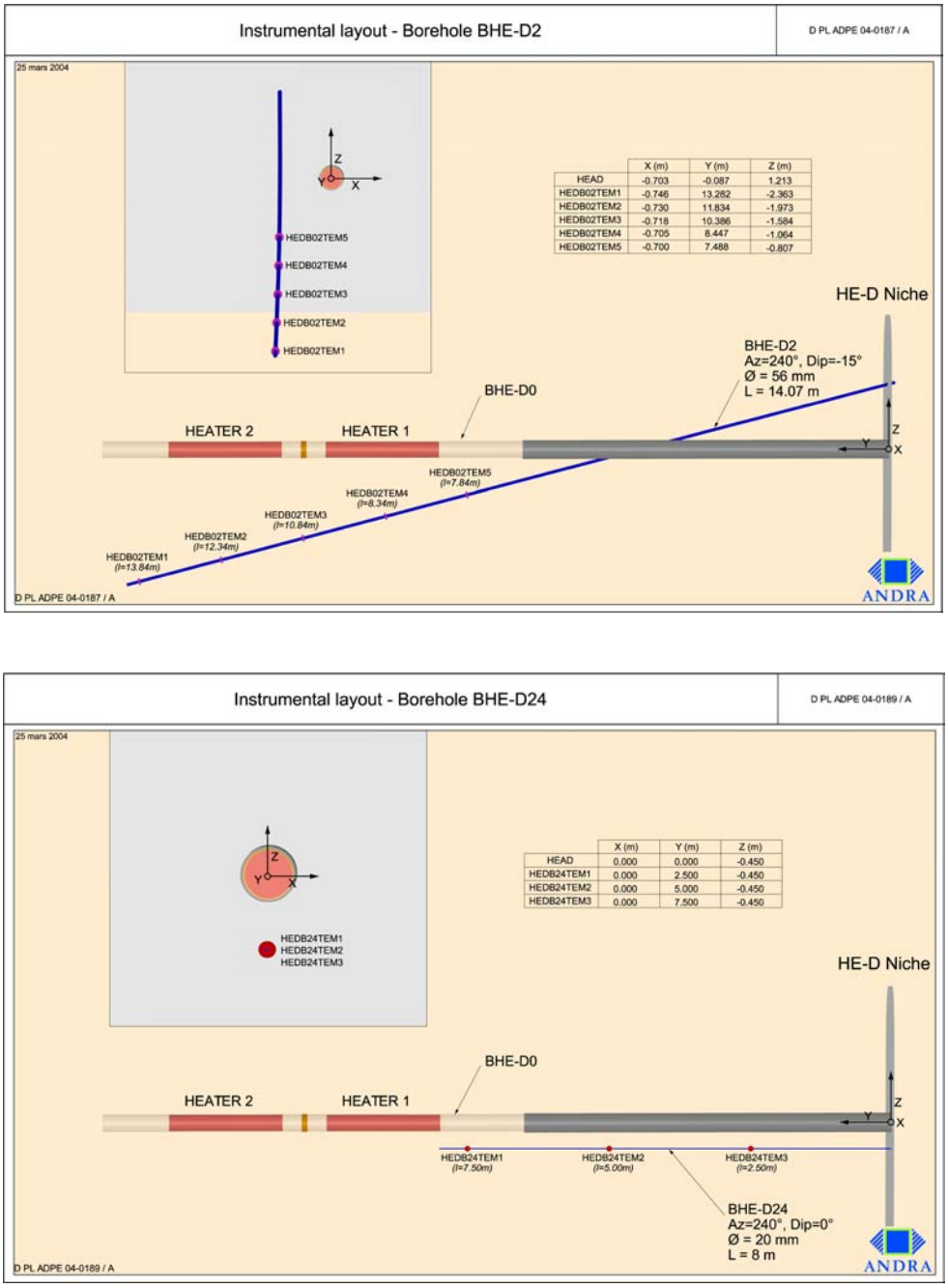

Figure 2-12 Positions of temperature sensors installed in boreholes BHE-D1/D2/D24

2.5.2 Deformation Measurement Arrangement

Two types of deformation sensors were applied for the measurement of rock deformation during the heating experiment. One type of them is the sliding micrometer installed by SOLEXPERTS in the two boreholes BHE-D4 / D5 of 101 mm diameter, and the other type is the anchored displacement system installed by DBE-TEC in borehole BHE-D6 of 86 mm diameter.

Figure 2-13 illustrates schematically the construction of the sliding micrometer used by SOLEXPERTS /WIL 03/. Basically, the probe consists of a displacement sensor between two spherical-shaped heads which can be displaced from each other in the axial direction by overcoming the force of a spring. A rod to the moveable armature of the displacement sensor connects one of the spherical-shaped heads, while the other is firmly connected to the sensor. The relative position of the heads is transmitted to the displacement transducer. The sliding micrometer probe is designed for temperatures up to 60 °C. This type of probes can measure displacements with accuracy up to ± 3 microns. HPVC tubes with measuring rings located every meter were installed in both boreholes BHE-D4 / D5. In the high temperature zone near the heaters, metal tubes with measuring rings were installed instead of the HPVC ones. The annulus between the tubes and the borehole walls were filled by injection of a bentonite/cement mortar.

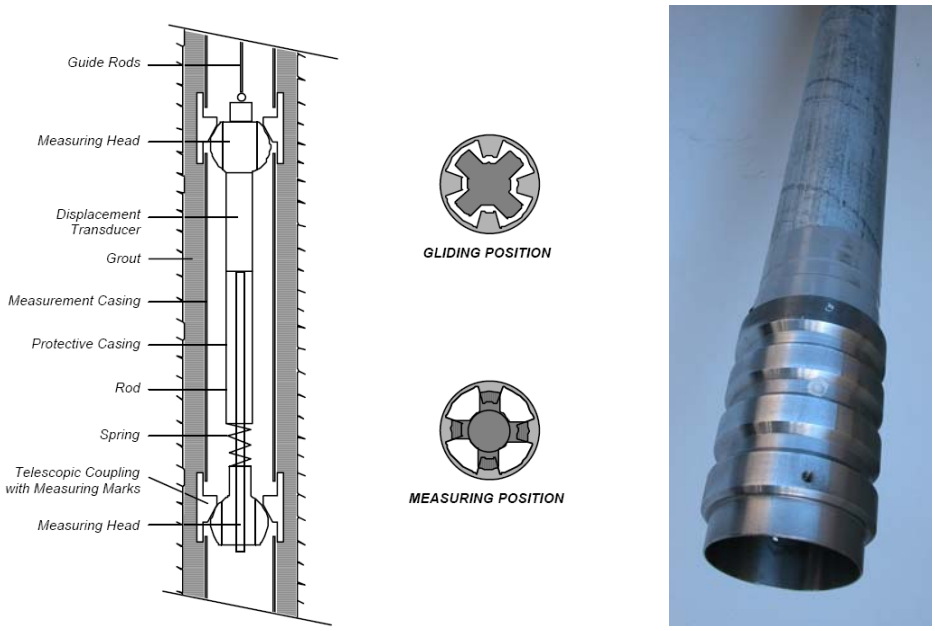

a. schematic drawing of sliding micrometer

b. connection between HPVC and metal tubes

Figure 2-13 Sliding micrometer used by SOLEXPERTS for measuring deformation

The positions of the measuring rings in the boreholes are shown in Figure 2-14. Ten measurement points (BHE-D4PT0x) were distributed along borehole BHE-D4 drilled from the MI niche downwards and inclined horizontally at an angle of 45° to the heater borehole, while the other 14 measurement points (BHE-D5PT0x) were positioned in borehole BHE-D5 drilled from the MI niche downwards at an angle of 5° in the middle

section between both heaters extending to the other side of the heater borehole by 6 m.

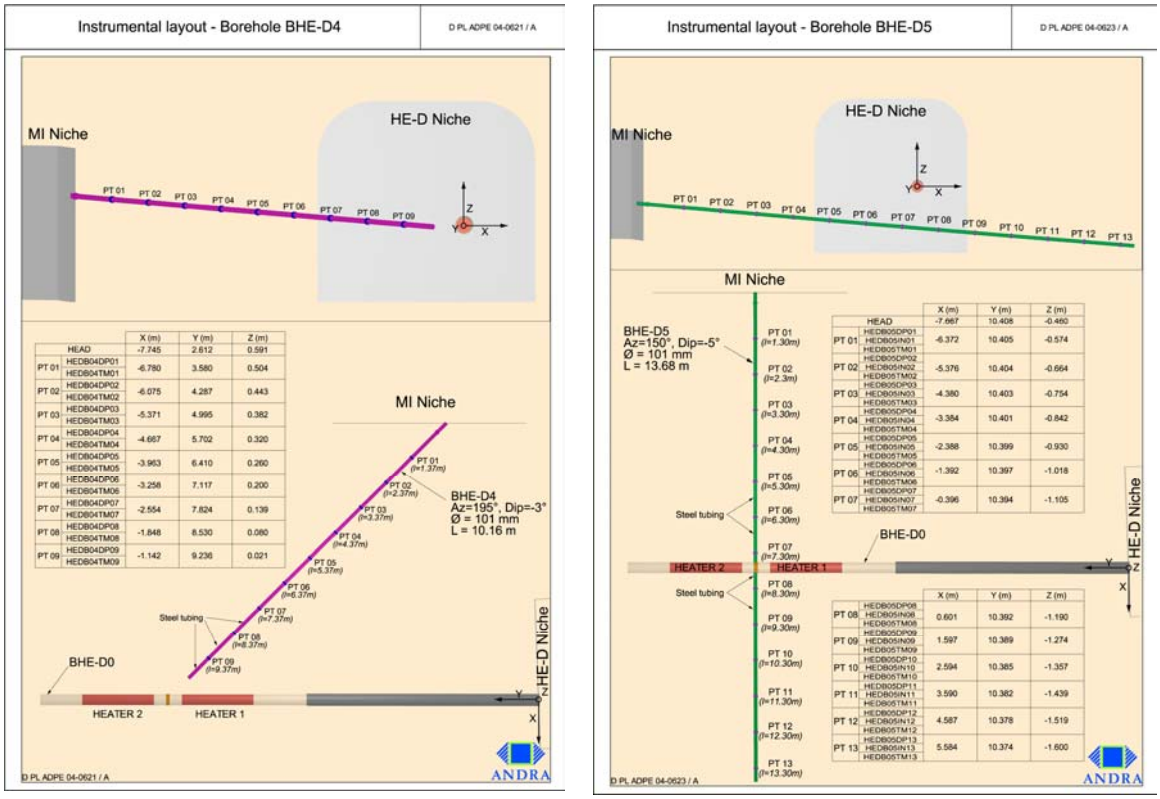

Figure 2-14 Positions of sliding micrometers installed in boreholes BHE-D4/D5

Figure 2-15 shows schematically the working principle of the anchored displacement system used by DBE-TEC /WIL 03/. This system consists of a number of extensometers outside the borehole which are placed in a canister. Within the borehole, different anchoring points are fixed at well defined positions by packers. To each anchoring point, a carbon extension cable is fixed and runs to the canister where the carbon extension cable is stretched using a spring mechanism. The extensometers in the canisters are connected to the outer ends of the carbon cable. In this way, any movement of the packers can be transferred to the extensometer and the displacement of the connected anchor is measured relative to the entrance of the borehole. The strain cable configuration contains sensors at the inner side of the borehole. These sensors give a very accurate measurement.

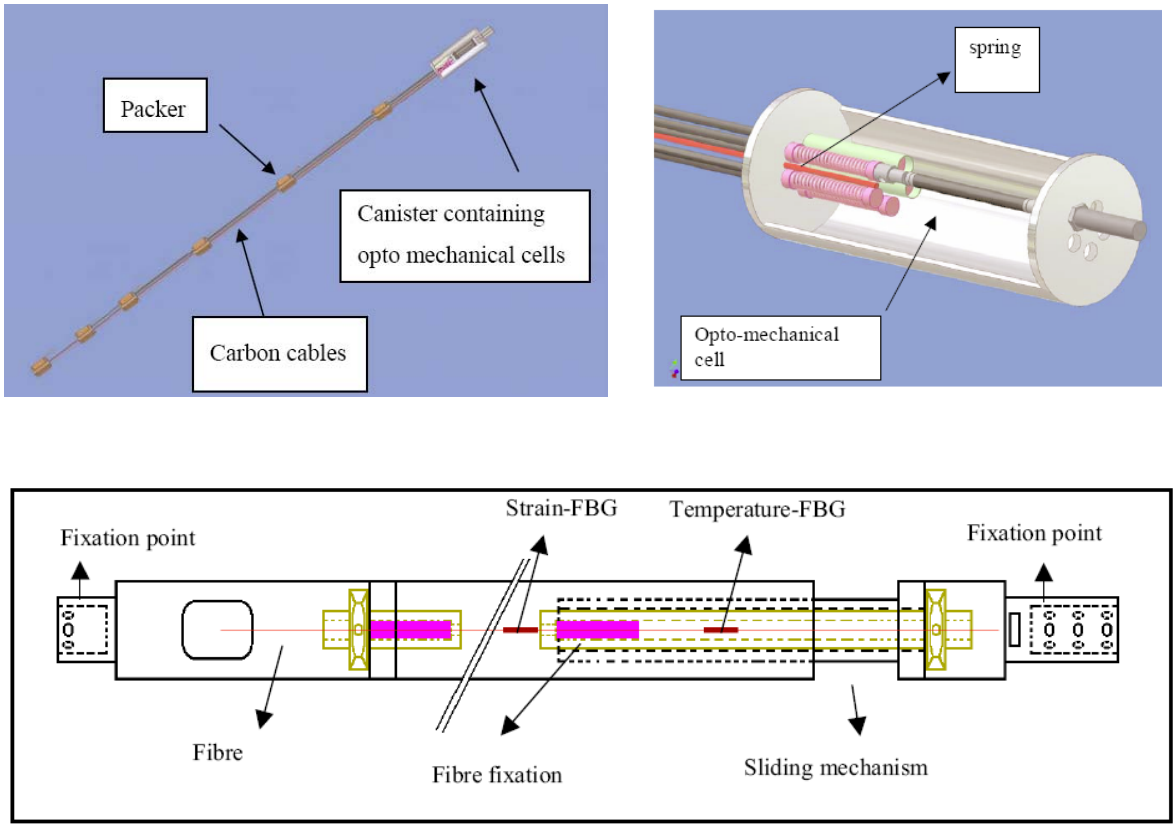

Figure 2-15 Schematic drawing of anchored displacement system used by DBE-TEC for displacement measurement

Combined with the five displacement sensors (HEDB06DP0x), seven additional optical fibre sensors (HEDB06TM0x) for temperature measurement were also placed at different locations in borehole BHE-D6 which was drilled horizontally perpendicular to the heater borehole in the middle section between both heaters. The temperature cable consists of a long fibre wherein FBGs can be located at several positions. The fibre is reinforced by carbon material in order to protect the fibre from environmental impacts. The locations of the optical-fibre sensors for measuring deformation and temperature are shown in Figure 2-16. After the installation, the borehole was closed but not sealed because the measuring system does not allow it.

Additionally, four inclinometric-measurement stations of SOLEXPERTS were also fixed on the drift walls to trace the evolution of the movements of the drifts walls. Figure 2-17 shows the stations above the heater borehole BHE-D0 and the measuring borehole BHE-D5.

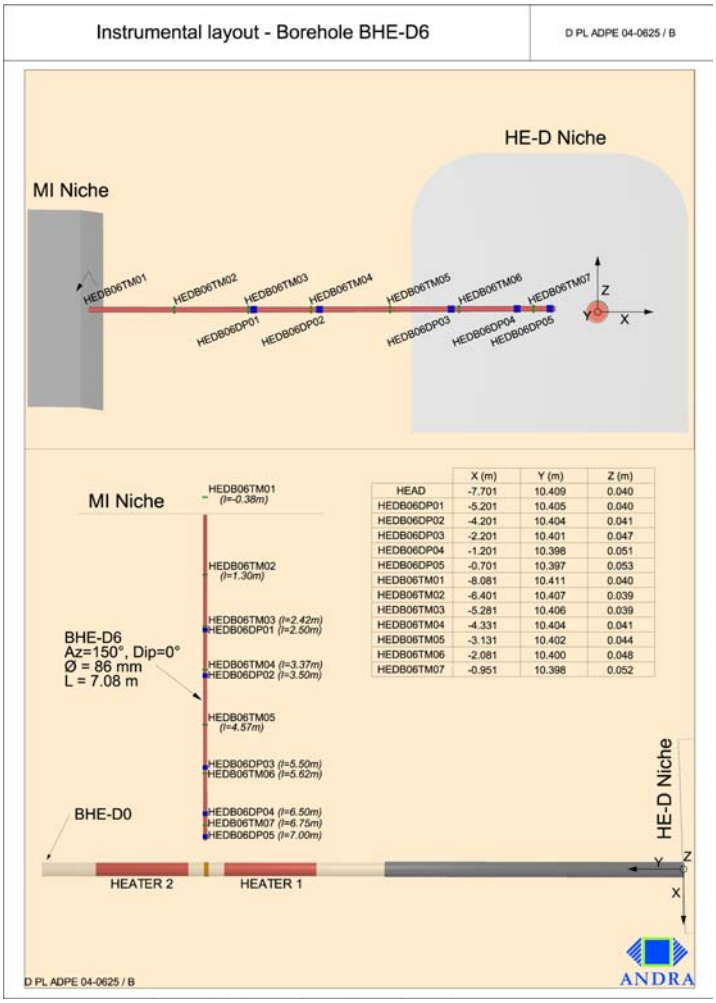

Figure 2-16 Positions of anchored displacement system and temperature sensors installed in borehole BHE-D6

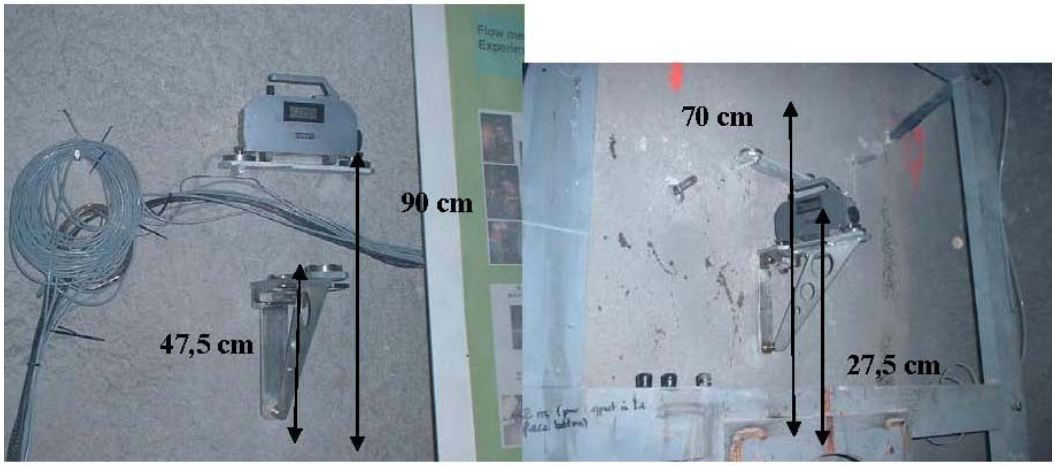

BHE-D05 BHE-D0

Figure 2-17 Inclinometers installed above the boreholes BHE-D5 (left) in the MI niche and BHE-D0 (right) in the HE-D niche

2.5.3 Pore-Water Pressure Measurement Arrangement

The particular conditions of very low permeability and free water content as well as water chemistry in argillaceous formations require adequate systems for monitoring the hydraulic behaviour such as pore pressure and permeability. For monitoring pore-water pressure in the Opalinus clay during the HE-D heating experiment, two types of mini-packer-systems were developed and applied by GSR and GEXTER. The following factors which may prove to be advantageous for the long-term monitoring systems have been considered during the development of the systems:

- minimisation of borehole diameter for limitation of damaged zone around the borehole,
- minimisation of the effective volume of the test interval for elimination of effects of thermal expansion of the water injected in the interval,
- mechanical support of the test interval and sealing of the borehole to prevent borehole collapse which would have an impact on the hydraulic state in the surrounding rock,
- connection of flow lines at both the top and bottom ends of the intervals to allow for a complete water flushing, and
- selection of adequate materials for the equipment to prevent corrosion.

GRS mini-packer system

The measurement equipment used by GRS for the measurement of pore-water pressure in the HE-D experiment consists of the slim-hole packer systems (mini-packer), a sensor rack with piezometric pressure transducers and PT100 temperature probes, a data acquisition system, and a computer with modem for data transfer (Figure 2-18). The mini-packer has a diameter of 20 mm and a length of 55 mm. In order to simultaneously measure the temperature, a PT100 sensor was additionally fixed at the bottom end. The mini-packer was installed at a distance of 3 mm to the borehole end and fixed by mechanically squeezing a rubber-ring of 10 mm length. The test interval volume of about 1 cm^3 is filled with PEARSON water through a 1/4”-sized inflow line. The air in the interval is displaced through the outflow line. The water pressure in the test interval is recorded by a piezo-resistive transducer connected to the outflow line. The system applied is designed for a maximum pressure of 5 MPa.

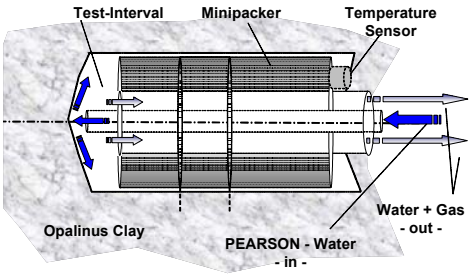

a. Construction of the mini-packer

b. Prototype of 20 mm diameter

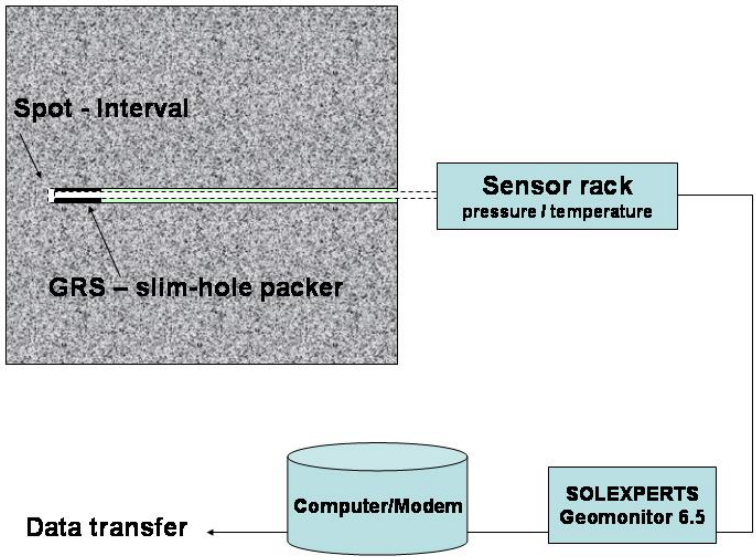

c. Configuration of the test equipment

Figure 2-18 GRS mini-packer system for monitoring pore pressure and temperature

Two arrays of 11 slim boreholes of 20 mm diameter and different lengths of up to 10 m were drilled from the MI niche upwards and downwards perpendicular to the heater borehole BHE-D0 and equipped with the mini-packer systems in October/November 2003 (Figure 2-19). Four boreholes BHE-D8 to D11 reached the upper area at distances of 0.9 - 3.0 m to heater 1, four other ones BHE-D14 to D17 were placed in the lower area at distances of 0.8 - 3.0 m to heater 2, and the remaining three BHE-D7, D12 and D13 were located near the MI niche at distances of 4.0 - 7.0 m to the heaters. To avoid possible leakage and collapse of the boreholes, resin was injected into the remaining free space.

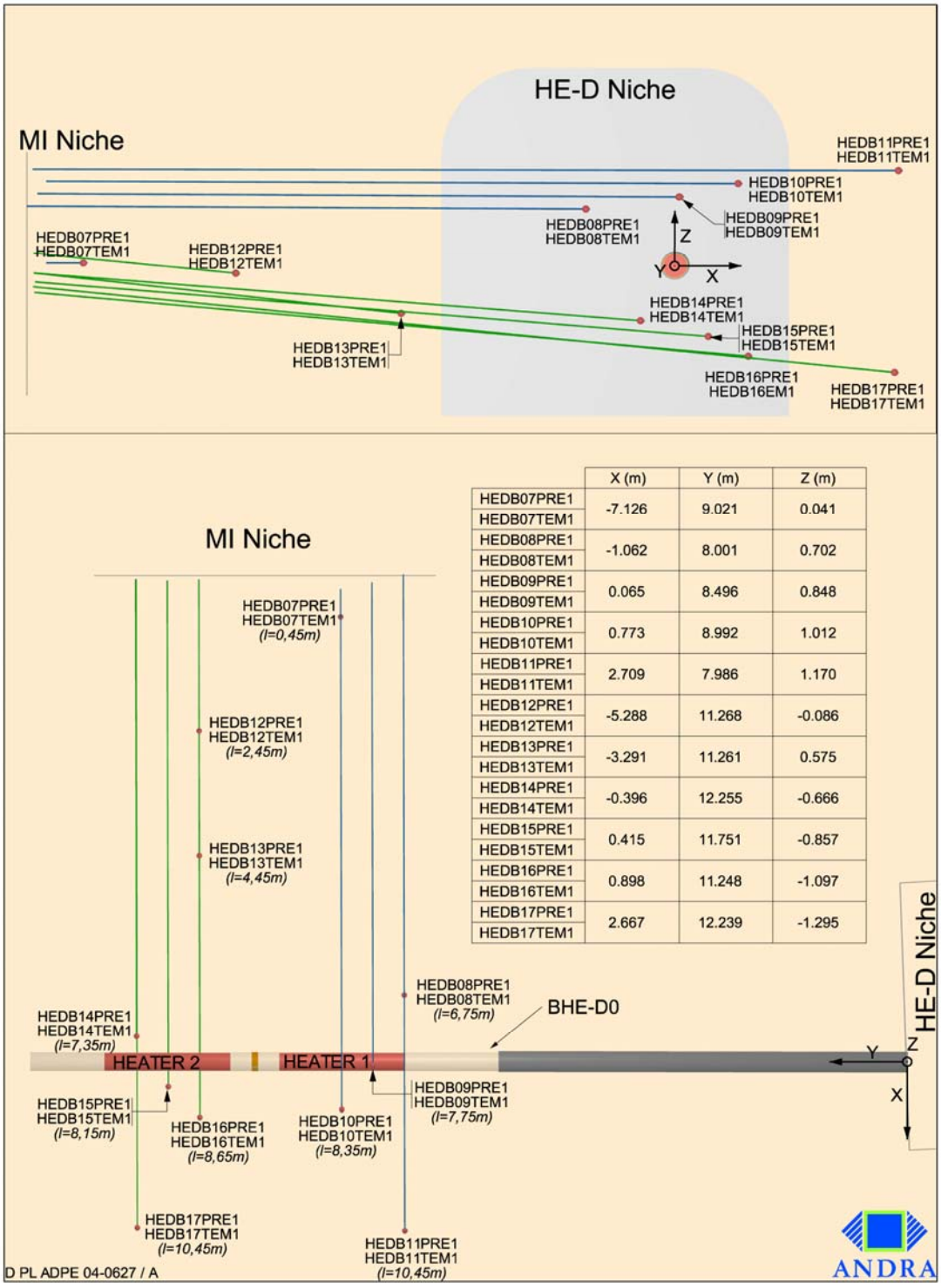

	X (m)	Y (m)	Z (m)
HEDB07PRE1 HEDB07TEM1	-7.126	9.021	0.041
HEDB08PRE1 HEDB08TEM1	-1.062	8.001	0.702
HEDB09PRE1 HEDB09TEM1	0.065	8.496	0.848
HEDB10PRE1 HEDB10TEM1	0.773	8.992	1.012
HEDB11PRE1 HEDB11TEM1	2.709	7.986	1.170
HEDB12PRE1 HEDB12TEM1	-5.288	11.268	-0.086
HEDB13PRE1 HEDB13TEM1	-3.291	11.261	0.575
HEDB14PRE1 HEDB14TEM1	-0.396	12.255	-0.666
HEDB15PRE1 HEDB15TEM1	0.415	11.751	-0.857
HEDB16PRE1 HEDB16TEM1	0.898	11.248	-1.097
HEDB17PRE1 HEDB17TEM1	2.667	12.239	-1.295

Figure 2-19 Positions of pore-water pressure test intervals and temperature sensors installed in boreholes D07 to D17

After connecting the probes to the sensor racks in the MI niche (Figure 2-20), the test intervals were flushed with PEARSON water and the air was removed. Then the intervals were closed at atmospheric or slightly increased (< 200 kPa) pressure. The

pressure and temperature transducers were connected to the data acquisition system (SOLEXPERTS GEOMONITOR Version 6.5). All components are assembled in a measuring cabinet (Figure 2-21). The system can be controlled locally via keyboard or remotely via modem.

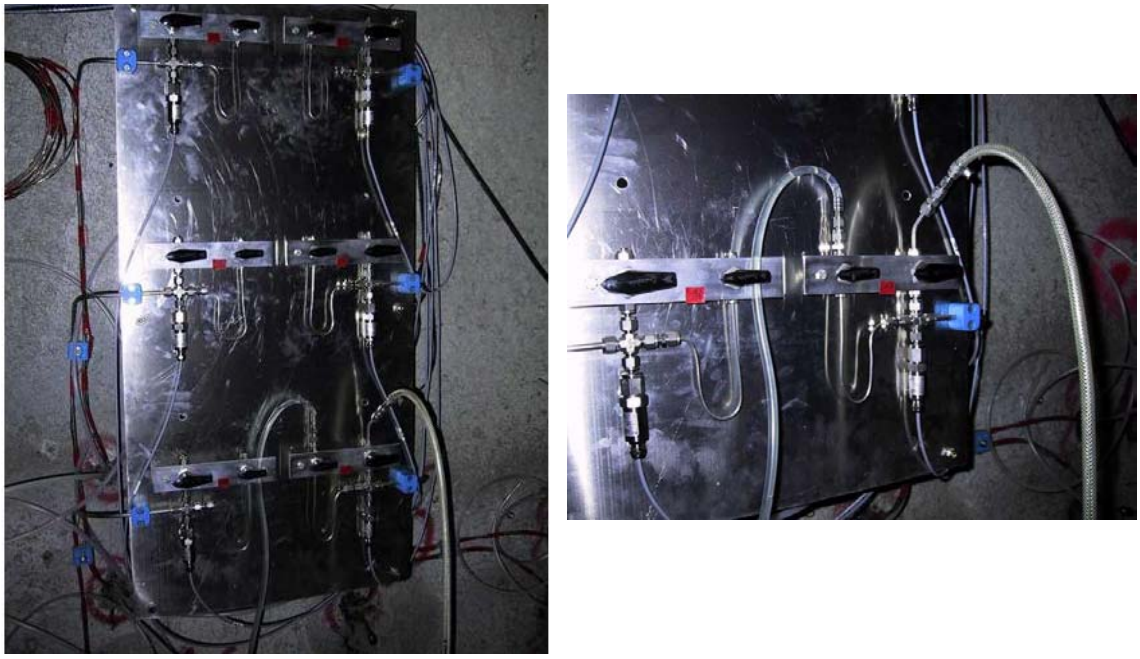

Figure 2-20 Sensor rack of array 2 with the valves connected to the 3 mm and 6 mm stainless steal tubes (left), and detail of the valve/sensor system of borehole BHE-D17 during saturation with PEARSON water (right)

Figure 2-21 Measuring cabinet for monitoring pore-water pressure and temperature

GEXTER mini-packer system

Figure 2-22 presents the GEXTER packer system installed in borehole BHE-D3 for measurement of the pore-water pressure and temperature near heater 1. The first part of the borehole was drilled with a diameter of 76 mm and then continued with 19 mm for the test interval, to minimize the damaged zone around the test interval. The test interval volume of 3.6 cm^3 was filled with synthetic formation water through a specific inflow line. The air in the interval was displaced out through another 1/8"-sized line. A temperature sensor was also installed in the test interval. The borehole was sealed by injection of resin.

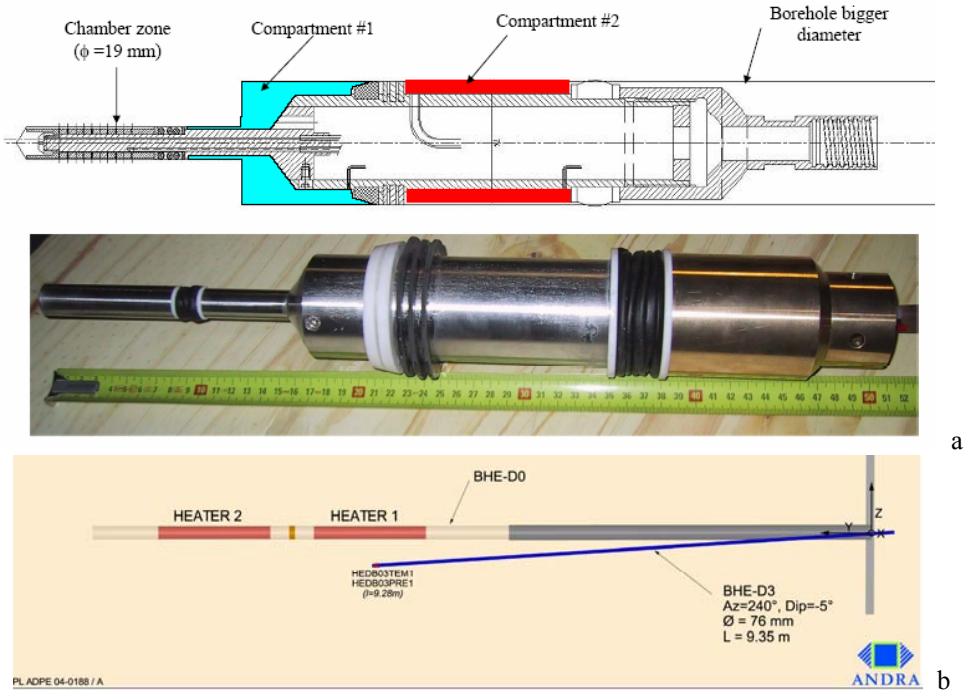

Figure 2-22 GEXTER mini-packer system for measuring pore-water pressure and temperature, a) packer, b) measurement location

2.5.4 Gas Migration Testing Arrangement

For investigating the gas pressure development in sealed boreholes and determining the gas permeability of the host rock in the different stages of the HE-D experiment, two sets of boreholes (BHE-D18 to BHE-D23) with a diameter of 76 mm and a length of about 10 m were drilled from the MI niche perpendicular to the heater borehole into the

test region. Each set consists of one injection borehole and two parallel extraction boreholes with a horizontal and vertical distance of 30 to 40 cm to the injection borehole, respectively. The injection boreholes pass the heater borehole at a distance of 0.70 m and 1.55 m, respectively. All six boreholes were sealed with a quadruple packer system for gas testing in separate intervals.

Figure 2-23 shows the arrangement of the boreholes with regard to the heater borehole BHE-D0. The multi-packer systems with a diameter of 76 mm are shown in Figure 2-24. They were manufactured by the Swiss company SOLEXPERTS AG. The packers consist of a 50 mm stainless steel tube to which four inflatable rubber seals are mounted. From each seal element a capillary runs to valve panels in the MI niche for inflation with water up to a pressure of 40 bars. Between these rubber seals sintered ceramic tubes with a porosity of 50 vol% were installed in order to have a central sample interval and two additional guard intervals which withstand the convergence pressure of the surrounding host rock and guarantee a defined volume. From the front end and the back end of each interval capillaries run to the MI niche. All capillaries were connected to valve panels mounted to the gallery wall. For observation and recording of the water pressure in the sealing elements and the gas pressure in the intervals, the panels were equipped with optical and electronic pressure gauges which were connected to the data acquisition system.

A principle drawing of the packer system with the capillaries for inflation of the sealing elements, for gas injection (FLOW 1 to FLOW 4), and for pressure measurement (PRESSURE 1 to PRESSURE 4) is shown in Figure 2-24, and Figure 2-25 shows the valve panels in the MI niche.

After installation of the packers in the respective boreholes and after connecting the capillaries to the corresponding valves, all the packers were inflated one after the other up to 35 bars with water by the use of a manual pump. The air in the injection tube and in the dead volume of the packer was not extracted; it remained in the system. Two hours after inflation of all packers, the pressure had decreased by about 5 bars to 30 bars. All packers were again inflated to 35 bars.

Two months after inflation the pressure was checked again. It had decreased in all the packers to a level of 25 to 30 bars. All packers were again inflated to 35 bars.

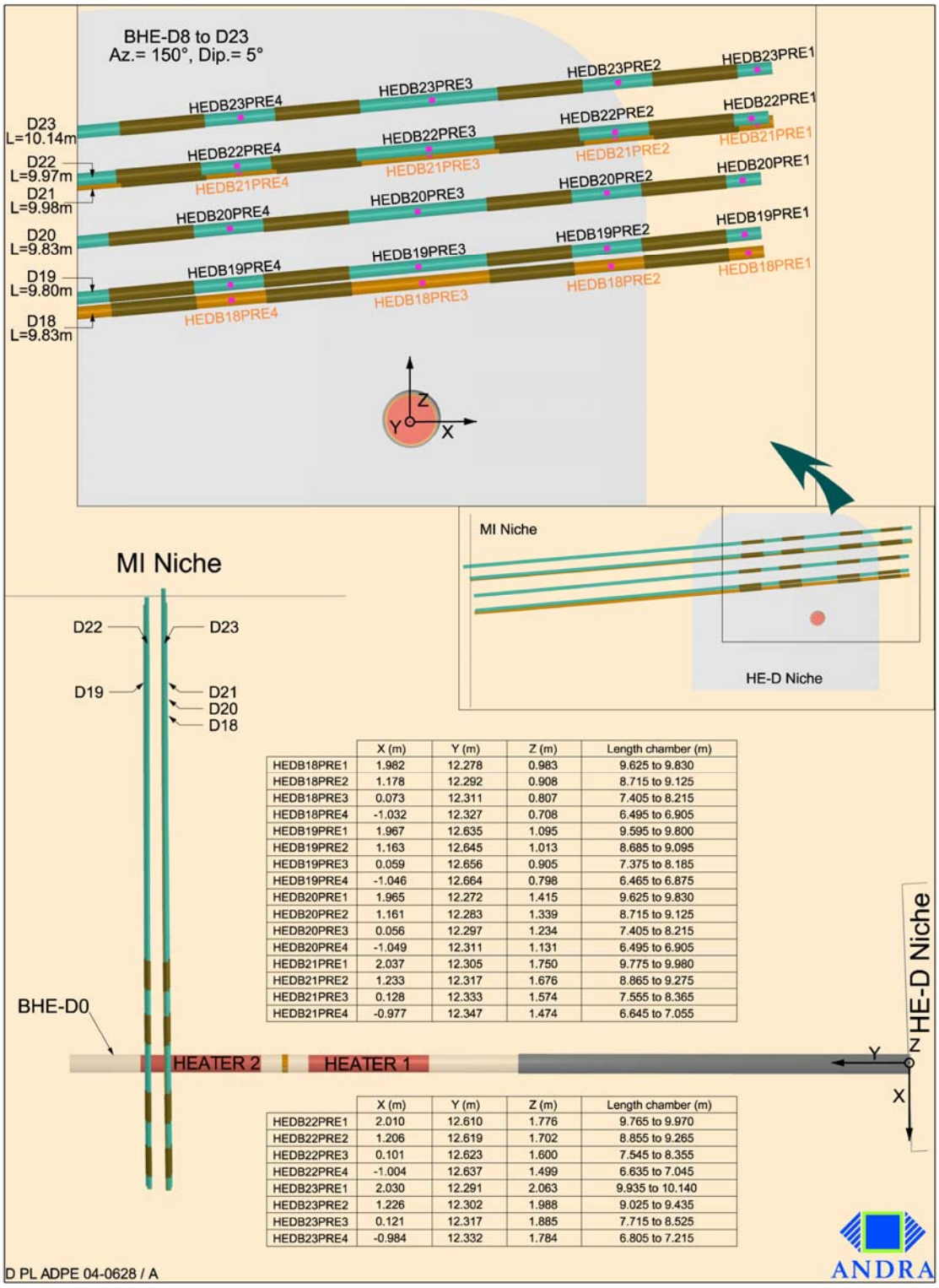

	X (m)	Y (m)	Z (m)	Length chamber (m)
HEDB18PRE1	1.982	12.278	0.983	9.625 to 9.830
HEDB18PRE2	1.178	12.292	0.908	8.715 to 9.125
HEDB18PRE3	0.073	12.311	0.807	7.405 to 8.215
HEDB18PRE4	-1.032	12.327	0.708	6.495 to 6.905
HEDB19PRE1	1.967	12.635	1.095	9.595 to 9.800
HEDB19PRE2	1.163	12.645	1.013	8.685 to 9.095
HEDB19PRE3	0.059	12.656	0.905	7.375 to 8.185
HEDB19PRE4	-1.046	12.664	0.798	6.465 to 6.875
HEDB20PRE1	1.965	12.272	1.415	9.625 to 9.830
HEDB20PRE2	1.161	12.283	1.339	8.715 to 9.125
HEDB20PRE3	0.056	12.297	1.234	7.405 to 8.215
HEDB20PRE4	-1.049	12.311	1.131	6.495 to 6.905
HEDB21PRE1	2.037	12.305	1.750	9.775 to 9.980
HEDB21PRE2	1.233	12.317	1.676	8.865 to 9.275
HEDB21PRE3	0.128	12.333	1.574	7.555 to 8.365
HEDB21PRE4	-0.977	12.347	1.474	6.645 to 7.055

	X (m)	Y (m)	Z (m)	Length chamber (m)
HEDB22PRE1	2.010	12.610	1.776	9.765 to 9.970
HEDB22PRE2	1.206	12.619	1.702	8.855 to 9.265
HEDB22PRE3	0.101	12.623	1.600	7.545 to 8.355
HEDB22PRE4	-1.004	12.637	1.499	6.635 to 7.045
HEDB23PRE1	2.030	12.291	2.063	9.935 to 10.140
HEDB23PRE2	1.226	12.302	1.988	9.025 to 9.435
HEDB23PRE3	0.121	12.317	1.885	7.715 to 8.525
HEDB23PRE4	-0.984	12.332	1.784	6.805 to 7.215

Figure 2-23 Arrangement of gas test intervals constructed in boreholes BHE-D18 to BHE-D23 with regard to the heater borehole BHE-D0

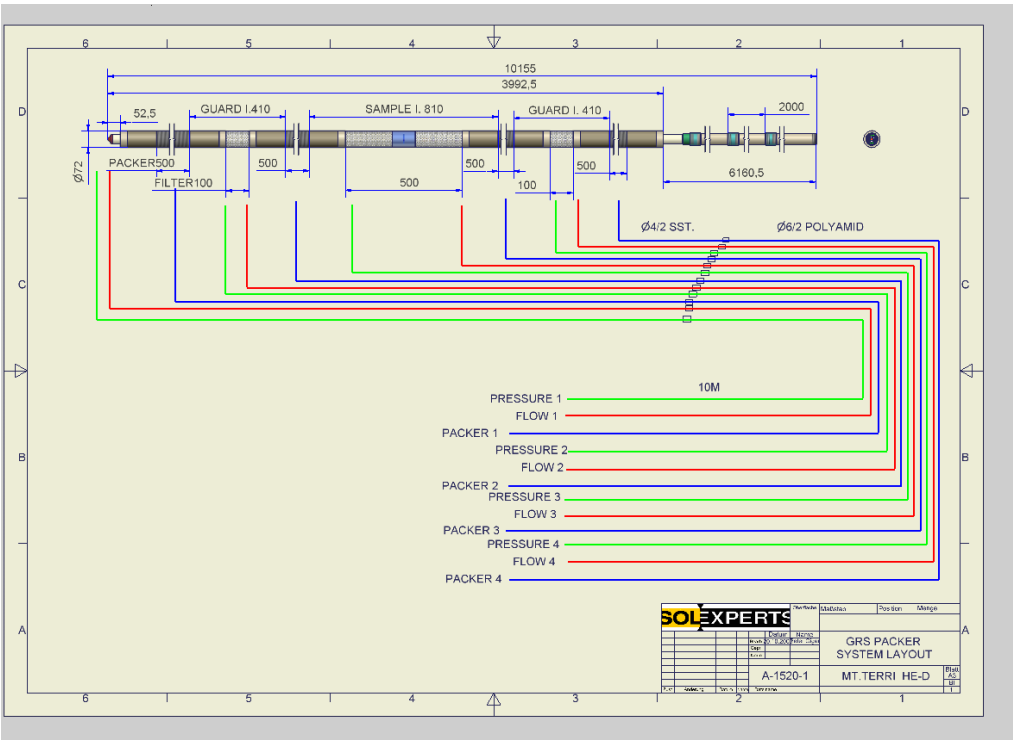

Figure 2-24 Principle drawing of a multi-packer system with the capillaries for inflation, gas injection, and pressure determination

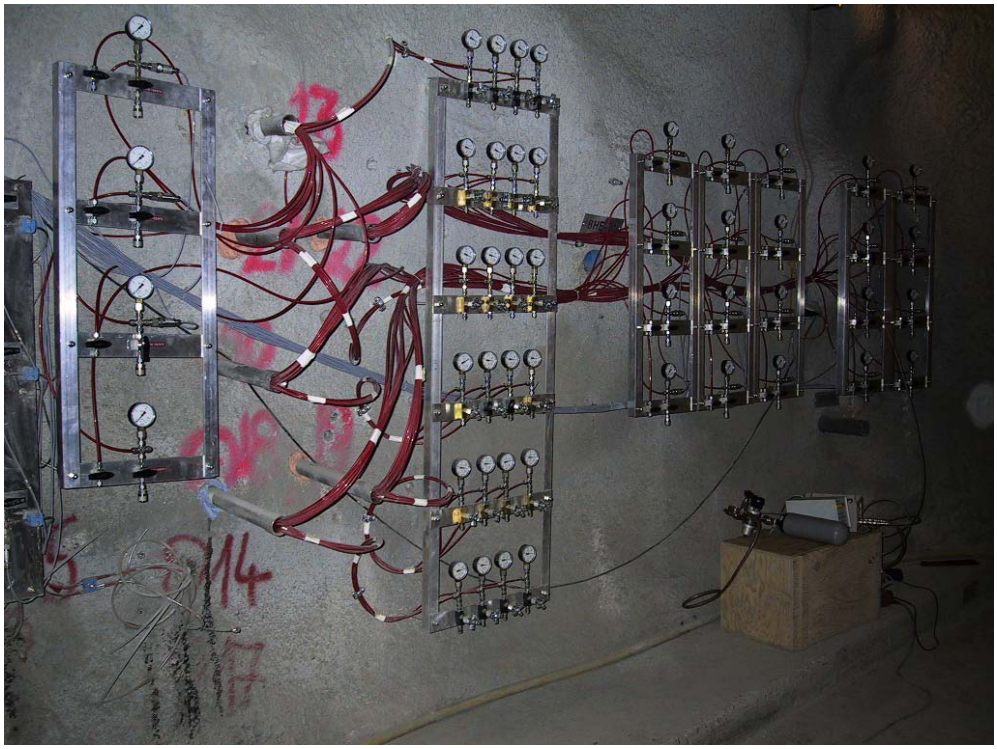

Figure 2-25 Valve panels for gas pressure measurement

In summary, one heater borehole and 24 measuring boreholes were drilled from the drifts into the clay rock in the HE-D experiment and equipped with 45 temperature sensors, 32 deformation sensors, 12 pore-water pressure sensors, and 24 gas pressure sensors. Before the installations, the measuring sensors as well as the systems were tested and calibrated. Most of the measurements and the data acquisition were performed automatically with remote supervision via modem and internet connection. The collected data were evaluated and provided quarterly by each partner to the other participants for the interpretation through numerical simulations. More details about the instrumentations by the other partners for monitoring temperature and deformation are found in the interim reports of the HE-D experiment /WIL 03; 05/, whereas the results of the GRS measurements of the pore-water pressure and gas migration are presented in detail in the following sections.

2.6 Test Conduction

The HE-D experiment was designed and prepared in the time period between January and September 2003. In this phase, the in-situ test field in the MTRL was selected, the positions of the heater equipment and the measuring instruments were identified, the test procedure was developed, and all the test equipments and measuring systems were tested and calibrated by the project partners. The test design was supported by pre-operational scoping calculations performed by the different modelling teams to estimate the initial conditions of the test field and to predict the evolution of potential THM processes in the clay rock during the experiment.

After the preparation, the in-situ experiment was started in October 2003 with excavation of the HE-D niche and the geological mappings of the test area. Following that, drilling and instrumentation of the measuring boreholes were performed step by step until January 2004. From the boreholes, core samples were taken for characterization of the clay rock. After the installation of the sensors, the measurements were immediately initiated. After a stabilized state had been reached, the heater borehole was drilled and equipped in March 2004.

One month later, on 6 April 2004, the first heating phase was launched by switching on both heaters with a total electric power supply of 650 Watts and by inflation of the heater-packers to a pressure of about 1 MPa. This first heating phase lasted over 3 months. On 7 July 2004, the power supply was increased up to 1950 Watts for the

second heating phase over more than 8 months. Within this heating phase, two disturbances took place. Two weeks after starting the second heating phase, the heater-packers were damaged, leading to a release of oil from the packers and thus a reduction of the pressure to zero for one week. In addition, the power supply was interrupted on 17 December 2004 for a short period of time. Following the heating phase, a cooling phase was carried out for further 7 months. At the end of the cooling phase, GRS performed a series of permeability measurements by injecting PEARSON water into the mini-packer intervals. In addition, the gas entry / breakthrough pressure and the gas permeability of the heated clay rock was measured in the multi-packer test intervals. Finally, a dismantling followed for examination of the heater equipment and the measuring instruments. Unfortunately, the heater equipment could not be retrieved from the borehole because the tubing was broken by pulling. Laboratory post-tests were also conducted on cores drilled from the heated area. Figure 2-26 illustrates the test procedure with various phases in terms of heat power supply and heater inflation pressure.

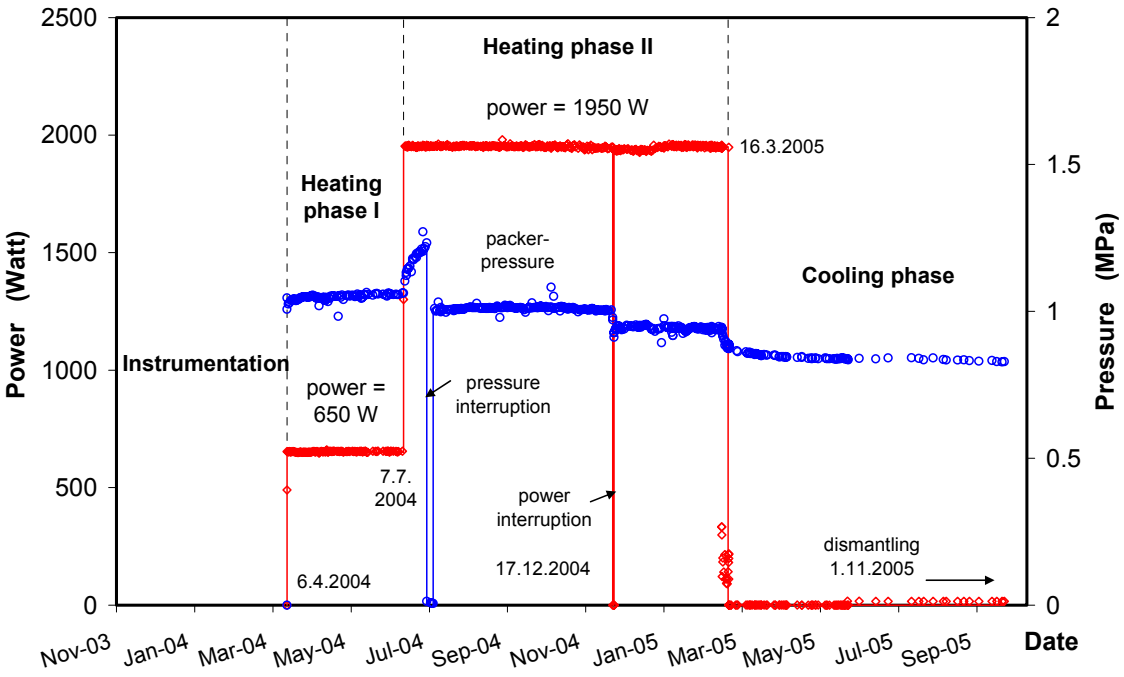

Figure 2-26 HE-D test procedure in terms of heat power supply and packer pressure

Accompanying the in-situ experiment, various laboratory tests were carried out at the GRS geotechnical laboratory in order to provide a database for identification of parameters associated with the constitutive models and to investigate thermal effects on the hydro-mechanical behaviour of the Opalinus clay (see Chapter 3).

Before and during the in-situ experiment, responses of the clay rock to the envisaged thermal loadings were blindly predicted numerically by the modelling teams of GRS, DBE-TEC, CEA, UPC, LML and LAEGO using different constitutive models and codes. The comparison between calculations and measurements served to calibrate the model parameters and to improve the models. With support of the final modelling results, the THM processes observed during the experiment were analyzed and interpreted, respectively. GRS's modelling work is presented in Chapter 4 in comparison with the measurement data.

2.7 Results of Measurements

2.7.1 Temperature

The recorded data of rock temperature are shown in summary diagrams in Figure 2-27 (Array 1; above the heater) and Figure 2-28 (Array 2; below the heater). The radial distance of each measuring location to the axis of the heater borehole BHE-D0 is given in the legend of the diagrams.

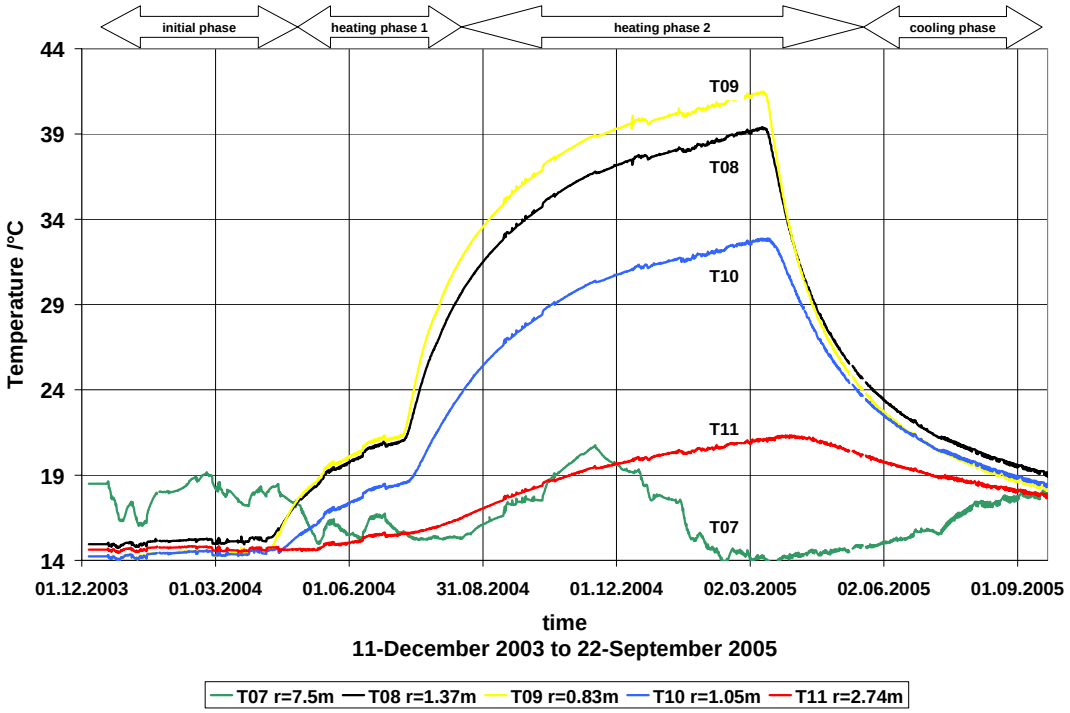

Figure 2-27 Evolution of temperature in Array 1 (above the heater)

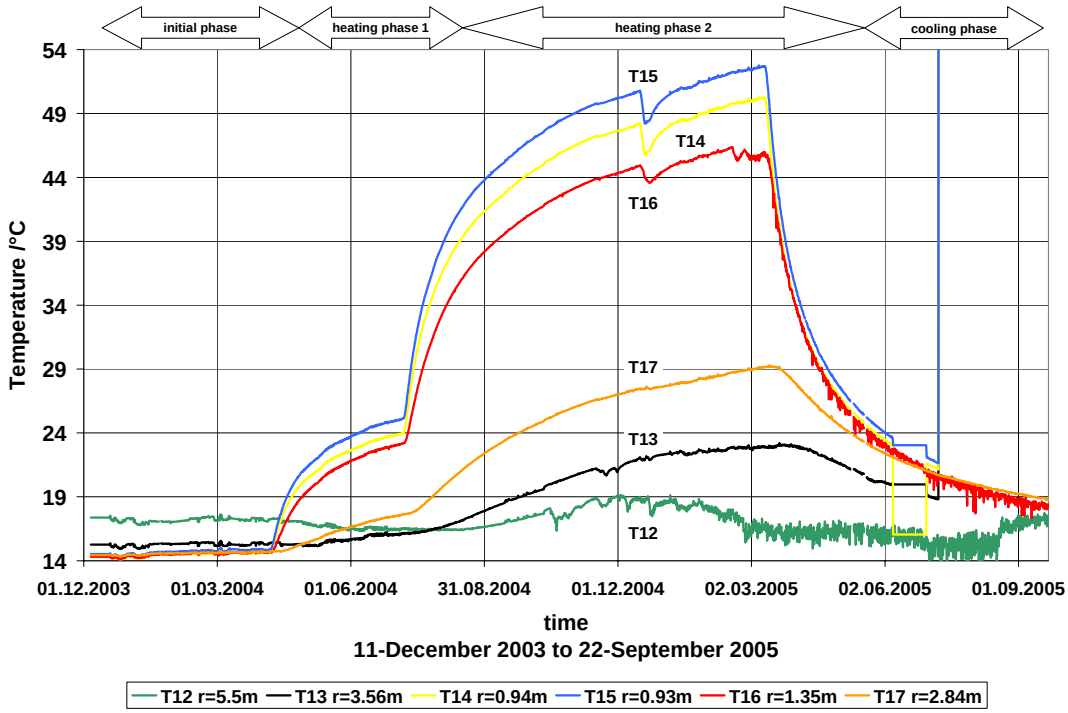

Figure 2-28 Evolution of temperature in Array 2 (below the heater)

Prior to heating, the rock temperature at 8 m in distance to the MI niche ranged between 14°C and 15°C. Close to the MI niche the temperature rose up to 19°C. The variation in temperature in the test intervals was predominantly caused by the temperature in the niche. The measured temperature effect was up to 0.25°C. This effect also influenced the measured pore-water pressure. A notable gradient in temperature was limited to a distance of approximately 7 m to the MI niche. The temperature in deeper rock areas is expected not to be influenced by the MI niche.

At the beginning of heating the rock temperature around the heater borehole BHE-D0 varied between 14°C and 15°C. Close to the MI niche, the temperature varied between 15 and 19°C. The maximum was measured at 50 cm distance to the MI niche in the test interval BHE-D07 which is assumed to lie in the excavation damaged zone (EDZ).

During the first heating phase (heater power 650 W, duration from April 6, 2004 until July 6, 2004) the temperature increased from 14 to 21°C (T08; T09) above heater 1 (Array 1) while below heater 2 (Array 2) a maximum temperature of 25°C (T15) was measured. The reaction time and the shape of the temperature curves differ between Array 1 and Array 2, which might be explained by the bedding of the clay and/or the anisotropy of the thermal conductivity, respectively.

Above the heater (Array 1) the temperature increased to 41°C in phase 2 (heater power 1950 W), while below the heater (Array 2) the temperature reached 53°C at the end of the heating phase in March 2005. The difference in the temperature levels between Array 1 and Array 2 hints to an anisotropy of the thermal conductivity. The temperature curve shapes are as expected.

The failure of the heater in December 2004 did not affect the evolution of temperature above the heater (Array 1), while below the heater (Array 2) the breakdown led to a temporary decrease of the rock temperature.

With heater shut-down on March 13, 2005 temperature started to decrease at all measurement locations previously affected by heating. By mid September 2005, temperature ranged between 17 °C and 19 °C at both arrays 1 and 2.

2.7.2 Pore-Water Pressure

The recorded pore-water pressure data are shown in summary diagrams in Figure 2-29 (Array 1; above the heater) and Figure 2-30 (Array 2; below the heater). The radial distance of each interval to the axis of the heater borehole BHE-D0 is given in the legend.

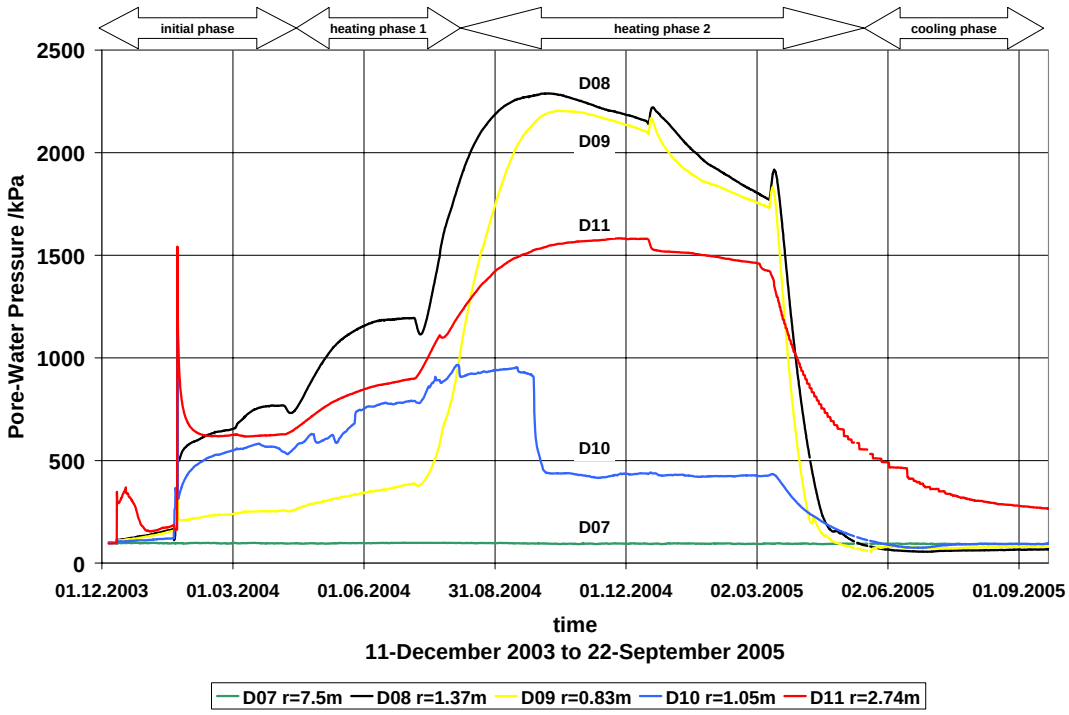

Figure 2-29 Evolution of pore-water pressure in Array 1 (above the heater)

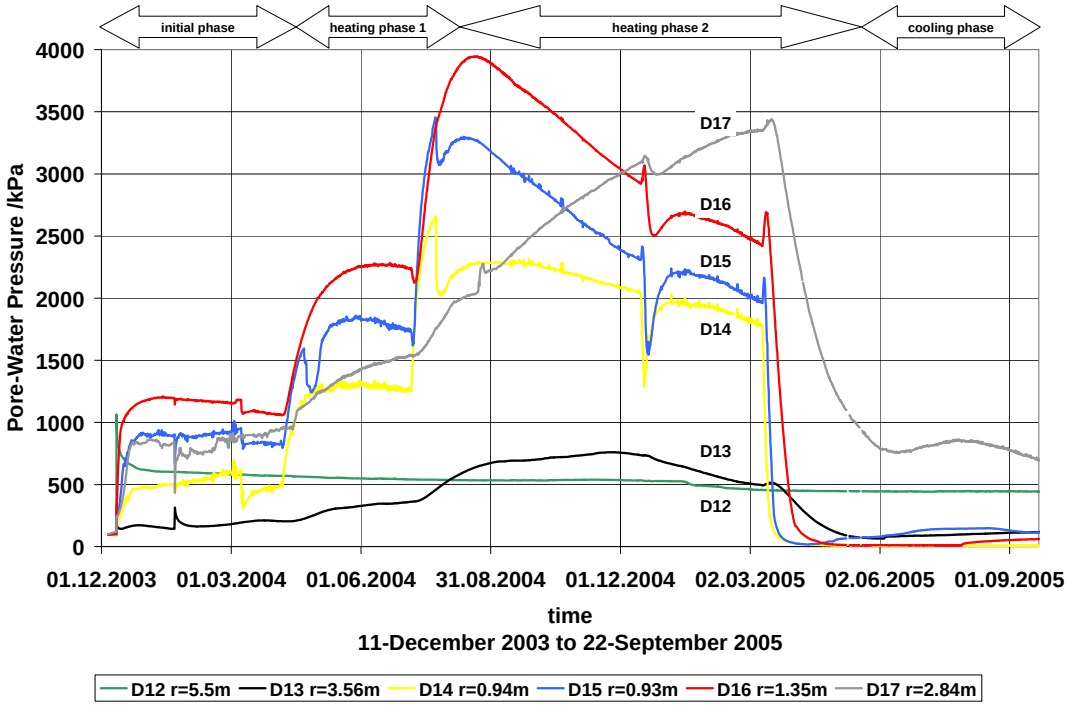

Figure 2-30 Evolution of pore-water pressure in Array 2 (below the heater)

The recording of pressure data started on December 11, 2003. In Array 1 no significant pressure increase was observed. The smooth gradient in the shape of the pressure curves is pointing to residual gas saturation in the system. In Array 2 a maximum initial pore-water pressure of approximately 1.2 MPa was built up in the test interval BHE-D16 within 14 days. In BHE-D15 and BHE-D17 the pressure increased to 0.8 to 0.9 MPa.

The drilling of the heater borehole BHE-D0 caused pressure variations in the deeper test intervals of Array 2 (D14, D15 and D16) which are positioned below the axis of the heater borehole (Figure 2-31). The corresponding test intervals of Array 1 (above the axis of the heater) were obviously not affected by the drilling activity.

Daily changes in pressure mostly correlate with changes in the temperature in the MI niche. In some cases the warming of the tube system caused an increase in pressure of 0.1 MPa.

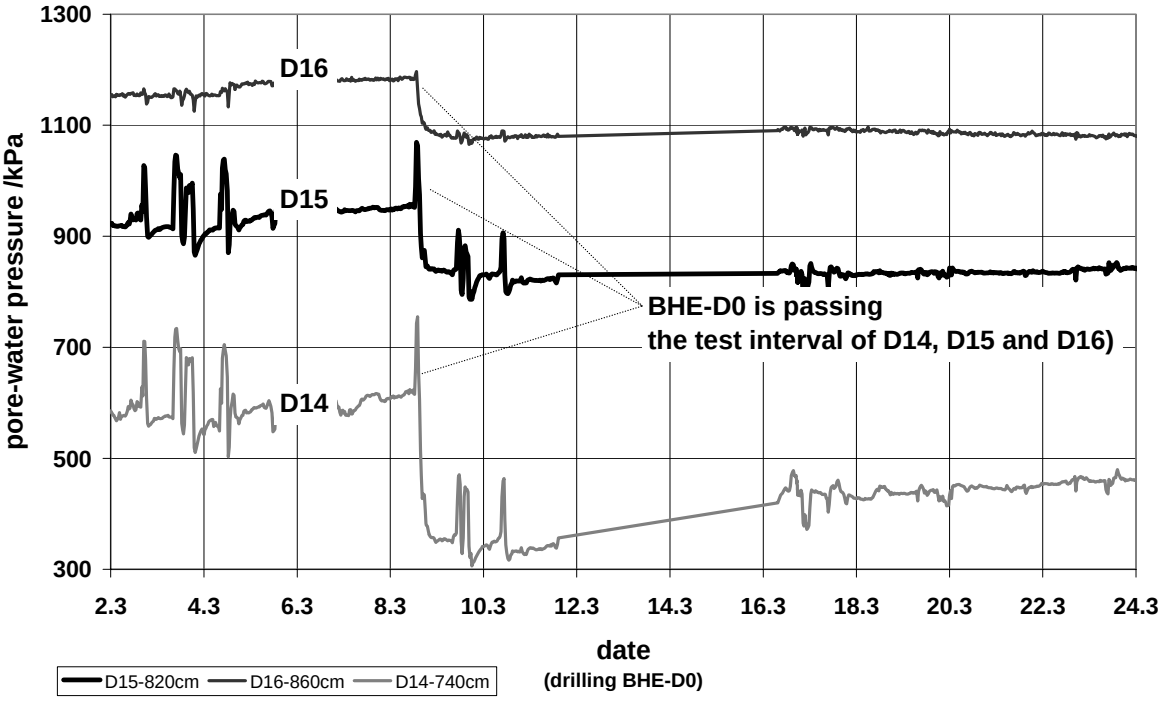

Figure 2-31 Observed pressure changes while drilling the heater borehole BHE-D0

Before start of the heating phase 1 the pore-water pressure in the single spot intervals of Array 1 and Array 2 was almost stationary. The smooth pressure increase in most of the intervals and the absence of tidal effects are still pointing to residual gas saturation in the system.

When heating started, the pore-water pressure in Array 1 increased in D08 up to 1.19 MPa and in D09 up to 0.38 MPa within 48 hours. In D08, the pressure development started with an initial decrease of pore-water pressure. The pore-water pressure in D10 indicates a drop of pressure in the vicinity of the interval. The reason for this behaviour is unknown. In D11, which is approximately 2.5 m distant to the heater, the pore-water pressure increased to 0.89 MPa.

In Array 2, the pore-water pressure increased to 0.35 MPa in D13 and to 2.28 MPa in D16. The evolution of the pore-water pressure in D14 and D15 seems to be representative for the clay formation. In both intervals the evolution started with a temporary decrease of pressure. The break in the pressure curve in D15 is probably caused by a local disturbance (natural phenomenon) near the interval. The effect of heating on the pore-water pressure measured in D17 started approximately one week

later. At the end of June, the pore-water pressure in Array 2 (except D17) had experienced its maximum.

At the beginning of the heating phase 2 (heater power was increased from 650 to 1950 W) the pore-water pressure close to the heater borehole increased immediately. 45 days later, the highest pressure of approximately 4.0 MPa was measured in D16 below the heater (Array 2). Above the heater (Array 1) the pressure increased to 2.2 to 2.3 MPa (D08, D09).

The pressure curve of the test interval D10 remained below 1.0 MPa. The pressure drop points to a communication of the test interval with a different flow field. In the deepest boreholes, 2.6 m distant from the heater (D11, D17), the pore-water pressure increased with a lower rate than close to the heater.

The appearance of a temporary pressure depression in D08, D15 and D16 at the very beginning of phase 2 and the spontaneous pressure drop in D14 and D15 on July 24, 2004 (loss of heater packer pressure) are caused by unclear effects in the rock. Close to the MI niche (D07, D13; data of D12 are not reliable) the pressure was hardly affected by the heating.

Three months after the beginning of the heating phase 2 the pore-water pressure near the heater had experienced its maximum (except D17) and was smoothly decreasing. The maximum pressure measured above heater 1 reached 2.3 MPa. The pressure in D10 which dropped in September from 0.95 to 0.45 MPa did not recover. The pressure below heater 2 decreased from approximately 4.0 MPa in September to 2.2 to 3.0 MPa in December 2004.

In December 2004 the evolution of the pressure was disturbed by the failure of the heater system. A significant effect of the failure was detected in the test intervals below the heater. The failure of the heater led to a temporary increase of pressure in D8 and D9, followed by a smooth decrease. In D15 and D16, the heater failure caused a temporary increase with a following sharp decrease of pressure. The pressure in D14 was not increased by the failure.

Heater shut-down on March 13, 2005 resulted in a short-term pressure peak at D08, D09, D15, D16, and D17, in much the same way as after the heater failure on December 15, 2004. Afterwards, there was a smooth pressure decrease at all

measurement points which had been affected by heating. No hints to fracturing and sudden pressure losses were detected. Pore-water pressure decreased to nearly atmospheric values in the following months, except for D11 and D17 which are located rather far from the heaters.

2.7.3 Permeability to Water

After cool-down, when a stationary temperature and pore pressure state had been reached, the mini-packer intervals were used for measurement of rock permeability to water and of gas entry pressure.

Four intervals were chosen for the permeability tests: D09 (Array 1, close to the heater), D11 (Array 1, undisturbed region beyond the heater), D13 (Array 2, between MI niche and heater), and D14 (Array 2, close to the heater). These intervals are marked blue in Figure 2-32.

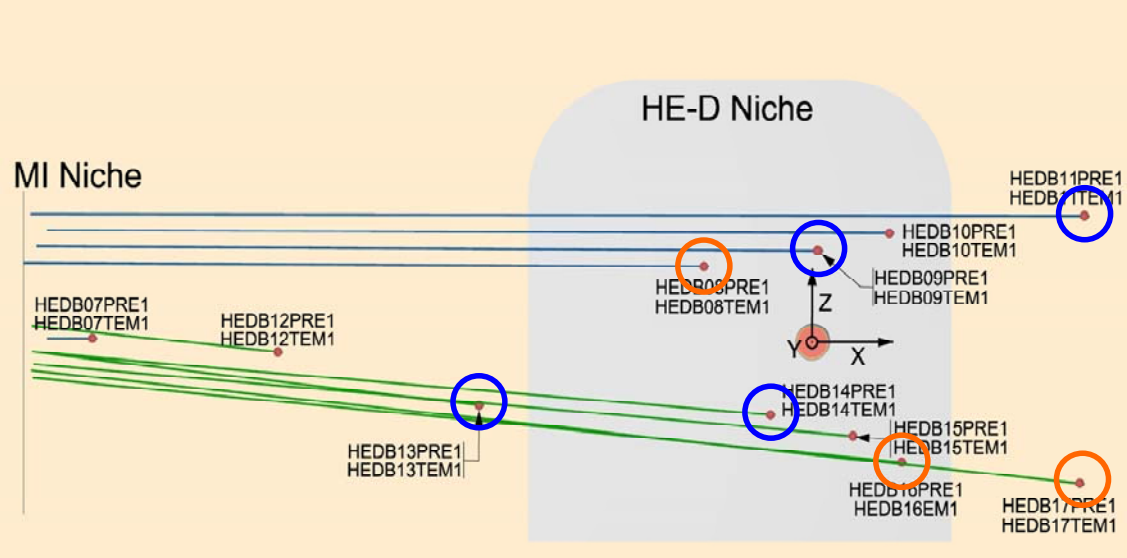

Figure 2-32 Test intervals chosen for water permeability testing (blue) and for gas entry pressure determination (blue and orange)

The tests were performed on September 27, 2005 by injecting a water pressure pulse of 0.5 to 0.8 MPa above pore pressure into the chosen intervals and monitoring the pressure decay during the subsequent shut-in phase. The recorded pressure curves are shown in Figure 2-33.

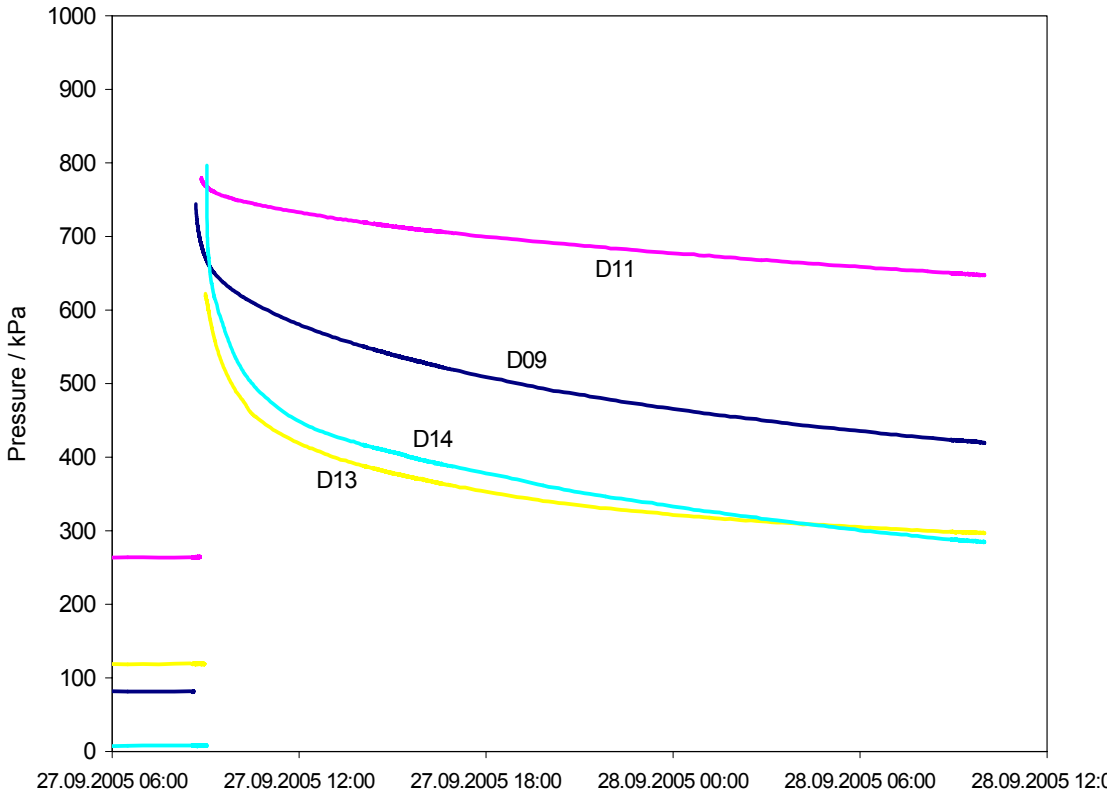

Figure 2-33 Pressure decay curves of the water permeability tests

The pressure curves were evaluated using the commercial code WELTEST. The following assumptions were made: The formation is homogeneous and infinite, flow is one-dimensional/radial, and there is no skin (disturbance of the borehole wall). Since the volume of injected water had to be estimated, the results are not exact, however, the order of magnitude of the permeability could be determined. All measurements resulted in permeabilities around 10^{-19} m^2, with the highest value of $2 \cdot 10^{-19}$ m^2 for D13 (between the MI niche and the heater) and the lowest of $3 \cdot 10^{-20}$ m^2 for D11 (beyond the heater). The measured and fitted pressure curve for the measurement at D11 is shown in Figure 2-34 as an example.

The results of these tests indicate that permeability of the rock to water was not affected by heating.

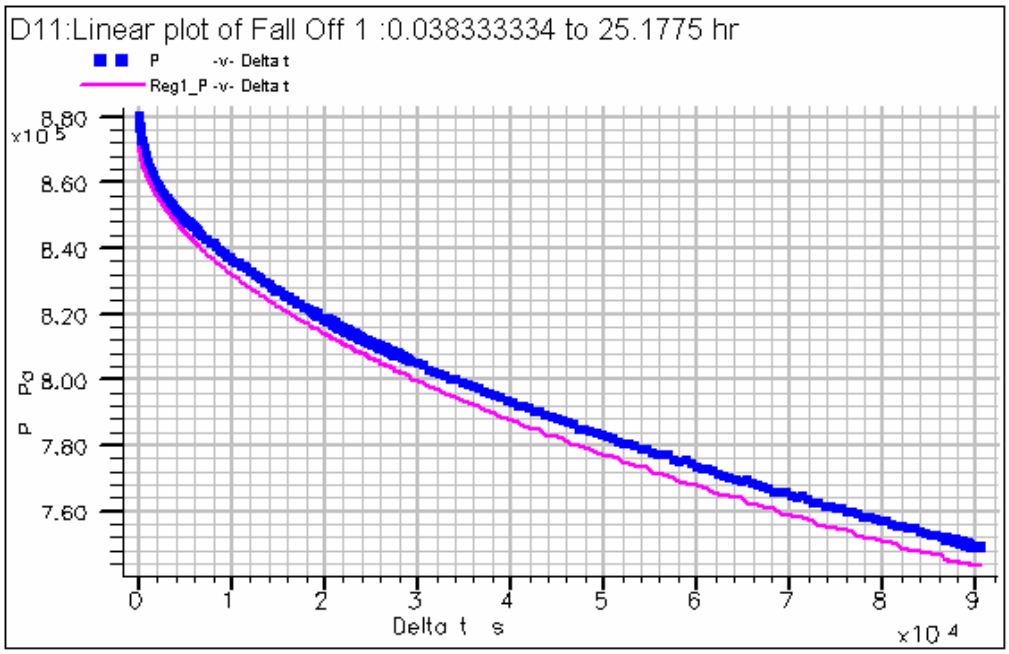

Figure 2-34 Measured (blue) and fitted (pink) pressure curves of the water permeability test at D11; fitted permeability $3 \cdot 10^{-20}$ m^2

2.7.4 Gas Entry Pressure

Gas injection tests for determining the gas entry pressure were performed in the test intervals D09, D11, D13, and D14 after completion of the water permeability tests on September 28, 2005. Additionally, the same tests were performed in the intervals D08, D16, and D17 on September 27 and 28, 2005 (Figure 2-32). The procedure was to purge the interval with nitrogen and to increase gas pressure in steps of 0.5 MPa. After each gas injection, the test interval was shut in, and the pressure evolution was recorded for at least 15 minutes. The idea was that transgression of gas entry pressure will be marked by measurable pressure decay down to nearly constant pressure during the shut-in phase.

For the interval D17, further pressure steps were taken up to the maximum achievable pressure of 5 MPa in order to see whether a gas fracture, marked by sharp pressure drop after shut-in, could be reached.

The pressure curves obtained during the tests are summarized in Figure 2-35. For all intervals, a significant pressure loss can be observed after exceeding the entry pressure. In the intervals D11, D13, and D16 a constant pressure is reached during the final shut-in phase. These values can be interpreted directly as the respective gas entry

pressure values. We obtain 0.86 MPa (D11), 0.64 MPa (D13), and 1.3 MPa (D16), respectively. For the other intervals, a constant gas pressure is not reached. The gas entry pressure can, however, be estimated from the recorded (still decreasing) shut-in pressure as upper limit and the next-lower pressure step where no gas flow was detected as lower limit. The respective values are 1.6 - 1.8 MPa (D08), 0.9 - 1.1 MPa (D09), 1.0 - 1.2 MPa (D14), and 2.8 - 3.4 MPa (D17).

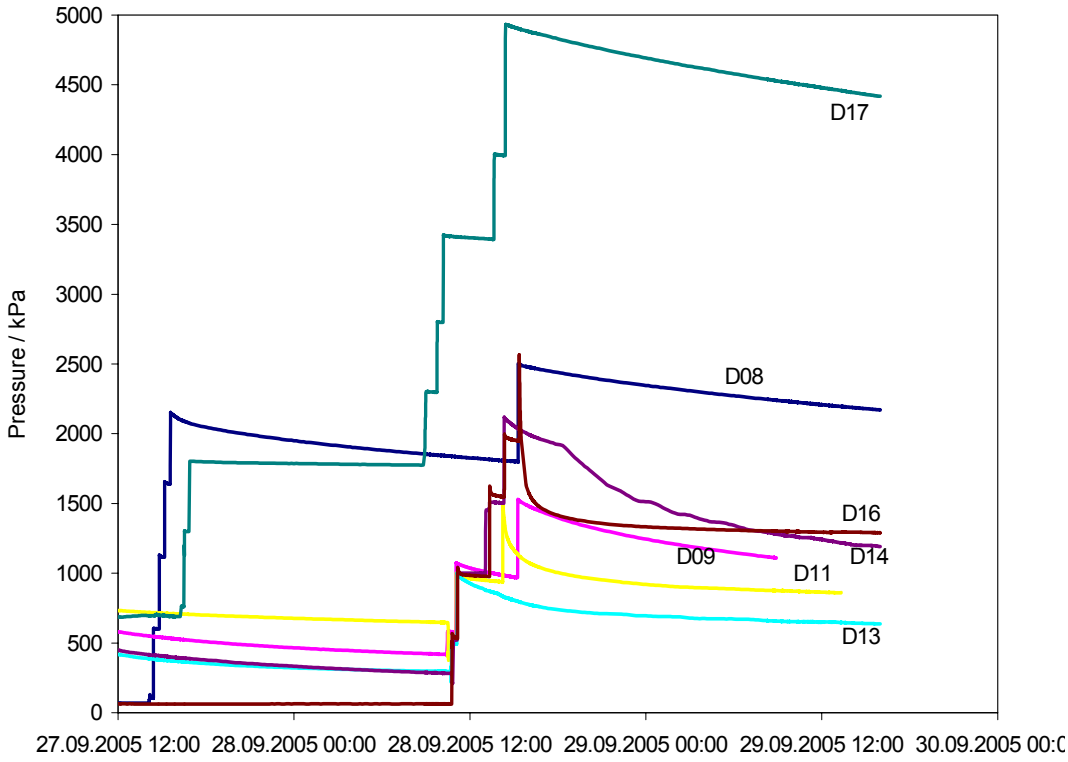

Figure 2-35 Pressure evolution in the test intervals during the gas entry pressure testing

In summary, the gas entry pressure is in most cases in the range of 0.8 to 1.8 MPa. There is no dependence on the distance from the heater borehole. The measured gas entry pressures are close to the minimum principal stress in a range of 2 - 3 MPa in the MTRL /BOS 03/. The gas entry pressure at D13 which is nearer to the MI niche is somewhat lower, which is consistent with the slightly higher water permeability.

An exception is the high gas entry pressure at D17. Here, the pressure was increased to the maximum possible value of 5 MPa in order to produce a gas fracture. The energy stored in the small interval volume was, however, not sufficient to achieve a fracture, as can be taken from the smooth pressure curve.

2.7.5 Gas Pressure Evolution

The intervals 3 of the boreholes BHE-D18 and BHE-D21 were inflated with nitrogen to 0.9 MPa on February 11, 2004 (Figure 2-23). For testing the whole system of pressure recording, the gas pressure in these intervals were reduced to atmospheric pressure and inflated right afterwards again to almost 0.9 MPa, on March 16, 2004.

Figures 2-35 to 2-41 show the evolution of gas pressure in the different intervals until October 2005. The actions inflation, deflation and inflation again in the intervals 3 of the boreholes BHE-D18 and BHE-D21 indicated that the systems of pressure gauges and data acquisition were working well. After both inflations, the pressures in these intervals decreased slightly, obviously as a result of gas flow into the surrounding host rock. After switching on the electric heaters in borehole BHE-D0 on April 6, 2004 (heating phase 1 with 650 W), the gas pressure in these intervals increased from 0.9 to 1.0 MPa in borehole BHE-D18 and from 0.91 to 0.92 MPa in boreholes BHE-D21 as a result of temperature increase in the host rock.

On July 6, 2004, the heating power was increased to 1950 watts (heating phase 2) which led to an acceleration of the pressure increase in the intervals.

The decrease of the pressure in the packer of the heaters in borehole BHE-D0 on July 24, 2004 did not show a significant influence on the gas pressure intervals of the boreholes BHE-D18 to BHE-D23.

As a result of borehole convergence, the inflation pressure in the sealing elements increased to a level higher than 5 MPa. The optical manometers for controlling the inflation pressure of the packer systems, however, had been selected for a maximal pressure of 4 MPa. In order to avoid a damage of the manometers and a sudden loss of the inflation pressure, this pressure was reduced to 3 MPa on August 19, 2004. Nevertheless, the inflation pressure increased again above 5 MPa within some weeks. Thus, new pressure gauges for determining the inflation pressure with a larger measuring range were installed on November 18, 2004. Due to this action, the inflation pressures were reduced shortly. Afterwards the packers were inflated again to 4 MPa. The reduction of inflation pressure led also to a reduction of the pressure in the intervals indicating that the whole system of packer and surrounding host rock is a complex interconnected system.

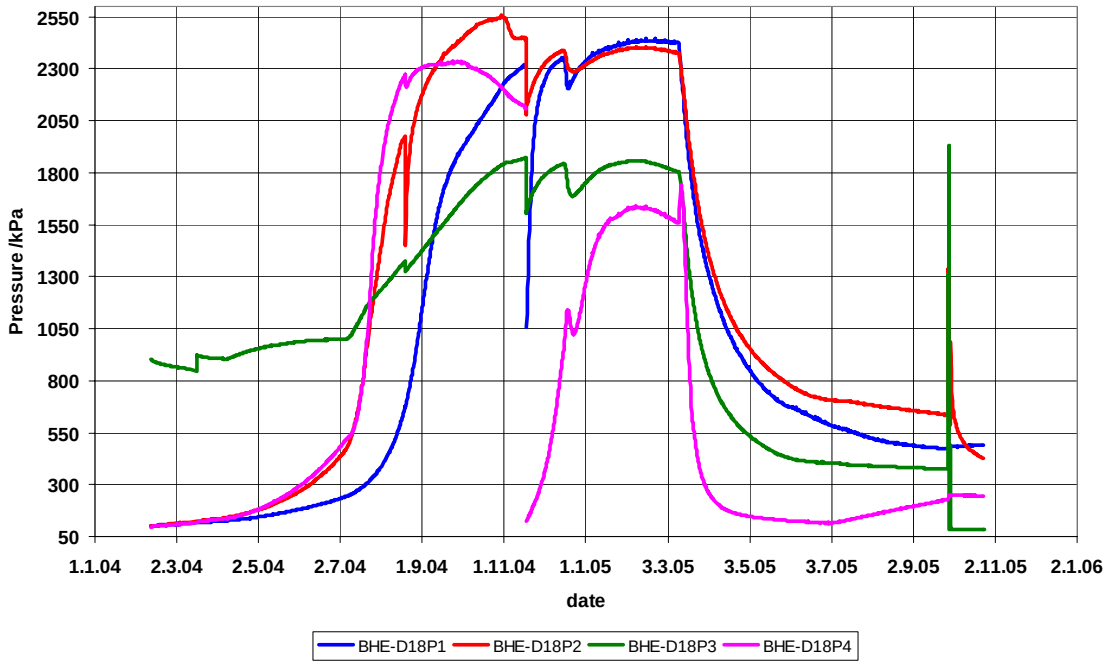

Figure 2-36 Evolution of gas pressure in the intervals of borehole BHE-D18

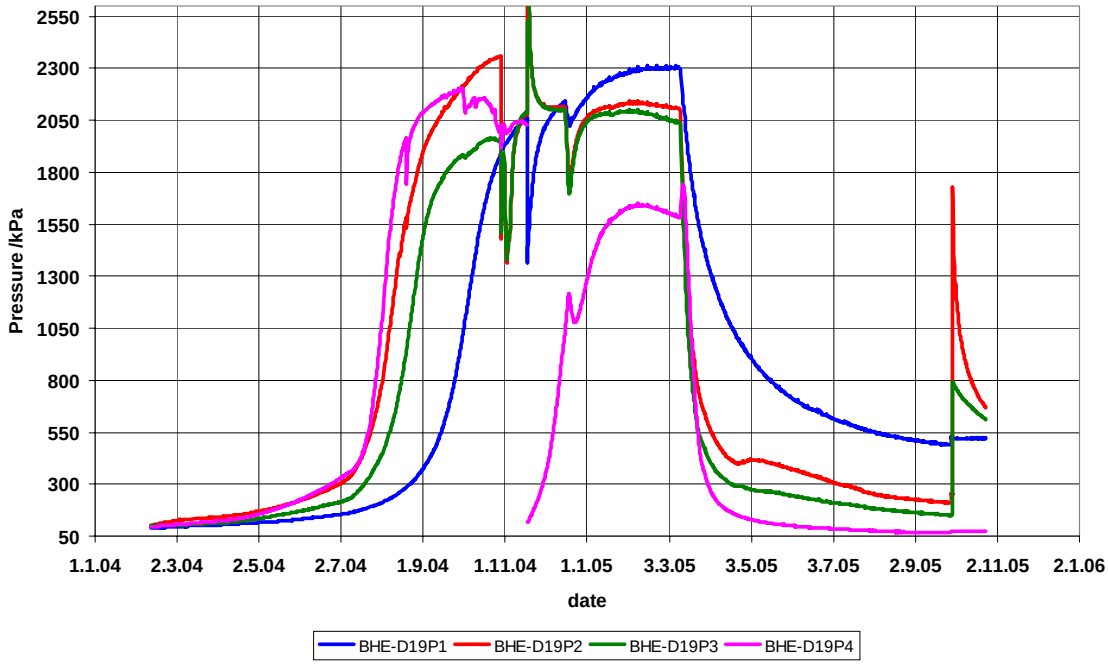

Figure 2-37 Evolution of gas pressure in the intervals of borehole BHE-D19

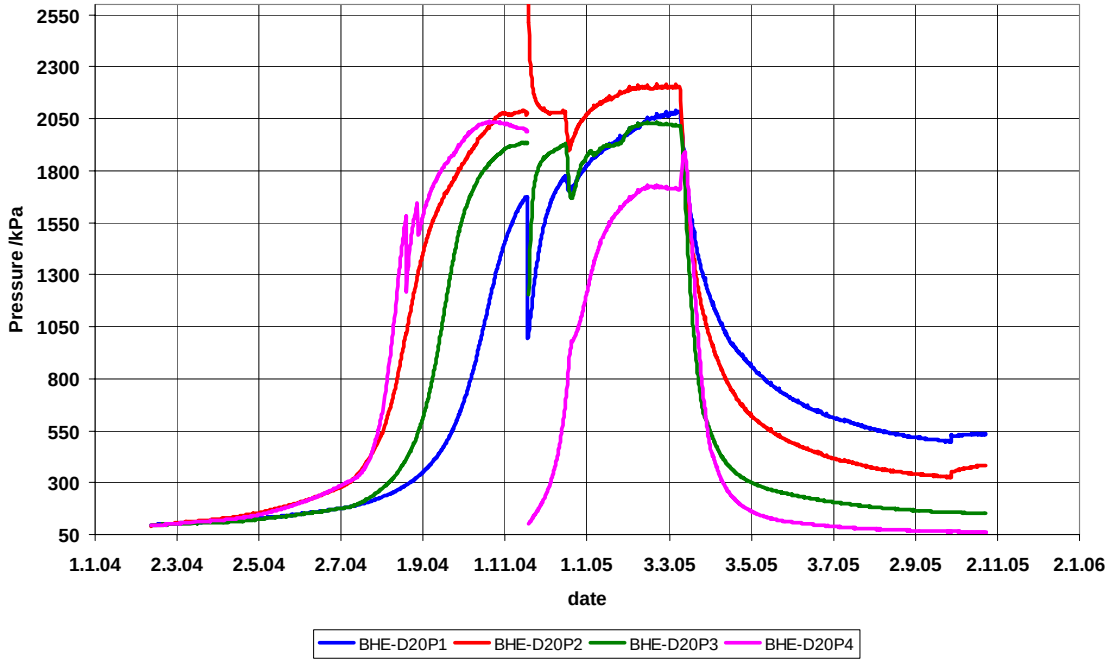

Figure 2-38 Evolution of gas pressure in the intervals of borehole BHE-D20

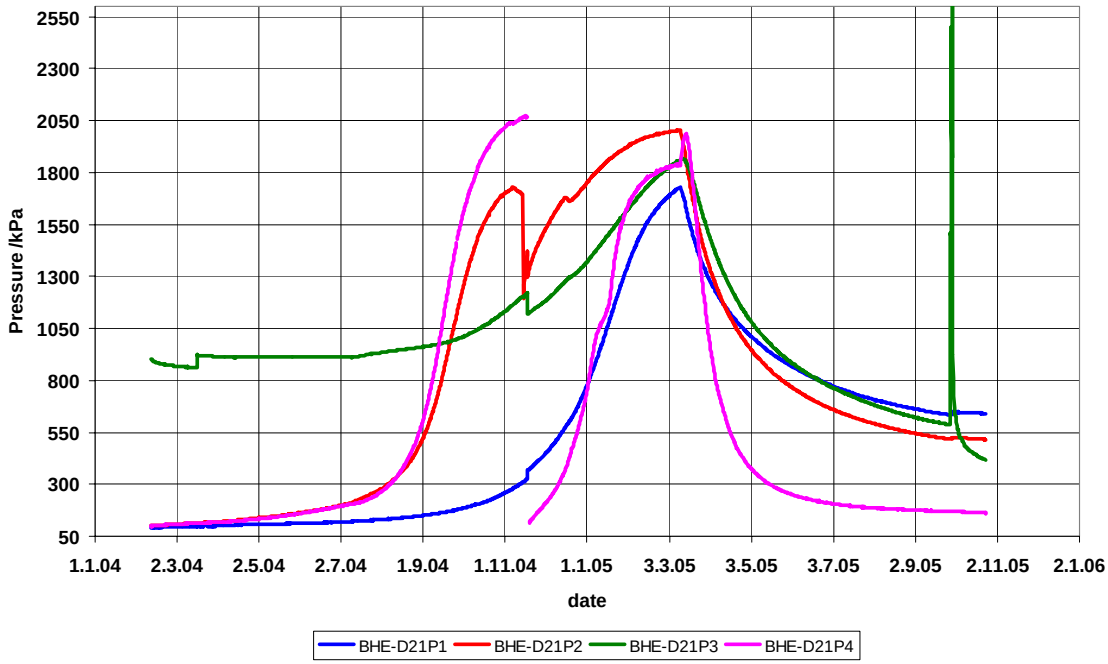

Figure 2-39 Evolution of gas pressure in the intervals of borehole BHE-D21

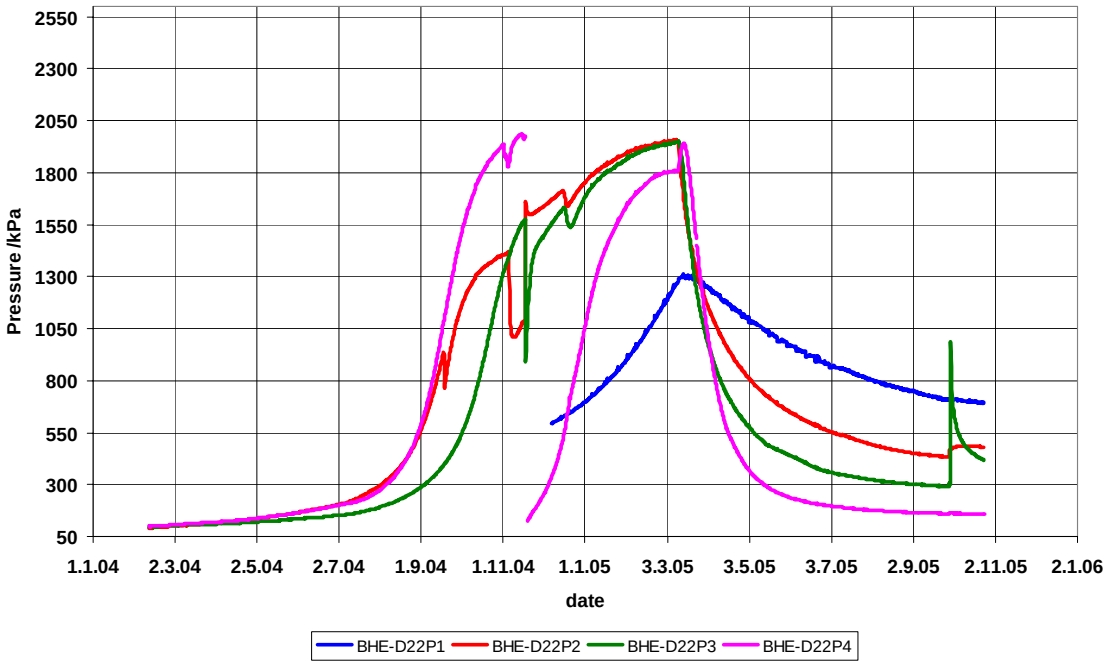

Figure 2-40 Evolution of gas pressure in the intervals of borehole BHE-D22

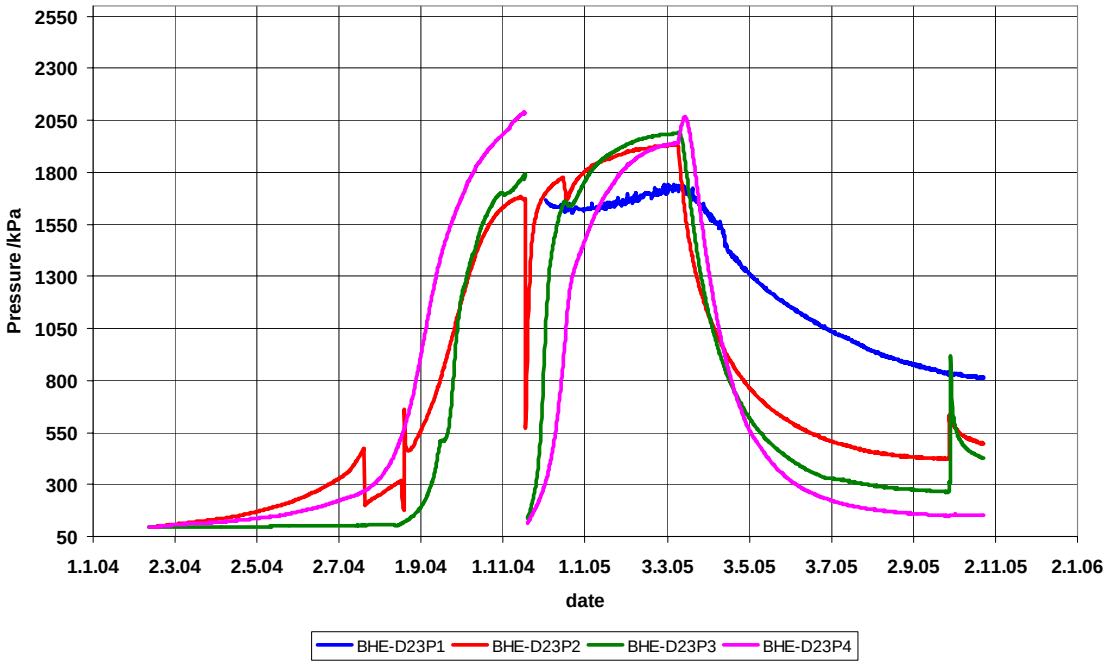

Figure 2-41 Evolution of gas pressure in the intervals of borehole BHE-D23

The heating interruption between December 16 and December 17, 2004 led directly to a pressure decrease in the intervals.

After restart of heating phase 2 the pressure in the different intervals increased slightly. Until March 2005 the pressures reached almost a constant level and it was planned to perform permeability measurements. These measurements however, could not be performed, since one heater failed in March 2005. It was decided to switch off the whole heating system and start the cool-down phase. All the measurements in the test field were continued during this phase until dismantling of the test field.

As a result of the temperature decrease in the whole test field the pressure in all the intervals decreased and reached almost constant level at the end of September 2005. On September 25 to 29 gas permeability measurements were performed. The methods and results are described in the next section.

From the pressure measurements in the boreholes BHE-D18 to BHE-D23 the following conclusions could be are drawn:

- The gas pressure increase in the different intervals is a result of borehole convergence or gas and water release from the rock mass. Both effects are influenced by the temperature, as the pressure increase was accelerated after switching the heaters on (heating phase 1) and after increasing the heater power to 1950 W (heating phase 2). Furthermore, the pressure increase is lower in the boreholes with greater distances to the heater than in those closer to the heater.

- The behaviour of the pressure in the different intervals indicates that the whole system of packer, tubes, valves, and pressure gauges is gas-tight; no interactions between the intervals are detectable. There are no pressure losses, the pressures in the different intervals increase differently, and the pressure reductions and inflations in the intervals 3 of the boreholes BHE-D18 and BHE-D21 do not influence the pressures in the other intervals.

- After switching off the heaters the pressures decreased in all the intervals, but with different rates. Different effects are the reason for these pressure decreases:
  - Thermal contraction of the surrounding host rock
  - Re-sorption of the released water and gases

- Solution of the released gases in the formation water of the host rock

- End of September 2005, the pressure in the intervals reached almost steady state and the envisaged permeability measurements were performed.

On November 18, 2004, Keller pressure gauges were installed at the intervals 1 of the boreholes BHE-D22 and BHE-D23. The pressures in the intervals were 0.4 MPa (BHE-D22P1) and 1.7 MPa (BHE-D23P1) determined at the optical pressure gauges. During this action water was extracted from these intervals for chemical analysis (227 ml from BHE-D22P1, 356 ml from BHE-D23P1). Table 2-1 shows the results of the analyses and for comparison the composition of the PEARSON water type A1. The comparison indicates a lower concentration of the ions except for potassium and sulphate. The reason may be dilution by water released from the surrounding Opalinus clay as a result of elevated temperature and thermal expansion.

Table 2-1 Chemical composition of water extracted from intervals BHE-D22P1 and BHE-D23P1

Interval	Amount (ml)	Calcium (mg/l)	Potassium (mg/l)	Magnesium (mg/l)	Sodium (mg/l)	Chloride (mg/l)	Sulphate (mg/l)
BHE-D22P1	227	611	72	381	5382	9236	1474
BHE-D23P1	356	733	71	372	5259	9135	1572
PEARSON water for comparison		1033	63	411	5517	10630	1352

2.7.6 Permeability to Gas

Gas permeability tests in the boreholes BHE-D18 and BHE-D21 were performed in September 2005, almost three months after switching off the electrical heaters. At that time almost constant levels with regard to gas pressure and temperature were reached in the test field.

First, the inflation pressures in all the sealing elements which were below 2 MPa were adjusted to 4.0 MPa. Afterwards the intervals 3 of the boreholes BHE-D18 and BHE-D21 were inflated with nitrogen to 0.38 MPa and to 0.59 MPa, respectively. Then the

outlets of both intervals were opened and they were purged to extract the water which could have been released from the host rock into these intervals. From both intervals only a few drops of water could be collected, which indicates that no significant amount of water was released from the Opalinus clay at the conditions within the test field. Afterwards, the gas injection tests were performed.

Test interval 3 in borehole BHE-D18

For gas injection tests the gas pressure was increased stepwise to 0.5; 1.5; 2.0; and 2.85 MPa as shown in Figure 2-42. After the inflation of the interval the valve to the inlet and also to the outlet were closed. The pressure in the injection interval and also in the other intervals of the boreholes BHE-D18; BHE-D19 and BHE-D20 was recorded. At the injection pressure of 1.5 MPa the first pressure drop was detected, meaning that the gas entry pressure was exceeded. The pressure remained nearly constant for almost 17 hours which indicates that the effective permeability to gas is very low. This part of the pressure curve was evaluated in terms of permeability using the code WELTEST. The resulting effective permeability to gas was $4 \cdot 10^{-22}$ m^2.

At the inflation to 2.85 MPa and closing the inlet there was a sudden drop of the pressure in the inflated interval 3 as a result of a gas fracture in the surrounding host rock. Within almost 2 hour the pressure decreased to a level below 0.1 MPa. Within 18 hour the pressure decreased to 0.085 MPa. The interval was then inflated to 0.5 MPa and the pressure decreased to 0.15 MPa with the next hour as a result of a reopening of the fracture in the surrounding host rock. The pressure curve of the re-frac was again used for permeability evaluation, yielding an effective value of $4 \cdot 10^{-18}$ m^2. Gas flow in this case, however, is obviously restricted to the fracture, so that this value cannot be associated to formation permeability.

Afterwards, a constant head injection test was performed. The pressure in the interval was adjusted to 0.508 MPa and the gas flow into the interval was determined by weighing the gas bottle. For the next 6 hours a constant gas flow of 18 g nitrogen per hour was measured which are 0.64 mol or 14.4 normal litres per hour. The pressures in all the other intervals were not significantly influenced by that gas flow. This fact indicates that the primary frac and the re-frac did not run through any of the intervals of the boreholes BHE-D18 to BHE-D20.

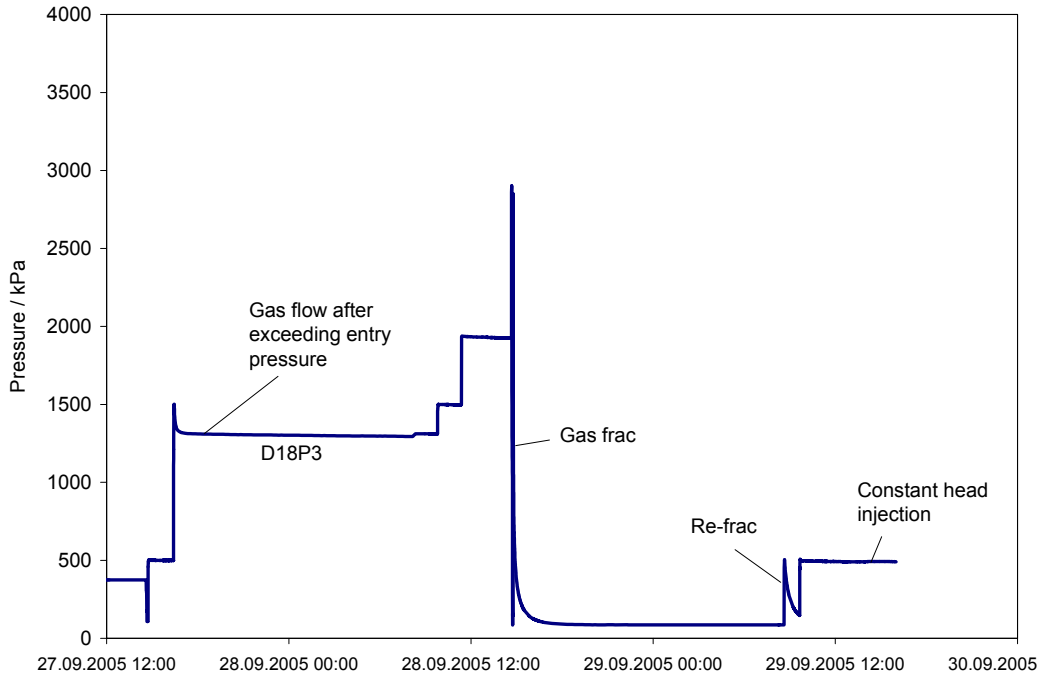

Figure 2-42 Gas injection tests into interval P3 of borehole BHE-D18

Test interval 3 in borehole BHE-D21

For gas injection tests the gas pressure was increased stepwise to 0.587; 1.02; and 1.50 MPa as shown in Figure 2-43. After each inflation step, the valves to the inlet and also to the outlet were closed. Slightly above 1.5 MPa a first slow pressure loss was detected. The permeability evaluation resulted in a value of 10^{-22} m^2 which is similar to the result from BHE-D18.

The pressure in the other intervals of the boreholes BHE-D21; BHE-D22 and BHE-D23 was not affected by this gas injection.

The injection pressure was increased in four more steps to 3.56 MPa. After each step the interval was sealed gastight. While during the first three steps the pressure losses were again very small, a sharp drop was detected after sealing the test interval at 3.56 MPa. Within the next 16 hour the pressure in that interval decreased to 1.8 MPa. Obviously a gas fracture had been produced. This fracture, however, was limited in extent and had no contact to the other test intervals.

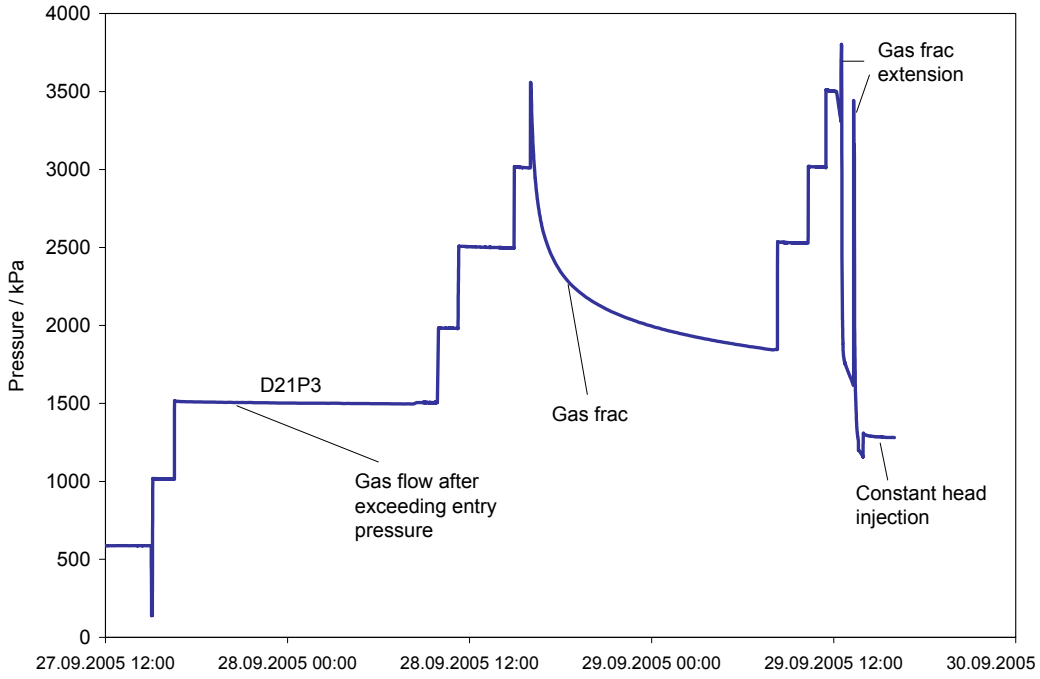

Figure 2-43 Gas injection tests in interval 3 of borehole BHE-D21

After 16 hours of shut-in the injection pressure was increased in 4 steps to 3.8 MPa in order to generate obtain a re-frac in the host rock. At 3.5 MPa shut-in pressure a correspondence between the intervals D21P3 and D19P3 occurred, as can be seen in Figure 2-44. At 3.8 MPa a sudden drop of the pressure in the inflated interval 3 was observed which indicated that the gas fracture in the surrounding host rock was enlarged. Figure 2-44 shows that the test intervals D22P3 and D23P3 were reached by the gas fracture.

The interval was then inflated to 3.0 MPa and the gas flow into that frac was determined by weighing the gas bottles. Within 5 minutes 446 grams of nitrogen flow into that frac which are 15.93 mol or 356.8 normal litres per 5 minutes (191.2 mol or 4282 normal litres per hour). This new injection resulted in the fracture reaching the test intervals D18P2 and D19P2 (Figure 2-44).

The repeated gas injection into interval 3 of borehole BHE-D21 resulted in gas pressure increases in interval 2 of borehole BHE-D18, in the intervals 2 and 3 of borehole BHE-D19, in interval 3 of borehole BHE-D22, and in interval 3 of borehole BHE-D23. From this information the orientation of the fracture can be derived. The assumed gas fracture which runs through the different intervals is shown in Figure 2-45. It is obviously parallel to the bedding of the rock.

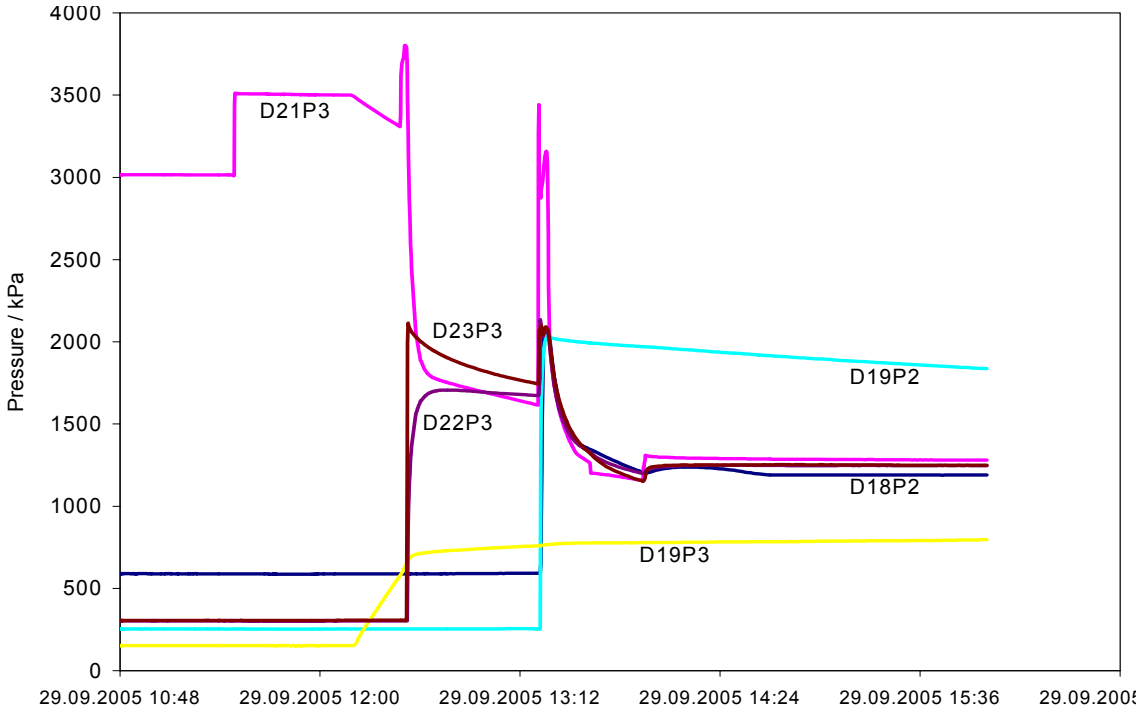

Figure 2-44 Gas injection tests in interval 3 of borehole BHE-D21 and resulting gas pressure increase in the other intervals

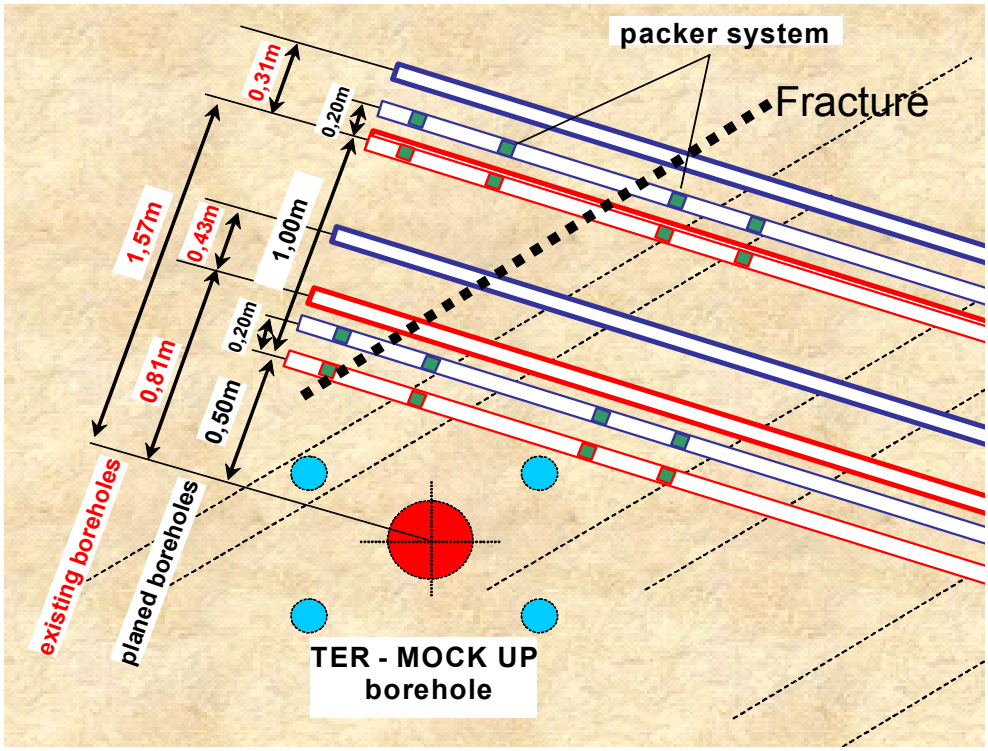

Figure 2-45 Boreholes BHE-D18 to BHE-D23 with the assumed fracture after gas injection into interval 3 of borehole BHE-D21

2.7.7 Deformation

Rock deformations were measured by SOLEXPERTS and DBE-TEC in the three boreholes D4, D5, and D6. Their positions are illustrated in Figures 2-14 and 2-16. The displacements measured between each extensometer point and the fixed point at the borehole end are illustrated in Figure 2-46.

The measurements along borehole D4 which is horizontally inclined at an angle of 45° to the heater borehole showed that each heating caused contraction (shortening) of the measuring sections in a short time followed by a gradual expansion (elongation). The extensive displacements continued even over the subsequent cooling phase. The maximum was reached at the longest section PT0-PT9 with 2.5 mm. The cooling resulted in contraction of the rock, starting near the heater and continuing in the far-field.

The measurements along borehole D5 perpendicular to but below the heater borehole in the middle section indicated some differences compared to the observations in D4. No contraction but only continual extension (elongation) within each heating period was observed. The expansion rate was accelerated by the temperature increase. The displacements accumulated over the two heating phases and they reached different values in the different measuring sections of up to 5 mm, depending on their distances. In contrast to heating, cooling gave a rise to gradual contraction of the rock. In the near-field, the initial state of the rock was recovered and even slightly over-consolidated after the cooling phase.

The extensometers installed in borehole D6 horizontally perpendicular to the heater borehole in the middle section showed much larger extensive displacements of up to 28 mm during the second heating phase. This unexpected high deformation might be due to a separation of the shotcrete from the rock wall. Because the head plate of the measuring system was anchored on the shotcrete, its movement could have produced a uniform elongation of all the measuring sections thus resulting in a systematic error of the measurements of the total displacements. However, this systematic error would not have any influence on the relative deformations between the measurement points in the borehole.

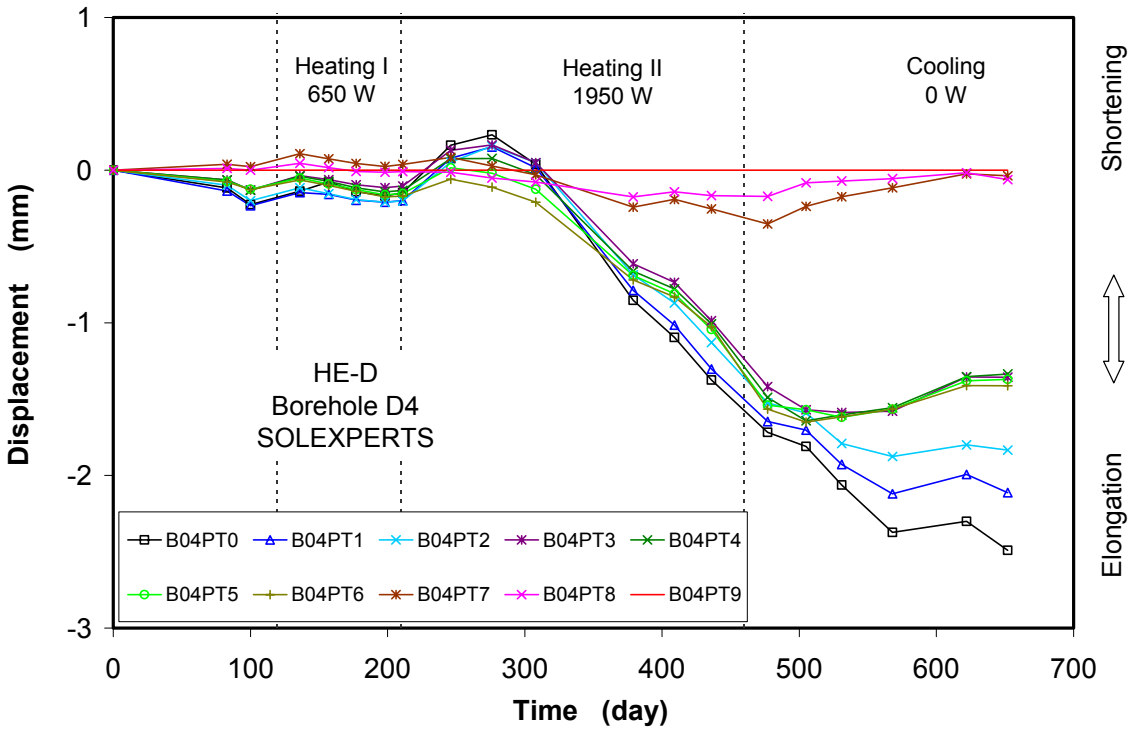

a. borehole D4

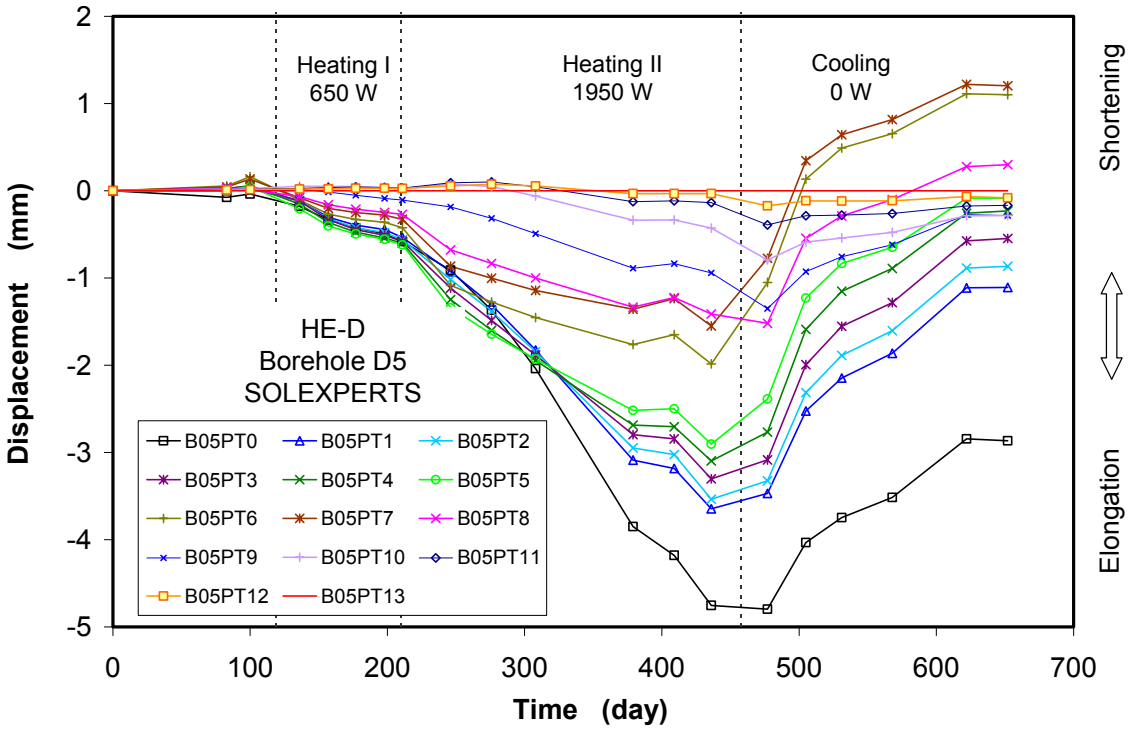

b. borehole D5

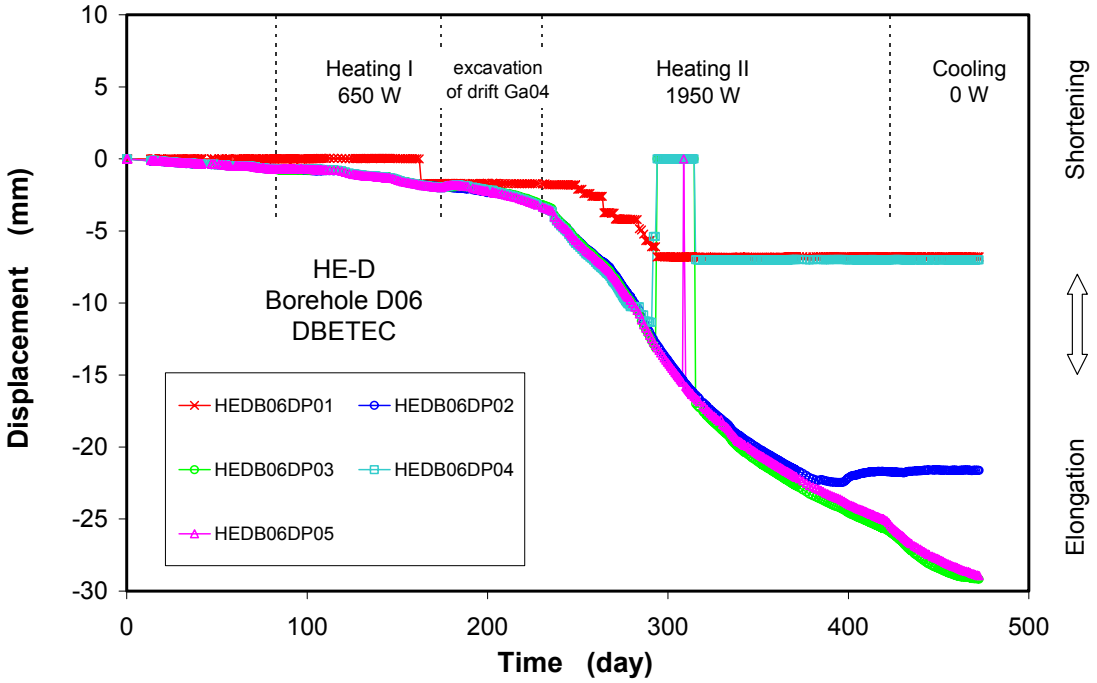

c. borehole D6

Figure 2-46 Displacements measured along boreholes D4, D5 and D6

3 Laboratory Experiments

3.1 Objectives

In the frame of the HE-D project, various laboratory experiments were performed at GRS's geotechnical laboratory to investigate the THM behaviour of the Opalinus clay as well as the Callovo-Oxfordian argillite. The experimental data served for estimating parameters associated with the constitutive models used by the modelling teams. The laboratory programme included two parts: the first part dealing with investigations on normally-sized samples (diameter D = 50 – 100 mm, length L = 50 – 200 mm), and the second part on large-scale samples (D = 260 mm, L = 700 mm).

On the normally-sized samples the following aspects were investigated:

- Petrophysical properties of the clay rocks;
- Relationship between suction and water content (water retention curve);
- Thermal expansion and contraction under loaded and unloaded conditions;
- Short-term compressive behaviour, damage and strength at different confining stresses and temperatures;
- Long-term deformation under different uniaxial stresses and temperatures;
- Swelling / shrinking behaviour due to moisture change;
- Responses of pore-water pressure and deformation to thermal loading.

On the large samples, mock-up heating experiments were carried out in GRS's big MTS triaxial apparatus, in which the in-situ heating experiment and the prevailing conditions were simulated.

3.2 Sampling and Preparation

Normal samples

A number of cores drilled pneumatically from the four boreholes BHE-D3 to D6 were used for the GRS laboratory tests. The locations of the boreholes are shown in Figures 2-14, 2-16 and 2-22. Figure 3-1 shows photos of these cores /NUS 04b/. The mapping

of the cores confirmed that the whole HE-D test field lies in the shaly facies with several thin sandy layers restricted to the area between 1.3 and 2.1 m from the MI niche wall. The cores were visually very compact and relatively homogeneous. The cores were delivered by ANDRA in sealed conditions to the GRS laboratory in Braunschweig and stored there at temperature of ~ 20 °C until testing. The list of the cores is presented in Table 3-1.

Table 3-1 Opalinus clay cores drilled from the HE-D test field at Mont Terri for the GRS laboratory experiments

Borehole	**Sample**	**Depth (m)** from	to	**Diameter** (mm)	**Length** (mm)
BHE-D3	BHE-D3/15	9.20	9.33	62	130
	BHE-D3/18	8.65	8.75		100
	BHE-D3/20	7.05	7.20		100
BHE-D4	BHE-D4/1	6.00	6.40	84	400
	BHE-D4/2	6.84	7.10		260
	BHE-D4/3	7.10	7.40		300
	BHE-D4/4	7.40	7.70		300
	BHE-D4/5	7.70	8.00		300
	BHE-D4/6	8.00	8.38		380
BHE-D5	BHE-D5/6	6.05	6.27	86	220
	BHE-D5/7	7.21	7.50		290
	BHE-D5/8	7.66	7.92		260
	BHE-D5/15	9.47	9.71		240
	BHE-D5/16	9.71	9.96		250
	BHE-D5/18	10.87	11.14		270
BHE-D6	BHE-D6/13	4.95	5.10	72	150
	BHE-D6/14	6.68	6.80		120
	BHE-D6/15	6.32	6.45		130
	BHE-D6/16	6.65	6.80		150
BHE-D0	BHE-D0/11	9.50	10.31	260	810
	BHE-D0/12	10.37	11.12		750
	BHE-D0/13	11.73	12.47		740

From the cores, cylindrical samples with different sizes for different tests were carefully prepared by cutting the cores and planishing the end faces in a lathe, as shown in Figure 3-2. The axes of the samples were inclined to the bedding plane with angles of 30° - 60°. Figure 3-3 shows three prepared samples.

a. Cores drilled from borehole BHE-D3 of D = 62 mm and L = 0 – 9.3 m

b. Cores drilled from borehole BHE-D4 of D = 84 mm and L = 6.7 – 10.2 m

c. Cores drilled from borehole BHE-D5 of D = 84 mm and L = 4.5 – 10.0 m

d. Cores drilled from borehole BHE-D6 of D = 72 mm and L = 0 – 7.0 m

Figure 3-1 Cores drilled from boreholes in the HE-D test field at Mont Terri

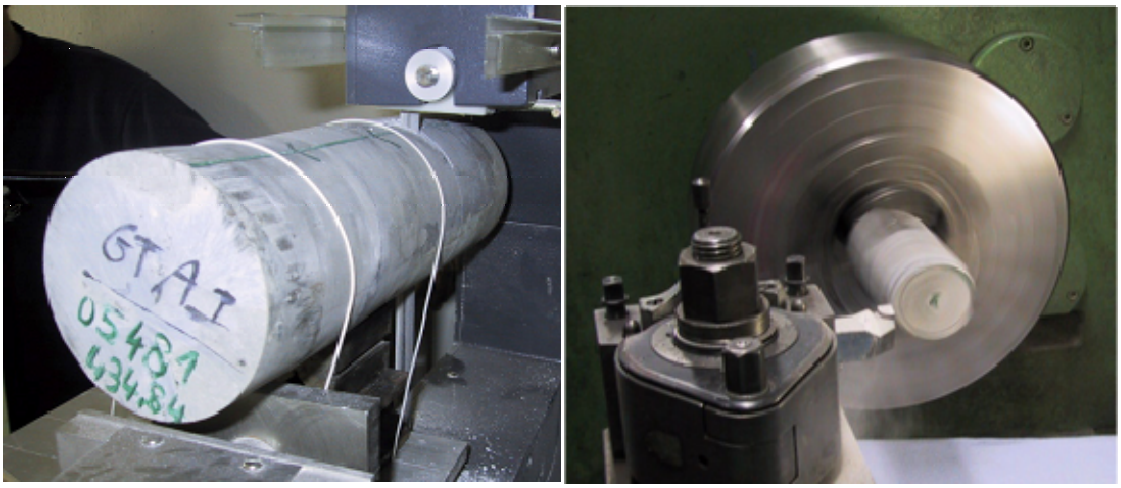

Figure 3-2 Preparation of a Callovo-Oxfordian argillite sample

Figure 3-3 Test samples prepared from drilled cores of the Opalinus clay

In addition to the Opalinus clay samples, some samples were also taken from the Callovo-Oxfordian argillite at the MHM-URL. These samples were provided by ANDRA in confined conditions in special sealing cells consisting of rubber jackets, cement mortar, PVC-tubes and steel cylinders. Figure 3-4 shows three Callovo-Oxfordian samples.

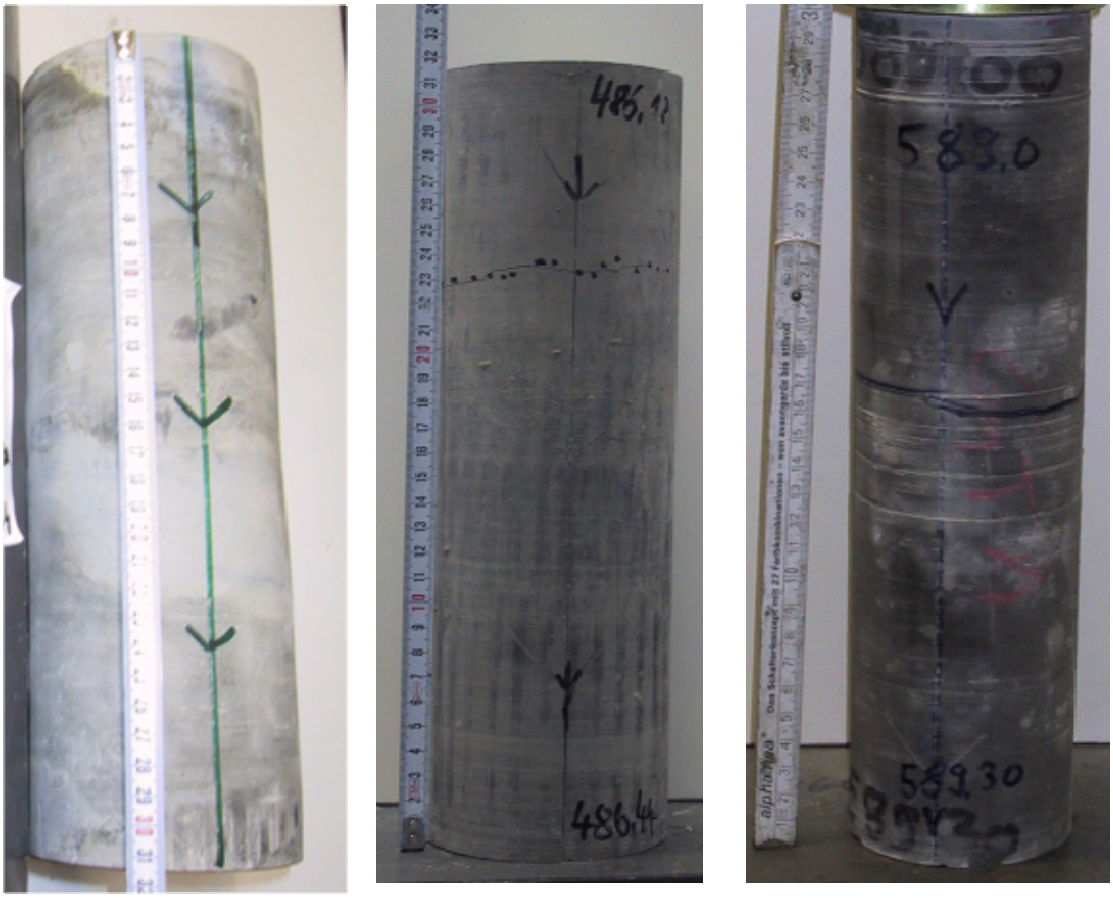

EST05481	EST05684	MSE00837
diameter: 100 mm	diameter: 100 mm	diameter: 84 mm
depth: 434.52-434.84 m	depth: 486.12-486.44 m	depth: 504.10-504.49 m

Figure 3-4 Test samples drilled from the Callovo-Oxfordian argillite at Bure

Large samples

Three large samples HE-D8, D9 and D12 were taken from the heater borehole HE-D0 of 300 mm diameter and 14 m length, which was drilled horizontally and parallel to the bedding plane. The drilled cores were also very compact and relatively homogeneous (Figure 2-7). Immediately after coring, the large cores were cut into several pieces in lengths of 0.8 - 0.9 m and sealed vacuum-tight in aluminium foils and covered by rubber jackets (Figure 3-5). In order to prevent damaging, the samples were then confined by pressing two half parts of hard plastic tube on the jackets with 5 stretching bands (5 x 3.2 kN) as well as by forcing two wood plates on the end faces with 2 bands (2 x 3.2 kN). The confined samples were transported to the GRS laboratory and stored in a climate-controlled room at temperature of ~ 22 °C.

Figure 3-5 Preparation and confinement of large clay samples

After a storage period of more than 1 year, the samples were unpacked for testing. However, some fissures visually appeared on the surfaces more oriented along the bedding planes, as shown in Figure 3-6. Especially in sample HE-D12 a large fracture penetrated so deeply into the sample that it was separated into two parts and could not be used for testing. The other two samples were less damaged. They were carefully prepared to a size of 260 mm diameter and 700 mm length.

HE-D8 (D/L=260/800mm) HE-D9 (D/L=260/900mm) HE-D12(D/L=260/800mm)

Figure 3-6 Large samples of the Opalinus clay after storage over one year

3.3 Petrophysical Properties

The Opalinus clay at Mont Terri and the Callovo-Oxfordian argillite at Bure are over-consolidated sedimentary clay rocks. The Opalinus clay shaly facies where the HE-D test field was positioned consists of 58 - 76 % clay minerals, 6 - 24 % quartz, 5 - 28 % carbonates and 1 - 3 % feldspars /PER 03/. The Callovo-Oxfordian argillite contains in average 40 - 45 % clay minerals, 20 - 30 % carbonates and 20 - 30 % quartz and feldspar /LEB 00/, /HOT 02/.

The petrophysical properties of both clay rocks such as grain density, dry density, bulk density, porosity and water content were measured according to ISRM suggested testing methods /ZHA 02; 04/. The definitions of the properties are given as follows:

- Grain density

$$\rho_s = \frac{M_s}{V_s} \tag{3.1}$$

with M_s = mass of solids, V_s = volume of solids.

- Bulk density

$$\rho_b = \frac{M}{V} = \frac{M_s + M_w}{V} \tag{3.2}$$

with M = mass of bulk sample, V = volume of bulk sample, M_s = mass of solids, M_w = mass of water.

- Dry density

$$\rho_d = \frac{M_s}{V} \tag{3.3}$$

with M_s = mass of solids, V = volume of bulk sample.

- Porosity

$$\phi = \frac{V_v}{V} 100 = \left(1 - \frac{\rho_d}{\rho_s}\right) \cdot 100 \ (\%) \tag{3.4}$$

with V_v = volume of voids, V = volume of bulk sample, ρ_d = dry density, ρ_s = grain density.

- Water content

$$w = \frac{M_w}{M_s} 100 \ (\%) \tag{3.5}$$

with M_w = mass of water, M_s = mass of solids.

- Relationship between bulk density, dry density and water content

$$\rho_d = \frac{\rho_b}{1 + w/100} \tag{3.6}$$

- Relationship between bulk density, dry density and water content

$$\rho_d = \frac{\rho_b}{1 + w/100} \tag{3.7}$$

- Degree of saturation

$$S_l = \frac{V_w}{V_v} 100 \ (\%) \tag{3.8}$$

with V_w = volume of pore water, V_v = volume of voids.

- Relationship between degree of saturation and the other physical characters

$$S_l = \frac{w}{\rho_w} \frac{1}{\left(1/\rho_d - 1/\rho_s\right)} = \frac{\rho_d w}{\rho_w \phi} 100 \ (\%) \tag{3.9}$$

with ρ_w = density of pore water.

Before starting each test, the bulk density of the samples with natural water content was determined by measuring their volume and weight. The water content was measured on pieces remaining from sample preparation. They were dried in an oven at a temperature of 105°C over 2 days. On basis of the measured bulk density and water content, the dry density was calculated. The grain density was measured on powder produced during sample preparation by use of Beckmann's air Pycnometer (Model 930) with helium gas. The porosity was calculated on basis of the measured grain and dry densities. The mean values of the properties measured on both the Opalinus clay the Callovo-Oxfordian argillite are compared in Table 3-2. It is to be pointed out that the Opalinus clay samples were slightly desaturated due to the drilling, preparation and storage. The undisturbed clay rock in-situ is, however, surely saturated.

Table 3-2 Physical properties of samples taken from the Opalinus clay at Mont Terri and the Callovo-Oxfordian argillite at Bure

Material	**Grain density** ρ_s (g/cm^3)	**Dry density** ρ_d (g/cm^3)	**Bulk density** ρ_b (g/cm^3)	**Porosity** ϕ (%)	**Water content** w (%)	**Degree of saturation** S_l (%)
Opalinus clay	2.71	2.28	2.43	16.0	6.7	95.5
CO argillite	2.70	2.25	2.41	16.8	7.7	100.0

The properties of the large samples are summarized in Table 3-3. Due to unavoidable evaporation of the pore-water during the long-term storage, the samples were de-saturated to degrees of 86 % - 92 %.

Table 3-3 Properties of the large samples taken from the HE-D heater borehole

Sample	**Grain density** ρ_s (g/cm^3)	**Bulk density** ρ_b (g/cm^3)	**Dry density** ρ_d (g/cm^3)	**Porosity** ϕ (%)	**Water content** w (%)	**Degree of saturation** S_l (%)
HE-D8	2.710	2.408	2.271	16.25	6.1	86.0
HE-D9	2.710	2.420	2.273	16.15	6.5	92.0
Average	2.710	2.414	2.272	16.20	6.3	89.0

3.4 Experiments on Normal Samples

3.4.1 Water Retention Curve

In highly-compacted indurated clays, a very significant portion of the water content is adsorbed on mineral surfaces. The adsorbed water is so strongly bonded that it may not be able to participate in advective transport under normally-encountered pressure gradients /HOR 96/, /ROD 99/. However, the adsorbed water is able to move out thermodynamically from the pores by the impact of high external suction, and in contrast to that, external water can be taken-up by unsaturated clays if the external suction is lower. De- and re-saturation are controlled by a relation between suction and water content, i.e. the water retention curve.

For the Opalinus clay the water retention curve was measured on unconfined pieces of 35 - 40 grams placed in desiccators at different relative humidities adjusted by means of salt solutions. Figure 3-7 shows the samples of the clay rock together with clay/sand-mixtures in the desiccators. The suction is related to the relative humidity by Kelvin's law /FRE 93/:

$$s = -\frac{RT}{v_{wo}\omega_v}\ln\left(\frac{p_v}{p_{vo}}\right) = -\frac{RT}{v_{wo}\omega_v}\ln(RH) \qquad (3.10)$$

where s = soil suction (kPa)

R = universal gas constant (= 8,31432 J/mol K)

T = absolute temperature (K)

v_{wo} = specific volume of water or the inverse of density of water (= $1/\rho_w$, m^3/kg)

ρ_w = density of water (= 998 kg/m^3 at 20°C)

ω_v = molecular mass of water vapour (= 18,016 kg/kmol)

p_v = partial pressure of pore-water vapour (kPa)

p_{vo} = saturation pressure of water vapour over a flat surface of pure water at the same temperature (kPa)

RH = relative humidity (= $p_v / p_{vo} \cdot 100\,\%$).

The tests were carried out at constant temperature of 22 ± 0.3 °C and different suctions in a range of 0.15 to 236 MPa. The relative humidity in each desiccator was continuously recorded by transistor psychrometer sensors, while the water content of each sample was measured at different periods of time outside the desiccator.

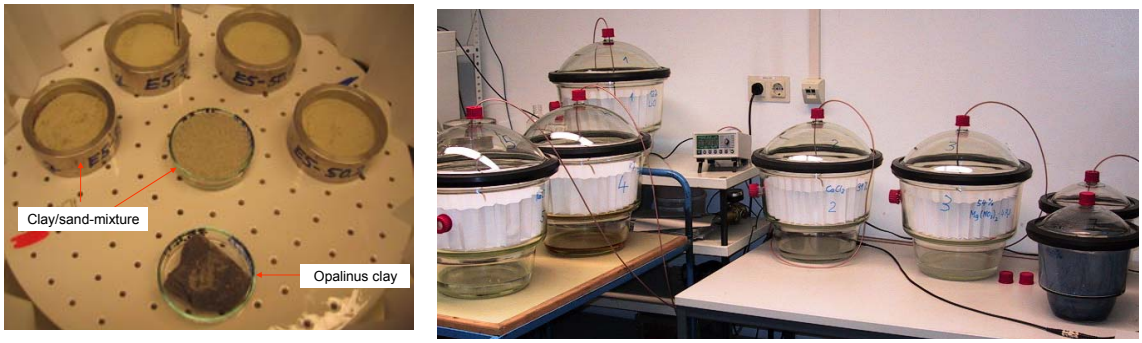

Figure 3-7 Samples of the Opalinus clay placed in desiccators

Table 3-4 shows the applied salt solutions, the resulting relative humidity values in equilibrium and the calculated suction values. Figure 3-8 illustrates the evolution of water content of the samples at different suctions. The samples had an initial water content of 6.6 % and a dry density of 2.31 g/cm^3. At high suctions over 24 MPa, the pore water evaporated from the samples, resulting in a reduction of the water content. Over about 40 days, a suction equilibrium in each desiccator was reached so that the water content of each sample did not change further. However, another sample which was subjected to a low suction of 0.15 MPa took up water from ambient. The water content increased steadily over 110 days.

Table 3-4 Salt solutions applied to the measurement of water retention curve

Salt solution	Relative humidity RH (%)	Suction s (MPa)
LiCl	17.6	236.04
$CaCl_2$	29.8	164.49
$Mg(NO_3)_2 \cdot 2H_2O$	50.9	91.75
KJ	67.4	53.60
NaCl	73.2	42.39
KCl	83.3	24.83
H_2O	99.9	0.15

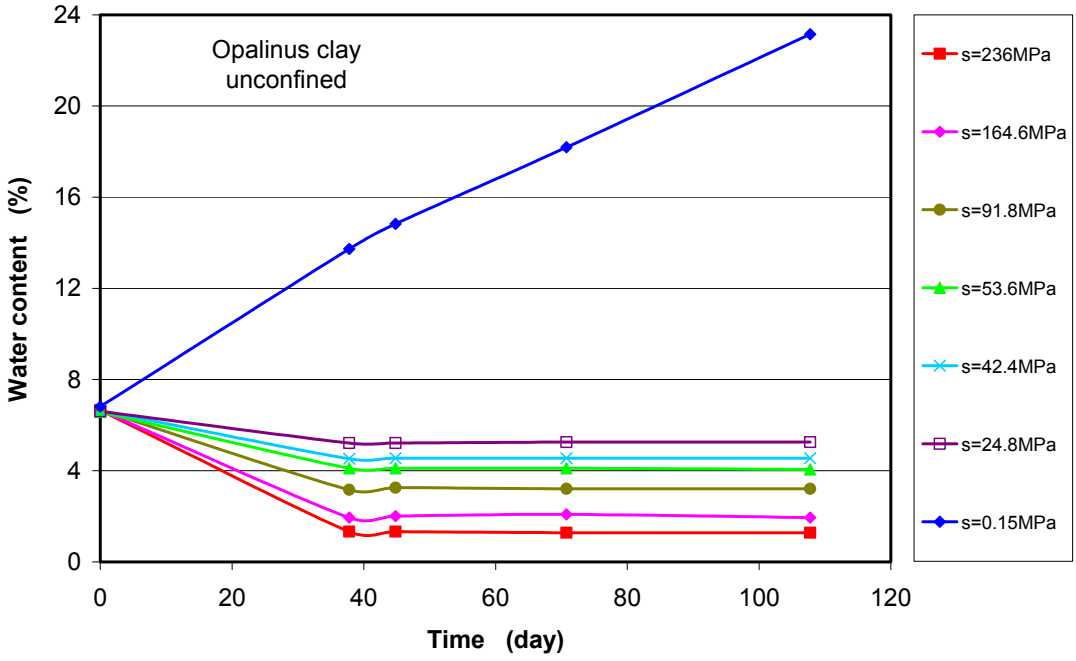

Figure 3-8 Evolution of water content of the Opalinus clay at different suctions

The water contents of the unconstraint samples in equilibrium are represented in Figure 3-9 as a function of suction, together with the UPC-data obtained on Opalinus samples (D/L = 50/20 mm) constraint in oedometer cells /MUN 03/. The GRS-data and the UPC-data are comparable in the high suction range over 20 MPa. It is evident that increasing suction leads to a reduction of the water content. It is also interesting to see

that the unconstraint sample at the low suction of 0.15 MPa (RH ≈ 100 %) took up much water to a water content of 24 % over 110 days, which is about 3 times the water content of ~ 8 % reached by the constraint samples at null suction (UPC-data). Similar observations and the water retention curve for the Callovo-Oxfordian argillite are reported in /LEB 00/. The water retention curve is usually expressed by the Van Genuchten model

$$S_e = \frac{S_l - S_{lr}}{S_{ls} - S_{lr}} = \left[1 + \left(\frac{s}{P_o}\right)^{1/(1-\beta)}\right]^{-\beta} \qquad (3.11)$$

where S_l, S_{lr}, S_{ls}, S_e are the actual, residual, maximum and effective saturation of liquid, respectively, s is the suction, P_o is a material parameter, and β controls the shape of the water retention curve. For the Opalinus clay, all the data obtained by GRS and UPC were employed for determining the parameters for both wetting and drying paths respectively, and a mean curve shown in Figure 3-10 was established. The parameters are: β = 0.3 for all the curves, P_o = 20 MPa for the wetting curve, P_o = 5 MPa for the drying curve, and P_o = 12 MPa for the mean curve. Generally, at a same suction, the degree of water saturation reached by wetting is somewhat higher than that by drying.

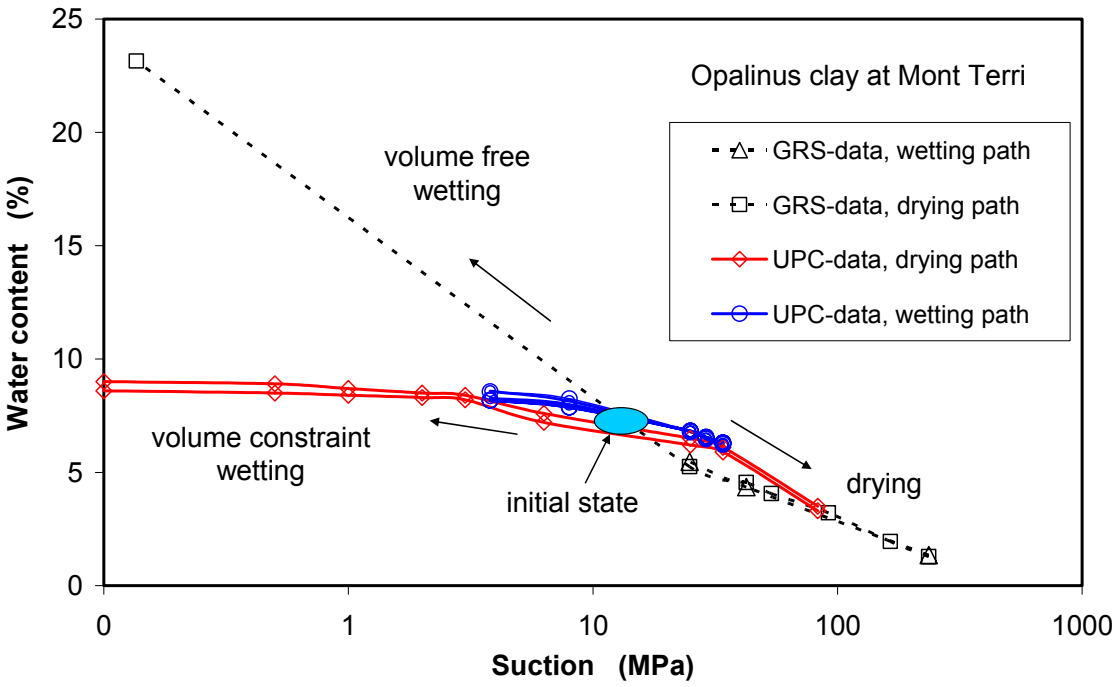

Figure 3-9 Suction / water content – relationship for the Opalinus clay under unconstraint (GRS-data) and constraint conditions (UPC-data)

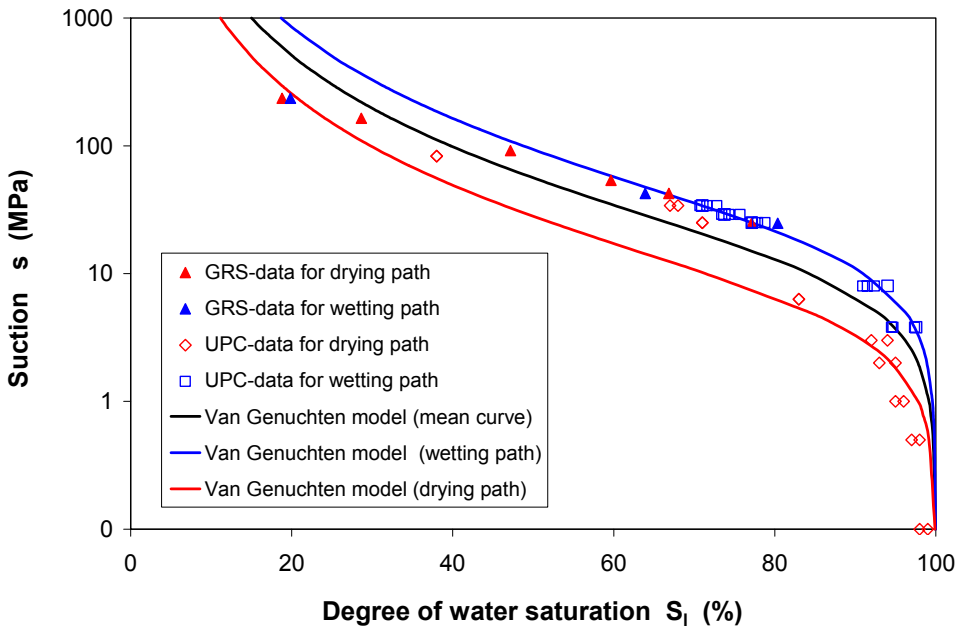

Figure 3-10 Water retention curves for the Opalinus clay obtained by drying and wetting as well as the averaged curve

3.4.2 Thermal Expansion

Thermal expansion of the Opalinus clay was measured on samples under unloaded and loaded conditions. One test was carried out on a sample in an oven under unloaded conditions by heating and cooling, whereas the other tests were performed on 4 samples loaded in a triaxial cell at elevating temperature. The test temperature varied between 20 and 85 °C. The samples and test conditions are given in Table 3-5.

Table 3-5 Opalinus clay samples tested for determination of thermal expansion

Sample	Diameter (mm)	Length (mm)	Bulk density (g/cm^3)	Dry density (g/cm^3)	Poro-sity (%)	Water content (%)	Tempe-rature (°C)	Confining pressure (MPa)
BHED5/15	83.5	160.6	2.420	2.282	15.90	6.06	32 - 75	0.0
BHED4/6A	83.5	120.0	2.433	2.280	16.01	6.70	22 - 30	3.1
BHED5/6	83.5	120.0	2.434	2.281	15.97	6.70	25 - 65	3.1
BHED5/8A	83.5	120.0	2.437	2.284	15.86	6.70	20 - 80	3.3
BHED5/8B	83.5	120.2	2.429	2.276	16.15	6.70	25 - 85	3.3

Thermal expansion under unloaded conditions

The thermal expansion test under unloaded conditions was carried out on sample BHED5/15 of 84 mm diameter and 160 mm length in an oven, as shown in Figure 3-11. Another small sample (D/L = 84/44 mm) was used for monitoring possible water evaporation during the test. Both samples were covered with silicone and sealed in rubber jackets to prevent water release. Thermal strains were measured on sample 1 by using strain gauges, which were directly attached on the end face and the peripheral surface of the sample parallel and perpendicular to the bedding (Figure 3-12). Both samples were heated stepwise from 32 to 35, 45, 54, 64 and 73 °C at a rate of 7.5°C/h. At each level, the temperature was maintained constant for 1 to 3 days, respectively. After the heating phase, the samples were cooled stepwise down to different levels for 1 to 4 days each at the same rate of 7.5°C/h.

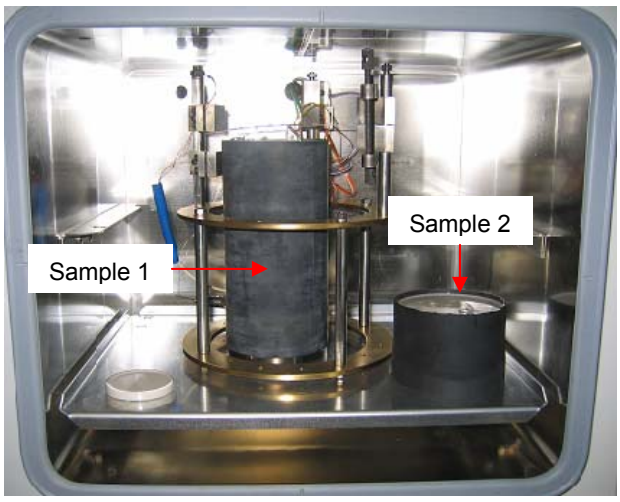

Figure 3-11 Thermal expansion test on an Opalinus clay sample in an oven under unloaded conditions

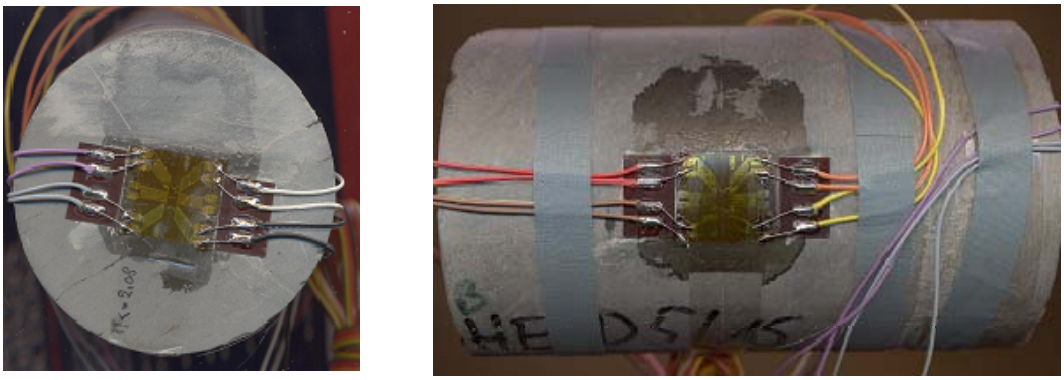

Figure 3-12 Measurement of thermal expansion by using strain gauges attached on sample surfaces

Figure 3-13 shows the evolution of the temperature, the thermally-induced water release of sample 2 and the thermal strains of sample 1 during the test. It is obvious that, although the samples were sealed, a steady water loss up to 1.2 % was observed over the heating and cooling periods of 26 days. Unfortunately, the strain gauges attached on the end face of sample 1 failed at the elevated temperature of 73 °C. By comparing both Figures 3-13a and 3-13b, the following phenomena can be clearly recognised:

1. Each temperature rise caused a rapid expansion in the direction perpendicular to the bedding ($\perp$), whereas the thermal expansion parallel to the bedding (//) was not significant.

2. At each constant temperature, the clay sample contracted with time in all directions, probably due to the water release. The contraction rates seemed to be relatively constant at each elevated temperature.

3. Each drop of the temperature induced a sudden contraction and then a small reversion in the direction perpendicular to the bedding, but conversely a sudden expansion parallel to the bedding. Strain changes are negligible at each constant temperature during the cooling phase.

Based on the data obtained during each temperature increase and decrease, the thermal expansion and contraction coefficients were determined (Figure 3-14). Whereas the thermal expansion coefficients measured perpendicular ($\alpha\perp$) and parallel ($\alpha_{//}$) to the bedding are relatively constant, the thermal contraction coefficients reduced somewhat with decreasing temperature. Both the thermal expansion coefficient and contraction coefficient perpendicular to the bedding are about one order of magnitude higher than those parallel to the bedding, indicating a significant thermal anisotropy of the clay rock.

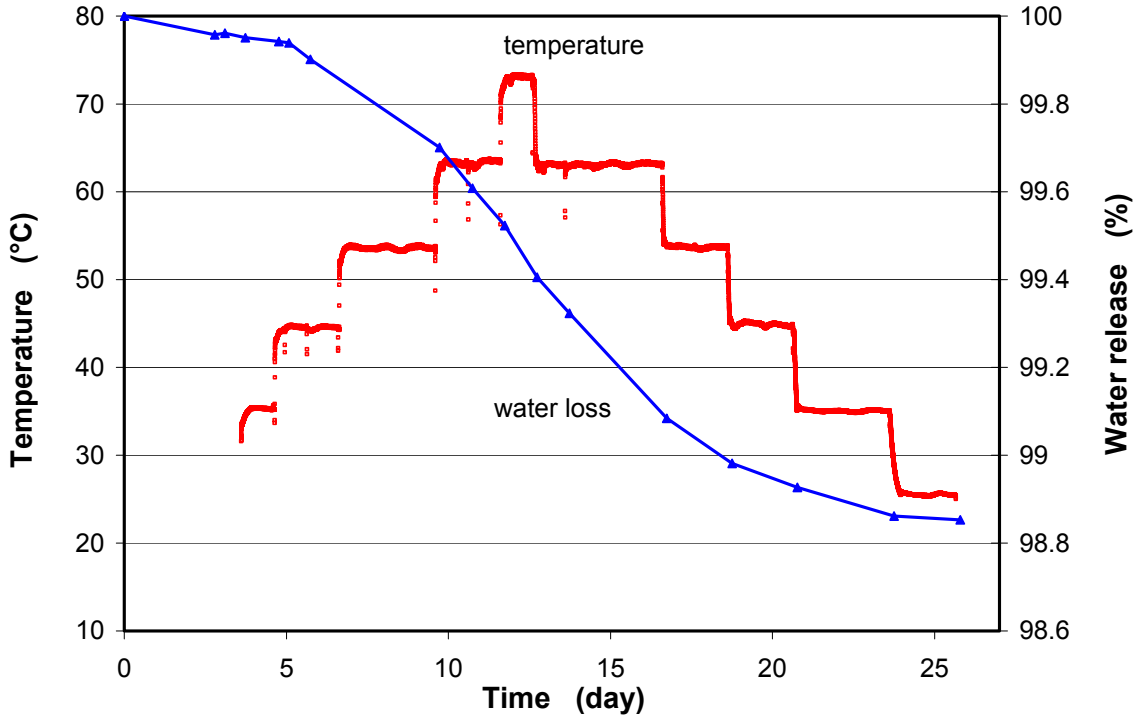

a. temperature and water release

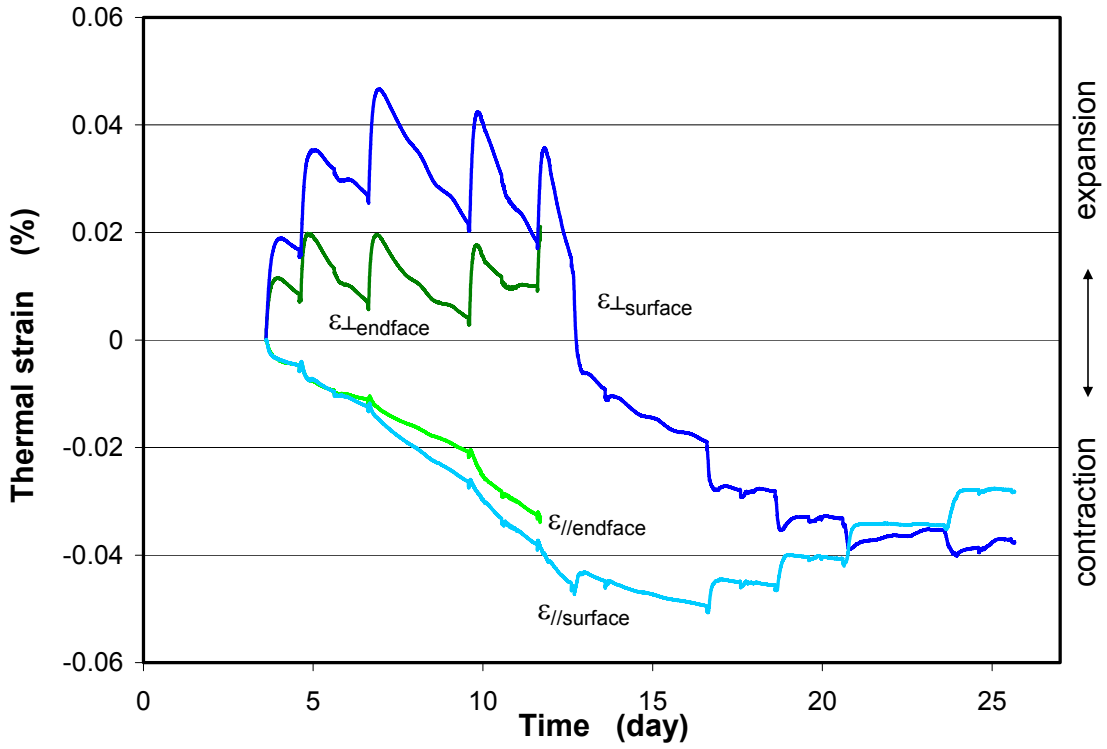

b. thermal strains

Figure 3-13 Measurement of temperature, water loss and strains of the unloaded Opalinus clay samples by heating and cooling

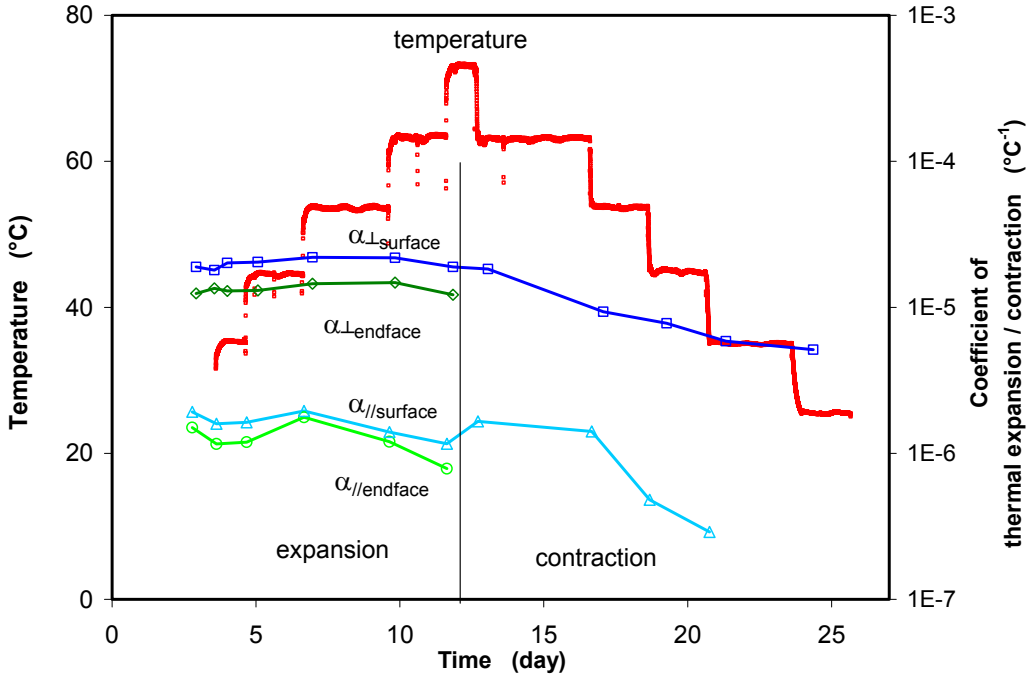

Figure 3-14 Thermal expansion and contraction coefficients of the Opalinus sample

The thermal expansion coefficients measured on the end face are slightly higher than those measured on the peripheral surface. The average value of the thermal expansion coefficient is $\alpha_{\perp} = 1.6 \cdot 10^{-5}$ °C^{-1} perpendicular to the bedding and $\alpha_{//} = 1.5 \cdot 10^{-6}$ °C^{-1} parallel to the bedding (Table 3-6). After testing, micro-fractures along the bedding planes appeared, as shown in Figure 3-15.

Table 3-6 Thermal expansion coefficients of the Opalinus clay measured under unloaded conditions

Measuring position	Thermal expansion coefficient (°C^{-1})	
End face	$\alpha_{\perp} = 1.3 \cdot 10^{-5} \pm 0.98 \cdot 10^{-6}$	$\alpha_{//} = 1.5 \cdot 10^{-6} \pm 0.34 \cdot 10^{-6}$
Peripheral surface	$\alpha_{\perp} = 2.0 \cdot 10^{-5} \pm 0.15 \cdot 10^{-5}$	$\alpha_{//} = 1.6 \cdot 10^{-6} \pm 0.28 \cdot 10^{-6}$
Mean value	$\alpha_{\perp} = 1.6 \cdot 10^{-5} \pm 0.13 \cdot 10^{-5}$	$\alpha_{//} = 1.5 \cdot 10^{-6} \pm 0.31 \cdot 10^{-6}$

Figure 3-15 Thermally-induced fractures in a sealed Opalinus sample during a heating / cooling cycle between 30 and 73 °C

Additionally, such thermally-induced fractures were also observed on a non-sealed piece of the Opalinus clay at 105 °C, as shown in Figure 3-16. It is obvious that the thermally-induced fractures penetrated mostly along the bedding planes and extended with time.

t = 0 d t = 14 d t = 22 d t = 32 d

Figure 3-16 Thermally-induced fractures in a non-sealed Opalinus clay sample at 105°C

Thermal expansion under loaded conditions

The thermal expansion tests under loaded conditions were performed on 4 Opalinus clay samples in a triaxial cell. The samples were sealed in rubber jackets, loaded to an isotropic stress of about 3 MPa and then heated to a desired temperature at rates of 2 - 5 °C/h. The thermal strains were measured by using strain gauges attached on the

surface at the mid-height perpendicular to the sample axis, which was inclined to the bedding plane with angles of 30° - 40°. Figure 3-17 illustrates the results of thermal expansion as a function of temperature. The slope of each curve represents the thermal expansion coefficient. The values determined are summarized in Table 3-7. The mean value of $1.5 \cdot 10^{-5}$ $°C^{-1}$ coincides with that measured perpendicular to the bedding under unloaded conditions (Table 3-6).

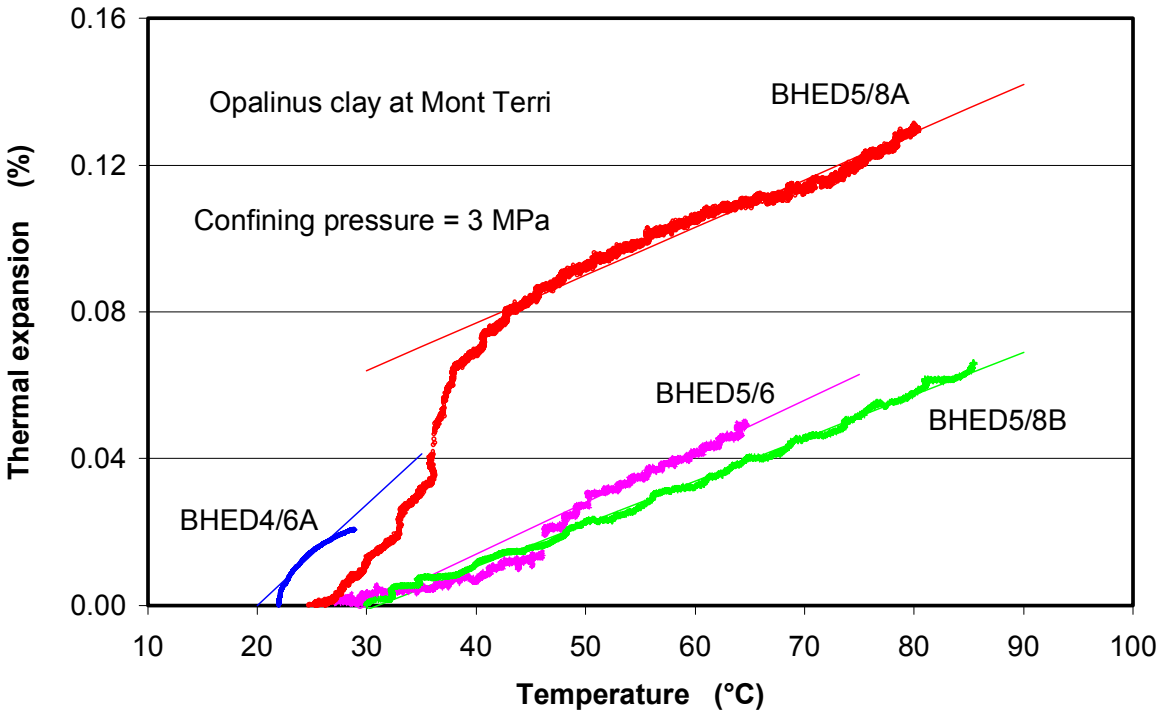

Figure 3-17 Thermal expansion measured on the Opalinus clay samples under confined conditions

Table 3-7 Thermal expansion coefficients of the Opalinus clay measured at 3 MPa confining stress

Sample	BHED4/6A	BHED5/6	BHED5/8A	BHED5/8B	Mean value
α ($°C^{-1}$)	$2.1 \cdot 10^{-5}$	$1.4 \cdot 10^{-5}$	$1.3 \cdot 10^{-5}$	$1.2 \cdot 10^{-5}$	$1.5 \cdot 10^{-5} \pm 0.5 \cdot 10^{-5}$

3.4.3 Triaxial Compressive Behaviour

The short-term compressive behaviour of the Opalinus clay was investigated on 8 samples in a triaxial apparatus, which permits a normal sample of D/L = 84/120 mm to be loaded to a maximum axial load of 1600 kN (~ 200 MPa) and a maximum lateral stress of 70 MPa and to be heated up to 200 °C /ZHA 02/. The characters of the samples, the test conditions and resulting strengths are given in Table 3-8. The average water content of the samples is 6.7 %. The samples were axially loaded until failure at different confining stresses of 2 - 8 MPa and at elevated temperatures between 20 and 116 °C. The axial loading direction was inclined to the bedding with angles of 30 - 40°.

Table 3-8 Overview of the triaxial compression tests on the Opalinus clay samples

Sample	**Diameter** (mm)	**Length** (mm)	**Bulk density** (g/cm^3)	**Porosity** (%)	**Temperature** (°C)	**Lateral stress** (MPa)	**Axial stress** (MPa)
BHED4/5A	83.5	120.1	2.56	11.65	20.0	2.0	22.8
BHED4/4B	83.5	119.9	2.47	14.78	20.0	5.0	23.0
BHED4/4A	83.5	119.8	2.44	15.64	20.0	8.0	27.1
BHED4/5B	83.5	115.0	2.50	13.87	20.0	1.1	7.5
BHED4/6A	83.5	120.0	2.43	16.01	41.5	3.1	14.9
BHED5/6	83.5	120.0	2.43	15.97	68.6	3.1	12.1
BHED5/8A	83.5	120.0	2.44	15.86	94.5	3.3	11.0
BHED5/8B	83.5	120.2	2.43	16.15	115.7	3.3	8.5

In the tests, the samples were first loaded to a desired isotropic stress and then heated at rates of 2 - 5 °C/h to a desired level for determination of the thermal expansion coefficient (see section 3.4.2). At constant lateral stress and temperature, the axial load was increased at a strain rate of $1 \cdot 10^{-7}$ s^{-1} or $2 \cdot 10^{-8}$ s^{-1}, respectively. Whereas the axial strain was recorded by a LVDT-transducer positioned outside of the cell, the radial strain was measured by use of strain gauges directly attached on the sample surface at

the mid-height. In order to detect damage evolution in the samples during loading, ultrasonic wave velocity was additionally measured.

Figure 3-18 shows a typical example of the tests on sample BHED4/4 at T = 20 °C and $\sigma_2 = \sigma_3 = 8$ MPa. Generally, the sample exhibited a typical elasto-plastic character with linear axial compression and radial extension until the onset of dilatancy and yield-strains with hardening until the peak strength and finally plastic-flow until failure. The wave velocity increased with the elastic compressive deformation and then reached a maximum value, at which micro-fractures in the sample were initiated, resulting in dilatancy. Over the dilatancy onset point the fractures penetrated further with increasing stress until failure. Figure 3-19 shows the fractures after testing, which appeared mostly along the bedding planes. This test suggested that the dilatant strength is about 80 % of the peak strength.

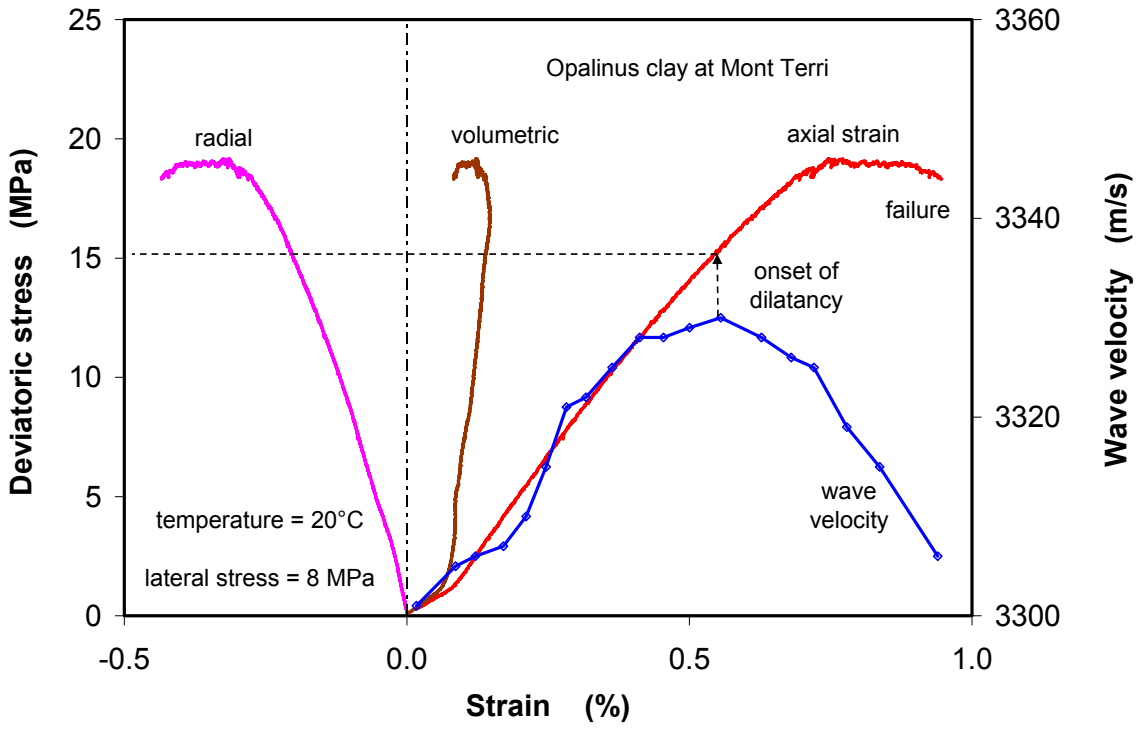

Figure 3-18 Results of a typical triaxial compression test on an Opalinus clay sample

Figure 3-19 Opalinus clay samples after failure

Figure 3-20 compares the stress / strain – curves obtained at different lateral stresses of 1, 2, 5 and 8 MPa and at a temperature of 20 °C. It can be seen that the strength increases with confining stress. The failure strains are limited within 1 %. The volumetric strain curves indicate that the samples were compacted progressively with increasing the deviatoric stress until the onset of dilatancy. The onset points of dilatancy obtained by the volume measurement on all the samples are very close to the peak strengths, significantly lower than that detected by means of ultrasonic wave. Figure 3-20 shows additionally that the sample laterally confined by σ_3 = 2 MPa has a relatively high strength.

The stress / strain – curves obtained at different temperatures of 20 to 116 °C are illustrated in Figure 3-21. It can be clearly identified that under undrained conditions and comparable lateral stress of about 3 MPa, the clay rock became more ductile and weaker with increasing temperature. The strength reduced significantly by a factor of 4 from 20 MPa at 20 °C down to 5 MPa at 116 °C. The weakness might be caused by thermally-induced pore over pressure, which in turn reduces the effective mean stress and may also generate fractures as the confining stress is exceeded. The previous tests made by GRS /ZHA 04/ and new ones (section 3.4.7) showed that thermally-induced pore-water over-pressures reached up to 5 - 6 MPa by increasing temperature from 25 - 30 °C to 60 - 90 °C. The pore-water over-pressures are much higher than the lateral confining stress of 3 MPa in the current tests at high temperatures over

70 - 116 °C. So the samples were probably subjected to the high extensional stresses and failed.

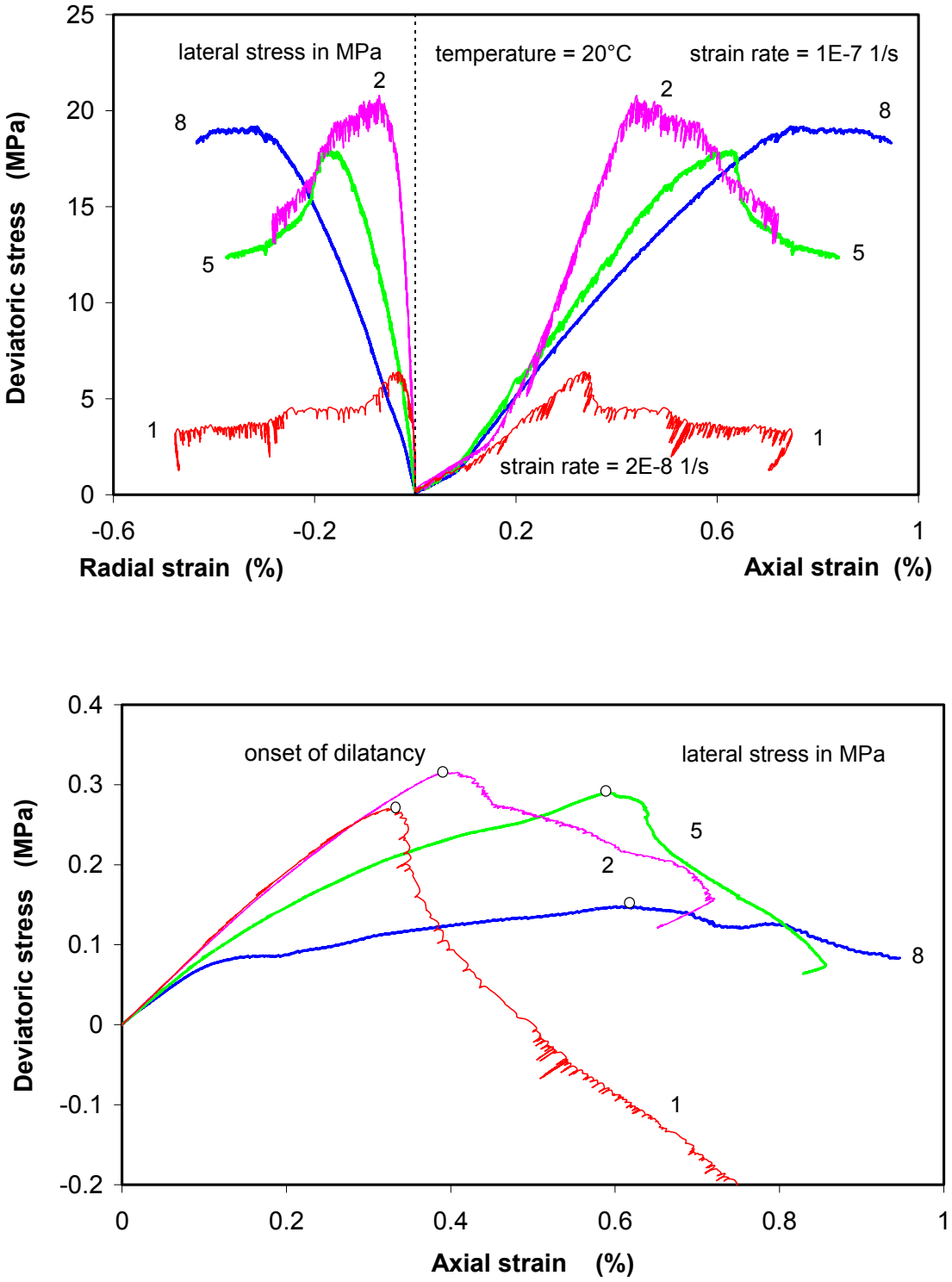

Figure 3-20 Stress / strain – behaviour of the Opalinus clay samples at different confining stresses

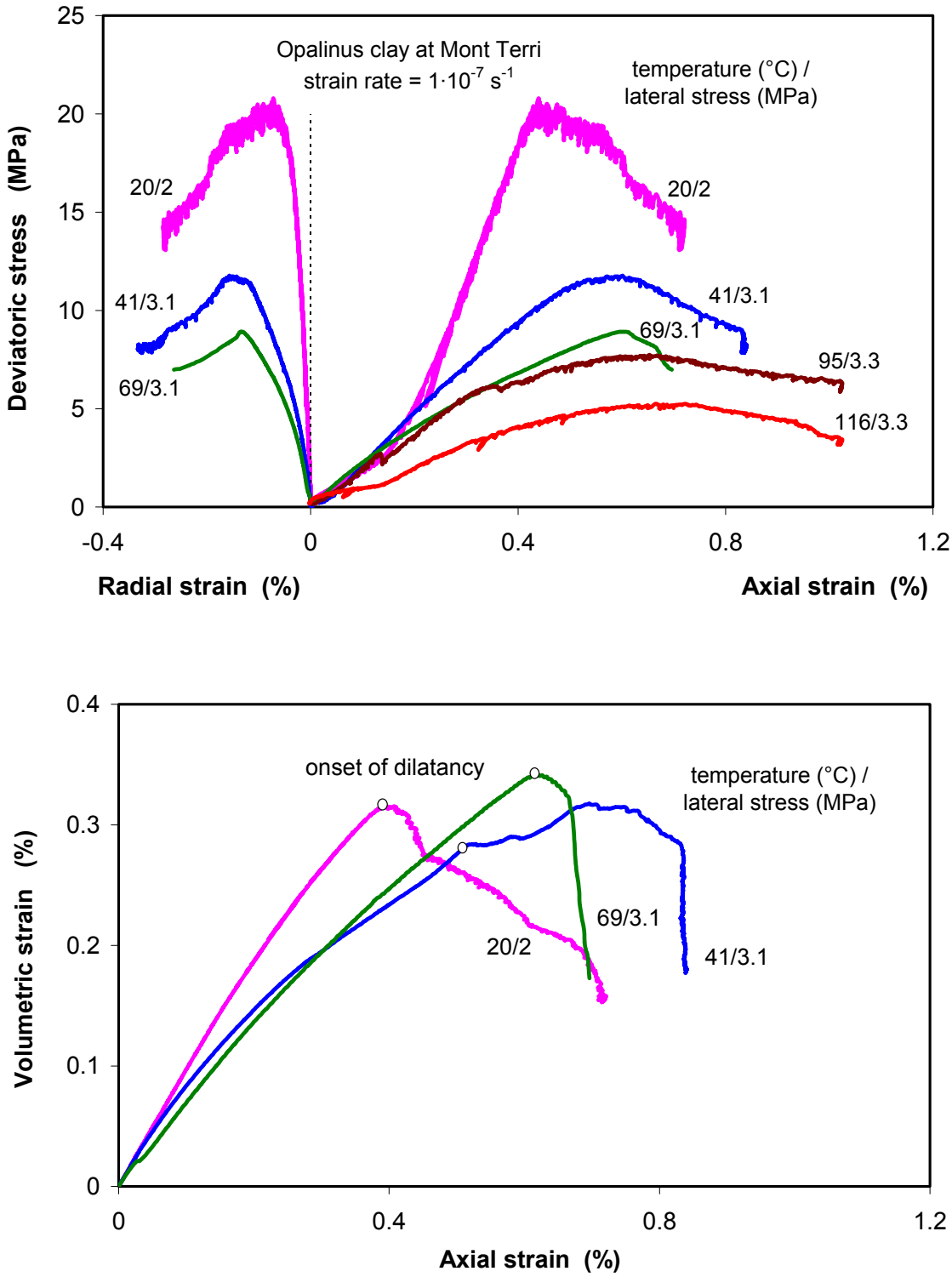

Figure 3-21 Stress / strain – behaviour of the Opalinus clay samples at different temperatures

Figure 3-221 compares the obtained strength values with the average strength curves given in /BOC 01/ for the Opalinus clay perpendicular and parallel to the bedding as well as the shear strength of the bedding planes. Generally, the Opalinus clay exhibits a significant anisotropy of the mechanical behaviour. GRS data are between the given strength curves. The strengths at high temperatures over 70 °C are comparable with the shear strength of the bedding planes at ambient temperature.

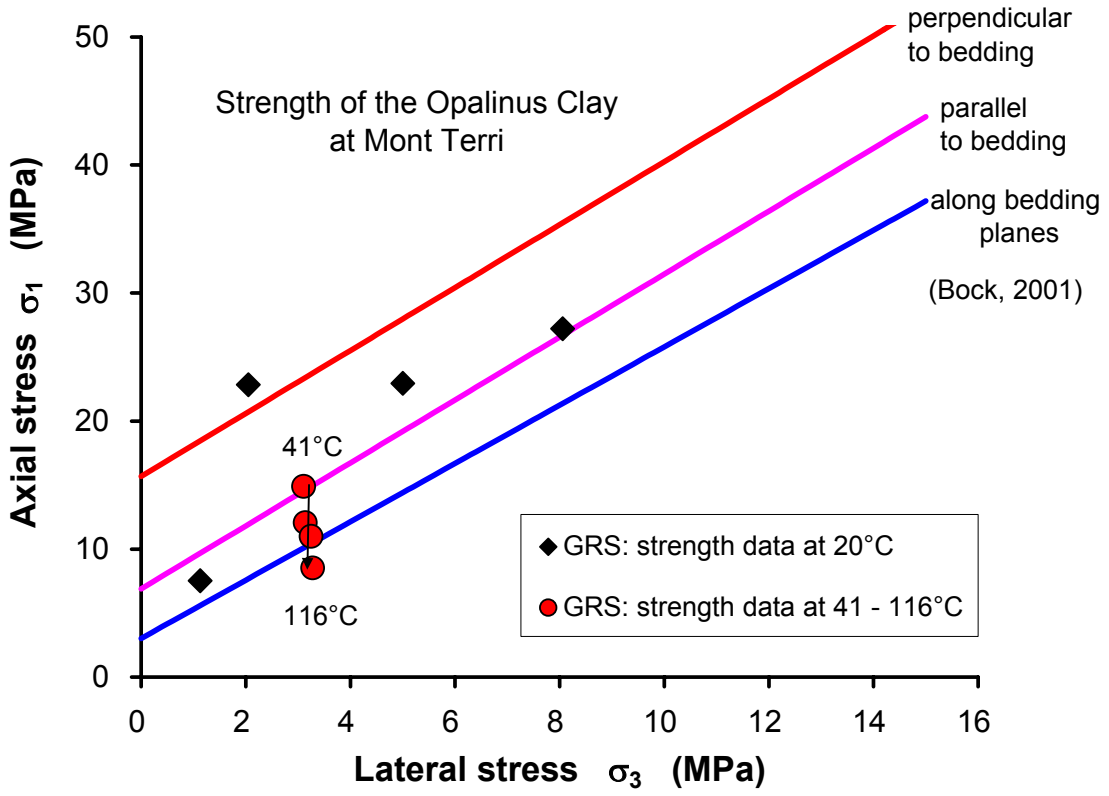

Figure 3-22 Strength of the Opalinus clay determined on core samples

3.4.4 Long-term Creep Behaviour

In the frame of the GRS previous projects, long-term deformation of the Callovo-Oxfordian argillite and the Opalinus clay was experimentally studied in uniaxial creep tests at ambient temperature. In order to examine temperature influence on the long-term deformation of the clay rock, four previous creep tests on the Callovo-Oxfordian samples were continued over the period of the HE-D project, totally lasting over exceptionally long durations of 2.5 - 4.5 years. An additional creep test was also conducted on an Opalinus clay sample taken from the shaly facies in the HE-B test

field near the HE-D test field at the MTRL. All the creep tests were conducted in the GRS creep rigs. Each rig allows two samples to be simultaneously tested at a same load up to 500 kN and at individual temperatures between 20 and 200°C. In order to prevent evaporation of the pore-water during testing, the samples were sealed in rubber jackets. According to the loading conditions, the four creep tests on the Callovo-Oxfordian samples were divided into 2 groups, group A including samples EST05671 and EST05481, and group B consisting of samples EST05684 and MSE00837. Test results obtained during the HE-D project period are evaluated in this report. Because the measurement of axial strain included not only the part of the sample but also the upper and lower pistons, the thermal expansion of the pistons by elevating temperature was carefully excluded from the measured total strain.

Results on the Callovo-Oxfordian argillite

In test group A, both samples EST05671 and EST05481 under an axial stress of 13.8 MPa were heated stepwise from 24 to 60 °C, then cooled down to 40 °C, and finally reheated to 90 °C. The test duration lasted over 2.7 years. The results are illustrated in Figures 3-23 and 3-24. It is to be noted that sample EST05671 was taken from the rheological zone B with relative low carbonate content and a water content of 7.4 %, while sample EST05481 originated from the stiff zone A with high carbonate content and a low water content of 5.0 % /ZHA 02/.

In test group B, the other two samples EST05684 and MSE00837 were subjected to very low axial stresses of 0.74 and 1.0 MPa. The same thermal loading path like in the test group A was applied for 2.7 years. The results are shown in Figures 3-25 and 3-26. Sample EST05684 was nearly saturated with a water content of 6.9 %, while sample MSE00837 was already de-saturated before testing with a low water content of 4.6 %.

From the measurements of the axial strain (Figures 3-23 to 3-26) and the creep rates (Figure 3-27) determined from the last linear parts of the strain / time curves at each elevated temperature, the following phenomena can be recognised:

- Suddenly increasing the temperature led to a short-term expansion (strain curve downwards), and after that, the compressive deformation took place and continued with time. The deformation rate was higher when the temperature was elevated, but only in a limited range below 40 - 50 °C.

- At elevated temperatures of 50 - 60 °C, the compressive strain rate slowed, possibly due to the dispersion of thermally-mobilized pore-water towards the annular space between sample and jacket. The pore-water release could result in collapse of the de-saturated pores and hence increase the shear resistances between solid particles.
- Reducing temperature from 60 to 40 °C resulted in a sudden contraction, but no further deformation was observed on all the samples over 3 months.
- Further increasing the temperature step by step from 40 to 90 °C produced a repeat of the short-term expansion and a progressive compression, but the deformation rates are slightly lower than before at lower temperatures between 30 and 60 °C.
- The creep rates measured on sample EST05481 from the rheological zone A with more carbonate content and less water content vary in a range between $5{\cdot}10^{-12}$ and $5{\cdot}10^{-11}$ s^{-1}, about one order of magnitude lower than that of $4{\cdot}10^{-11}$ to $5{\cdot}10^{-10}$ s^{-1} determined on the other samples from zone B, even at lower stresses (Fig. 3-27).

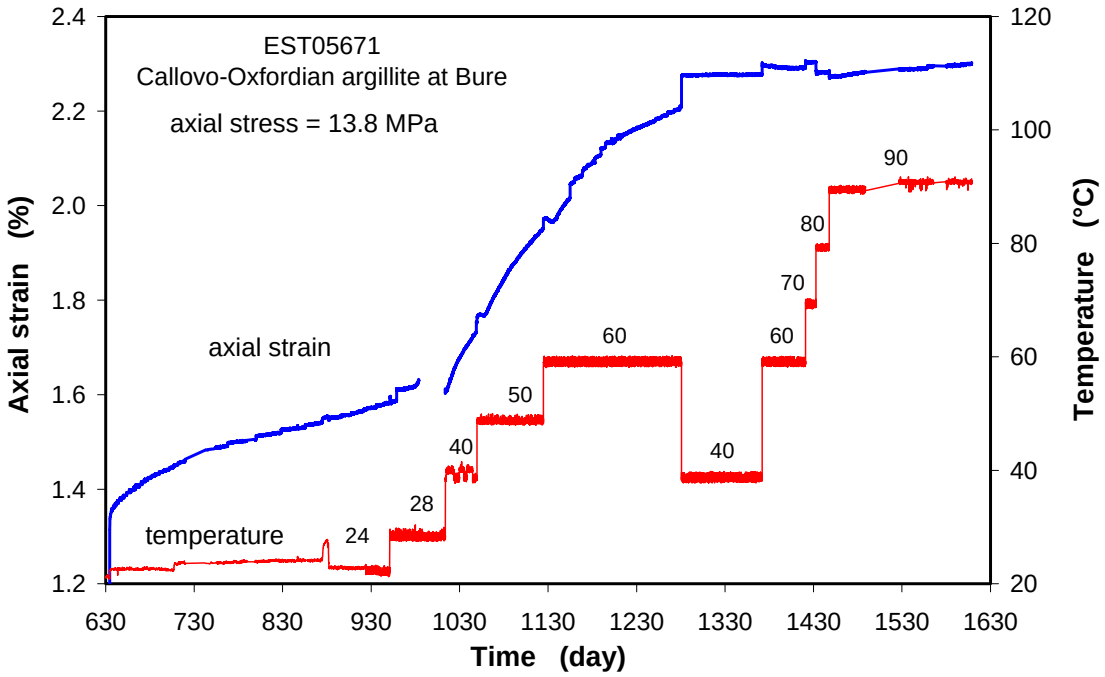

Figure 3-23 Uniaxial creep test on Callovo-Oxfordian sample EST05671 from zone B at elevated temperatures under axial stress of 13.8 MPa

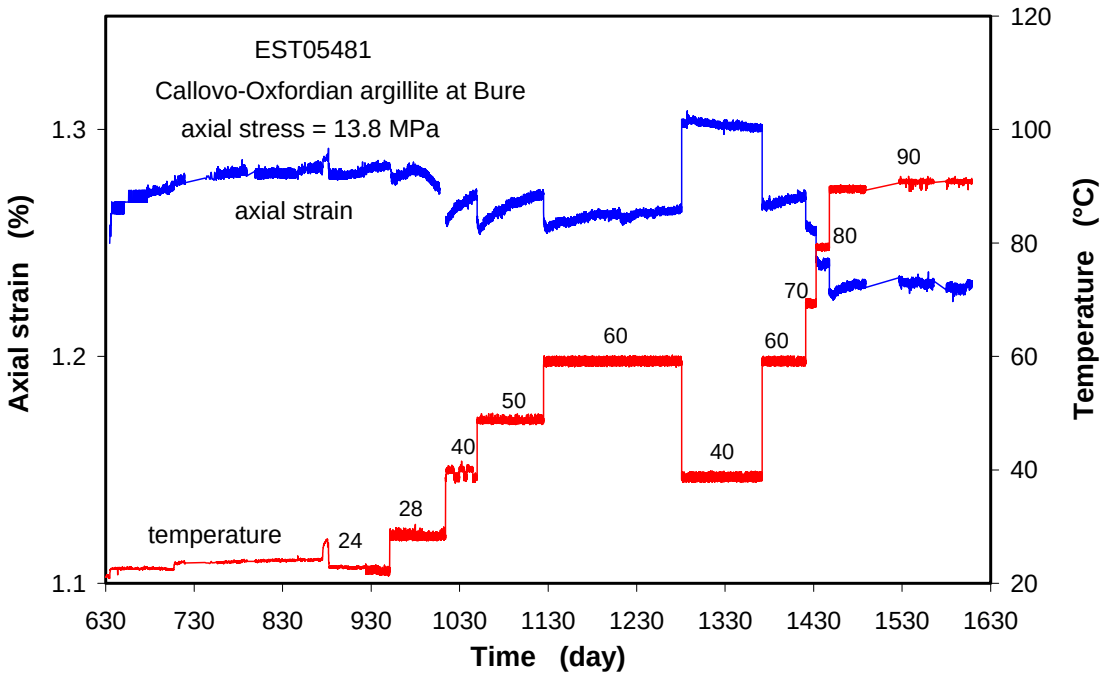

Figure 3-24 Uniaxial creep test on Callovo-Oxfordian sample EST05481 at elevated temperatures under axial stress of 13.8 MPa

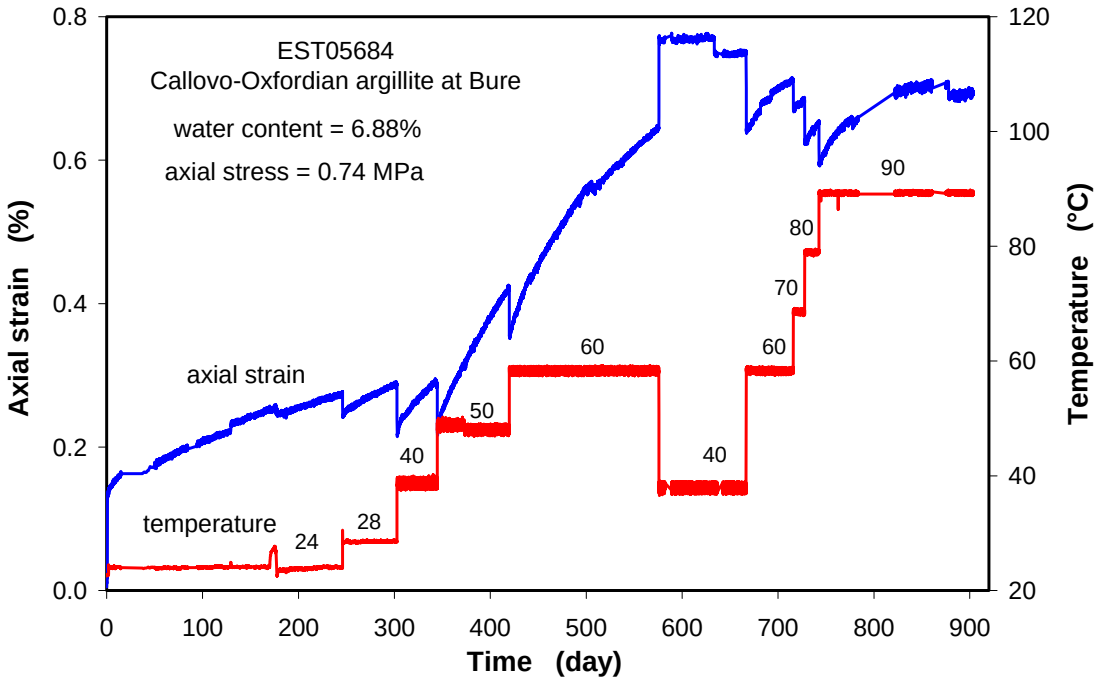

Figure 3-25 Uniaxial creep test on Callovo-Oxfordian sample EST05684 at elevated temperatures under axial stress of 0.74 MPa

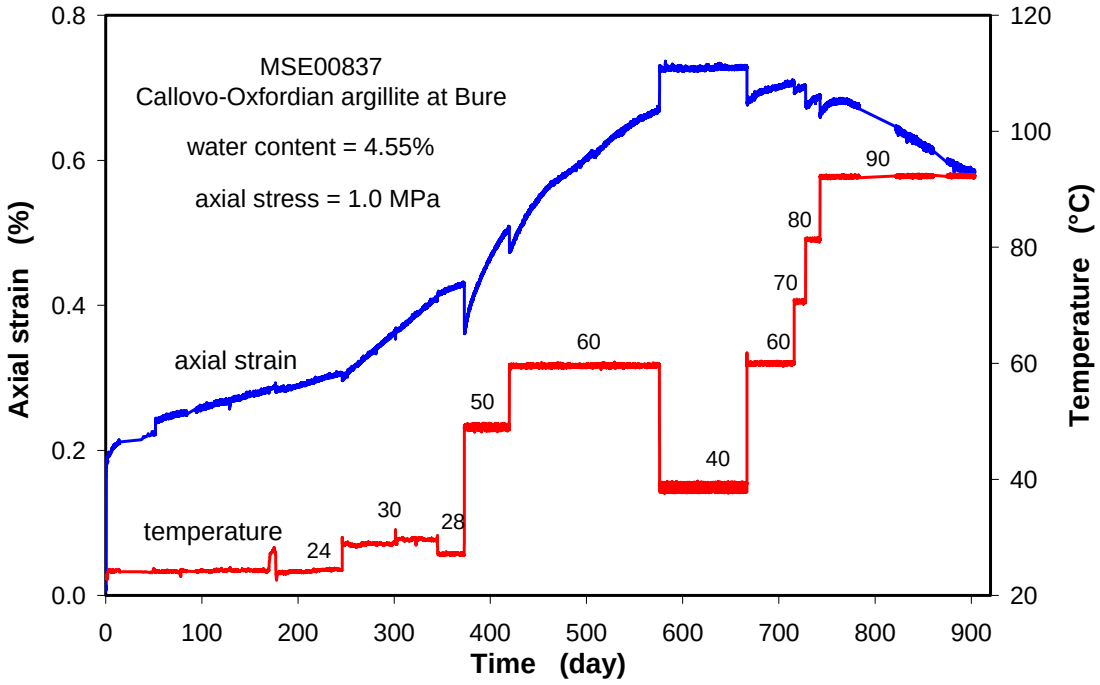

Figure 3-26 Uniaxial creep test on Callovo-Oxfordian sample MSE00837 at elevated temperatures under axial stress of 1.0 MPa

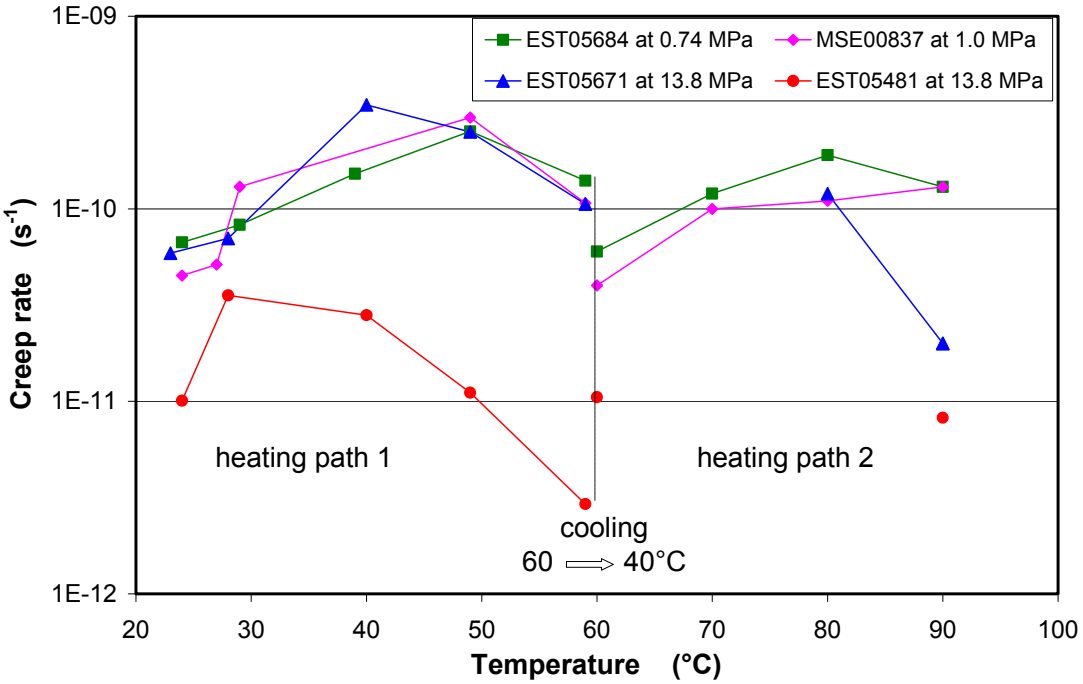

Figure 3-27 Creep rates measured in the end phase at each elevated temperature for the Callovo-Oxfordian argillite

Results on the Opalinus clay

Figure 3-28 presents the creep test on the Opalinus sample BHE-27 with an initial water content of 7.0 %. The sample was sealed in a rubber jacket and placed in the testing chamber. The test was performed over 1.4 years in several steps by changing the conditions of axial load, temperature and relative humidity to examine their effects on the deformation:

- First, the sample was axially loaded to a low stress of 0.74 MPa under a relative humidity of about 30 % and at a temperature of 24 °C. Unexpectedly, after the compressive loading, a slight expansion (strain curve downwards) occurred rather than a compression for the first 20 days.
- In the second stage, the sample was heated stepwise by increasing temperature to 28 °C and then to 38 °C for 2 and 3 months respectively. Each sudden heating induced a short-term expansion. After that, the axial compressive strain increased with time. However, the creep rate of $1.9 \cdot 10^{-10}$ s^{-1} measured at 38 °C is slightly lower that of $2.9 \cdot 10^{-10}$ s^{-1} at 28 °C. This might be caused by evaporation of the pore-water towards the annular space between sample and jacket.

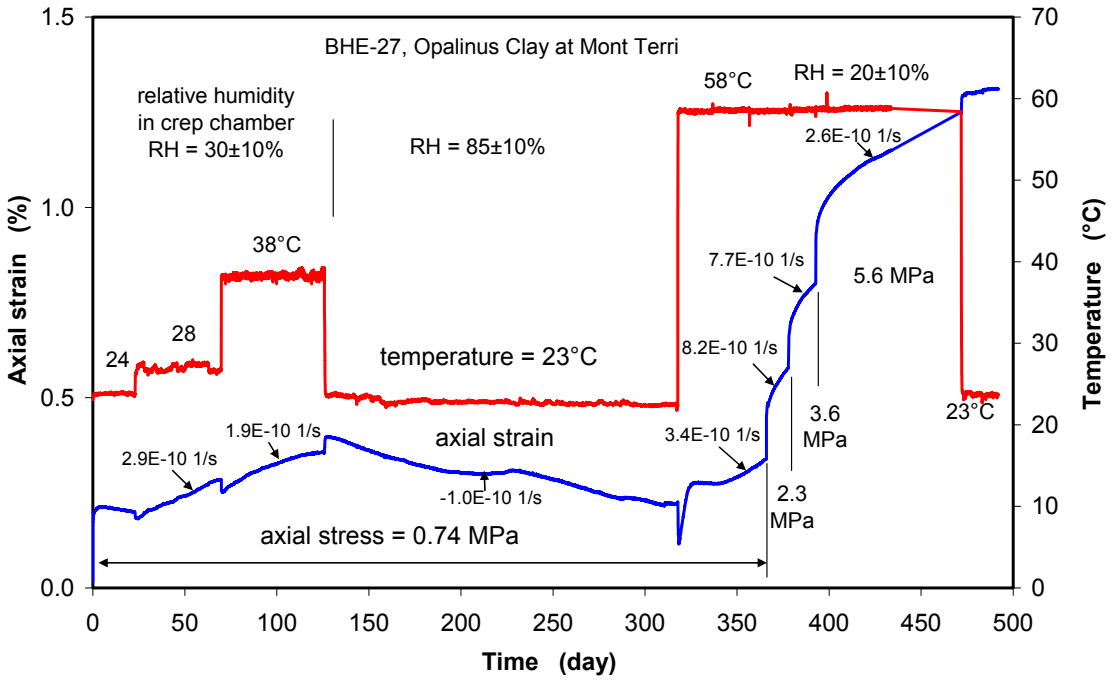

Figure 3-28 Uniaxial creep test on Opalinus clay sample at elevated temperatures and different loads

- After the heating, the sample was cooled down to 23 °C and simultaneously wetted by increasing the relative humidity to about 85 %. After a short-term thermal contraction, the sample swelled steadily with time. This indicates that the sample might not be absolutely isolated from the ambient, and thus re-hydrated by taking up water from the air. The re-hydration led to an expansion even in the loaded axial direction to 0.17 % over 6 months.
- Subsequently, rising temperature to 58 °C and reducing the relative humidity to 20 % led to a repeat of the short-term expansion and then continuous compressive strain. At 58 °C, the axial load was increased step by step from 0.74 MPa to 2.3, 3.6 and 5.6 MPa. At each load, the compressive strain continued with time, no steady state of the deformation was observed within the time intervals between 0.5 and 2.7 months.
- Finally, the sample was cooled down to 23 °C at a stress of 5.6 MPa, resulting in a sudden contraction and subsequent negligible time-dependent deformation.

Generally, the acceleration of the deformation at elevated temperature might result from two mechanisms: a) the thermally-induced reduction of the pore-water viscosity decreases the shear resistances between particles in saturated condition and b) the release of thermally-mobilized pore-water causes collapse of the de-saturated pores. Since the shrinkage due to collapse of pores actually does not belong to the creep defined as irreversible and nearly crack-free change of shape in time /CRI 98/, the shear resistances between particles may dominate the pure creep deformation in clay rocks. When the clay rock is highly de-saturated, the shear resistances between particles will increase until creep ceases. Generally, creep mechanisms in clays are still not well understood. But the observations suggest that water-films adsorbed in indurated clays play a key role in the deformation.

3.4.5 Swelling / Shrinking Behaviour

Swelling in clays is the physico-chemical process by which water is drawn into the material and interacts with particle surfaces. The clay-water interactions cause adsorption of water on the internal and external surfaces of clay minerals, forming electrostatic double-layers. In the narrow spaces between clay particles the double-layers are usually overlapping. This generates local over-pressures (disjoining pressures) acting in the water-films. The average disjoining pressure is equivalent to

the swelling pressure observed in volume-confined clay-based material /HOR 96/, /ROD 99/. In unconfined case as well as at certain loads, the clay-based materials will expand due to the internal disjoining pressures.

The previous GRS experiments /ZHA 04a/ suggested that even under axially-fixed and laterally-unconstraint conditions, high swelling pressures of 10 - 12 MPa were observed on the Callovo-Oxfordian argillite due to wetting with water vapour. These values are coincidental with the lithostatic stress (~ 11 MPa) at the sampling depth of 455 m. In the other tests on the Callovo-Oxfordian samples under uniaxial loads up to 18 MPa, significant axial swelling strains were also observed by wetting. These findings indicate that the interparticle water-films in the clay rock are capable to support the lithostatic stress.

The swelling behaviour of the Opalinus clay was also investigated in this project. An Opalinus sample BHE-D4/3 (D/L = 83/215 mm) from the HE-D test field was axially loaded to 1.0 MPa in a chamber. Under constant stress, the initially saturated sample with a water content of 7.1 % was dried and wetted by changing temperature and by circulating water vapour or dried air on its spherical surface over a long period of more than 1 year. Figure 3-29 shows schematically the assembly of the so called axial swelling / shrinking test. During the test, axial and radial strains were measured by a LVDT deformation transducer and a MTS circumferential extensometer mounted around the sample at the mid-height. In addition to that, the change in water content by wetting and drying was also recorded but on another small piece of 310 g, which was placed in the same chamber. This way made it possible to examine correlations between the applied relative humidity, the resulting changes in water content and deformation.

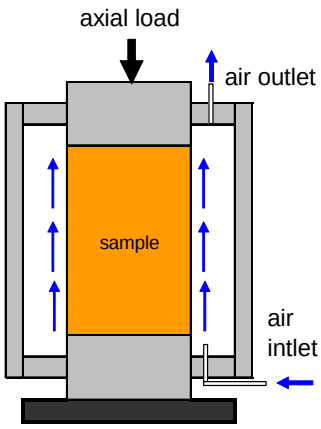

Figure 3-29 Schematic assembly of swelling / shrinking test

Figure 3-30 illustrates the applied axial stress, temperature, relative humidity, and the changes in water content as well as in axial / radial / volumetric strains. The test was performed in the following steps:

1. In the first phase, the sample was de-saturated by pumping dried air to the samples at elevated temperatures from 24 to 28 and 38 °C. Drying caused a strong reduction of the water content of the unstressed sample from 7.1 % to 1.5 %. Correspondingly, the stressed sample shrank in all directions by 0.46 % axial strain, 0.56 % radial strain and 1.6 % volumetric strain. In the unconstraint radial direction the shrinkage is slightly higher than that in axial direction stressed at 1 MPa. At 28 and 38 °C over other 100 days, changes of the strains are small and well correlated with the fluctuation of the water content. The large scatter of relative humidity between 18 % and 55 % in the early phase was produced by a refill of water into the circulating system weekly.

2. In the second phase, the sample was wetted by pumping water vapour to the samples at a reduced temperature of 23 °C, leading to an increase of the relative humidity from about 20 % to 75 % - 95 %. Correspondingly, the water content of the unstressed sample was increased to 5.0 % - 6.3 %. This re-hydration generated a significant expansion of the stressed sample in all directions, so that the pre-shrinkages were almost fully recovered. Over further 6 months, the relative humidity was progressively decreased to about 75 % and then two times readjusted to a high level of 95 %. In a good correlation with the humidity change, the water content fell and rose, resulting in shrinking and swelling of the stressed sample. At the end of the re-saturation phase, the total volumetric increment reached 2.4 %.

3. Drying the sample again by elevating the temperature to 58 °C and reducing the relative humidity to 3.0 % caused a strong reduction of the water content to 0.9 % and a large volumetric shrinkage of 1.8 % over other 2 months.

4. Finally, at 58 °C, the axial load was increased to 3.3 MPa. This loading produced an axial compression of $\varepsilon_1 \approx 0.4$ % and a radial extension of $\varepsilon_3 \approx 0.5$ %, resulting in a ratio of radial to axial strain of $\mu = \varepsilon_3 / \varepsilon_1 \approx 1.25$. This relatively large radial strain suggests that tensile fracturing occurred and developed until failure.

The swelling and shrinking deformations due to re-hydration / de-hydration suggest that the deformation of the highly-compacted clay rock is partly determined by the amount of water uptake and release. Because the water content change was measured on an

accompanying reference sample, a quantitative correlation between water content and swelling / shrinking strain could not be established here for the stressed sample. Additionally, the swelling and shrinking strains are also partly reversible.

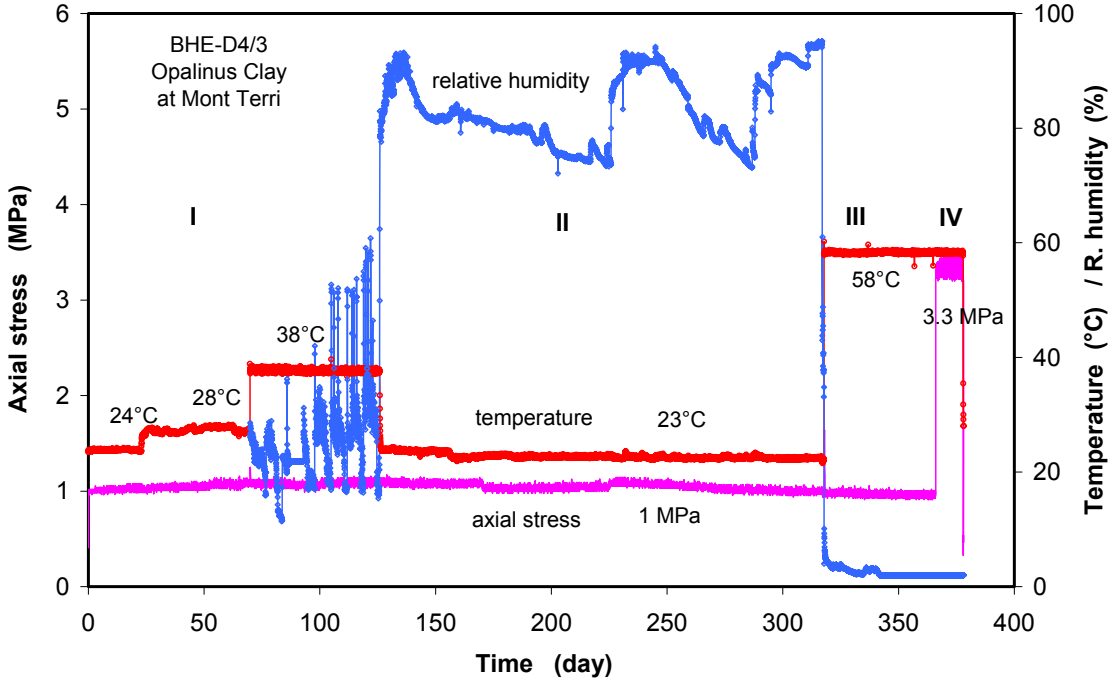

a. Applied conditions of stress, temperature and relative humidity

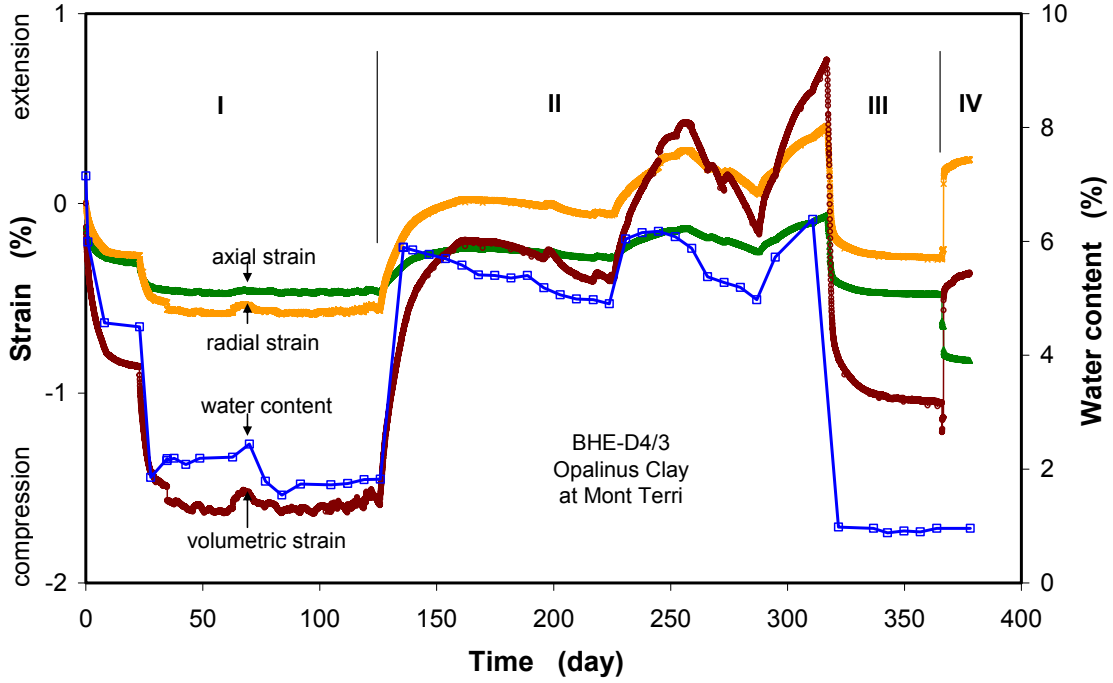

b. Responses of water content and axial / radial / volumetric strains

Figure 3-30 Swelling / shrinking behaviour of an axially-stressed Opalinus clay sample

3.4.6 Consolidation and Expansion

The consolidation behaviour of the Opalinus clay was investigated on cylindrical samples in a triaxial apparatus. Figure 3-31 shows schematically the assembly of the triaxial testing apparatus and the loading conditions. The sample is triaxially loaded by increasing the axial stress σ_1 and the radial stress $\sigma_2 = \sigma_3$, and it is subjected to water back-pressures at the bottom (inlet) p_{in} and the top (outlet) p_{out}. According to the stress concept of Horseman et al. /HOR 96/ for compacted clays, the pore-water pressure must be distinguished between the pressure of free pore-water (p_w) and the pressure prevailing in interparticle water-films (p_{fm}) which consists of the free pore-water pressure (p_w) and the disjoining pressure in water-films (Π_D).

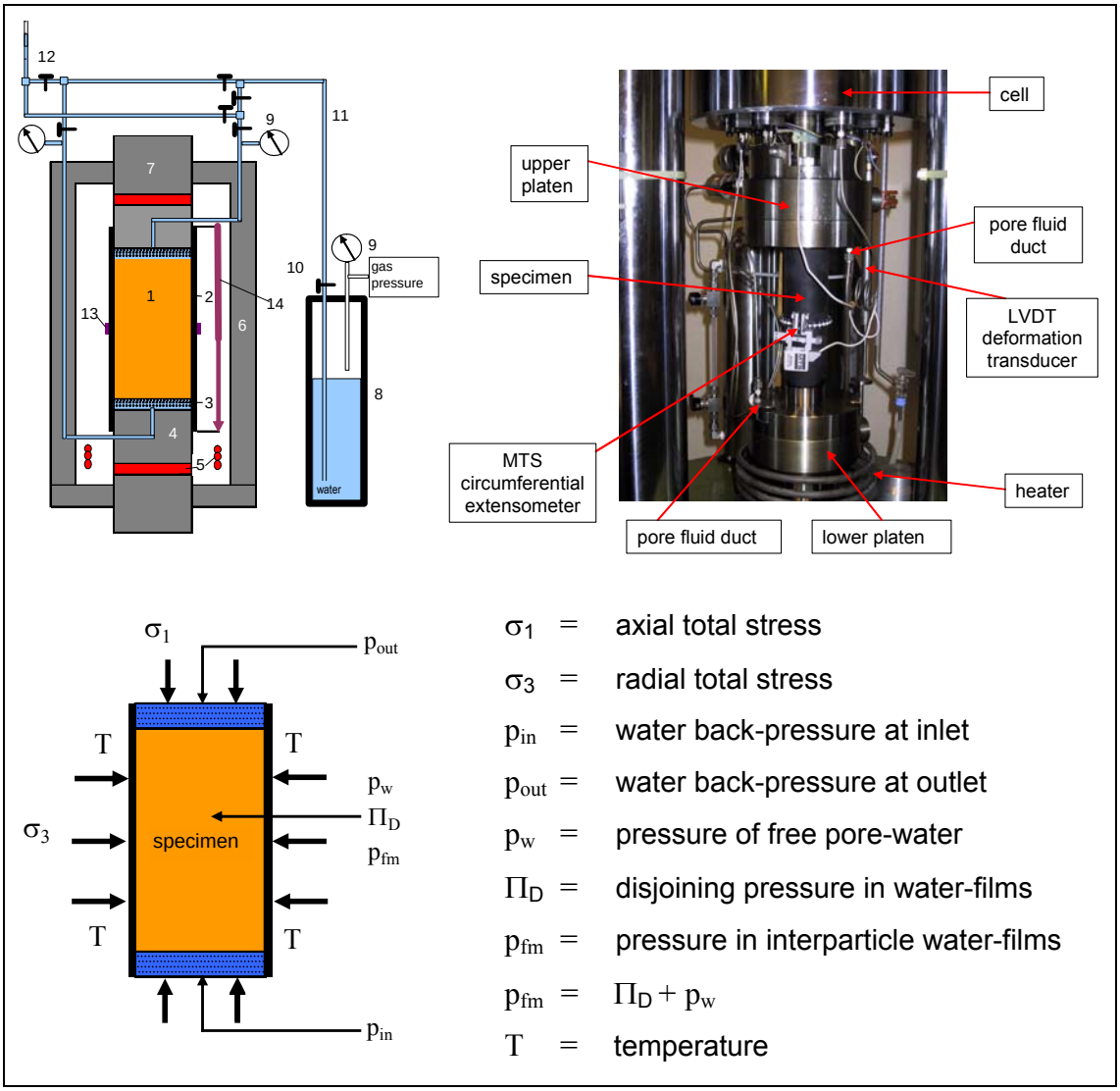

1: specimen 2: jacket 3: sintered porous disc 4: steel platen 5: heater 6: triaxial cell
7: load piston 8: fluid pressure vessel 9: pressure transducer 10: valve 11: pipe line
12: burette 13: MTS circumferential extensometer 14: LVDT deformation transducer

Figure 3-31 THM triaxial testing system and test conditions

Three Opalinus clay samples from the HE-D test field, BHE-D6/16 with water content of w = 6.3 %, BHE-D5/7 with w = 7.3 % and BHE-D3/18 with w = 6.0 % were compressed under similar conditions, i.e. temperature T = 28 °C, isotropic stress σ = 5 MPa and water back-pressures $p_{in} = p_{out}$ = 4 MPa. PEARSON water was used. The test results are illustrated in Figures 3-32 to 3-34.

In the test BHE-D6/16 (Figure 3-321), the sample was first loaded at a very low stress of 0.25 MPa and wetted with the water at the end faces at atmospheric pressure. Due to the wetting the sample expanded (curves downwards) in all directions to a volume increase of $\Delta\varepsilon_v$ = 0.18 % over 17 hours. The following loading to σ = 5 MPa led to a compaction of $\Delta\varepsilon_a$ = 0.22 %, $\Delta\varepsilon_r$ = 0.05 % and $\Delta\varepsilon_v$ = 0.32 %. Based on the data, a bulk modulus is determined by $K = \Delta\sigma / \Delta\varepsilon_v$ = 1500 MPa for the drained condition. The subsequent increase in the back-pressures to $p_{in} = p_{out}$ = 4 MPa resulted in an effective compressive stress $\sigma_{eff} = \sigma - p$ = 1 MPa. Even under the compression condition, the sample did not compact but it welled. The volumetric increment reached $\Delta\varepsilon_v$ = 0.4 % in 2 days.

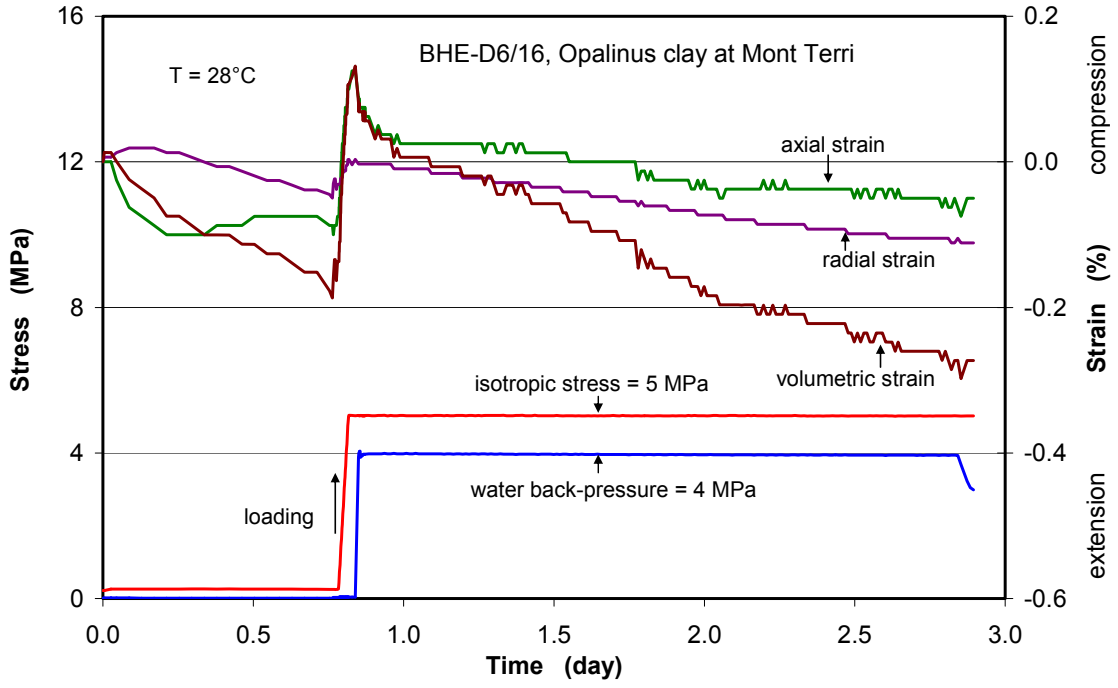

Figure 3-32 Consolidation and expansion of the Opalinus clay sample BHE-D6/16

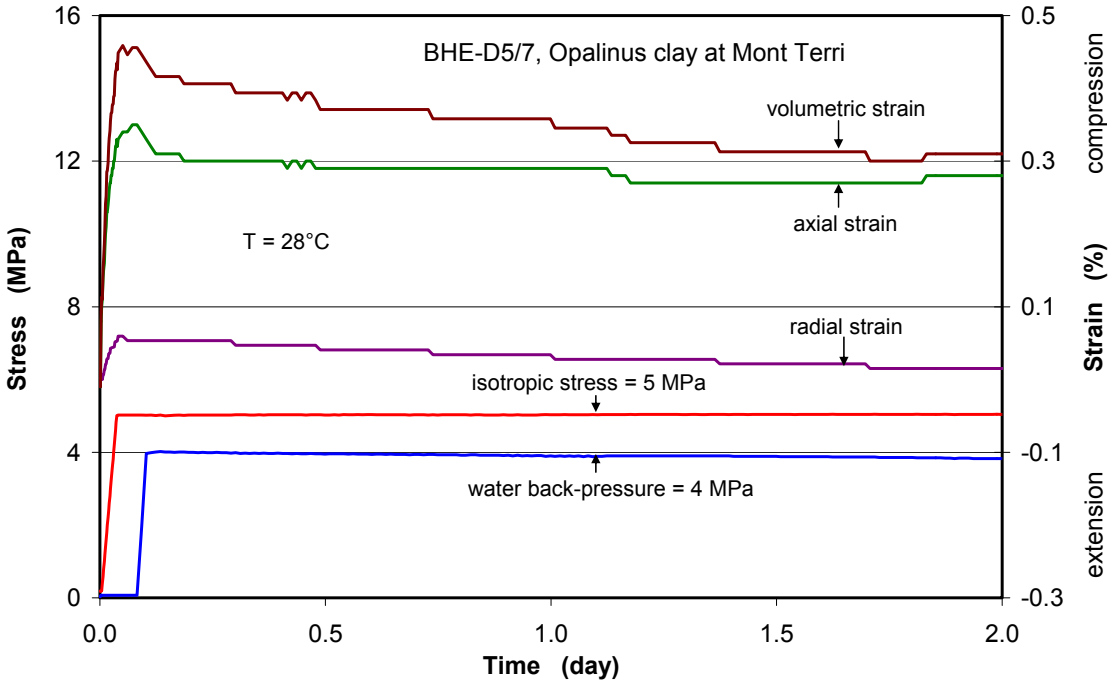

Figure 3-33 Consolidation and expansion of the Opalinus clay sample BHE-D5/7

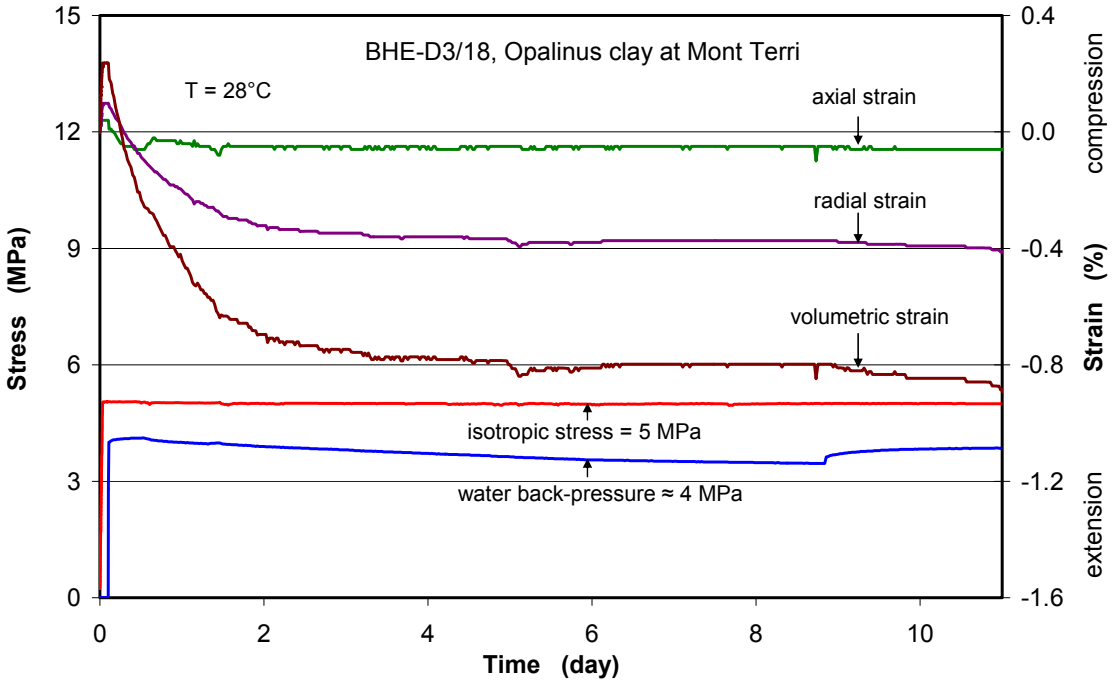

Figure 3-34 Consolidation and expansion of the Opalinus clay sample BHE-D3/18

The other two samples (Figures 3-33 and 3-34) exhibited a very similar behaviour. The drained loading to σ = 5 MPa at $p_{in} = p_{out} = 0$ led to compaction of $\Delta\varepsilon_a$ = 0.33%, $\Delta\varepsilon_r$ = 0.06 % and $\Delta\varepsilon_v$ = 0.45 % for sample BHE-D5/7, and $\Delta\varepsilon_a$ = 0.05 %, $\Delta\varepsilon_r$ = 0.10 % and

$\Delta\varepsilon_v$ = 0.25 % for sample BHE-D3/18. A bulk modulus of K = 1100 MPa for sample BHE-D5/7 and K = 2000 MPa for sample BHE-D3/18 is obtained. Under the impact of a following water injection at $p_{in} = p_{out}$ = 4 MPa and σ = 5 MPa, the samples expanded to $\Delta\varepsilon_v$ = 0.15 % (BHE-D5/7) in 2 days and $\Delta\varepsilon_v$ = 1.1 % (BHE-D3/18) in 11 days, respectively.

The experimental observations suggest that the Opalinus clay has a high swelling capacity when contacting water.

3.4.7 Responses to Thermal Loading

Two heating tests were carried out on an Opalinus clay sample (OPA) and a Callovo-Oxfordian argillite sample (CO) in a triaxial apparatus (shown in Figure 3-31) to examine thermal effects. The Opalinus sample BHE-D6/14 from the HE-D test field had a water content of w = 7.6 % and a porosity of ϕ = 16.8 %, whereas the Callovo-Oxfordian sample EST17317 data were w = 8.4 % and ϕ = 16.1 %. Both samples were nearly saturated before testing. The following general testing procedure was applied in both tests:

1. *Saturation* by injecting PEARSON water to the sample top and bottom at a pressure of $p_{in} = p_{out}$ = 2.5 MPa under constant confining stress of σ = 5 MPa to ensure full saturation;

2. *Undrained consolidation* by raising the stress to 15 MPa for the determination of the change in pore-water pressure under undrained conditions;

3. *Heating* the sample step by step from 30 to 60, 80, 100, and 120 °C, and then *cooling* it down to 80 and 30 °C for examination of the thermal effects on pore-water pressure and deformation;

4. *Drained consolidation* at 15 MPa confining stress and null water back-pressure after the heating / cooling cycles;

5. Following the above common test steps, some other aspects were investigated under different conditions.

The test results are illustrated in Figure 3-35 for the OPA sample and in Figure 3-36 for the CO sample, respectively.

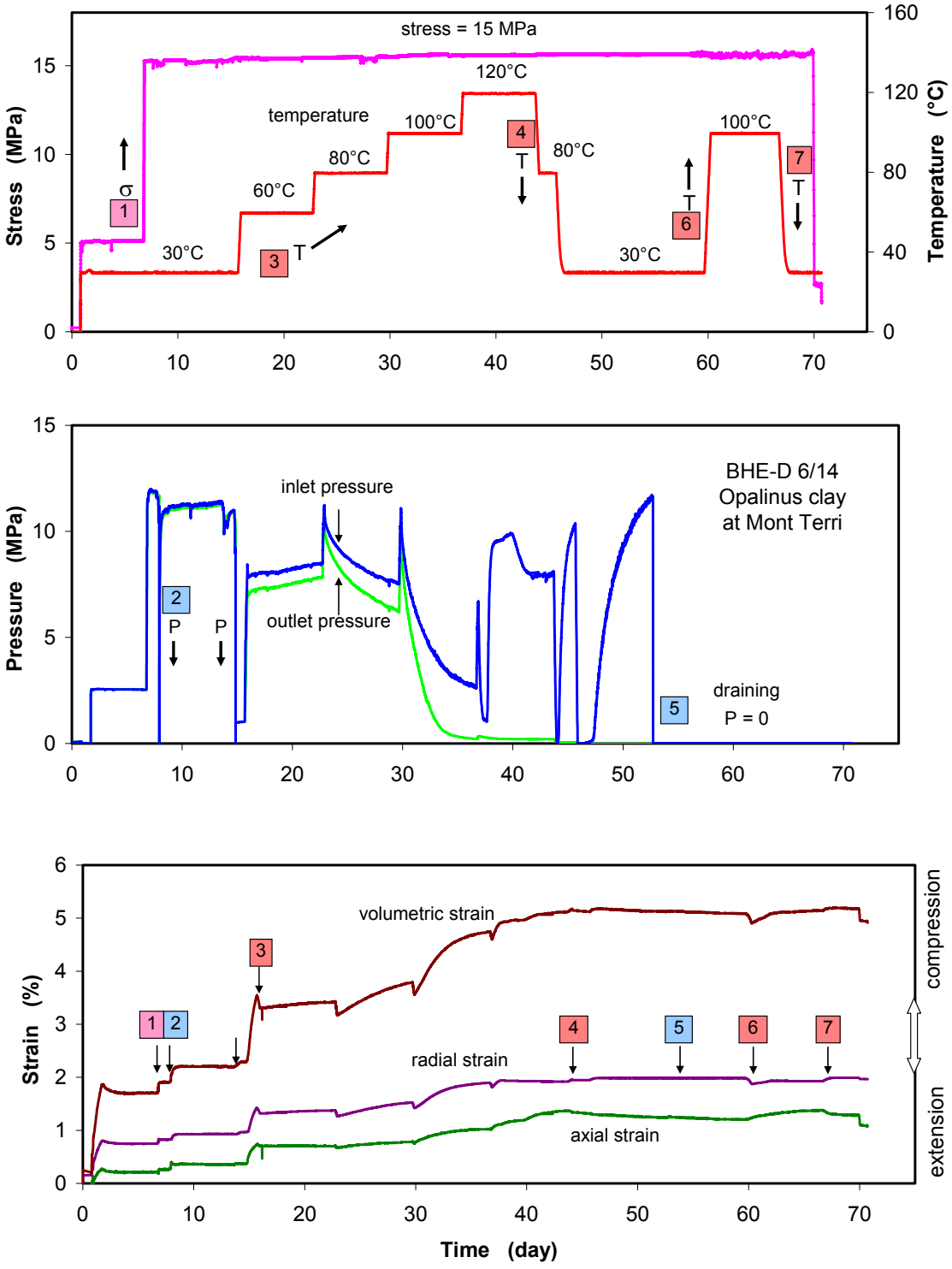

Figure 3-35 Results of a THM coupling test on an Opalinus clay sample

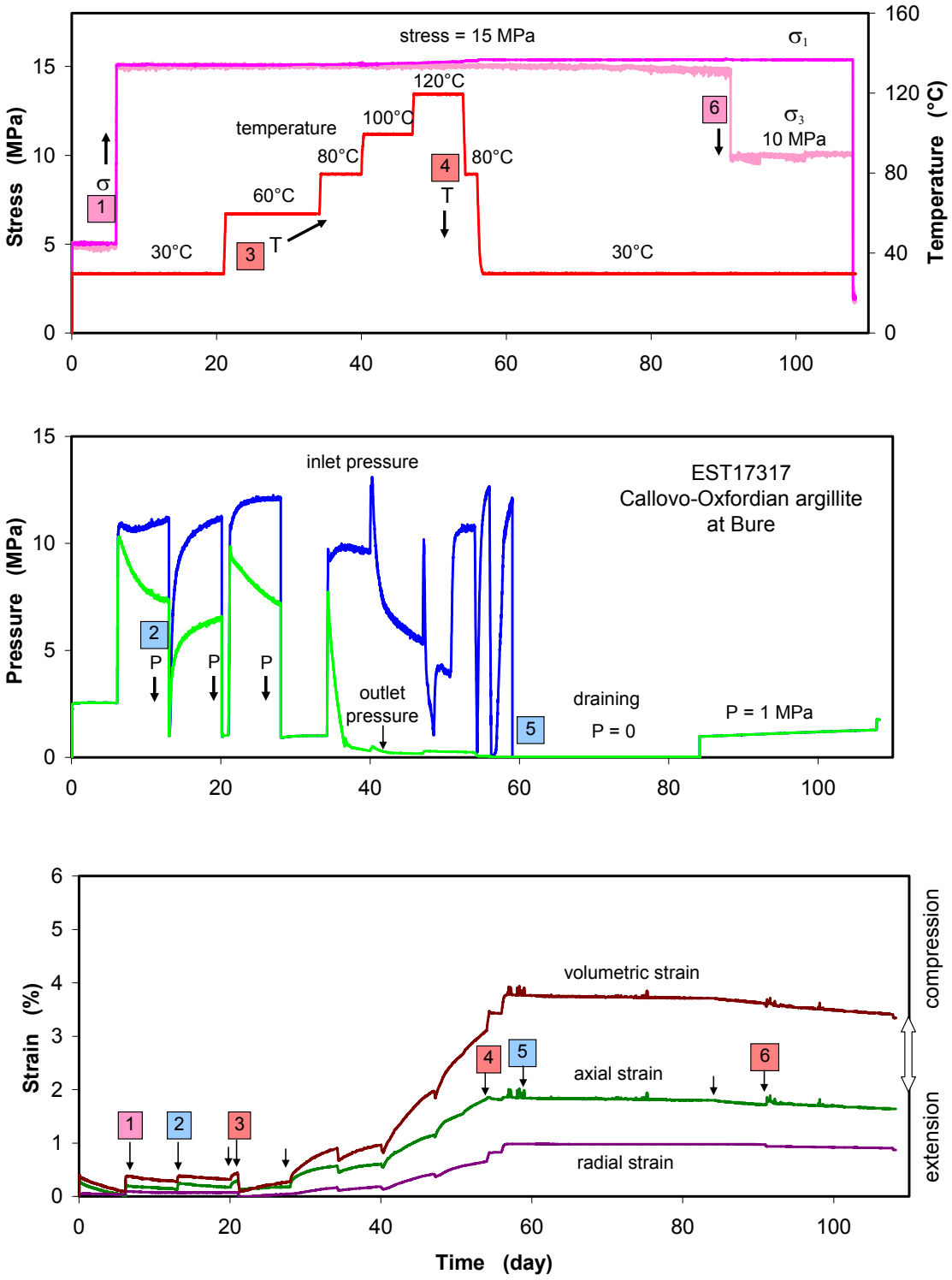

Figure 3-36 Results of a THM coupling test on a Callovo-Oxfordian argillite sample

Saturation

At T = 30 °C and $p_{in} = p_{out} = 0$, the first loading to 5 MPa led to a volumetric compaction of $\varepsilon_v \approx 1.8$ % for the OPA sample and of $\varepsilon_v \approx 0.4$ % for the CO sample, respectively. The relatively large compaction of the OPA sample was mainly caused due to the strong radial compression of $\varepsilon_r \approx 0.7$ % and the axial one of $\varepsilon_a \approx 0.2$ %. The large radial strain indicated pre-existence of fissures existing more along the bedding planes inclined to the sample axis at an angle of 20°. During the following water injection at top and bottom at a pressure of $p_{in} = p_{out} = 2.5$ MPa, a gradual expansion occurred in both samples.

Undrained consolidation

The subsequent consolidation phase was carried out by increasing the stress to 15 MPa after closing the inlet and outlet valves. Correspondingly, the inlet and outlet pressures rose simultaneously to the same value of $p_{in} = p_{out} = 11.9$ MPa for the OPA sample, but different values of $p_{in} = 10.8$ MPa and $p_{out} = 10.1$ MPa for the CO sample. The same behaviour of the back-pressures indicates that there existed hydraulic pathways through the OPA sample. So the free pore-water pressure is equal to the back-pressure $p_w = p_{in} = p_{out} = 11.9$ MPa. From the undrained consolidation data, Skempton's pore pressure coefficient can be determined by $B = \Delta p_w/\Delta\sigma = 9.4 / 10 = 94$ %. The different responses of the back-pressures at the CO sample imply no hydraulic interconnection through it. This finding may indicate that the adsorbed pore-water in the sample was highly pressured by the external confining stress, i.e. the local pressure in the water-films (Π_D) may be equal or close to the external stress of 15 MPa. So the adsorbed pore-water films act practically as barriers against advective flow of free water. On the other hand, the samples were also slightly compacted under the undrained conditions.

The following reduction of the back-pressures to zero for the OPA sample and to 1 MPa for the CO sample caused a sudden compaction of $\Delta\varepsilon_v \approx 0.3$ % and $\Delta\varepsilon_v \approx 0.02$ %, respectively. Closing the inlet and outlet valves, the water back-pressures on the OPA sample increased rapidly to the previous high level and kept constant, but on the CO sample the back-pressures rose steadily to different values of $p_{in} = 11.2$ MPa and $p_{out} = 6.5$ MPa over a week. Under the undrained conditions, the samples were slightly consolidated. After reaching a relative stable state in each sample, the back-

pressures on both samples were reduced again to 1 MPa for one day and then the inlet and outlet valves were closed.

Heating

Under the undrained conditions, both samples were heated by elevating temperature from 30 to 60, 80, 100 and 120 °C. Each heating phase lasted for one week.

T = 30 → 60 °C: The temperature increment from 30 to 60 °C generated a rapid increase of the back-pressures from 1 MPa to different values of p_{in} = 8.2 / p_{out} = 7.2 MPa at the OPA sample and p_{in} = 12.0 MPa / p_{out} = 9.6 MPa at the CO sample, respectively. The inlet and outlet pressures at the OPA sample rose slowly in parallel, while the pressures on the CO sample behaved differently, i.e. the inlet pressure increased but the outlet one decreased with time. On the other hand, the heating produced a short-term expansion in both samples and after that a slight consolidation occurred over the heating phase. In order to examine consolidation under drained conditions at a high temperature of 60 °C, the back-pressures at the CO sample were reduced to 1 MPa for one week, resulting in a significant compaction of $\Delta\varepsilon_v \approx 0.4$ %.

T = 60 → 80 °C: The second heating phase from 60 to 80 °C caused another sudden increase of the pressures to p_{in} = 11.0 MPa / p_{out} = 10.0 MPa at the OPA sample and then they dropped slowly down to p_{in} = 8.0 MPa / p_{out} = 6.5 MPa over one week. At the CO sample the heating induced a sudden increase of the back-pressures to p_{in} = 9.5 MPa / p_{out} = 7.5 MPa. These values are obviously lower than those observed before at heating from 20 to 60 °C. After that, the inlet pressure maintained constant, while the outlet pressure fell dramatically down to zero. This reduction indicates that there existed a leakage in the outlet reservoir. So the CO sample was subjected to a partly-drained condition, under which a relatively large consolidation at $\Delta\varepsilon_v$ = 0.15 % was observed over one week.

T = 80 → 100 °C: The third heating phase from 80 to 100 °C produced a maximum back-pressure of 11 MPa at the OPA sample and of 13 MPa at the CO sample, respectively. However, the peak pressures dissipated quickly down to 3 MPa and 5 MPa over one week. It is to be noted that this heating probably caused leakage in the outlet system in the OPA test, indicated by the rapid drop of the outlet pressure. The partly-drained conditions on both samples led to relatively large volumetric reduction of $\Delta\varepsilon_v$ = 0.5 % for the OPA sample and of $\Delta\varepsilon_v$ = 0.9 % for the CO sample over one week.

T = 100 → 120 °C: In the last heating phase, the temperature was increased to 120 °C. Even at this high temperature, no higher pressure above the previously arrived values was observed on both samples. The pressures were unstable at 120 °C. They fell quickly down and rose again to 9.5 MPa and 10.5 MPa, respectively. In the last days, the pressures tended to be constant. Under the high temperature and the partly-drained conditions, the samples were largely consolidated to $\Delta\varepsilon_v$ = 0.4 % for the OPA sample and $\Delta\varepsilon_v$ = 1.2 % for the CO sample over one week.

Cooling

A cooling phase followed by decreasing the temperature from 120 to 80 and 30°C. In response to cooling from 120 to 80 °C, the back-pressures at both samples dropped quickly down to zero for a short time and then rose rapidly again to high levels of 10 MPa at the OPA sample and 12.5 MPa at the CO sample, respectively. The subsequent cooling to 30 °C produced a similar process. The increase in the water back-pressure during the cooling phase might be caused by contraction of the pore-water and thus compaction of the samples.

Drained consolidation

After cooling the samples down to 30 °C, the inlet and outlet valves were opened. Unexpectedly, at the high confining stress of 15 MPa and null water back-pressure, no consolidation took place, but expansion appeared up to $\Delta\varepsilon_v \approx$ 0.1 % at the OPA sample and $\Delta\varepsilon_v \approx$ 0.07 % at the CO sample. This indicates the high swelling capacity of both clay rocks even after the heating/cooling cycles in the range from 30 to 120°C.

Following the drained consolidation phase, the OPA sample was heated to 100 °C and then cooled down again to 30°C. Figure 3-35 illustrates that under the drained conditions, the heating / cooling cycle led to a slight compaction. The heating-induced consolidation might be contributed mainly by a release of thermally-mobilised pore-water, while the consolidation during the cooling phase resulted from the contraction of the pore-water.

On the CO sample the water back-pressure was adjusted to 1 MPa and the radial stress was reduced to 10 MPa (Figure 3-36). The stress reduction resulted in only a negligible radial extension and a small axial compression. After that, however, the sample expanded in axial direction while the radial strain remained constant over two

weeks. The expansion observation under the deviatoric stress state of σ_1 = 15 MPa and σ_2 = σ_3 = 10 MPa provides further evidence for the high swelling capacity of the clay rock even after heating to 120 °C.

3.5 Large-Scale THM Experiments

As the second part of the laboratory programme, mock-up heating experiments were carried out in GRS's big triaxial MTS apparatus, in which the in-situ heating experiment and its conditions were simulated. Two big samples (D/L = 260 mm/700 mm) drilled from the HE-D heater borehole (Figure 3-6) were used. One sample was tested at ambient temperature for the examination of hydro-mechanical coupling effects, while another one was heated for the investigation of thermal effects on the hydro-mechanical behaviour of the Opalinus clay rock.

3.5.1 Large Triaxial Apparatus

Figure 3-37 shows a photo and a schematic of GRS's big triaxial apparatus for THM coupling tests on geo-materials. The apparatus was manufactured by MTS Systems Corporation in 1992 and extended two times by the company FREUNDL with a hydraulic system in 1996 and with a heating system in 2004. The heating system was added in the frame of the HE-D project.

The triaxial apparatus consists of a stiff load frame and a triaxial cell, which allows testing a big cylindrical sample of 280 mm diameter and 700 mm length. The loading system has a maximum capacity of 50 MPa radial stress and 75 MPa axial stress (maximum axial force = 4600 kN). The axial and radial loads are controlled individually by servo-regulation of the oil pressures in the axial load cylinder and in the triaxial cell with accuracy better than 0.1 %. The axial load can be applied with a constant force rate or displacement rate. The axial displacement is measured by a LVDT deformation transducer mounted in the lower piston outside the cell with accuracy better than 0.1 %. The measurement of the radial strain is performed by using a MTS circumferential extensometer installed outside the jacket around the sample with accuracy better than 0.2 %.

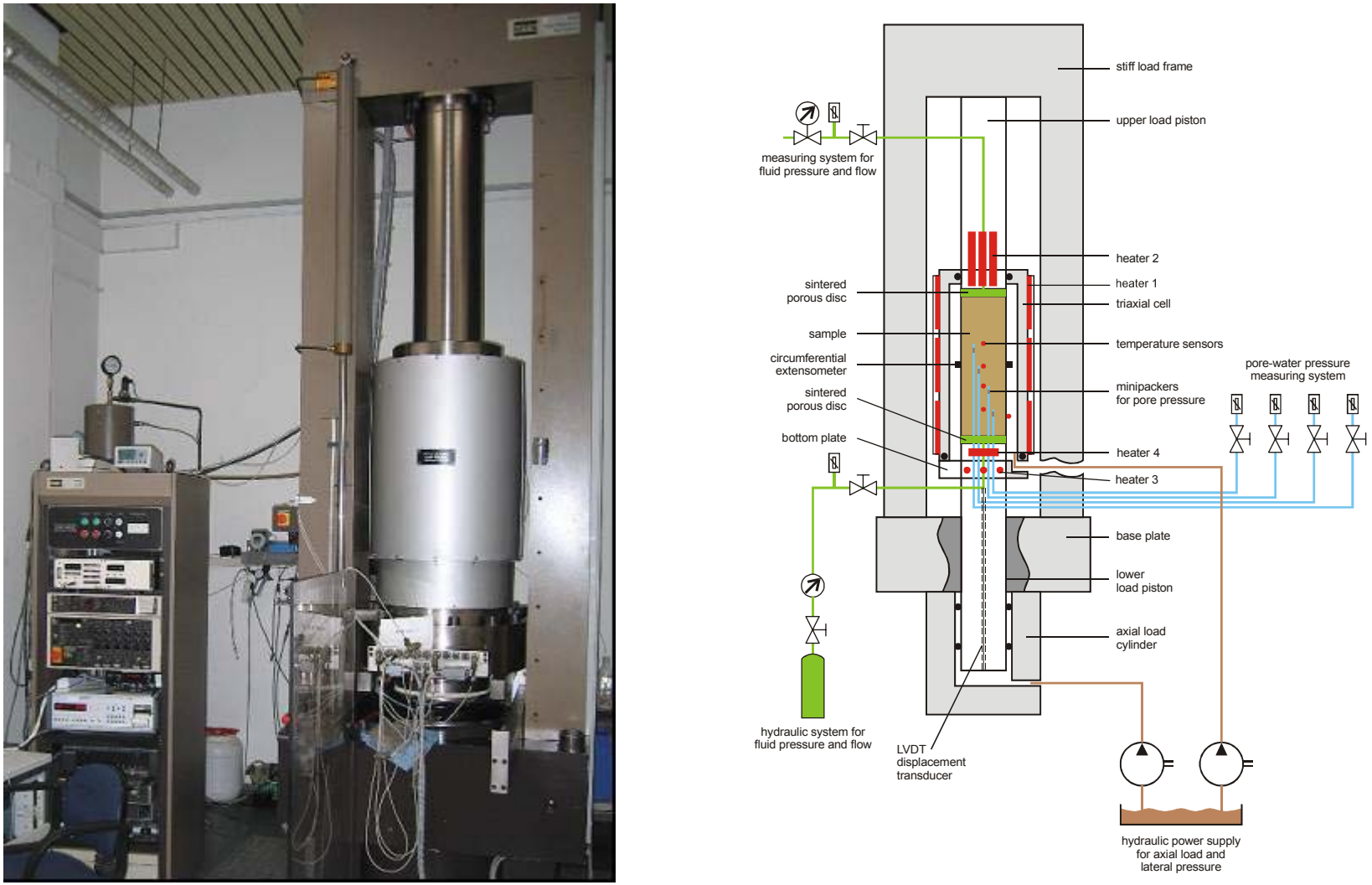

Figure 3-37 Large triaxial apparatus for THM experiments on big samples of 280 mm diameter and 700 mm length

Fluid is allowed to be injected into the stressed sample through both the upper and the lower sintered porous discs. The fluid pressure is usually generated by pressuring the fluid in a pressure vessel with gas. The pressure in this system can be regulated in a range between 0.04 and 0.8 MPa. Instead of this, a syringe pump MOD-260D can also be used for generating a high pressure of up to 50 MPa with accuracy of ± 0.5 %. The fluid pressures at the lower and upper end faces of the sample are recorded by means of two piezo-resistive transducers with a measuring range of up to 16 MPa and an error of less than 0.5 %. The flow rate through the sample is measured with an adequate flow meter or a precise burette with accuracy better than ± 0.05 cm^3. In addition to these hydraulic measurements, a new hydraulic system was developed by GRS for measuring the pore pressure inside the sample. Four individual GRS mini-packers with 10 mm diameter and 30 mm length can be installed inside a sample to seal off mini-intervals.

As mentioned above, the heating system was installed in the big apparatus by the company FREUNDL. The system consists of four independent electrical heaters, a central control unit, a circulation pump, a number of measuring sensors and a data acquisition system. Figure 3-38 shows photos of the heater's control unit and the circulation pump. Heater 1 is mounted outside the triaxial cell with three heating mats, each of which having a maximum power of 1300 Watts. Heater 2 consists of three heating rods vertically installed in the lower part of the upper piston, whereas the three heating rods of heater 3 are horizontally inserted in the upper part of the lower piston. Each of the heating rods has a maximum power of 800 Watts. In order to heat the sample directly on the end face, heater 4 with a maximum power of 1500 Watts is embedded in the bottom plate. The heating system can provide a total power of 10.2 kW. The sample can be heated in different ways: at the circumferential surface, at the lower or at the upper end face, or simultaneously at all the boundaries. Each heater can generate a maximum temperature of 150°C at the heater / sample interface. Additionally, the temperature in the cell can be controlled by exchanging the heated oil in the cell and cooled oil outside by means of the circulation pump, which was designed for a range between 30 and 50°C with accuracy of ± 1 %. In addition to this heating system, GRS developed a measuring system for monitoring the temperature inside the sample. Four temperature sensors PT100 can be inserted in the sample. The electric cables and hydraulic lines are led through the bottom plate to the data acquisition system.

Heater control unit

Circulation pump

Figure 3-38 Heater control unit and circulation pump for controlling temperature in the big triaxial cell

3.5.2 Consolidation Tests

The consolidation tests were carried out on sample BHE-D9 at room temperature. As shown in Figure 3-39, there were two visible fissures at the bottom end face, which probably penetrated more deeply into the sample. The sample was sealed with double jackets to fit the required diameter of 280 mm.

3.5.2.1 First Test

Figure 3-40a illustrates the applied test conditions of temperature, axial and radial stresses, inlet and outlet water back-pressures versus time, while the responses of axial, radial and volumetric strains are presented in Figure 3-40b. First, a re-saturation phase was carried out for 4 days by wetting the end faces of the sample with PEARSON water at atmospheric pressure (p_t = p_b = 0) under low confining stress of σ_1 = 1.5 MPa / σ_3 = 1 MPa. After that, the stresses were increased to σ_1 = 5.5 MPa and

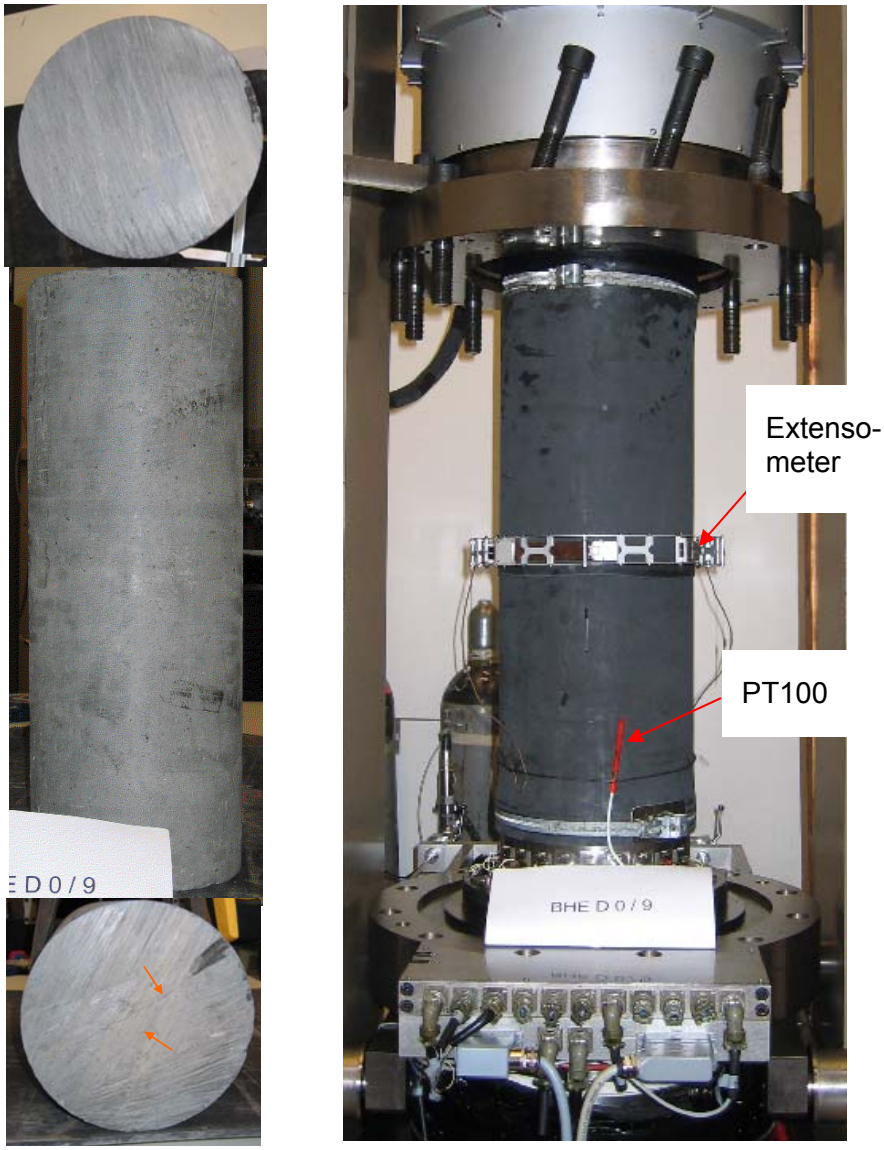

Figure 3-39 Triaxial compression test on a large Opalinus clay sample

σ_3 = 5 MPa. This drained loading led to a compression of $\Delta\varepsilon_1$ = 0.11 %, $\Delta\varepsilon_3$ = 0.05 % and $\Delta\varepsilon_v$ = 0.12 %. According to these data, a bulk modulus is determined to K = $\Delta\sigma$ / $\Delta\varepsilon_v$ = 3330 MPa. A short time after loading, the inlet and outlet water pressures were increased to 4 MPa, resulting in a small axial extension. Slight change in temperature from 23 to 25 °C caused a small radial expansion. At an effective compressive stress of σ - p = 1.2 MPa expansion took place and reached values of $\Delta\varepsilon_3$ = - 0.23 %, $\Delta\varepsilon_1$ = - 0.10 % and $\Delta\varepsilon_v$ = - 0.43 % over 10 days.

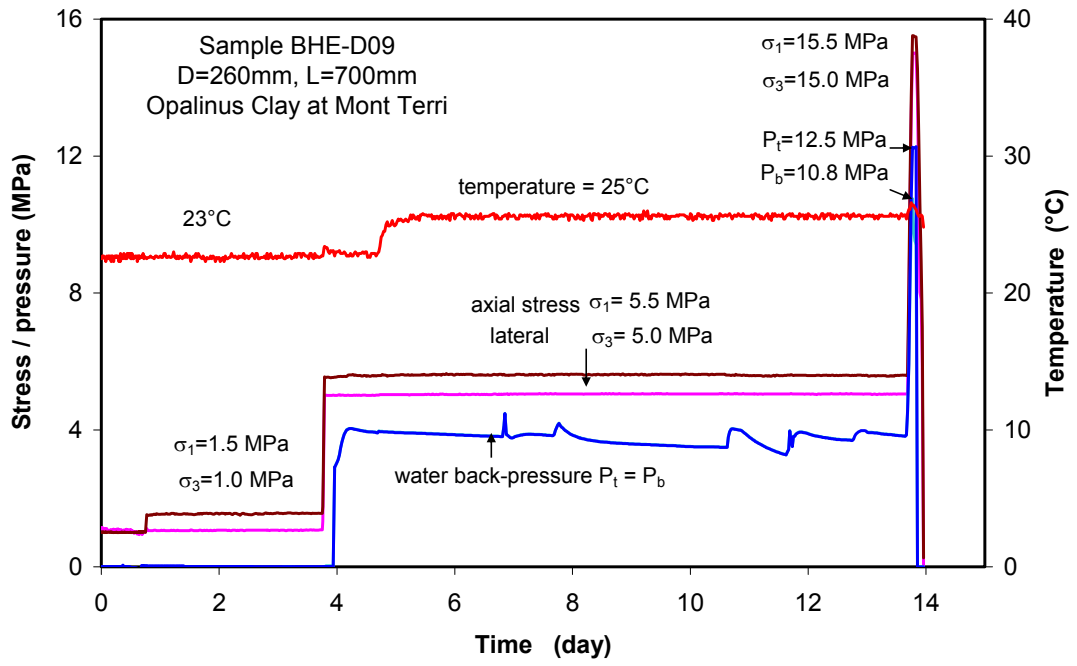

a. applied temperature, stress and water back-pressures

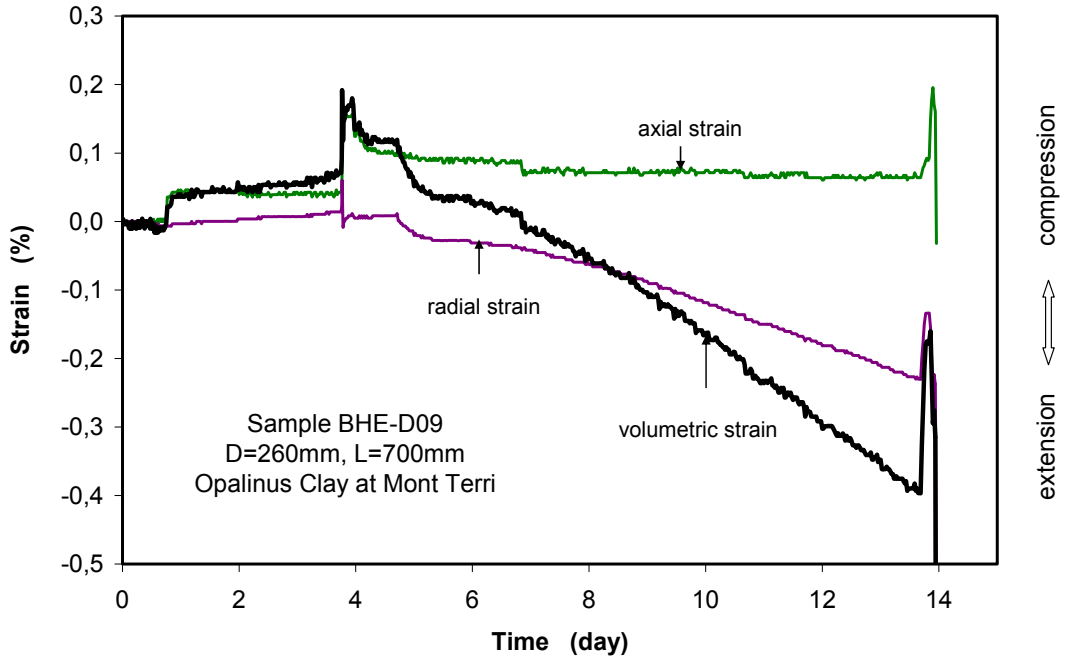

b. deformation responses

Figure 3-40 Measurements of the first HM coupling test on a large Opalinus clay sample

In order to examine the pore pressure response to the mechanical loading, both water reservoirs were closed and the confining stresses were increased to σ_1 = 15.5 MPa

and σ_3 = 15 MPa. This undrained compression resulted in an increase of the back-pressures to different values of p_t = 12.5 MPa at the top and p_b = 10.8 MPa at the bottom, respectively. This means that no pathways existed in the sample. Based on the data, two different Skempton's coefficients are established to B = Δp / $\Delta\sigma$ = 70 % and 87 % respectively. Additionally, the loading also caused compression to $\Delta\varepsilon_1$ = 0.12 %, $\Delta\varepsilon_3$ = 0.10 %, and $\Delta\varepsilon_v$ = 0.22 %. From these data the bulk modulus is determined to K = $\Delta\sigma$ / $\Delta\varepsilon_v$ = 4550 MPa.

3.5.2.2 Second Test

On the same sample a second test followed. The test results are shown in Figure 3-41. During the first day, the sample was loaded to an isotropic stress of 1 MPa, wetted with PEARSON water at both end faces, and slightly heated from 23 to 31 °C. In response to the temperature rise, the sample expanded by 0.14 %. The subsequent increase of stress to σ_1 = 5.3 MPa and σ_3 = 5.0 MPa caused compression of $\Delta\varepsilon_1$ = 0.10 %, $\Delta\varepsilon_3$ = 0.05 % and $\Delta\varepsilon_v$ = 0.20 %, leading to a bulk modulus of K = 2000 MPa. Subsequently, increasing the back-pressure to p_t = p_b = 4 MPa resulted in a volumetric increment of 0.23 % over 4 days.

After closing the inlet and outlet valves, the confining stresses were increased to σ_1 = 15.3 MPa and σ_3 = 15 MPa. This undrained loading produced an increase of the back-pressures from 4 MPa to 13 MPa. Skempton's coefficient is determined to 90 %. Additionally, even under undrained conditions this loading caused also a compaction of $\Delta\varepsilon_1$ = 0.01 %, $\Delta\varepsilon_3$ = 0.05 % and $\Delta\varepsilon_v$ = 0.11 %. The corresponding bulk modulus is estimated to K = 9100 MPa. After the compaction, the high pressure p_t at the top maintained, while the pressure p_b at the bottom dropped down in an instable way. This might be caused by a possible leakage in the bottom reservoir. Even under the reduction of the back-pressure and hence the increase in effective stress, a steady axial expansion of $\Delta\varepsilon_1$ = 0.16 % was observed over 3 days, but no radial strain change.

Finally, the back-pressures were reduced to 1 MPa. As a result of this a sudden axial compression occurred while the radial strain did not change. By closing the inlet and outlet valves again, the sample was compressed significantly under the high confining stress of 15 MPa, accompanied by a slight increase of the back-pressure from 1 to 1.6 MPa over 4 days.

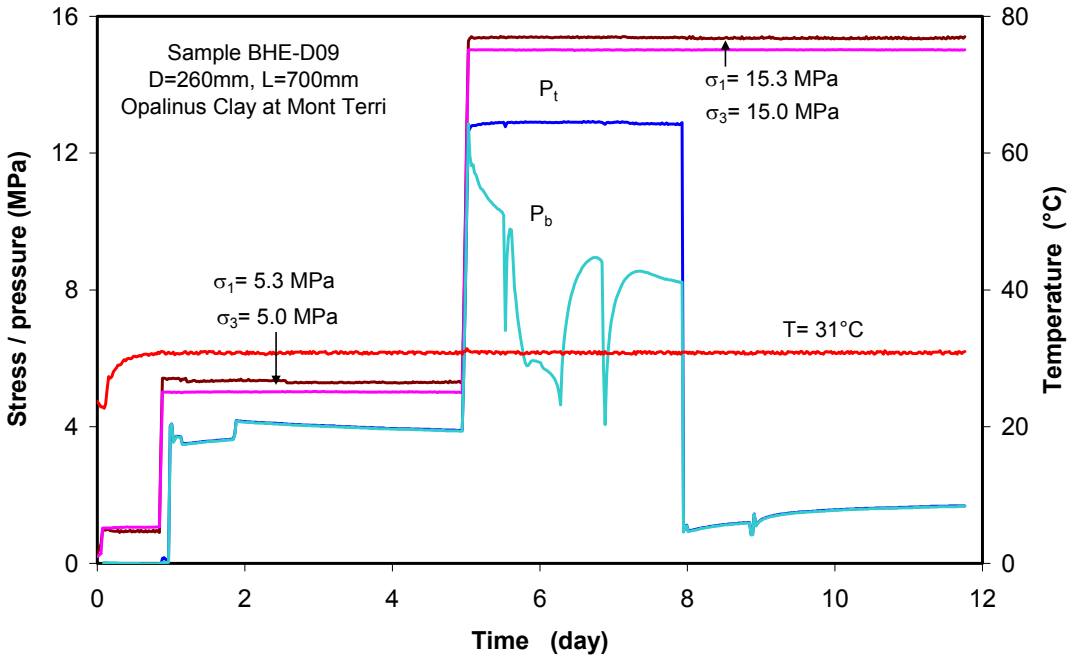

a. applied temperature, stresses and water back-pressures

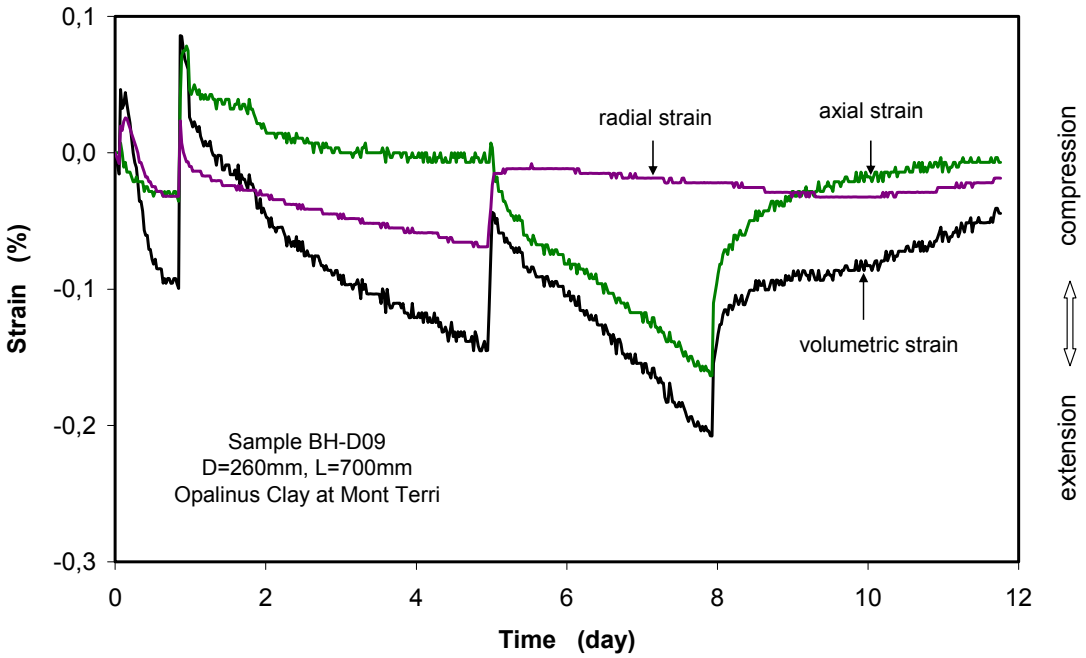

b. deformation responses

Figure 3-41 Measurements of the second HM coupling test on a large Opalinus clay sample

The following conclusions are drawn by comparing the experimental results obtained on the large sample (Figures 3-40 to 3-41) and the normal samples (Figures 3-32 to 3-34) under very similar test conditions:

- The bulk modulus determined on the normal samples at drained compaction varies between 1100 and 2000 MPa, which is a relatively lower value than that of 2000 to 3330 MPa estimated at the large sample. The undrained bulk modulus of 7300 MPa determined on the normal samples, however, lies between the values of 4550 and 9100 MPa determined on the large sample.
- The undrained compression leads to an increase in the pore pressure. Skempton's pore pressure coefficient measured on the large sample varies in a range from 87 % to 90 %, which is comparable with that of 94 % observed on the normal samples.
- Significant swelling deformation was observed on all the samples when contacting them with water at effective compressive stresses over 1 MPa.
- At a confining stress of about 15 MPa, a reduction of the back-pressures from 10 - 13 MPa to 0 - 1 MPa resulted in a volume reduction between 0.1 % and 0.3 %, independent of the sample sizes.

The comparison of the results indicates an insignificant scale-effect for the investigated clay rock. Anyway, one has to take into account the experimental results of clay rocks is very dependent on the quality of testing samples, which are often disturbed by the coring process as well as by the storage and preparation conditions.

3.5.3 Mock-up Heating Tests

The in-situ experiment enables direct observations of complex THM processes occurring in the investigated clay rock. However, because the boundary conditions are usually not well known, the interpretation of the results and the validation of numerical models may be difficult. Therefore, mock-up heating tests were carried out on a large Opalinus clay sample by simulating the in-situ heating experiment mentioned in Chapter 2 in order to calibrate model parameters by back-calculations of the tests.

3.5.3.1 Instrumentation

The mock-up heating tests were designed under consideration of the in-situ prevailing conditions and the technical possibilities in the laboratory. Figure 3-42 shows schematically the test assembly in GRS's big triaxial cell and the layout of the instrumentation inside and outside a large sample. In the first test, sample BHE-D8 of D/L = 260mm/700mm from the HE-D heater borehole was used. The test was designed to be carried out in four stages: 1) re-saturation by injecting PEARSON water to the sample's top and bottom; 2) re-consolidation under the in-situ representative overburden stress of about 8 MPa and the pore-water pressure measured in the HE-D test field; 3) heating the sample at the top to 80 °C by keeping a constant temperature of 30 °C at the bottom and the circumferential surface to create a temperature gradient in the sample; and 4) cooling the sample down to 30 °C.

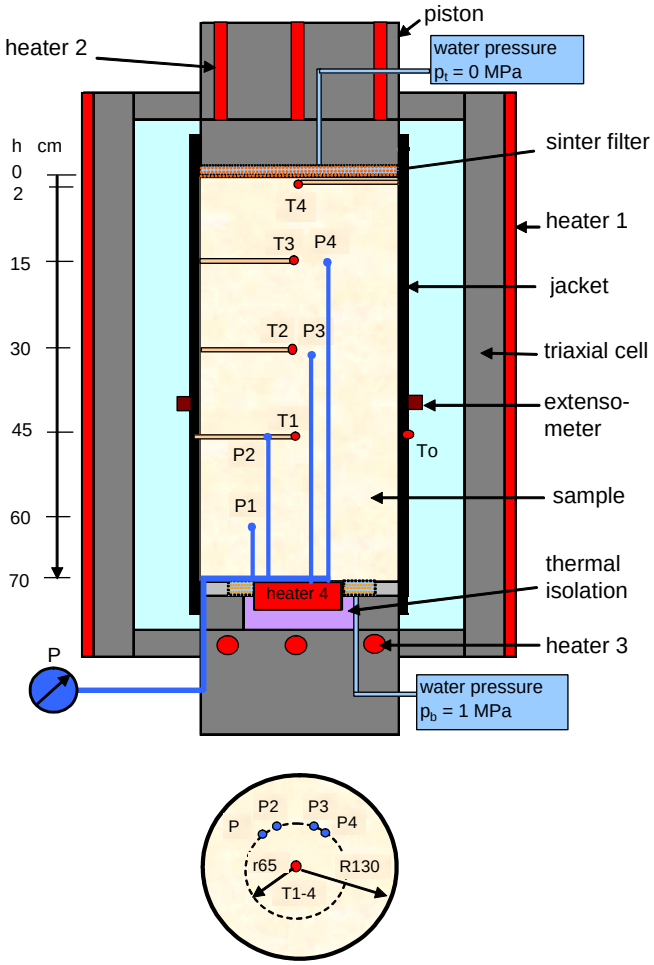

Figure 3-42 Principle design and instrumentation of the mock-up heating test on a large Opalinus clay sample in GRS's big triaxial apparatus

Responses of the sample to THM loadings were recorded by monitoring temperature, pore-water pressure, and axial / radial deformation with various instruments installed outside and inside the sample, as shown in Figure 3-42. The axial / radial stresses, the axial / radial strains, the water back-pressures at both end faces, and the boundary temperatures were controlled by instruments mounted outside the sample. The pore-water pressure and the temperature in the sample were monitored by means of four GRS mini-packer-systems and four sensors PT100 installed inside the sample.

Four mini-packers of 10 mm diameter and 30 mm length (Figure 3-43) were installed individually in four slim boreholes drilled from the sample bottom at a radius of 65 mm to different depths (Figure 3-42, h = distance to the top): P_1 at h = 60 cm, P_2 at h = 45 cm, P_3 at h = 30 cm and P_4 at h = 15 cm. The mini-packers were fixed at the borehole ends by squeezing rubber-rings of 15 mm length. The volumes of the test intervals were less than 0.1 cm^3 and filled with PEARSON water through 1/8”-wide inflow lines, which were led for the pressure measurement through the bottom plate to piezo-resistive transducers outside the cell. The air in the intervals was displaced through the short outflow lines. The boreholes were finally sealed with resin. The system allows a maximum pressure of 16 MPa. Figure 3-43 shows some pictures of the installation of the mini-packers. Two small cavities were excavated at the bottom for the connection of the hydraulic lines to the pressure transducers and finally filled with concrete. From the photos one can recognise some fissures at the sample surfaces.

For installation of PT100 temperature sensors, four boreholes of 10 mm diameter were drilled from the circumferential surface at different levels to the central axis (Fig. 3-42): T_1 at h = 45 cm, T_2 at h = 30 cm, T_3 at h = 15 cm, and T_4 at h = 2 cm. The electric wires were embedded in narrow channels on the sample surface, which were finally sealed with silicon. Figure 3-44 presents some photos made during the installation.

Obviously, the instrumentation caused additional disturbances of the sample. After the instrumentation, the sample was inserted in double jackets and equipped with the MTS circumferential extensometer at its mid-height for the measurement of lateral strain. A PT100 sensor was attached on the jacket at the lower part for controlling the temperature in the cell. All the electric wires and the hydraulic lines were led outside the cell and connected to the data acquisition system. The collected data were evaluated and displayed on a computer screen to show the actual state of the test. Figure 3-45 shows the instrumented sample in the apparatus.

a. GRS-mini-packers

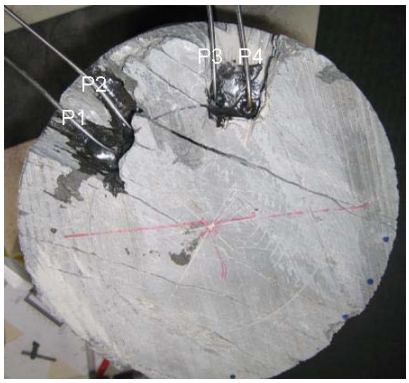

c. borehole sealing

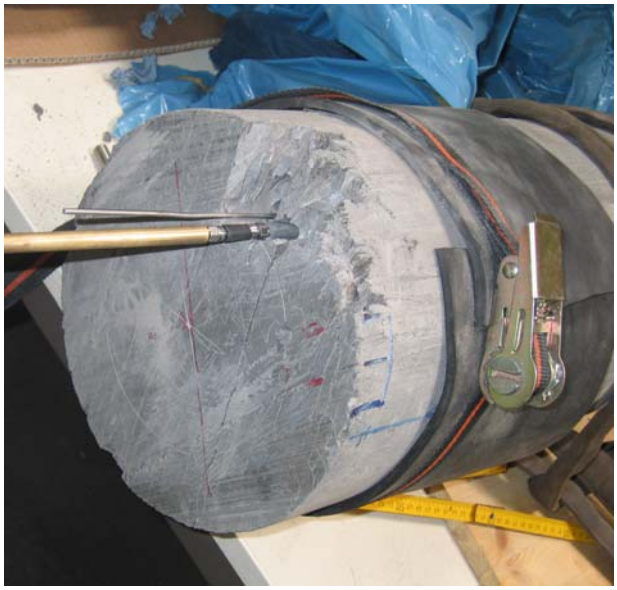

b. installation

Figure 3-43 Installation of GRS mini-packers for pore pressure measurement

a. borehole drilling

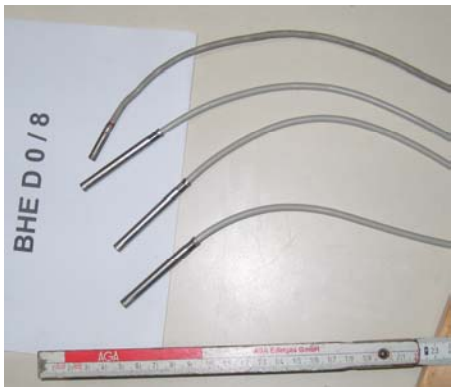

b. PT100

c. installed cable

Figure 3-44 Installation of PT100 sensors for temperature measurement

Figure 3-45 Installation of a mock-up heating test in GRS's big triaxial apparatus

3.5.3.2 First Test

The first mock-up heating test was conducted as planned in four stages of re-saturation, re-consolidation, heating and cooling. Figure 3-46 illustrates the applied test conditions of axial and radial stresses (σ_1, σ_3), water back-pressures at the top and bottom (p_t, p_b), and heater temperature at the top versus time.

1. *Re-saturation*: First, the reservoirs at the top and the bottom and the four test intervals in the sample were filled with PEARSON water at atmospheric pressure under a low confining stress of 0.8 MPa at an ambient temperature of 24 °C over 3 days. Under drained conditions, the axial and radial stresses were then increased to σ_1 = 3.5 MPa / σ_3 = 3.0 MPa and the temperature of the sample to 30 °C. One day later, the water pressures at the end faces and in the test intervals were increased to 1 MPa. The atmospheric pore-water pressure at the heater / rock interface in the in-situ test was simulated by reduction of the back-pressure at the top heater / sample interface to zero after 10 days, while the back-pressure at the bottom was kept at 1 MPa, simulating the pore pressure in the rock around the

heater. Additionally, the test intervals were shut off. This re-saturation phase lasted for 15 days.

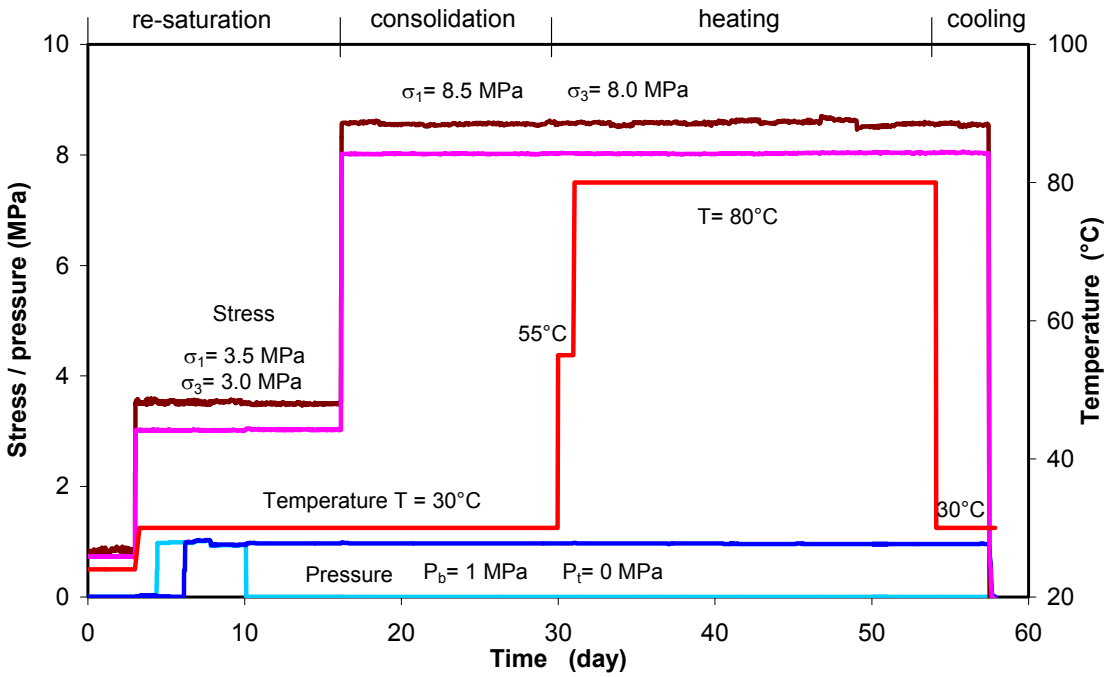

Figure 3-46 Boundary conditions of the first mock-up heating test (applied stresses, water back-pressures and heater temperature)

2. *Re-consolidation*: The overburden stress of about 8 MPa in the HE-D test field at the MTRL was simulated by increasing the confining stress to $\sigma_1 = 8.5$ MPa and $\sigma_3 = 8.0$ MPa. Because of the drained conditions at the back-pressures $p_b = 1$ MPa and $p_t = 0$ MPa, the sample would be more or less re-consolidated. Additionally, the water pressures in the test intervals would react on the mechanical loading. This re-consolidation phase lasted over 15 days.

3. *Heating:* Under the applied HM boundary conditions, the sample was heated at the top by increasing the temperature of heater 2 in two steps: from 30 to 55 °C for one day and then to 80 °C for another 23 days. During the heating phase, the temperatures at the bottom and circumferential boundaries were kept constant at 30 °C by controlling the corresponding heaters and by controlled heating of oil in the cell.

4. *Cooling*: After the heating phase, the heater temperature was dropped down to 30°C for 3 days.

Finally, the sample was dismantled to retrieve and check the measuring sensors.

Figure 3-47 presents the temperature evolution recorded at the different locations along the sample central axis. In the first 3 days, the ambient temperature in the cell was stabilised at 24 °C. After that, the temperature was slightly increased to 30 °C and kept constant during the re-saturation and the re-consolidation phases. Subsequently, the heater temperature was increased to 55 °C and 80 °C at a controlled temperature of $T_b = 30$ °C at the bottom and $T_0 = 31.5$ °C at the circumferential surface. Correspondingly, temperature rising was recorded by all the sensors in the sample. After one day the temperature became constant with T_4 = 76 °C (h = 2 cm), T_3 = 52 °C (h = 15 cm), T_2 = 40°C (h = 30 cm), and T_1 = 35 °C (h = 45 cm). The temperature decreases with the distance to the heater, but not linearly. Finally, decreasing the heater temperature to 30 °C led to a quick drop of the temperature at the measurement points to the similar values.

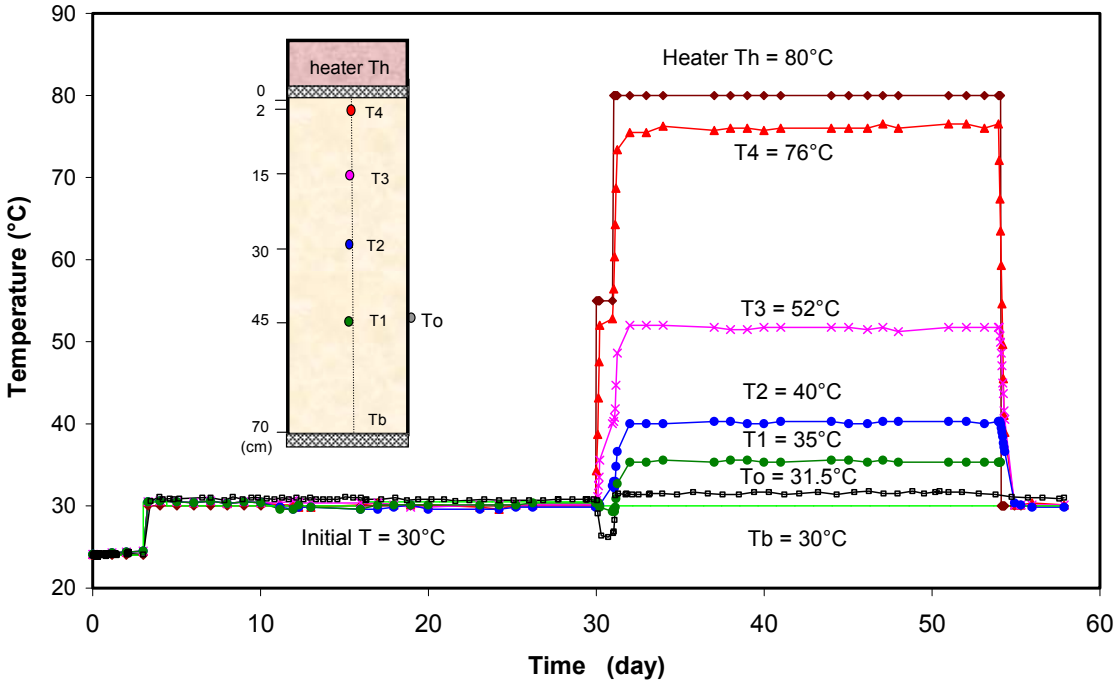

Figure 3-47 Temperatures measured in the large Opalinus clay sample during the first mock-up heating test

Figure 3-48 shows the responses of pore-water pressures at the measurement points to the mechanical and thermal loadings. After closing the test intervals, slight changes of the pressures took place at P_2 (h = 0.45 cm) from 1 to 0.7 MPa and at P_3 (h = 0.3 cm) from 1 to 1.1 MPa, but no change was observed at P_1 (h = 0.60 cm). The mini-

packer P_4 (h = 15 cm) failed. Under the drained conditions of P_b = 1 MPa at the bottom and P_t = 0 MPa at the top, the increase of the confining stress of $\Delta\sigma$ = 5 MPa (σ_3 = 3 → 8 MPa and σ_1 = 3.5 → 8.5 MPa) generated a significant increase of the pressures of ΔP_3 = 4.5 MPa, ΔP_2 = 3.9 MPa, and ΔP_1 = 2.0 MPa. The different values might be caused by different local conditions (porosity, fractures, etc.) in the large sample, which may have been produced by the drilling and sealing of the boreholes. For instance, the area near the bottom was obviously disturbed by the excavation of two small cavities. So the pore pressure P_1 in this area was relatively low. Due to the drained conditions, the pore pressures dissipated progressively over the re-consolidation period of 15 days with P_3 = 5.5 → 3.5 MPa, P_2 = 4.5 → 2.1 MPa, and P_1 = 2.9 → 1.9 MPa.

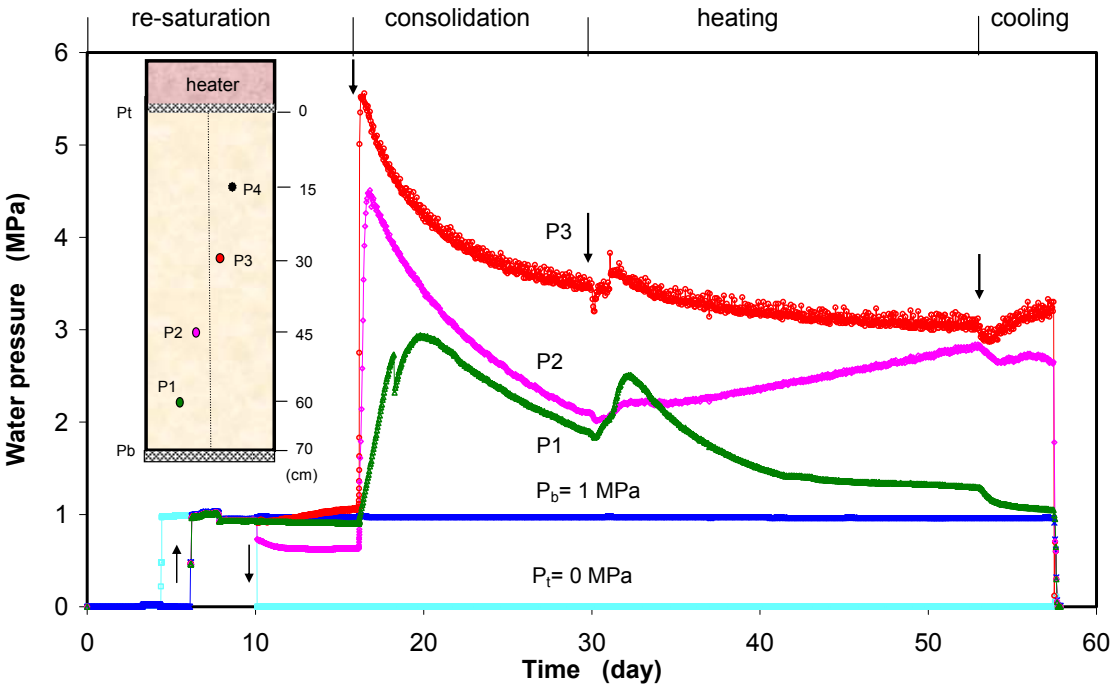

Figure 3-48 Pore-water pressures measured in the large Opalinus clay sample during the first mock-up heating test

The heating resulted in an increase of the pore-water pressures at the different locations, but it was not very significant due to the drained conditions. The pressure increments at the measurement points were ΔP_3 = 0.4 MPa, ΔP_2 = 0.2 MPa, and ΔP_1 = 0.6 MPa, respectively. After reaching the peak values in the first days, P_3 and P_1 decreased steadily, but conversely P_2 increased after 30 days towards the higher level of P_3. This pressure increase may indicate an existence of relatively significant pathways between P_2 and P_3.

The subsequent cooling led to a small drop in the pressures by a mean value of $\Delta P \approx 0.2$ MPa. Finally, P_1 tended to the level of $P_b = 1$ MPa at the bottom, while P_3 and P_2 rose slightly.

Figure 3-49 shows the evolution of the measured axial, radial, and volumetric strains. Under the drained conditions of $P_b = P_t = 0$ MPa, increasing the external stress from 0.8 MPa to $\sigma_1 = 3.5$ MPa and $\sigma_3 = 3$ MPa led to a compression of $\Delta\varepsilon_3 = 0.37$ %, $\Delta\varepsilon_1 = 0.1$ % and $\Delta\varepsilon_v = 0.85$ %. The relatively large radial compression might be caused by closure of pre-existing fractures oriented along the sample axis. The following water injection at 1 MPa produced a significant radial extension of $\Delta\varepsilon_3 = 0.7$%, which is assumed to be due to fracture opening by water penetration. The second loading to $\sigma_1 = 8.5$ MPa / $\sigma_3 = 8$ MPa at $P_b = 1$ MPa and $P_t = 0$ MPa resulted in a large radial compression of $\Delta\varepsilon_3 = 0.55$ % over 15 days, but an insignificant axial strain.

The subsequent heating induced a rapid expansion of $\Delta\varepsilon_3 = 0.08$ %, $\Delta\varepsilon_1 = 0.05$ % and $\Delta\varepsilon_v = 0.21$ %. At the elevated temperatures, a gradual consolidation occurred. The radial compression of $\Delta\varepsilon_3 = 0.20$ % reached after 23 days is three times larger than the axial one of $\Delta\varepsilon_1 = 0.05$ %. The cooling resulted in a rapid compaction of $\Delta\varepsilon_3 = 0.04$ %, $\Delta\varepsilon_1 = 0.05$ % and $\Delta\varepsilon_v = 0.13$ %, and then no further deformation was observed.

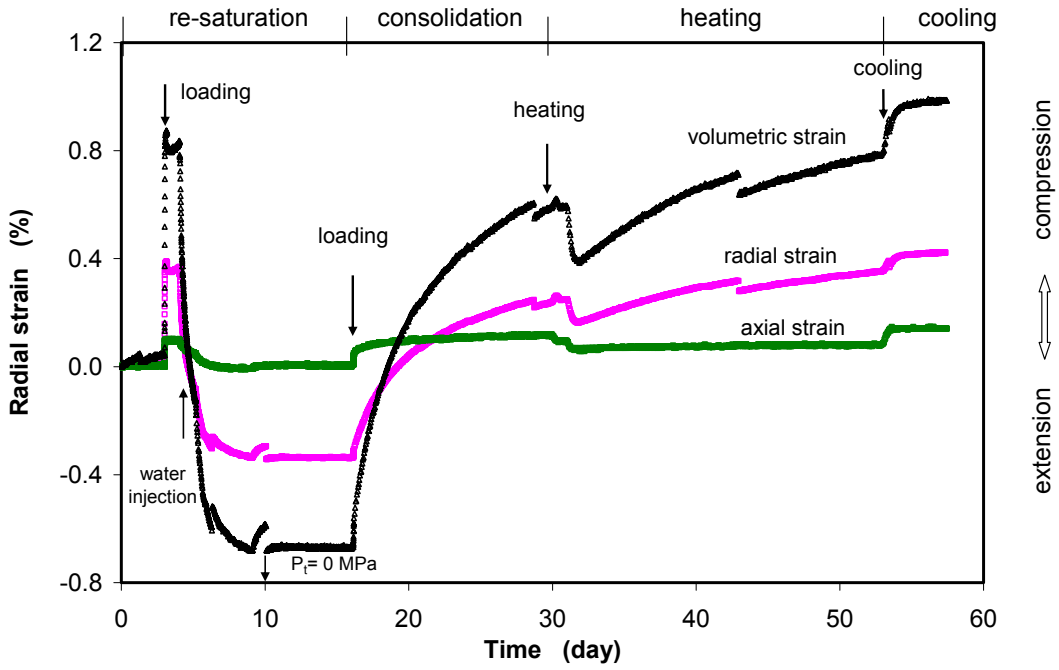

Figure 3-49 Deformations of the large Opalinus clay sample measured during the first mock-up heating test

3.5.3.3 Second Test

In order to gain more data, the sample was heated again under axially-fixed and laterally-unconstraint conditions ($\Delta\varepsilon_1 = 0$, $\sigma_3 = 0$) and null water back-pressures ($P_t = P_b = 0$). However, the water pressures in the test intervals P_1, P_2, P_3 and P_4 were increased to 1 MPa and then closed. The triaxial cell was not filled with oil. The top heater temperature T_h was increased from 24 to 80 °C, while the temperature in the cell T_o was not controlled and T_b = 24 °C at the bottom was kept constant.

Figure 3-50 summarises the temperature evolution curves recorded by all sensors (T_1 failed). The rapid increase of the heater temperature from 24 to 80 °C produced a thermal transient phase for a short time of about 3 days. After that, the temperatures at all positions reached maximum values and remained at T_h = 80 °C, T_4 = 77 °C, T_3 = 62 °C, T_2 = 52 °C, T_b = 24 °C, and T_0 = 39 °C, forming a steady thermal field in the sample. Following the 18-days heating phase, the sample was cooled down by shutting off the heater. As a consequence, the temperatures at different locations dropped quickly down to 24 – 26 °C and then remained at ambient condition.

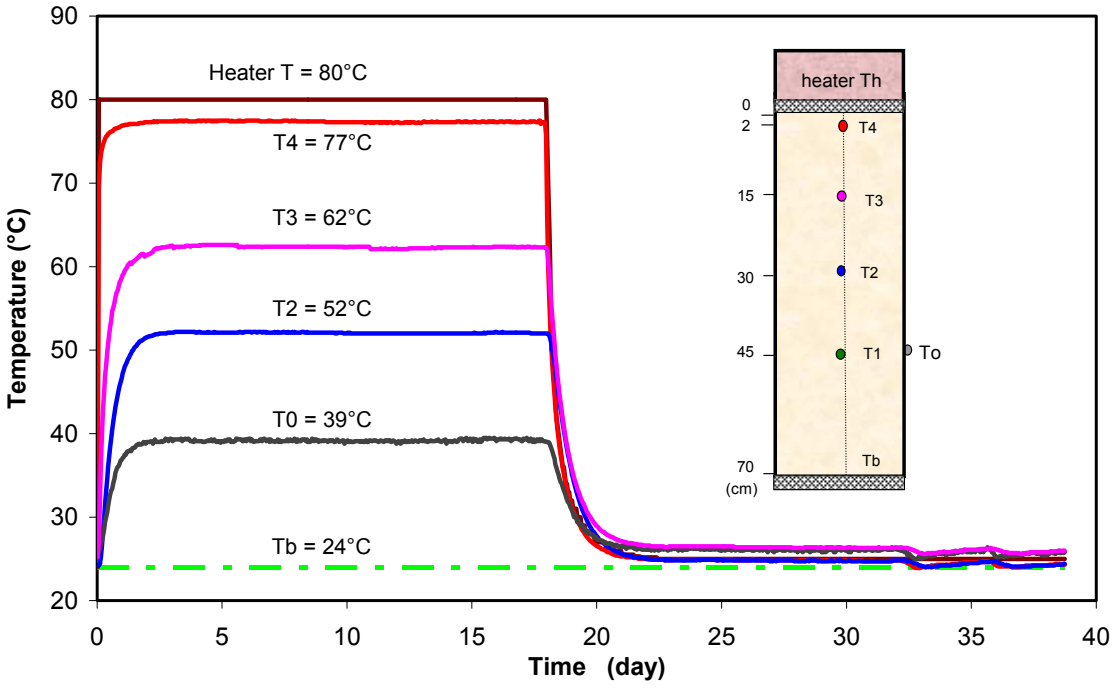

Figure 3-50 Temperatures measured in the large Opalinus clay sample during the second mock-up heating test

The responses of the water pressures in the mini-intervals to heating and cooling are shown in Figure 3-51. The pore pressures at P_1, P_2 and P_3 (P_4 failed) dropped from 1 MPa down to 0.3 - 0.4 MPa during the 18-days heating phase. The pressure evolution at P_2 and P_3 was not influenced by cooling. The pressure drop at P_1 might be due to a local damage near the excavated cavities at the sample bottom.

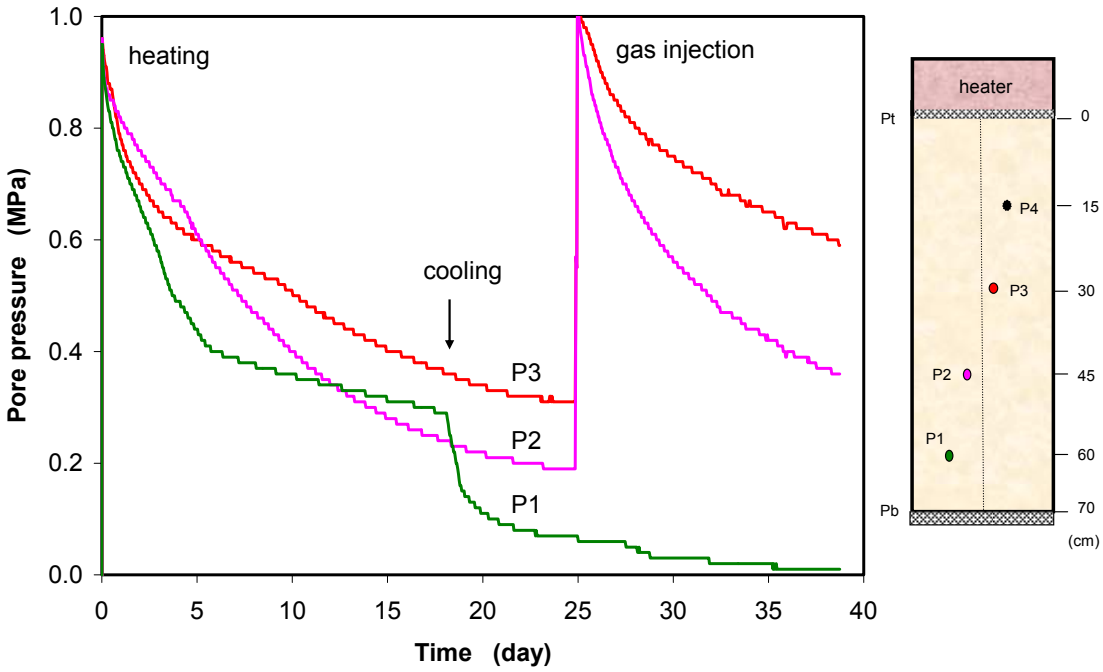

Figure 3-51 Evolution of the pore pressures during the second heating test

At the lower temperature of 24 °C, the water in the test intervals P_2 and P_3 was pumped out by injection of nitrogen gas to 1 MPa. After closing the valves, the gas pressure dropped gradually down (Figure 3-51). The reduction rates are comparable with the reduction of the water pressures before during the heating phase. This means that the pore-structure and thus the permeability of the sample were not significantly altered by the heating / cooling cycles.

After testing, the sample was dismantled. Figure 3-52 shows photos of the dismantled sample. From the left picture one can clearly see that the lower part of the sample expanded laterally up to breaking. This might be due to the high swelling and softening at the high water pressure and local weakness induced by the excavation of the two cavities at the bottom. From the right picture one can identify the positions of the pore-water test intervals. The interval P_4 was not sufficiently sealed and failed. The PT100

temperature sensors were re-calibrated and the calibration results were considered in the final evaluation of the data.

a. sample after dismantling b. mini-packers sealed in boreholes

Figure 3-52 Dismantled sample after the second mock-up heating test

4 Modelling

4.1 Objectives

In addition to the in-situ measurements and the laboratory investigations, a series of modelling exercises was also performed by GRS for analysing the complex THM processes observed in the in-situ and laboratory heating experiments. The modelling work included

- estimation of parameters associated with the constitutive models;
- modelling of the lab mock-up heating tests for calibration of key parameters;
- pre-operational calculations for the design of the in-situ heating experiment;
- simulation and analysis of the in-situ experiment.

4.2 THM Coupling Theories

For these modelling exercises, the computer programme CODE-BRIGHT /UPC 02/ developed by the Technical University of Catalonia in Barcelona for the analysis of coupled THM processes in geological media was used. Details about the basic theories with the formulated governing equations (balance equations, constitutive models and equilibrium relationships) are described in the code manual /UPC 02/ and in /OLI 94/, /GEN 98; 06/, /ALO 02/. In the following, the balance equations, constitutive models and equilibrium relationships, which are to be solved in the calculations, are briefly summarized. Values of the parameters of the investigated Opalinus clay associated with the constitutive models are established, too.

4.2.1 Balance Equations

Generally, for the calculations of coupled THM processes in geological media, a set of balance equations for internal energy, solid mass, water mass, air mass, and stress equilibrium are to be solved in a consistent way.

- Internal energy balance:

$$\frac{\partial}{\partial t}\left[E_s \rho_s (1-\phi) + E_l \rho_l S_l \phi + E_g \rho_g S_g \phi\right] + \nabla \cdot (\mathbf{i}_c + \mathbf{j}_{Es} + \mathbf{j}_{El} + \mathbf{j}_{Eg}) = f^E \quad (4.1)$$

Where E_s, E_l and E_g are specific internal energies corresponding to the solid, liquid and gaseous phases, ρ_s, ρ_l and ρ_g are the densities of the three phases, ϕ is porosity, S_l is the volumetric liquid fraction and S_g is the volumetric gaseous fraction with respect to the pore volume, $S_l + S_g = 1$. $\mathbf{i}_c$ is the conductive heat flux and $\mathbf{j}_{Es}$, $\mathbf{j}_{El}$, $\mathbf{j}_{Eg}$ are the advective energy flux of each of the three phases with respect to a fixed reference system. The most relevant advection energy fluxes correspond to vapour and liquid water motion. f^E is the energy supply per unit volume of the considered medium.

- Water mass balance:

$$\frac{\partial}{\partial t}(\theta_l^w S_l \phi + \theta_g^w S_g \phi) + \nabla \cdot (\mathbf{j}_l^w + \mathbf{j}_g^w) = f^w \quad (4.2)$$

where θ_l^w and θ_g^w are the mass of water per unit volume of liquid and gas, respectively, $\mathbf{j}_l^w$ and $\mathbf{j}_g^w$ denote the total mass flux of water in the liquid and gas phases with respect to a fixed reference system and f^w is the external mass supply of water per unit volume of medium.

- Air mass balance:

$$\frac{\partial}{\partial t}(\theta_l^a S_l \phi + \theta_g^a S_g \phi) + \nabla \cdot (\mathbf{j}_l^a + \mathbf{j}_g^a) = f^a \quad (4.3)$$

where θ_l^a and θ_g^a are the mass of dry air per unit volume of liquid and gas, respectively, $\mathbf{j}_l^a$ and $\mathbf{j}_g^a$ indicate the total mass flux of air in the liquid and gas phases with respect to a fixed reference system, and f^a is the external mass supply of air per unit volume of medium.

- Solid mass balance:

$$\frac{\partial}{\partial t}(\theta^s (1-\phi)) + \nabla \cdot (\mathbf{j}^s) = 0 \quad (4.4)$$

where θ^s is the solid density and $\mathbf{j}^s$ is the flux of solid.

- Stress equilibrium:

$$\nabla \cdot \boldsymbol{\sigma} + \mathbf{b} = \mathbf{0} \tag{4.5}$$

where $\boldsymbol{\sigma}$ represents the stresses and **b** the body forces.

The state variables are the solid displacements **u** (three spatial directions), liquid pressure p_l, gas pressure p_g, and temperature T.

4.2.2 Constitutive Models and Parameters

The set of the balance equations are completed by constitutive equations and equilibrium restrictions which link between the state variables and the dependent variables. The constitutive models describe the thermal, hydraulic and mechanical behaviours of the material under study, while the equilibrium restrictions are given for the concentration of water vapour in gas and of dissolved air in water. All the equations involve physical parameters, some of which also depend on the state variables of pressure and temperature.

For the modelling of the in-situ and laboratory heating experiments, a series of constitutive models and equilibrium relationships are assumed. The associated parameters are estimated for the Opalinus clay on basis of the test results obtained in the frame of this project and the data given in /BOC 01/, /THU 99/, /FLO 02/, /MUN 03/, /ZHA 04/. The clay rock is assumed as a homogeneous and isotropic porous medium, even though anisotropy is prevailing due to sedimentation and other factors.

4.2.2.1 Basic Properties

The basic petrophysical properties of the clay rock in the HE-D test field were determined on the drill cores, as given in chapter 3. Table 4-1 summarises the mean values of the grain density, dry density, porosity and water content, which are used in the models. The clay rock is fully saturated by formation water.

For the liquid water and the gas in the porous medium, their density and viscosity vary with change in pressure and temperature, as expressed in Table 4-2.

Table 4-1 Physical properties of the Opalinus clay

Property	Value
Grain density	ρ_s = 2710 kg/m^3
Dry density	ρ_d = 2340 kg/m^3
Porosity	ϕ =16 %
Water content	w = 6.85 %
Initial saturation	S = 100 %

Table 4-2 Physical properties of liquid and gas

Law	Equation	Parameter
Liquid density	$\frac{\rho_l}{\rho_{lo}} = 1 + \beta(P_l + P_{lo}) + \alpha T$	ρ_{lo} = 1000 kg/m^3 , α = -3.4·10^{-4} K^{-1} ß = 4.5·10^{-4} MPa^{-1}, P_{lo} = 0.1 MPa
Liquid viscosity	$\mu_l = A \exp\left(\frac{B}{273.15 + T}\right)$	A = 2.1·10^{-12} MPa s B = 1808.5 K
Gas density (Ideal gas law)	$P_g = \frac{\rho_g}{m} TR$	m = 28.966 kg/kmol for molecular mass of air m = 18.016 kg/kmol for molecular mass of vapour
Gas viscosity	$\mu_g = A \exp\left(\frac{B}{273.15 + T}\right)$	A = 1.48·10^{-12} MPa s B = 119.4 K

4.2.2.2 Thermal Models and Parameters

It is assumed that the three phases of solid, liquid and gas are in a thermal equilibrium, i.e., at the same temperature. Heat transport is governed by conduction through the rock and by advective flow of liquid water and vapour. Thermal conduction is expressed by Fourier's law, as presented in Table 4-3. Usually, the thermal conductivity of an unsaturated porous medium depends on the porosity and the degree of water saturation. Because of a lack of respective data, these dependencies are not taken into account in the calculations. Additionally, the Opalinus clay exhibits a strong anisotropy of the thermal conductivity with $\lambda_{//}$ = 2.1 W·m^{-1}·K^{-1} parallel to the bedding

plane and $\lambda_{\perp}$ = 1.0 $W \cdot m^{-1} \cdot K^{-1}$ perpendicular to the bedding /BOC 01/. This anisotropic property is not considered. A mean value of $\lambda = (\lambda_{\perp} + 2 \cdot \lambda_{//})/3$ = 1.7 $W \cdot m^{-1} \cdot K^{-1}$ is adopted for the modelling.

The internal energy of each phase (solid, liquid, gas) is determined by the mass fraction and specific heat capacity of its components. According to /BOC 01/, a specific heat capacity of C_s = 800 $J \cdot kg^{-1} \cdot K^{-1}$ is taken for the solid grains in the clay rock. The specific heat capacities of liquid water (C_l^w), water vapour (C_g^w), and air ($C_g^a = C_l^a$) are given in Table 4-3 for the calculation of the internal energies of the liquid and gas phases.

Another key parameter is the thermal expansion coefficient, which determines the rock deformation due to a temperature change. For the Opalinus clay this parameter is also anisotropic with $\alpha_{s//}$ = $1.5 \cdot 10^{-6}$ K^{-1} parallel and $\alpha_{s\perp}$ = $1.6 \cdot 10^{-5}$ K^{-1} perpendicular to the bedding plane (see section 3.4.2). It should be remarked here that the thermal expansion of a porous medium in saturated condition is governed by the thermal expansion coefficients of both the solid minerals and the pore water. In accordance to literature /NOY 00/, the thermal expansion coefficient for clay minerals amounts to α_s = $2 \cdot 10^{-6}$ K^{-1}, which is very close to the low limit value of $1.5 \cdot 10^{-6}$ K^{-1} measured on the Opalinus clay. So this low value is assumed for the solid grains of the clay rock.

For the pore-water, a constant value of $\alpha_w \approx 3.4 \cdot 10^{-4}$ K^{-1} is taken for its volumetric thermal expansion coefficient /UPC 02/, which is about two orders of the magnitude higher than that of $\alpha_v = 3 \cdot \alpha_s = 4.5 \cdot 10^{-6}$ K^{-1} for the solid grains. This means that the thermal expansion of the saturated clay rock with a porosity of 16 % is dominated by the water expansion. In accordance to the α_w- and α_s-values given above for water and solids and the porosity ϕ, one can calculate the linear thermal expansion coefficient for the saturated porous medium by

$$\alpha_m = \alpha_s(1-\phi) + \frac{\alpha_w}{3} \cdot \phi \qquad (4.6)$$

The calculated value of $\alpha_m = 1.9 \cdot 10^{-5}$ K^{-1} for the clay rock agrees well with that of α_m = $1.5 \cdot 10^{-5}$ K^{-1} measured on the samples with natural water contents under undrained conditions (section 3.4.2). The calculated and measured values are averaged to a value of $\alpha_m = 1.7 \cdot 10^{-5}$ K^{-1}, which is adopted for the rock mass in the modelling.

Table 4-3 Thermal laws and parameters

Law	Equation	Parameter
Fourier's law for conductive heat flow	$\mathbf{i}_c = -\lambda \nabla T$	λ = 1.7 W/(m·K)
Internal energy of solid	$E_s = C_s \cdot T$	C_s = 800 J/(kg·K)
Internal energy of liquid	$E_l = E_l^w \omega_l^w + E_l^a \omega_l^a$ $E_l^w = C_l^w \cdot T$ $E_l^a = C_l^a \cdot T$	C_l^w = 4184 J/(kg·K) C_l^a = 1006 J/(kg·K)
Internal energy of gas	$E_g = E_g^w \omega_g^w + E_g^a \omega_g^a$ $E_g^w = E_v + C_g^w \cdot T$ $E_g^a = C_g^a \cdot T$	$E_v = 2.5 \cdot 10^6$ J/kg C_g^w = 1900 J/(kg·K) C_g^a = 1006 J/(kg·K)
Linear thermal expansion coefficient of solid grains		$\alpha_s = 1.5 \cdot 10^{-6}$ K^{-1}
Volumetric thermal expansion coefficient of the pore water		$\alpha_w = 3.4 \cdot 10^{-4}$ K^{-1}
Linear thermal expansion coefficient of the rock mass		$\alpha_m = 1.7 \cdot 10^{-5}$ K^{-1}

4.2.2.3 Hydraulic Models and Parameters

Liquid and gas advection follow Darcy's law, as represented in Table 4-4. The hydraulic conductivity $\mathbf{K}_\alpha$ of each phase (α = l for liquid, α = g for gas) is a tensor, depending on intrinsic permeability **k**, relative permeability $k_{r\alpha}$, and dynamic viscosity μ_α. Because the hydraulic anisotropy of the Opalinus clay is ignored in the modelling, the intrinsic permeability and thus the hydraulic conductivity become scalar quantities. In fact, the hydraulic parameters depend on the material state, i.e. porosity, degree of saturation, temperature, etc. For instance, the intrinsic permeability k is related to the porosity ϕ via Kozeny's model (Figure 4-1). The initial permeability of $k_o = 2 \cdot 10^{-20}$ m^2 is obtained by averaging the values determined perpendicular and parallel to the bedding plane. The relative permeability $k_{r\alpha}$ is a function of the degree of water saturation S_e (Figure 4-2), which is in turn determined by the suction via water retention curve (Figure 3-9), and the viscosity of each phase varies with temperature (Table 4-2).

In addition to the advective transport of water and air, vapour diffusion in air and the solubility of air in liquid water are taken into account by Fick's law and Henry's law,

respectively. The changes of liquid and gas phases are represented by the psychrometric law. The hydraulic models and parameters for the Opalinus clay are listed in Table 4-4.

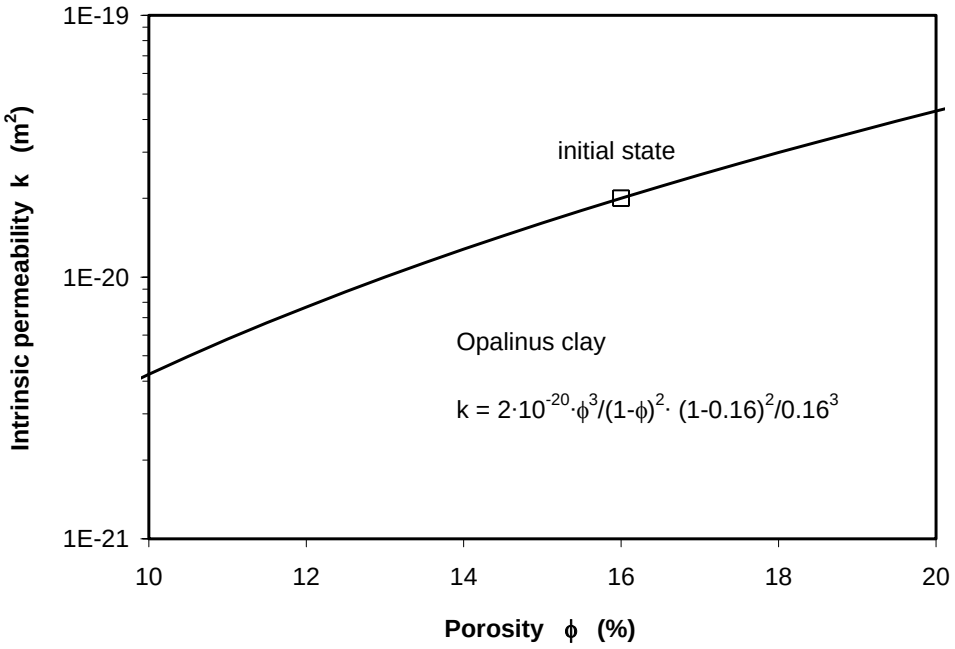

Figure 4-1 Kozeny's model for intrinsic permeability / porosity – relationship

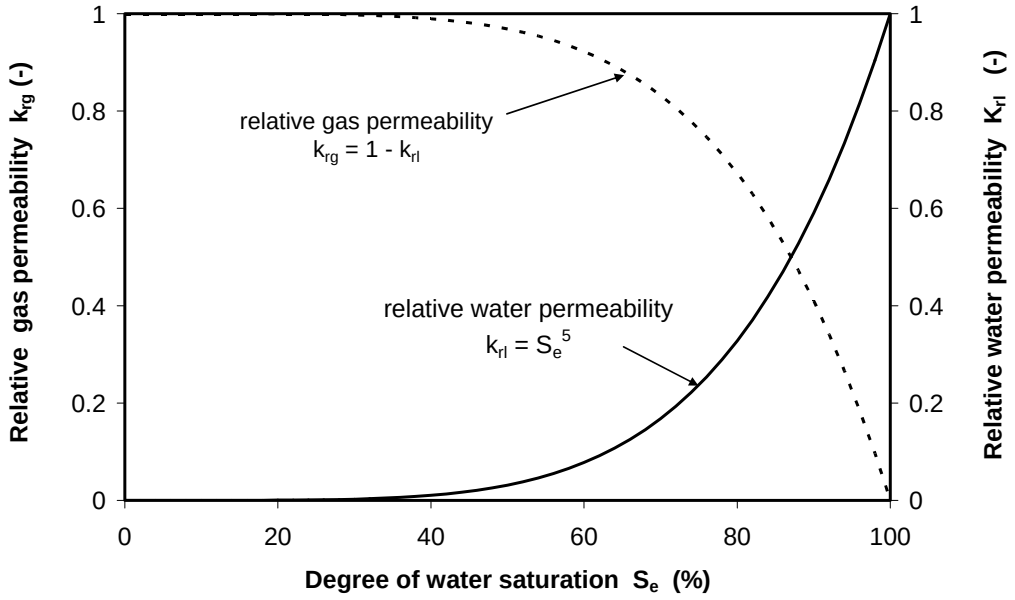

Figure 4-2 Relative permeability of liquid and gas as a function of water saturation

Table 4-4 Hydraulic laws and parameters

Law	Equation	Parameter
Darcy's law for advective flux of liquid and gas	$\mathbf{q}_\alpha = -\mathbf{K}_\alpha (\nabla P_\alpha - \rho_\alpha \mathbf{g})$ $\mathbf{K}_\alpha = \mathbf{k}\, k_{r\alpha} / \mu_\alpha$	$\mathbf{k}$ = permeability tensor $k_{r\alpha}$ = relative permeability μ_α = dynamic viscosity α = l for liquid, α = g for gas
Kozeny's model for permeability / porosity - relationship	$\mathbf{k} = \mathbf{k}_0 \frac{\phi^3}{(1-\phi)^2} \frac{(1-\phi_0)^2}{\phi_0^3}$	$k_o = k_o = 2 \cdot 10^{-20}$ m^2 $\phi_o = 0.16$ ϕ = porosity
Relative permeability of liquid and gas	$k_{rl} = A \cdot S_{el}^B$ $k_{rg} = 1 - k_{rl}$	A = 1 B = 5
Saturation of liquid and gas	$S_e = \frac{S_l - S_{lr}}{S_{ls} - S_{lr}}$ $S_g = 1 - S_l$	S_{lr} = residual saturation = 0.01 S_{lr} = maximum saturation = 1 S_l = actual saturation S_e = effective saturation
Water retention curve	$S_e = \left[1 + \left(\frac{s}{P_0} \right)^{1/(1-\beta)} \right]^{-\beta}$	P_o = 20 MPa ß = 0.3 s = suction (=$P_g - P_l$)
Fick's law for vapour non-advective flux	$\mathbf{i}_g^w = -\mathbf{D}_g^w \nabla \omega_g^w$ $= -(\phi \ \rho_g S_g \tau \mathbf{D}_m^w \ \mathbf{I}) \nabla \omega_g^w$	$D_m^w = 5.9 \cdot 10^{-12} \cdot \frac{(273.15+T)^{2.3}}{P_g}$ m^2/s τ = tortuosity = 0.8
Psychrometric law for vapour mass per unit gas volume	$\theta_g^w = (\theta_g^w)^0 \exp\left[\frac{-(P_g - P_l) M_w}{R(273.15+T)\rho_l} \right]$	M_w = molecular mass of water = 0.018 kg/mol R = gas constant = 8.314 J/(molK)
Henry's law for solubility of air in water	$\omega_l^a = \frac{P_a}{H} \frac{M_a}{M_w}$	M_a = molecular mass of air = 0.02895 kg/mol H = 10000 MPa

4.2.2.4 Mechanical Model and Parameters

The mechanical behaviour of the Opalinus clay is described by a thermo-elasto-plastic model (BBM), which has been developed by UPC /GEN 98/, /ALO 02/, and which is represented in Table 4-5. This model is able to represent many mechanical features of unsaturated soils in a consistent and unified manner, such as thermal expansion and contraction by temperature change, swelling and shrinking due to moisture change, elasto-plastic deformation with strain hardening, and increase in stiffness and strength with decreasing water content. Some of the features are demonstrated for the Opalinus clay below.

Table 4-5 Mechanical model and parameters

BBM Model	Equation	Parameter
Elastic volumetric strain	$d\varepsilon_v^e = d\varepsilon_{vp}^e + d\varepsilon_{vs}^e + d\varepsilon_{vT}^e$ $d\varepsilon_{vp}^e = \frac{k_i}{v}\frac{dp'}{p'}$ $d\varepsilon_{vs}^e = \frac{k_s}{v}\frac{ds}{(s+p_{at})}$ $d\varepsilon_{vT}^e = \alpha_v \Delta T$	k_i = 0.0035 $k_s = 4 \cdot 10^{-5}$ v = 1+e e = void ratio e_o = 0.19 $\alpha_v = \alpha_{sv} = 3 \cdot \alpha_s = 4.5 \cdot 10^{-6}\,K^{-1}$ for solid skeleton $\alpha_v = \alpha_{mv} = 3 \cdot \alpha_m = 5.1 \cdot 10^{-5}\,K^{-1}$ for saturated rock mass
Elastic deviatoric strain	$d\varepsilon_q^e = \frac{G}{3} dq$ $G = \frac{3(1-2\nu)}{2(1+\nu)}\frac{(1+e)}{k_i}p'$	ν = 0.33 K_o = 3300 MPa G_o = 2510 MPa E_o = 6680 MPa
Yield locus	$q^2 - M^2(p'+p_s)(p_o - p') = 0$ $p_s = k \cdot s$ $p_o = p^c\left(\frac{p_o^*}{p^c}\right)^{\frac{\lambda(o)-k_i}{\lambda(s)-k_i}}$ $\lambda(s) = \lambda(o)\left[(1-r)\exp(-\beta s) + r\right]$ $q = M \cdot p'$	k = -0.007 p^c = 0.1 MPa p_o^* = 20 MPa $\lambda(o)$ = 0.027 r = 0.6 ß = 0.015 MPa^{-1} M = 1.5
Hardening	$\frac{dp_o^*}{p_o^*} = \frac{v}{\lambda(o)-k_i} d\varepsilon_v^p$	

Figure 4-3 compares the results of measured and calculated swelling pressures perpendicular and parallel to the bedding plane. The tests were performed in conventional swelling cells with water wetting /THU 99/. The swelling behaviour perpendicular to bedding is used in the isotropic model, which may lead to an underestimation of the significant swelling / shrinking deformations observed on the clay rock by changing the surrounding air humidity (section 3.4.5).

Figure 4-4 shows the modelled triaxial tests on saturated samples at different lateral stresses. Under the stress conditions in the HE-D test field mentioned in chapter 2, the deformation of the clay rock is expected to be elastic.

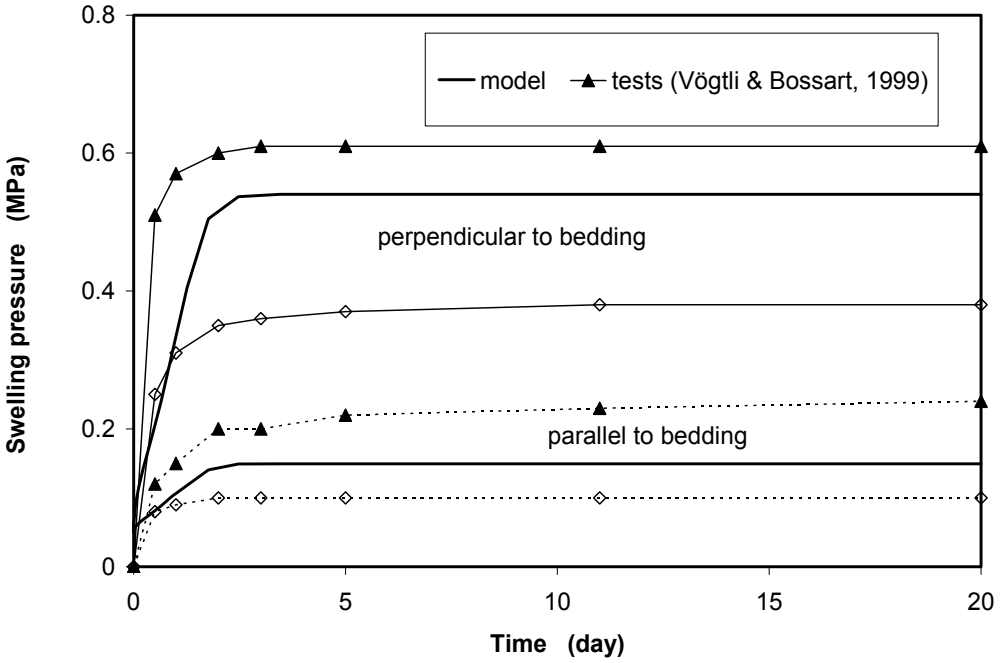

Figure 4-3 Swelling pressure measured and calculated for the Opalinus clay

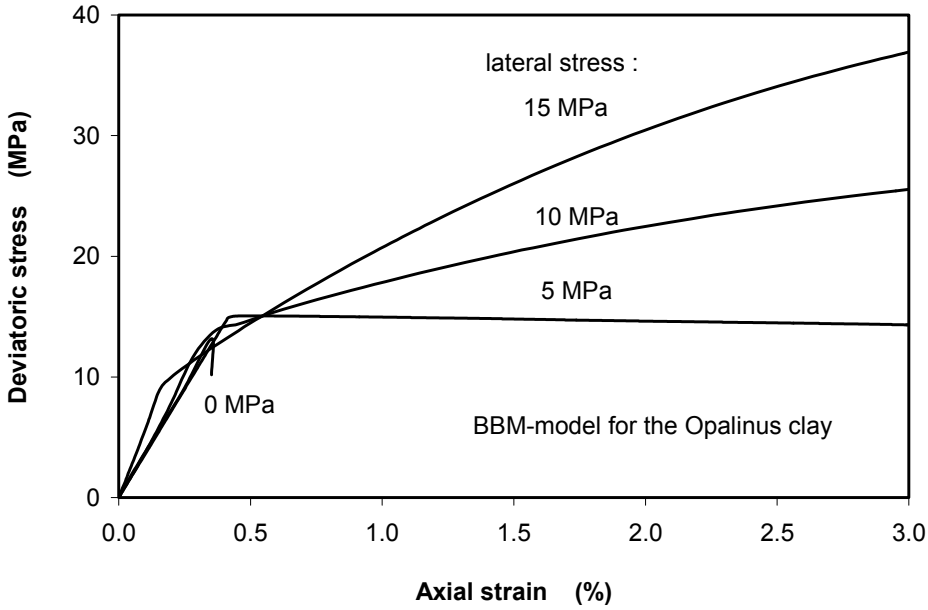

Figure 4-4 Stress / strain curves calculated with the BBM-model for saturated conditions

The Opalinus clay exhibits a significant anisotropy of the mechanical behaviour, which is not yet taken into account in this work. The mean values of the elastic parameters determined on basis of the data given in /BOC 01/ are taken into account in the

modelling. As Figure 4-5 shows, Young's modulus E, the shear modulus G, and the bulk modulus K increase with confining mean stress.

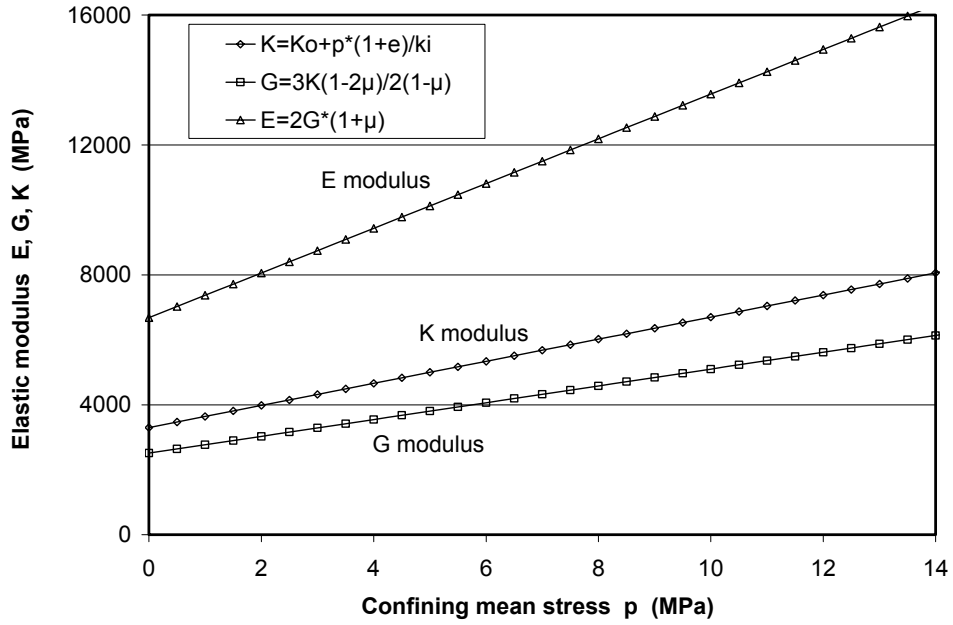

Figure 4-5 Dependence of elastic parameters on confining stress

The average strength of the rock is employed in the model (Figure 4-6). The dependence of the strength on the water content is depicted in Figure 4-7. The increase of the strength with decreasing the water content can be revealed by BBM model, too.

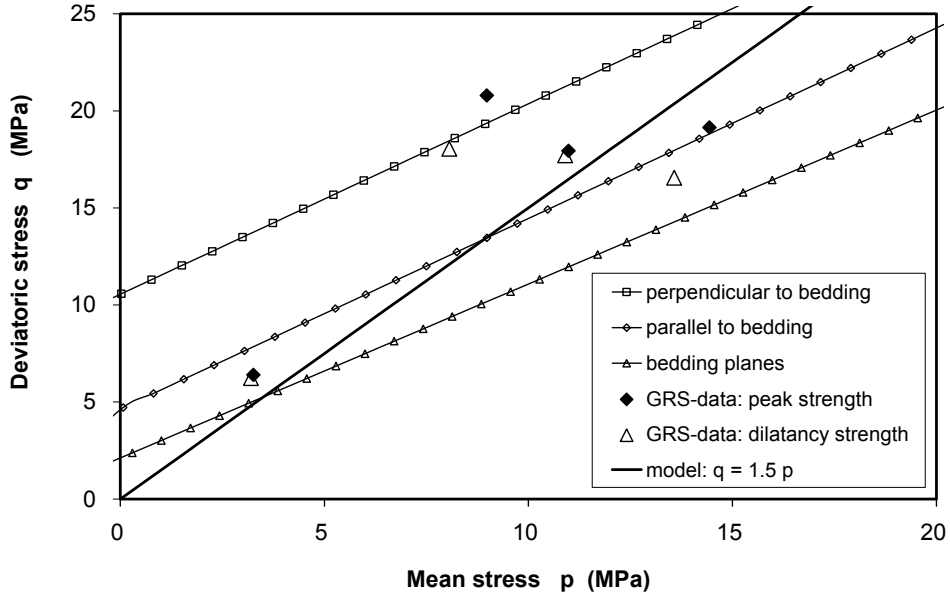

Figure 4-6 Measured and calculated strength of the Opalinus clay

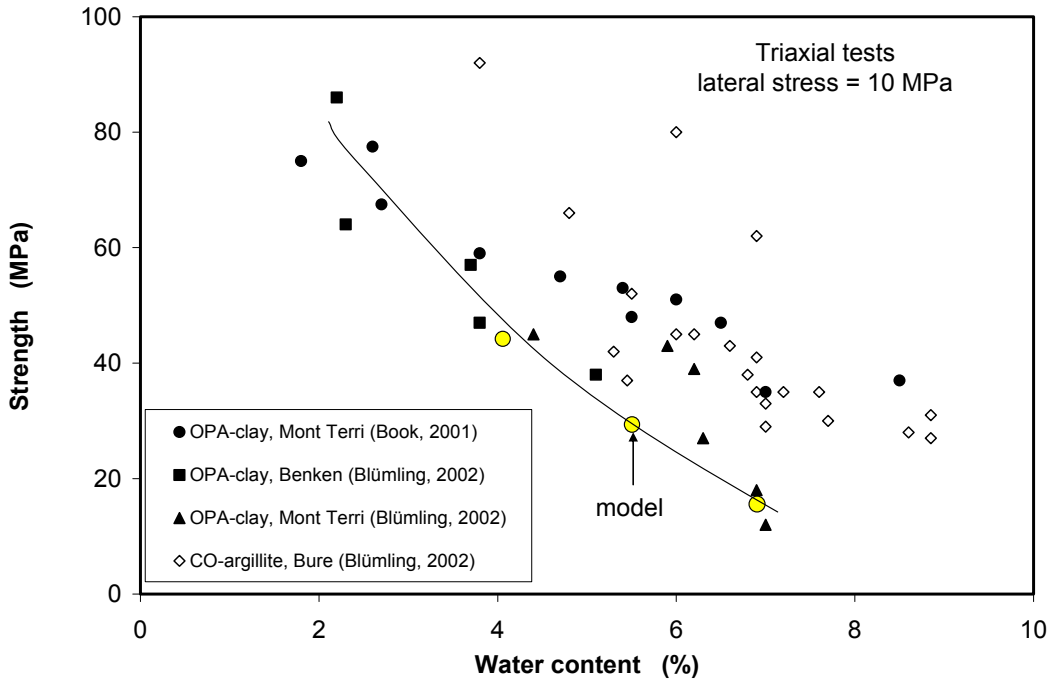

Figure 4-7 Strength of the clay rocks as a function of water content

According to the BBM formulation, the thermal deformation is computed for the solid skeleton and not for the whole porous medium consisting of solid grains, pore-water and gas. Usually, laboratory and field observations of thermal deformation deal with the whole porous medium. For reasons of comparison, the thermal deformation of the porous medium consisting of solid grains, pore-water and gas shall be calculated. In case of a fully water-saturated porous medium, the linear thermal volumetric strain can be calculated by

$$d\varepsilon^{e}_{mvT} = d\varepsilon^{e}_{svT} + d\varepsilon_{wT} = \left[\alpha_{sv}(1-\phi)+\alpha_{w}\phi\right]\cdot\Delta T = \alpha_{mv}\cdot\Delta T \qquad (4.7)$$

where $d\varepsilon^{e}_{svT}$, $d\varepsilon_{wT}$, $d\varepsilon^{e}_{mvT}$ are the thermal volumetric strains of the solid grains, the pore-water and the porous medium, α_{sv}, α_{w}, α_{mv} are the volumetric thermal expansion coefficients of the solid grains, the pore-water and the porous medium, ϕ is the porosity, and ΔT is the temperature change.

The thermal expansion coefficient used in the modelling is determined according to equation (4.6) by $\alpha_{mv} = 3\cdot\alpha_{m} = 5.1\cdot10^{-5}\,K^{-1}$.

4.3 Modelling of the Laboratory Mock-up Heating Tests

The laboratory mock-up heating tests on large Opalinus samples (section 3.5.3) were simulated in order to calibrate some key parameters. As well known, thermal loading is the driving force for THM coupling processes. So first of all, the thermal parameters were to be established. This was done by back-calculations of the temperature evolution and distribution observed in the second mock-up heating test. Then the complete THM processes observed in the first heating test were simulated, whereby some other hydraulic and mechanical parameters could be identified.

4.3.1 Thermal Modelling

The second heating test aimed at investigating the thermal process in the large clay sample. According to the test configuration and conditions (Figure 3-41), the temperature in the sample is computed by using an axisymmetric model (Figure 4-8). In the model, the jacket and the air in the cell are also taken into account. The heater temperature is taken as T_h = 80 °C at the sample top and at the bottom fixed with T_b = 24 °C. No heat flow is permitted through the cell wall. The thermal parameters of the jacket and of air are taken from /LAX 67/, /SOM 92/. The thermal conductivity λ and the heat capacity C of the clay rock are examined within the ranges of λ = 1 – 2.1 $W \cdot m^{-1} \cdot K^{-1}$ and C = 800 - 1000 $J \cdot kg^{-1} \cdot K^{-1}$, respectively.

The modelling results obtained by application of several typical sets of λ- and C-values are compared in Figures 4-9a to 4-9d with the temperatures measured in the sample. The best agreement between calculation and measurement for all the measurement points is achieved with the parameter-set of λ = 1.7 $W \cdot m^{-1} \cdot K^{-1}$ and C = 800 $J \cdot kg^{-1} \cdot K^{-1}$ (Fig. 4-9a). The discrepancies are lower than 0.5 °C for T_o, T_3, and T_4, except for which is $T_2 \approx$ 1.5 °C. However, the calculated temperature rising rates in the transient phase are somewhat lower than the measured ones. It is interesting to see that the application of the high λ-value of 2.1 $W \cdot m^{-1} \cdot K^{-1}$, which is determined along the bedding plane, provides also a good agreement between modelling and measurement results. This is probably due to the boundary conditions of the test which limit the heat flow more along the sample axis which is nearly parallel to the bedding plane. In contrast to that, the low λ-value of 1.0 $W \cdot m^{-1} \cdot K^{-1}$, which is measured perpendicular to the bedding plane, does not fit the measurements (Fig. 4-9c). Comparing Figures 7-9a and 7-9d, one can find that two different C-values of 800 and 1000 $J \cdot kg^{-1} \cdot K^{-1}$ produce almost the

same results. It seems that the heat capacity C has a negligible influence on the thermal process in this test.

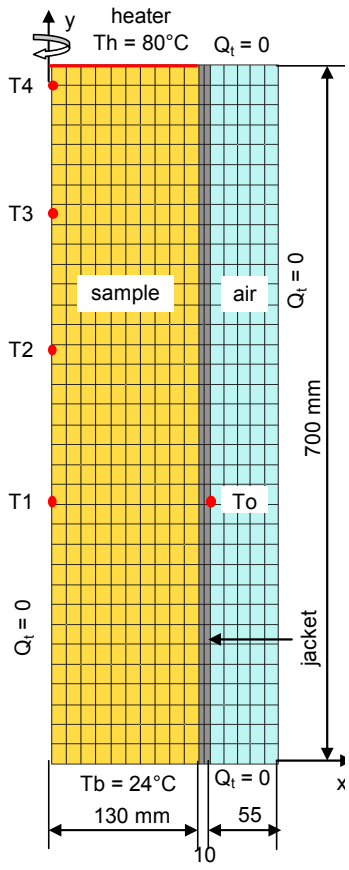

Thermal parameters

Parameter	Opalinus clay	Rubber jacket	Air
Density ρ (kg/m^3)	2340	1150	1.2
Heat capacity C (J/kg·K)	800 – 1000	1200	1010
Thermal conductivity λ (W/m·K)	1.0 – 2.1	0.23	0.022

Heating phase t = 0 – 18 days

Cooling phase t = 18 – 39 days

Figure 4-8 Model geometry, boundary conditions and thermal parameters for modelling of the second mock-up heating test

4.3.2 Coupled THM Modelling

The THM processes observed in the first mock-up heating test were simulated by THM coupling calculations. According to the test configuration and conditions (Figure 3-41), an axisymmetric model is adopted, in which the sample and the surrounding jacket are taken into account. The realized test procedure with several steps is simulated by applying the corresponding conditions to the model, as shown in Figure 4-10.

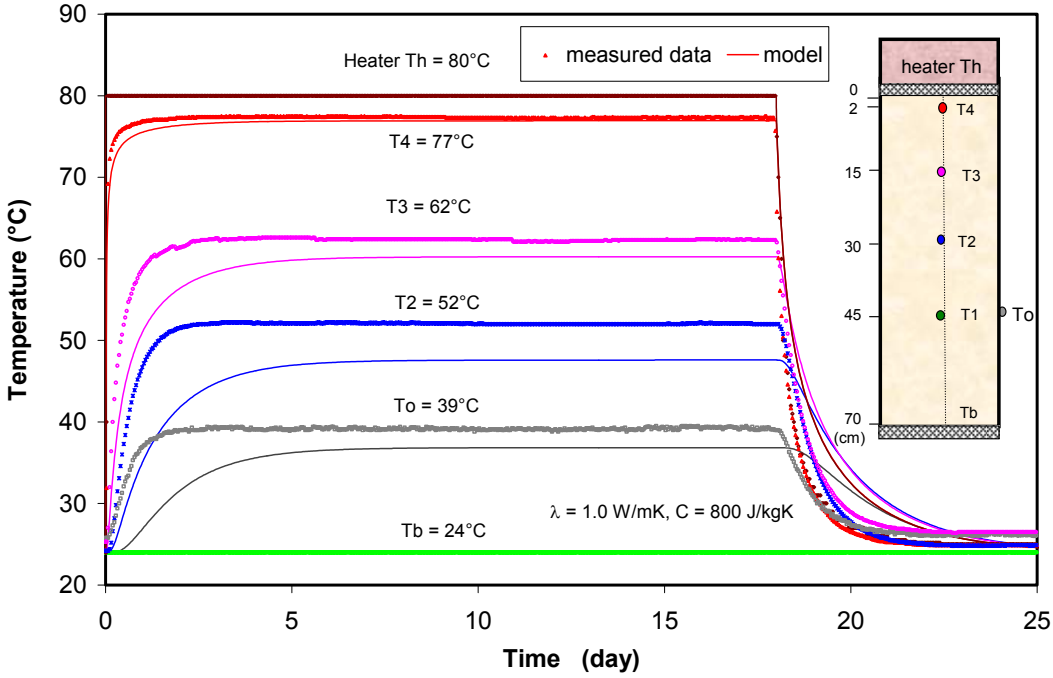

a. thermal conductivity of 1.7 $W \cdot m^{-1} \cdot K^{-1}$ and specific heat capacity of 800 $J \cdot kg^{-1} \cdot K^{-1}$

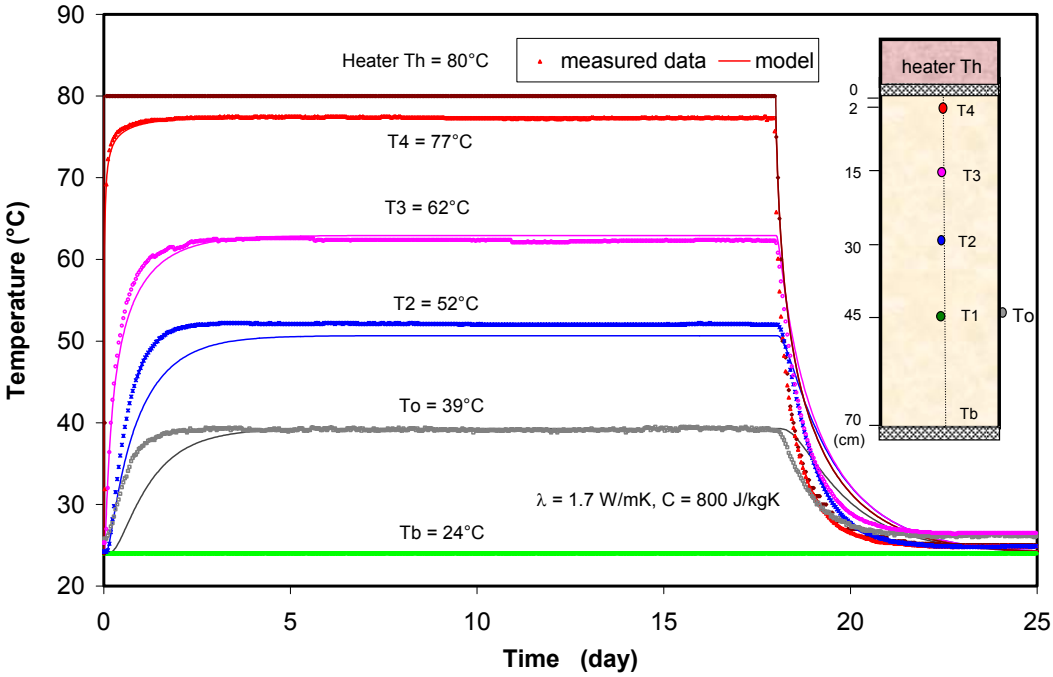

b. thermal conductivity of 2.1 $W \cdot m^{-1} \cdot K^{-1}$ and specific heat capacity of 800 $J \cdot kg^{-1} \cdot K^{-1}$

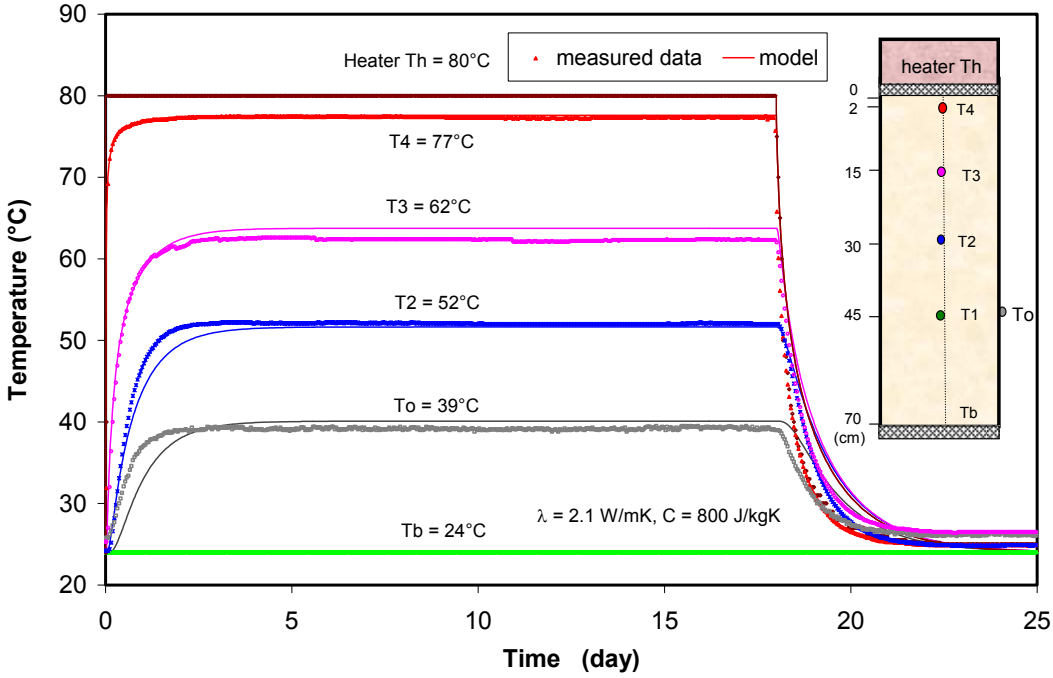

c. thermal conductivity of 1.0 $W \cdot m^{-1} \cdot K^{-1}$ and specific heat capacity of 800 $J \cdot kg^{-1} \cdot K^{-1}$

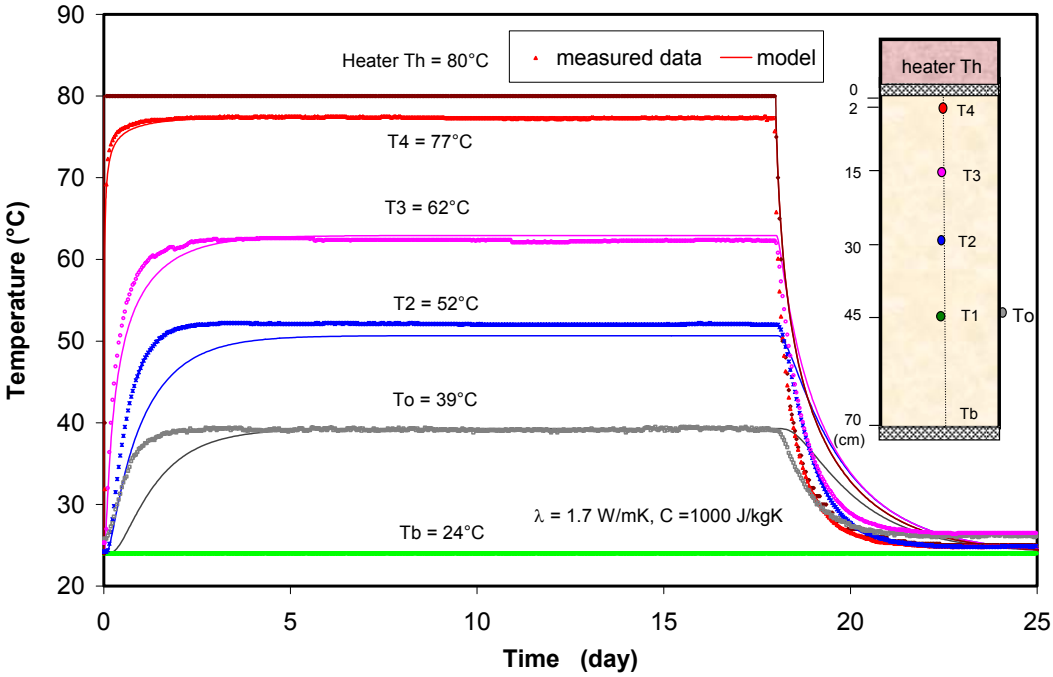

d. thermal conductivity of 1.7 $W \cdot m^{-1} \cdot K^{-1}$ and specific heat capacity of 1000 $J \cdot kg^{-1} \cdot K^{-1}$

Figure 4-9 Comparison of calculated and measured temperatures during the second mock-up heating test on a large Opalinus clay sample

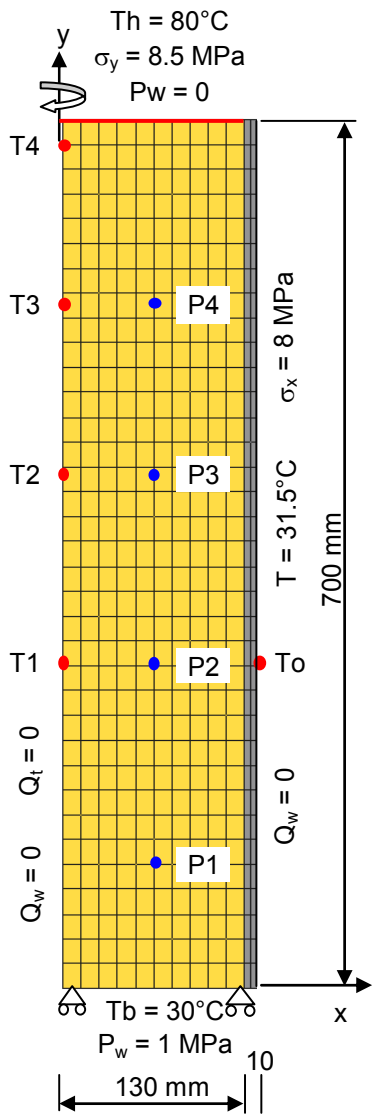

Calculation procedure:

Step 0: t = 0 day, initial conditions
temperature T = 24 °C
water pressure P_l = 0.1 MPa
gas pressure P_g = 0.1 MPa
vertical stress σ_z = 0.2 MPa
horizontal stresses $\sigma_x = \sigma_y$ = 0.2 MPa

Step 1: t = 0 – 3 days, loading
isotropic stress at boundaries $\sigma_x = \sigma_y$ = 0.85 MPa

Step 2: t = 3 – 4.5 days, loading and heating
radial stress σ_x = 3.1 MPa
axial stress σ_y = 3.6 MPa
temperature at boundaries T = 30 °C

Step 3: t = 4.5 – 10 days, water injection
pore water pressure P_l = 1.1 MPa

Step 4: t = 10 – 16 days, water back-pressures
P_{lt} = 0.1 MPa at the top
P_{lb} = 1.1 MPa at the bottom

Step 5: t = 16 – 30 days, loading
radial stress σ_x = 8.1 MPa
axial stress σ_y = 8.6 MPa

Step 6: t = 30 – 31 days, heating phase I
heater temperature T = 55 °C
T = 30 °C at the other boundaries

Step 7: t = 31 – 53 days, heating phase II
heater temperature T = 80 °C
T = 30 °C at the bottom
T = 31.5 °C at the periphery surface

Step 8: t = 53 – 58 days, cooling
heater temperature T = 30 °C
T = 30 °C at the other boundaries

Figure 4-10 Model geometry, calculation procedure, and conditions for coupled THM modelling of the first mock-up heating test

The mechanical parameters for the rubber jacket are taken from /LAX 67/ with elastic modulus E = 100 MPa and Poisson's ratio ν = 0.45. The jacket is assumed impermeable by using an extremely low permeability of k = $1 \cdot 10^{-25}$ m^2. Because the thermal conductivity of λ = 0.23 $W \cdot m^{-1} \cdot K^{-1}$ given in literature leads to an overestimation of the temperature in the model, a lower value of λ = 0.03 $W \cdot m^{-1} \cdot K^{-1}$ was used for the jacket. For the sample, the previously optimised thermal parameters of λ=1.7 $W \cdot m^{-1} \cdot K^{-1}$ and C = 800 $J \cdot kg^{-1} \cdot K^{-1}$ were used, whereas some other parameters were changed to examine their sensitivity. Typical modelling exercises are summarized in Table 4-6.

Table 4-6 Parameter values used for simulating the first mock-up heating test

Model	Young's modulus E_o (MPa)	Thermal expansion coefficient α_v (K^{-1})	Permeability k (m^2)
THM1	3300	$1.7 \cdot 10^{-5}$	$2 \cdot 10^{-20}$
THM2	3300	$1.5 \cdot 10^{-6}$	$2 \cdot 10^{-20}$
THM3	6680	$1.7 \cdot 10^{-5}$	$2 \cdot 10^{-20}$
THM4	3300	$1.5 \cdot 10^{-6}$	$1 \cdot 10^{-20}$
THM5	3300	$1.5 \cdot 10^{-6}$	$3 \cdot 10^{-20}$

Figure 4-11 compares the calculated and measured temperatures at the different measurement locations in the sample. An excellent agreement is obtained for all positions, confirming the thermal parameters of λ = 1.7 $W \cdot m^{-1} \cdot K^{-1}$ and C=800 $J \cdot kg^{-1} \cdot K^{-1}$. However, there is a remaining uncertainty regarding the low λ-value used for the jacket.

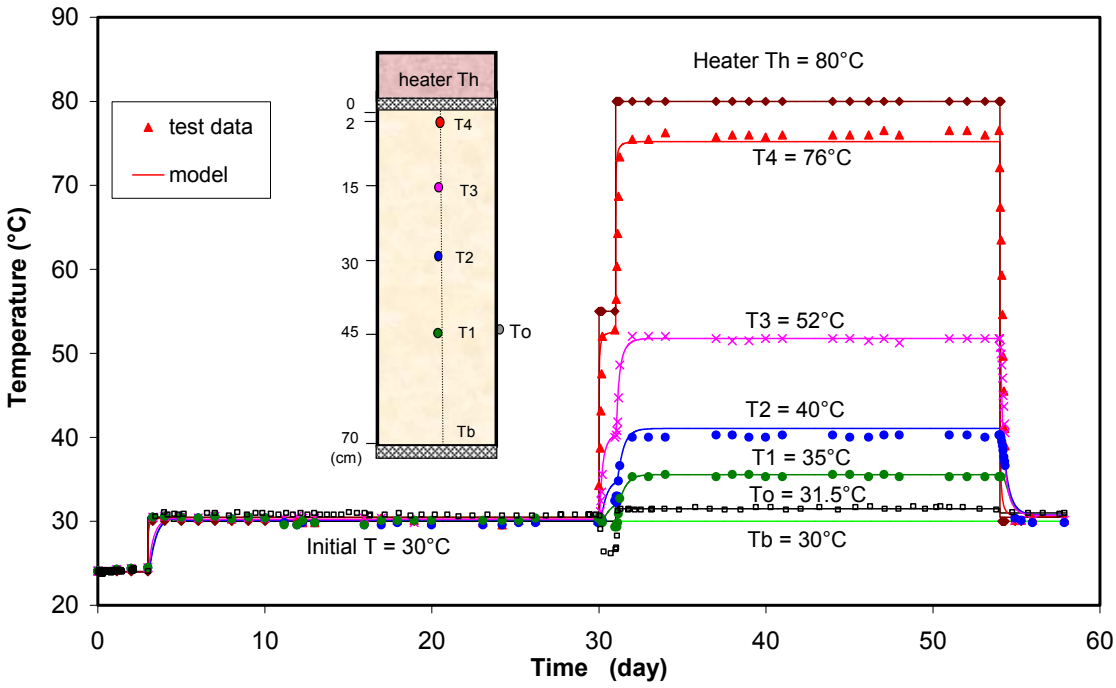

Figure 4-11 Comparison of calculated and measured temperature data in the first mock-up heating test

In Figures 4-12 and 4-13, the measured axial and radial strains are compared with the results calculated with different parameters. Figure 4-12 shows that model THM3 with a high E_o–value of 6680 MPa which is estimated for the intact rock provides a relatively low axial compression at each stress increase, while the low value of E_o = 3300 MPa in models THM1 / THM2 fits the strain quite well. The low elastic stiffness of the sample might be due to the disturbance introduced by sampling and instrumentation. It is also obvious that these models can not well represent the large axial extension due to the water injection to the end faces of the sample. This indicates that the parameter $k_s = 4 \cdot 10^{-5}$ in the BBM model, which controls the swelling/shrinking behaviour, is underestimated when using the literature based data (Fig. 4-3). Neglecting this large swelling effect by moving the modelling curves (THM1 / THM2) down to the measured level, the axial strain evolution recorded before heating is well represented by the modified curves THM1c and THM2c. The following thermal expansion by heating is also underestimated by all the models. This discrepancy might be due to the large thermal expansion of the water in the porous discs at the sample's top and bottom and the upper load piston. These test conditions are not taken into account in the modelling. The subsequent gradual evolution of the axial strain during the heating phase is very well represented by the models. Finally, the thermal contraction by cooling is also underestimated by the models due to the same reason mentioned above.

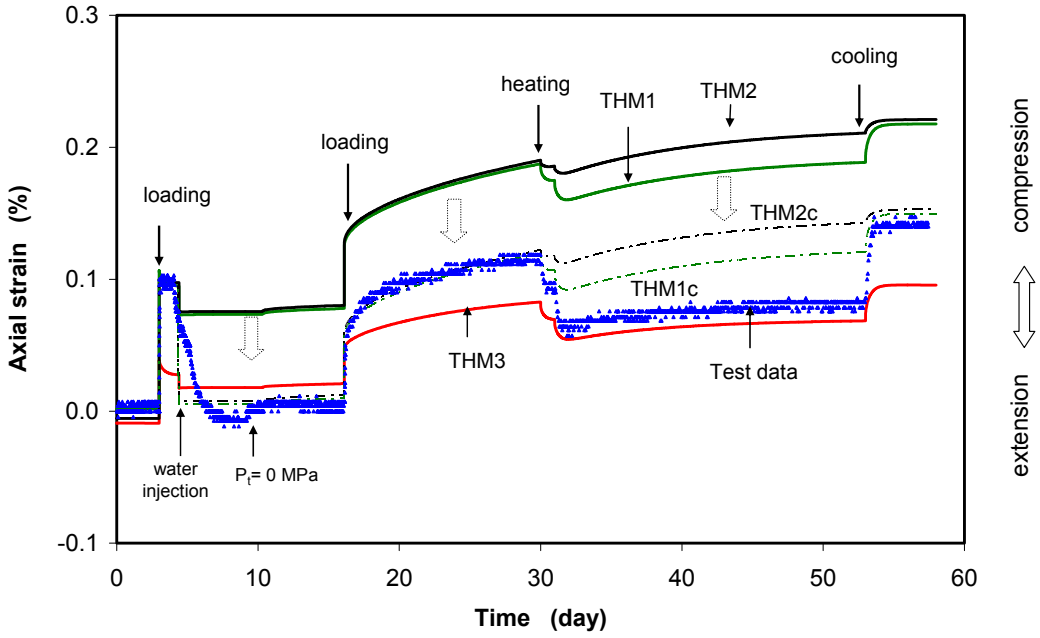

Figure 4-12 Calculated and measured axial strain during the first mock-up heating test on a large Opalinus clay sample

Figure 4-13 shows that the modelling results of the radial strain are only qualitatively comparable with the measurements. The large radial deformation observed in the test is probably due to closing and opening of the pre-existing fractures which were more oriented along the sample axis. The fractures are not considered in the models. However, the magnitudes of the thermal expansion by heating and the contraction by cooling are reasonably predicted.

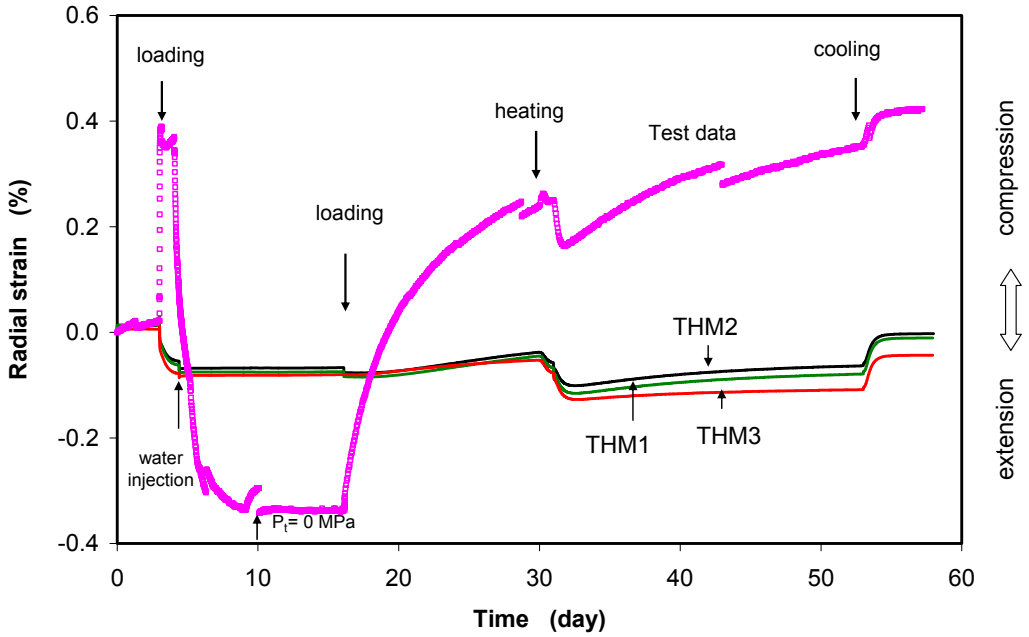

Figure 4-13 Calculated and measured radial strain during the first mock-up heating test on a large Opalinus clay sample

The pore-water pressures recorded at the different locations in the large sample are modelled by using different permeability values of k = $1 \cdot 10^{-20}$, $2 \cdot 10^{-20}$ and $3 \cdot 10^{-20}$ m^2. Figure 4-14 compares the modelling results and the measured pore pressure data. It is obvious that the pressure increments at P_2 and P_3 due to the mechanical loading are well represented by these models, but not at P_1, which is due to the local damage there. The subsequent pressure drops are differently predicted by the different k-values. The lower k-value of $1 \cdot 10^{-20}$ m^2 (THM4) results in a slow pressure drop, and conversely the higher k-value of k = $3 \cdot 10^{-20}$ m^2 (THM5) leads to a sharp pressure reduction. The mean value of k = $2 \cdot 10^{-20}$ m^2 (THM2) fits the pressure drop rates relatively well.

The thermally-induced pore-water over-pressures to 0.2 - 0.6 MPa are well captured by the models with computed values of 0.1 - 0.5 MPa. The further pressure reduction

during the heating phase shows large differences between the model and the observation. Furthermore, the cooling-induced pressure drop rates are also largely overestimated by the model at P_2 and P_3, whereas a good match is achieved at P_1.

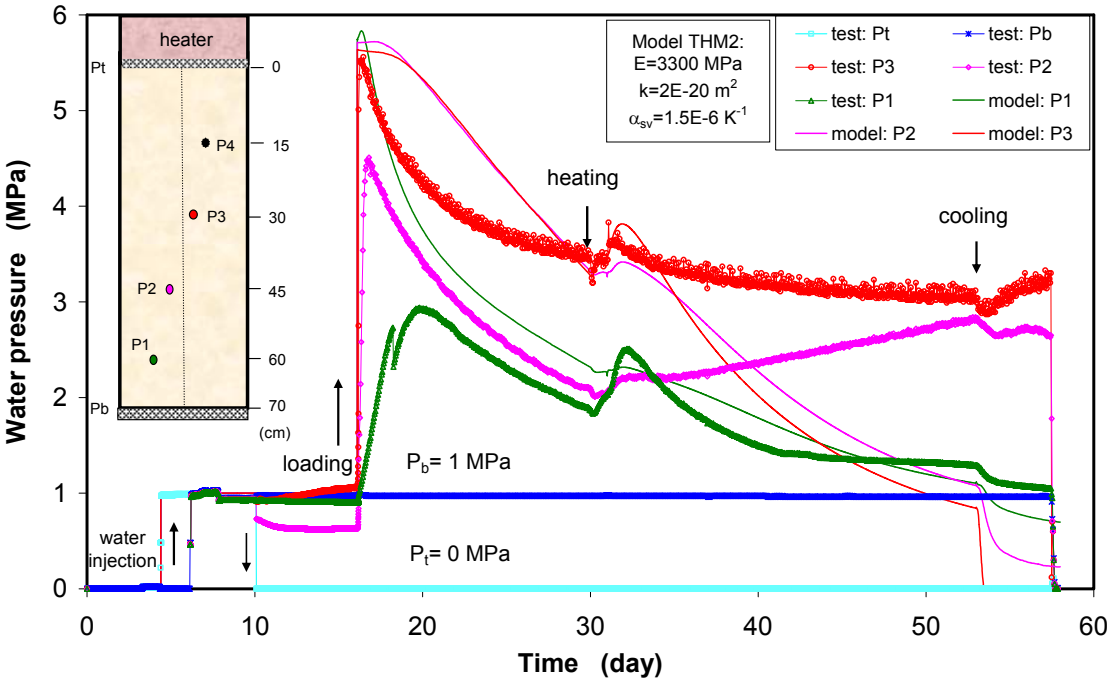

THM2: permeability k = $2 \cdot 10^{-20}$ m^2

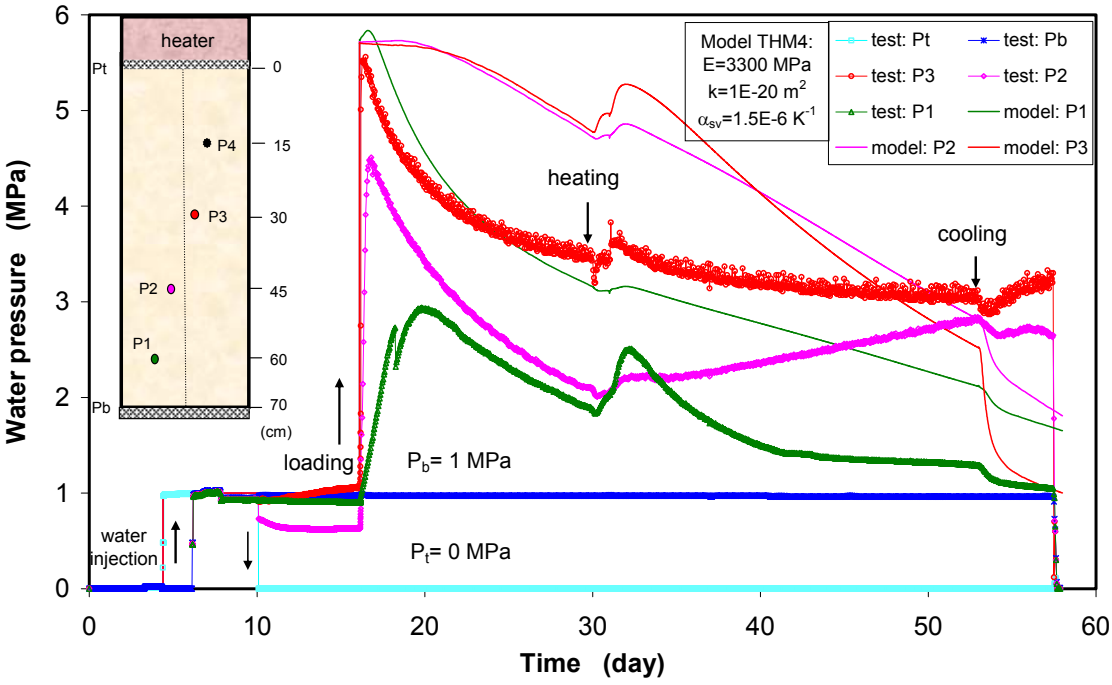

THM4: permeability k = $1 \cdot 10^{-20}$ m^2

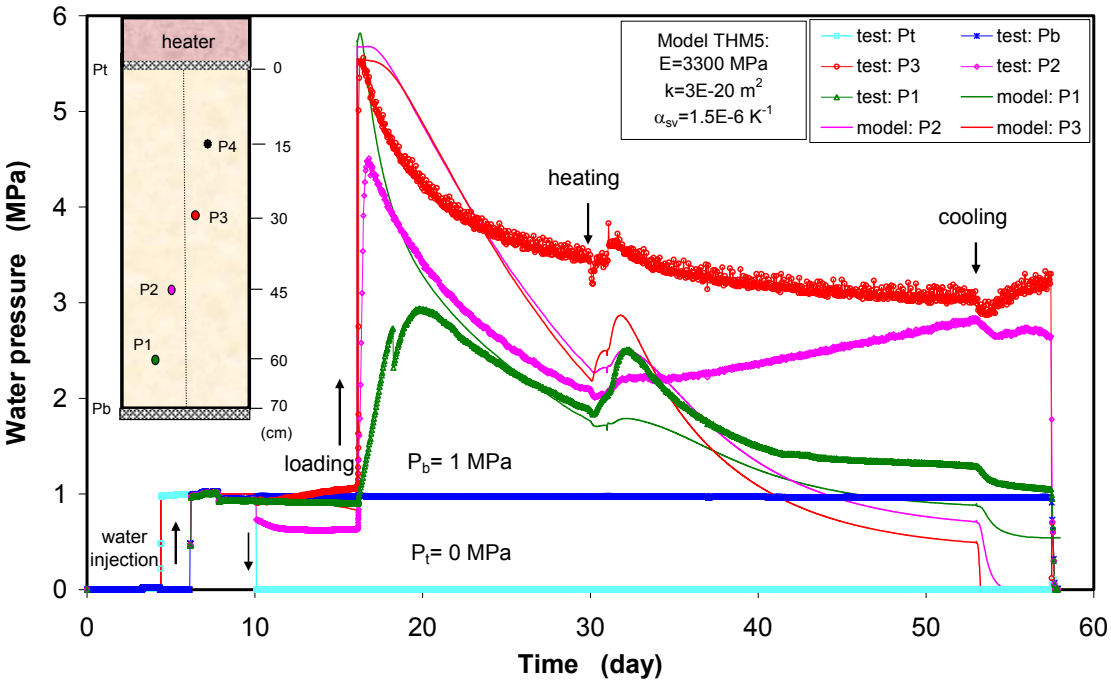

THM5: permeability k = $3 \cdot 10^{-20}$ m^2

Figure 4-14 Calculated and measured pore-water pressure during the first mock-up heating test on a large Opalinus clay sample

Based on the comparisons between the calculated and measured temperatures, deformations and pore-water pressures in the large Opalinus clay sample during the mock-up heating tests, some key parameters are estimated as average properties of the clay rock:

- thermal conductivity λ = 1.7 $W \cdot m^{-1} \cdot K^{-1}$
- specific heat capacity C = 800 $J \cdot kg^{-1} \cdot K^{-1}$
- linear thermal expansion coefficient for the solid grains $\alpha_s = 1.5 \cdot 10^{-6}$ K^{-1}
- linear thermal expansion coefficient for the rock mass $\alpha_m = 1.7 \cdot 10^{-5}$ K^{-1}
- initial elastic modulus E_o = 6680 MPa for the intact rock
- initial elastic modulus E_o = 3300 MPa for the disturbed rock
- intrinsic permeability k = $2 \cdot 10^{-20}$ m^2.

4.4 Scoping Calculation for the Design of the in-situ Experiment

In order to ensure a successful conduction of the envisaged in-situ experiment, its design was carefully performed with support of pre-operational calculations. One of the objectives was to identify the test field conditions after excavation and ventilation of the gallery Ga98 and the MI niche. By this, the positions of the heater equipment and measuring instruments were chosen.

The heater equipment was installed in a horizontal borehole parallel to the MI niche (Figure 4-15). To ensure the heater to be positioned in a undisturbed zone in the shaly facies but far away from the sandy facies, a reasonable distance of the borehole to the niche wall was required. This problem was solved by numerical analysis of the hydro-mechanical processes in the rock that took place after excavation and during ventilation of the MI niche.

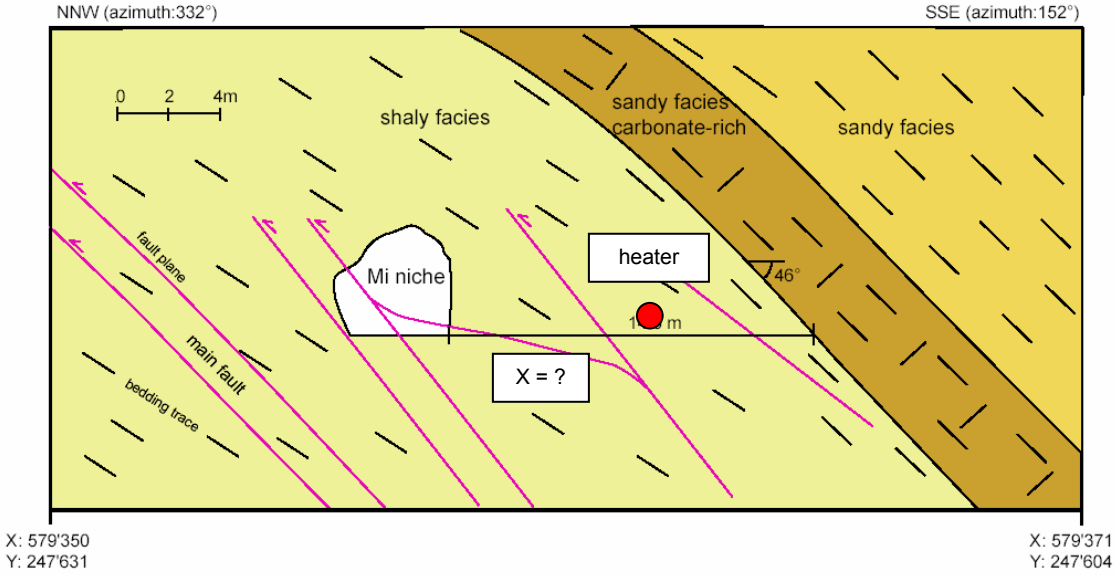

Figure 4-15 Geological situation of the HE-D test field in a cross section normal to the MI niche

The MI niche with an irregular cross section of about 4.5 m width and 4 m height was excavated and then ventilated over 6 years. In the modelling, the geometry of the niche is simplified by a circular section with a radius of 2.5 m. The 2D modelling region extends by 50 m x 50 m. The clay rock is assumed isotropic and homogeneous. Based on the in-situ conditions at the MTRL mentioned in section 2.2, the boundary and initial conditions for the modelling are defined, as shown in Figure 4-16. The temperature in

the rock and drift is 15 °C. A vertical stress of 6.0 MPa applied on the top boundary and the effect of gravity result in an initial vertical stress equal to 7.3 MPa at the drift level (y = 0), while a constant horizontal stress of 4.8 MPa is assumed. A water pressure of 1.6 MPa supplied to the top boundary and the effect of gravity produces a water pressure of 2.1 MPa at the drift level. Any water flow through the other boundaries is not allowed. The drift excavation is simulated in one step by reducing the normal stress of 4.8 MPa on the drift wall to zero. After that, the drift is ventilated by air flowing with a relative humidity of 85 % along the wall for 6 years, leading to diffusive vapour flow from the rock. The turbulence coefficient of 10^{-4} m/s is employed for the wall surface. The parameters established by the back-calculations of the laboratory mock-up heating tests (section 4.3) are used.

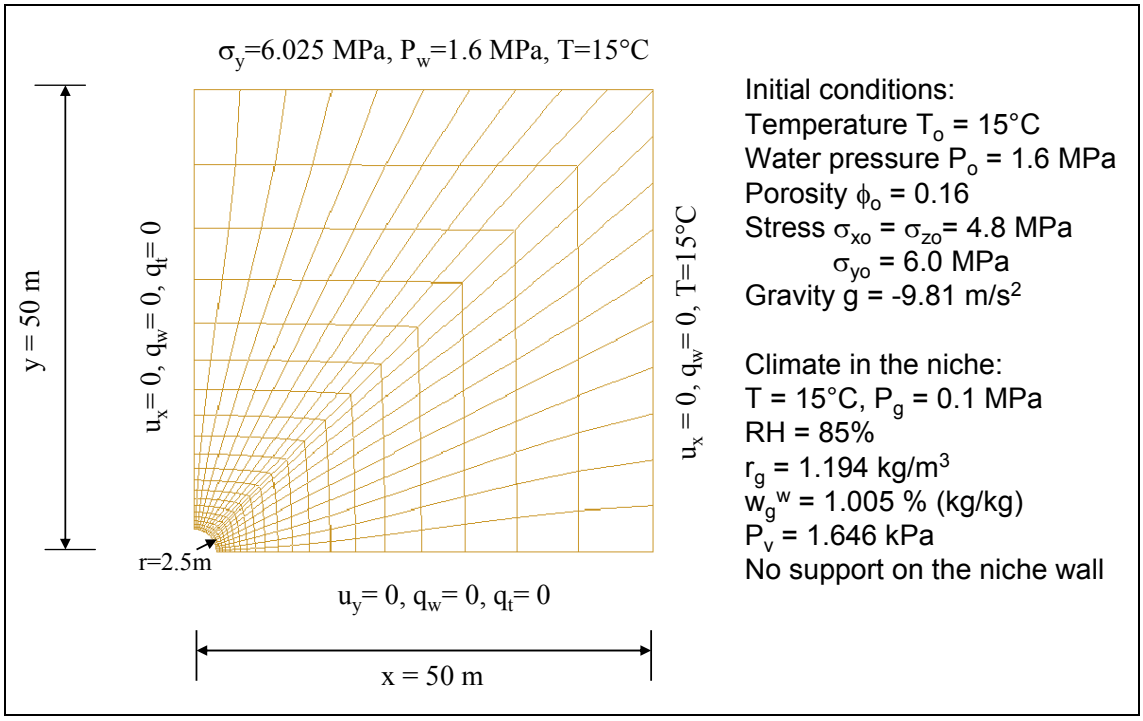

Figure 4-16 Model geometry and boundary conditions applied to the rock mass around the MI niche

Figure 4-17 illustrates the modelling results of the horizontal and vertical stresses (Fig. 4-17a) and the radial displacement (Fig. 4-17b) along the radial axis. After the drift excavation, the horizontal stress near the drift wall relieves, while the vertical stress increases up to 14 MPa. The stress changes lead to a drift convergence of up to 5 mm. In the far-field over about 10 m from the wall, the stress state remains relatively stable,

but deformation increases steadily with time. Due to the increase of stiffness by de-saturation, the convergence near the wall ceases.

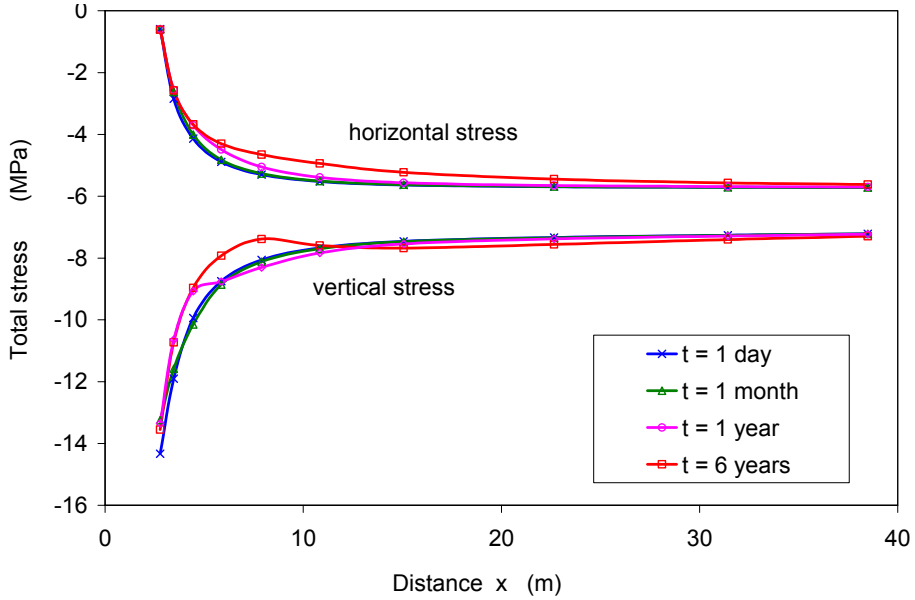

a. horizontal and vertical stresses along the x – axis

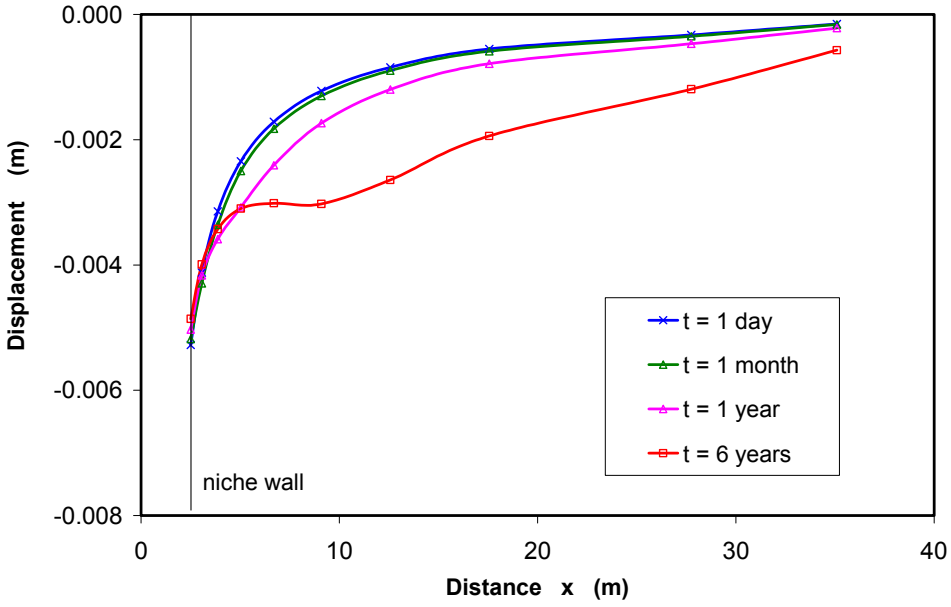

b. radial displacement along the x – axis

Figure 4-17 Evolution and distribution of the stresses and radial displacement

Figure 4-18 compares the calculated stress states at different distances to the niche wall with the yield locus. The stresses in the near-field within a radius of about 1.3 m attain the yield limit. That means this zone is damaged. In the far region beyond the

radius of about 8 m, the stress states are far away from the yield limit, i.e. the rock mass in the far region is less disturbed.

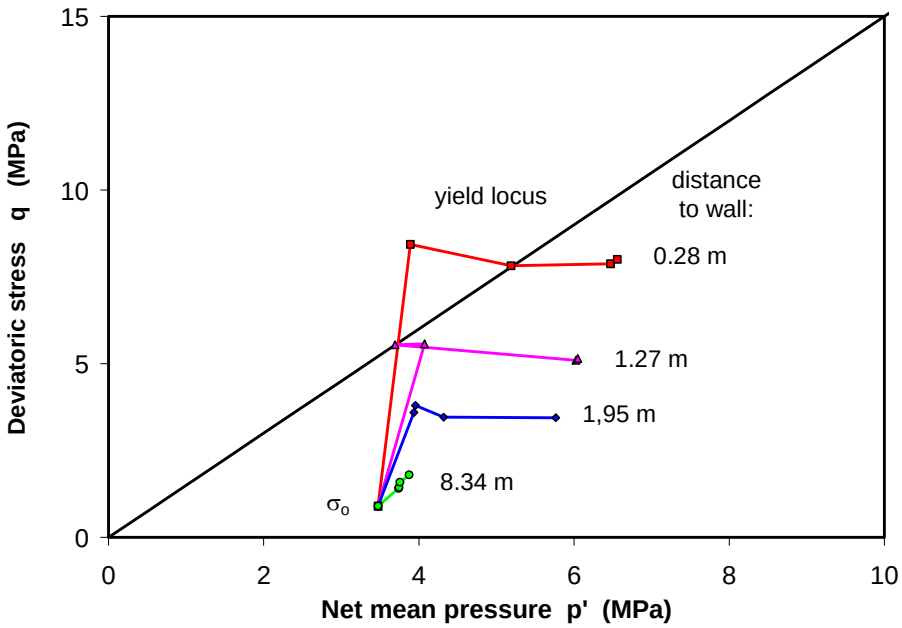

Figure 4-18 Examination of the damaged zone around the MI niche

Figure 4-19 shows the prediction of the pore-water pressure distribution along the radial distance to the niche in comparison with measurement results obtained around several drifts in the MTRL /THU 99/, /HEI 04/. Generally, the pore-water pressure in the less or undisturbed far-field is higher than in the disturbed zone. Because of the complicated geological and geohydraulic boundary conditions, the inhomogeneity of the rock mass, the drift excavation techniques applied and the duration of ventilation, the pore pressure distribution differs from one location to another. The pore pressures measured by GRS in the HE-D test field (BHE-D08-17) are somewhat lower than the predicted values, but the pattern is qualitatively well matched by the model. The overestimation may be due to the fact that the ventilation effect of the adjacent drift Ga98 near the test field (Figure 2-2) is not considered in the model. The calculated negative values of pore-water pressure indicate that the rock with an extension to about 5 m from the niche wall might be de-saturated.

Taking into account the predictions before testing, it was decided to install the heater equipment in the saturated and less disturbed area at a distance of 8 m from the niche wall.

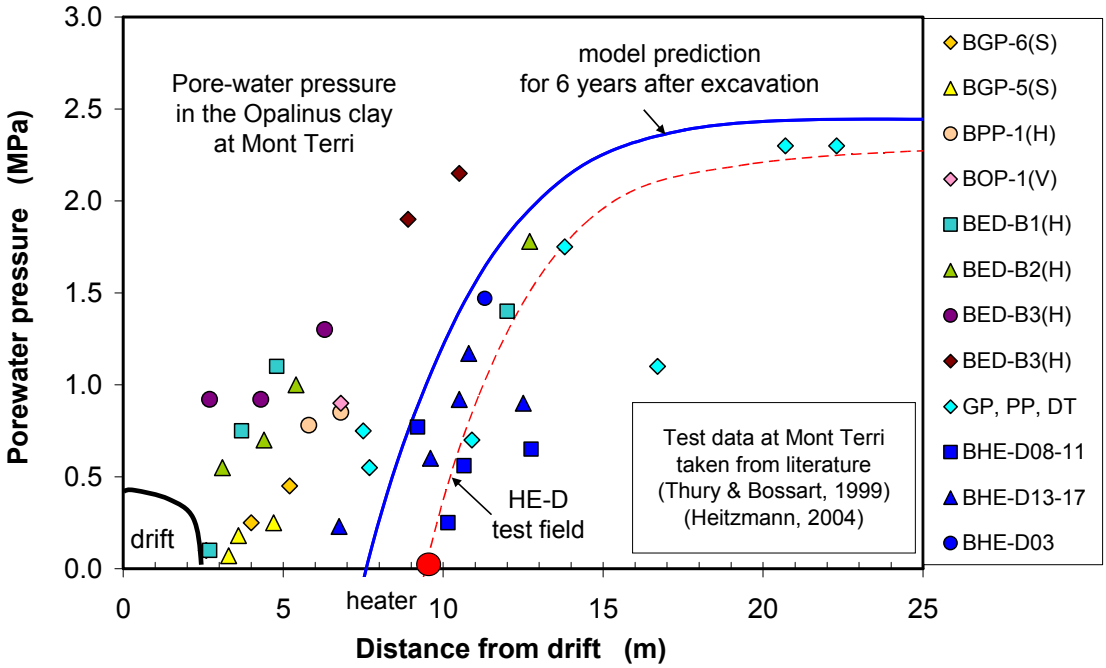

Figure 4-19 Comparison between model prediction and the measurements of the pore-water pressure in the clay rock around the MI niche in the MTRL

4.5 Simulation of the in-situ Heating Experiment

The final modelling task was to simulate the in-situ heating experiment for the analysis of the complex THM processes taking place in the test field. The other purpose of the modelling is to validate the applied models by comparing the calculations with the measurements. It is to be noted that before and during the experiment proceeding, predictive calculations were already performed and the results of which reported in /WIL 03; 05/, /KUL 05/, /ZHA05; 06/. In this report only the final modelling results are presented.

4.5.1 Assumptions

The simulations are performed by solving the set of balance equations of energy, solid mass, water mass, air mass and stress equilibrium in a coupling way (section 4.2). The major assumptions are made for the THM coupled calculations:

- Heat transport includes conduction (Fourier's law) through the porous medium, advection of liquid water and vapour flow.

- Water transport is controlled by liquid water advection (Darcy's law), vapour diffusion in air (Fick's law), and liquid / gas phase changes (psychrometric law).
- Flow of dry air due to air pressure gradient (Darcy's law) and dissolved air in the liquid phase (Henry's law).
- A thermo-elasto-plastic model is used for the description of the mechanical behaviour of the clay rock with the main features of thermal expansion and contraction, swelling and shrinking.
- As mentioned before, the clay rock is assumed isotropic and homogeneous and the parameters established by the back-calculations of the laboratory mock-up heating experiment are applied.

4.5.2 Model and Conditions

The complicated geometry of the test field (Figure 2-5) is simplified by an axisymmetric model of 25 m length and 8 m radius, as shown in Figure 4-20. In fact, this model represents a cylindrical rock mass with the axis along the heater borehole. The upper part of 9.5 m length is confined by the surrounding rock, while the lower part of 15.5 m length is bounded either by the drift walls or by the surrounding rock. Effects of both assumed boundary conditions are examined in the modelling. The heater borehole is sized by a diameter of 0.3 m and a total length of 15.5 m, which is lined with a metal tube of 10 m length, two heaters of 2 m length each, two heater-caps and a heater-link, each with length of 0.75 m (see section 2.4).

The in-situ prevailing conditions are applied to the initial state of the rock before the test. The initial temperature is 15 °C. An isotropic stress of 4.8 MPa is assumed, which is obtained by averaging the stress components (σ_1 = 6 - 7 MPa, σ_2 = 4 - 5 MPa, σ_3 = 2 - 3 MPa). While a pore-water pressure of 2.2 MPa is adopted for the upper part of the rock, a linear pressure distribution along the length of the lower part is assumed from 1.2 MPa at the top to 0.2 MPa at the bottom in order to match the pore-water state in the test field. The atmospheric gas pressure is set to 0.1 MPa.

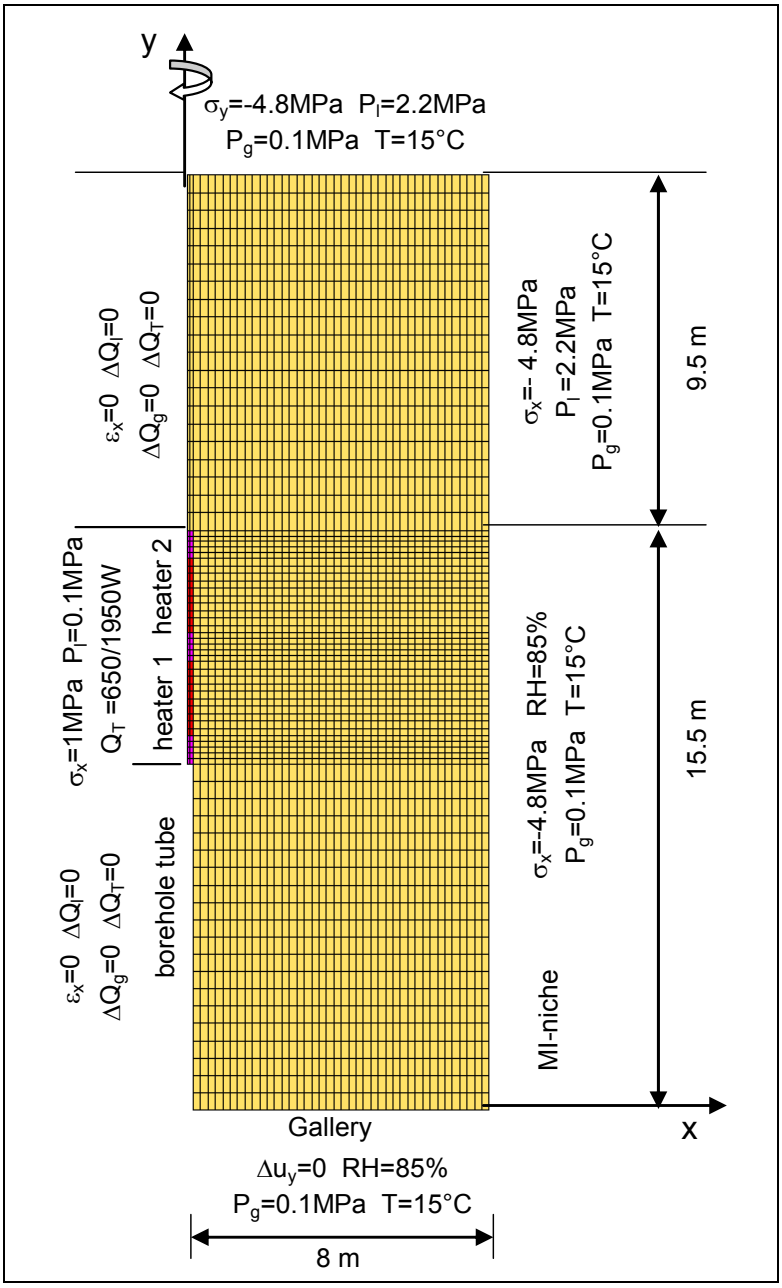

Figure 4-20 Axisymmetric model for simulating the in-situ heating experiment

4.5.3 Calculation Sequence

The whole procedure of the in-situ experiment, including the drilling and support of the heater borehole, the two heating phases, the failure of the heater-packers, the power interruption, and the cooling phase, is simulated by sequential calculation steps with application of reasonable boundary conditions. Figure 4-21 shows the calculation sequence together with the power supply and the packer inflation pressure.

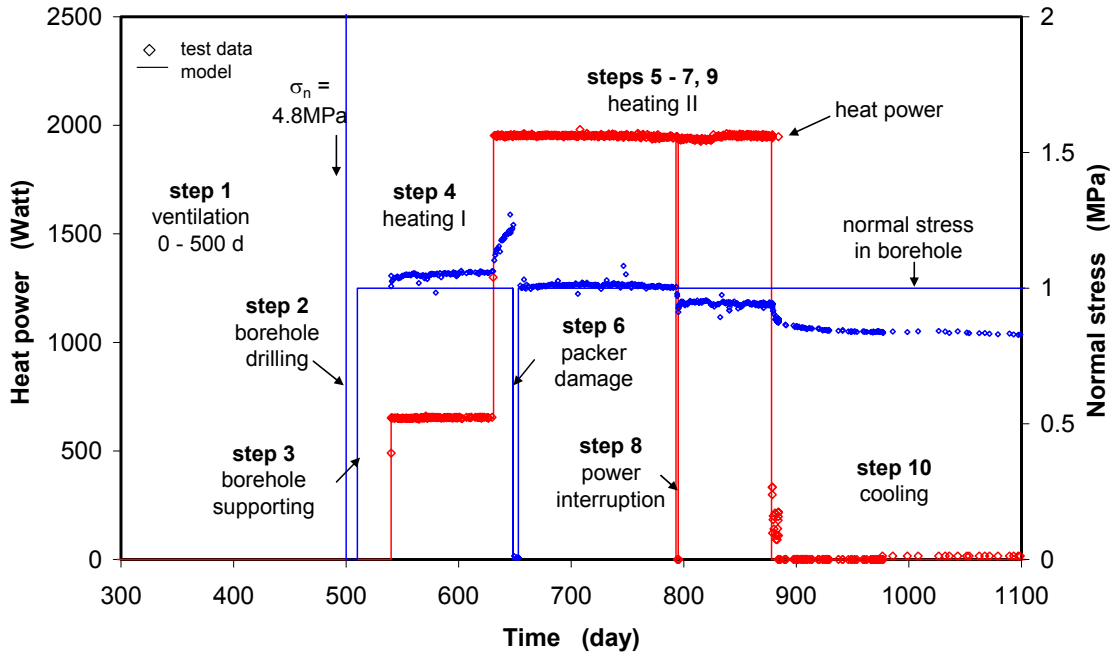

Figure 4-21 Calculation sequence for modelling the in-situ heating experiment

Details of the calculation steps are also given in Table 4-7. In addition to this reference case, some other aspects such as the effects of different boundary conditions and parameters are also examined. The following points of the modelling are to be noted:

- Step 1 of the ventilation of the opened boundaries over 500 days aims at gaining a similar initial pore-water pressure distribution as observed in the test field.
- A drained condition for the borehole wall is assumed by fixing the water pressure of P_l = 0.1 MPa. In fact, although the borehole was carefully sealed with the tube and also by the inflated packers, a certain roughness of the interface remained, which allows water flow. Additionally, an undrained condition for the borehole wall is also examined.
- 91 % of the total heat power (650 W and 1950 W for the first and second heating phase, respectively) is attributed to the two heaters and the heater link, and the rest of 9 % is attributed to the heater-caps, whereby considering the construction of the heater equipment (section 4.4).
- Influences of parameters such as thermal conductivity, thermal expansion coefficient and intrinsic permeability are studied again in the modelling of the in-situ heating experiment.

Table 4-7 Calculation steps and corresponding boundary conditions for modelling the in-situ heating experiment

Step 0: t = 0 days, application of initial conditions temperature T = 15 °C, isotropic stress $\sigma_z = \sigma_x = \sigma_y$ = 4.8 MPa, atmospheric gas pressure P_g = 0.1 MPa, water pressure P_l = 2.2 MPa to the upper part, and a linear distribution of the water pressure is applied to the low part from P_l = 1.2 MPa at the top to 0.2 MPa at the bottom.
Step 1: t = 0 – 500 days, ventilation of the gallery G98 and the MI niche temperature T = 15 °C, ventilation by air flow with relative humidity of RH = 85% and a turbulence coefficient of 10^{-5} m/s at a pressure P_g = 0.1 MPa, null displacement on the wall of the Gallery, stress $\sigma_z = \sigma_x = \sigma_y$ = 4.8 MPa on the M-niche wall.
Step 2: t = 500 – 510 days, drilling of the heater borehole the borehole is excavated by moving away the elements, a water pressure of P_l = 0.1 MPa is applied to the borehole wall.
Step 3: t = 510 – 540 days, installation of the heater borehole a normal stress of σ_n = 1.1 MPa is applied on the borehole wall (packer-inflation), whereas the tube installation is simulated by applying a null displacement to the wall. A drained boundary condition for the borehole wall is assumed by application of a fixed water pressure of P_l = 0.1 MPa.
Step 4: t = 540 – 631 days, heating phase I the total power of 650 W is attributed to the heater equipment by imposing a heat flux of 125 W/m to both heater/rock interfaces with a length of 2x2 + 0.75 m (91% of the total power) and 37.5 W/m to the heater caps with a length of 2x 0.75 m.
Step 5: t = 631 – 648 day, heating phase II The total power of 1950 W is attributed to the heater equipment by imposing a heat flux of 365 W/m to both heater/rock interfaces with a length of 2x2 + 0.75 m (91% of the total power) and 144.2 W/m to the heater caps with a length of 2x 0.75 m.
Step 6: t = 648 – 653 day, damage of the heater-packer the damage of the heater-packer is simulated by reduction of the normal stress on the borehole wall down to zero.
Step 7: t = 653 – 793 day, Re-inflation of the packer The packer pressure was reapplied to 1.1 MPa during heating phase II.
Step 8: t = 793 – 795 day, interruption of power supply a constant heat flux of 0 W/m was applied to the heater/rock interface.
Step 9: t = 795 – 878 day, restart of heating the conditions applied for step 7 are adopted again for this step.
Step 10: t = 878 – 1100 day, cooling phase a constant heat flux of 0 W/m was applied to the heater/rock interface.

4.5.4 Results

The modelling results are compared with the measurement data of temperature, pore-water pressure and deformation and the THM phenomena observed during the experiment are analyzed with the support of the modelling results.

4.5.4.1 Temperature

The thermal results are obtained by using the optimized thermal parameters of λ = 1.7 $W \cdot m^{-1} \cdot K^{-1}$ and C = 800 $J \cdot kg^{-1} \cdot K^{-1}$. First, the modelling results of the temperatures at the interfaces between heater 1 / 2 and the rock are compared with the measured data in Figure 4-22. The first heating with a power of 650 Watts generated an increase of the temperature from 15 °C to 43 °C over the first 3 months. The following heating with a power of 1950 Watts led to different maximum temperatures of 102 °C at heater 1 and 105 °C at heater 2 over other 8 months. However, the maximum temperature of up to 110 °C is reached at the heater-link. Generally, the temperature rise at the heater/rock interfaces is very fast in the first days of each heating and then slows down gradually. The interruption of the power supply caused a rapid reduction of the temperature. Also after switching off the heaters, the temperature dropped rapidly down in the first days and then tended to the ambient temperature. It is obvious that the temperatures at the heater/rock interfaces are very well revealed by the model, only slightly over-predicted by $\Delta T \leq 5$ °C at heater 1 in the second heating phase.

The temperatures at the other 30 measuring positions are computed and compared with the measured data in Figure 4-23. One can see that most of the calculated curves match to the measured curves very well. The differences between them are less than 3 °C. Only at a few positions (HEDB01TEM3/4, BHE-DT10, B24TEM1) the differences are overestimated by 4 - 6 °C. In borehole HEDB06, the sensors provided relatively low initial values of 11 - 13 °C compared to ~15 °C measured at the other positions. Neglecting these initial differences, the calculated temperature increments are in a good agreement with the observations. Generally, the temperature evolution and distribution in the test field is excellently represented by the model.

Figure 4-24 shows an overview of the temperature field calculated at the ends of both heating phases. The heated zone (T > 17 °C) around the heaters extends to 3 m and 6.5 m after the first and second heating phase, respectively.

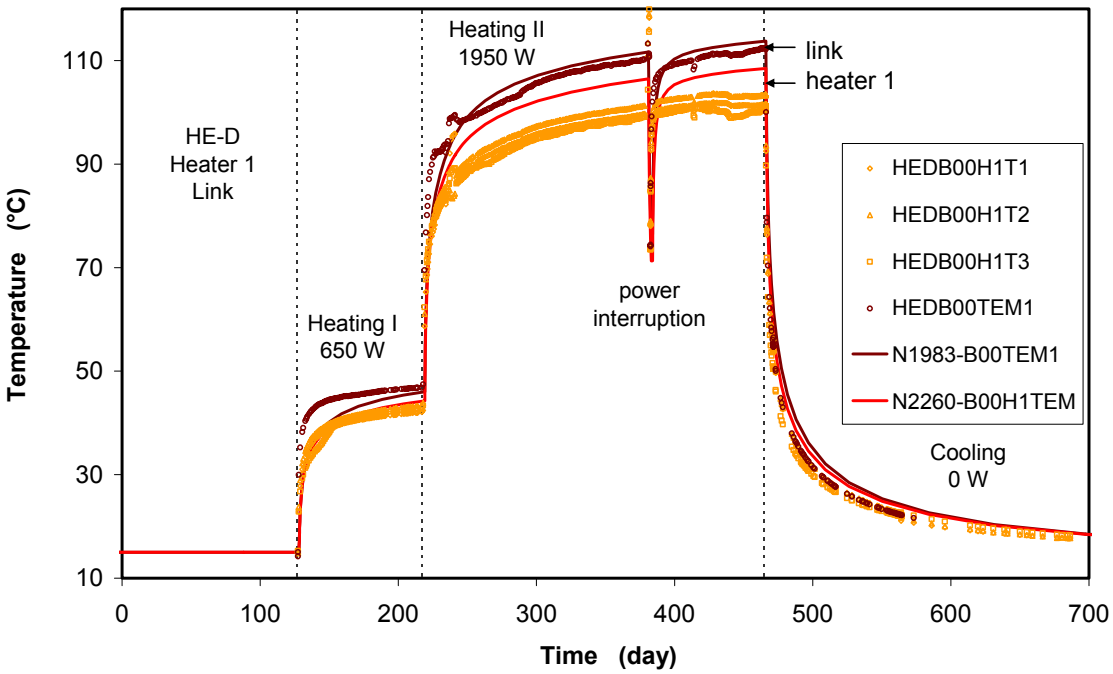

a: heater 1

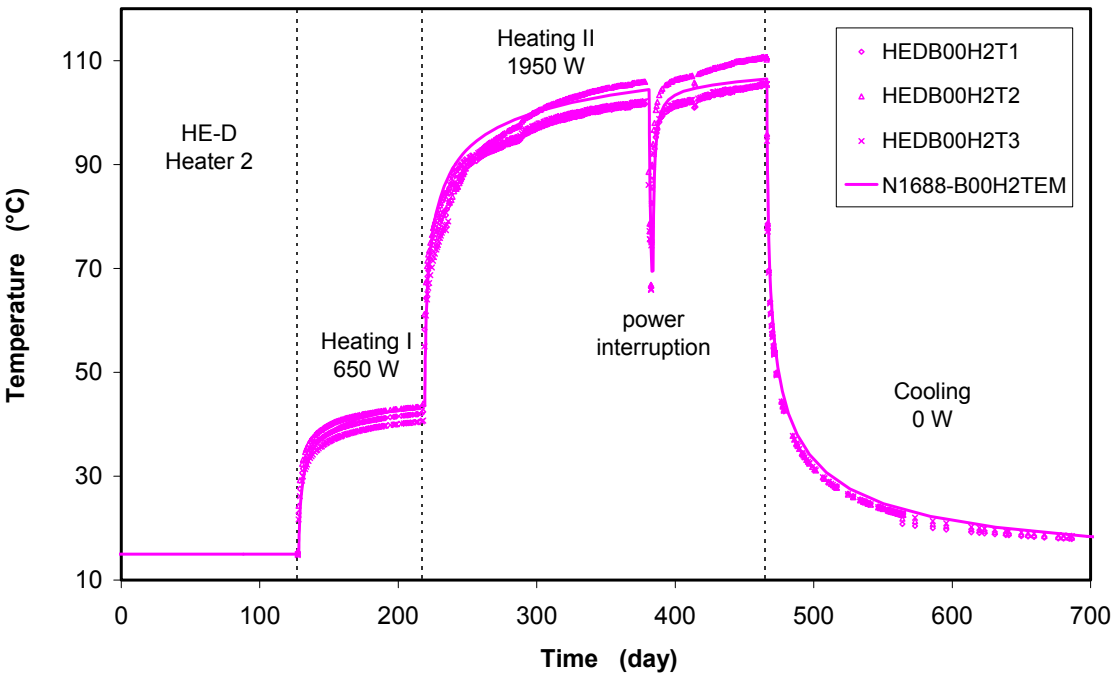

b: heater 2

Figure 4-22 Temperature evolution measured and calculated at the heater/rock interface

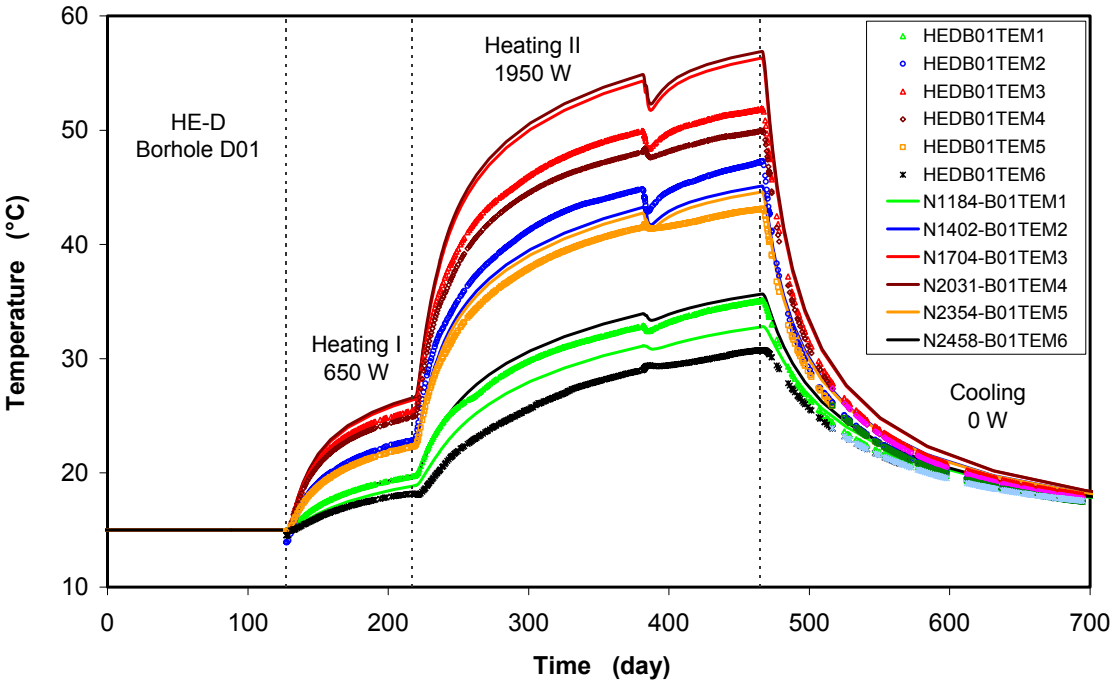

a. BHE-D01

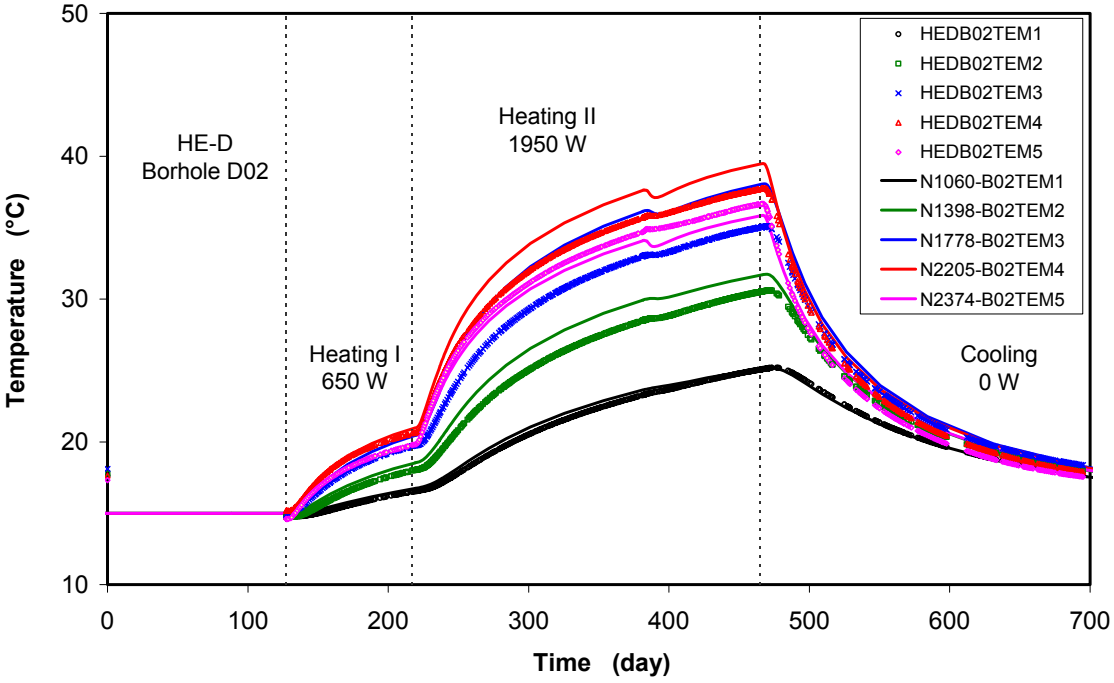

b. BHE-D02

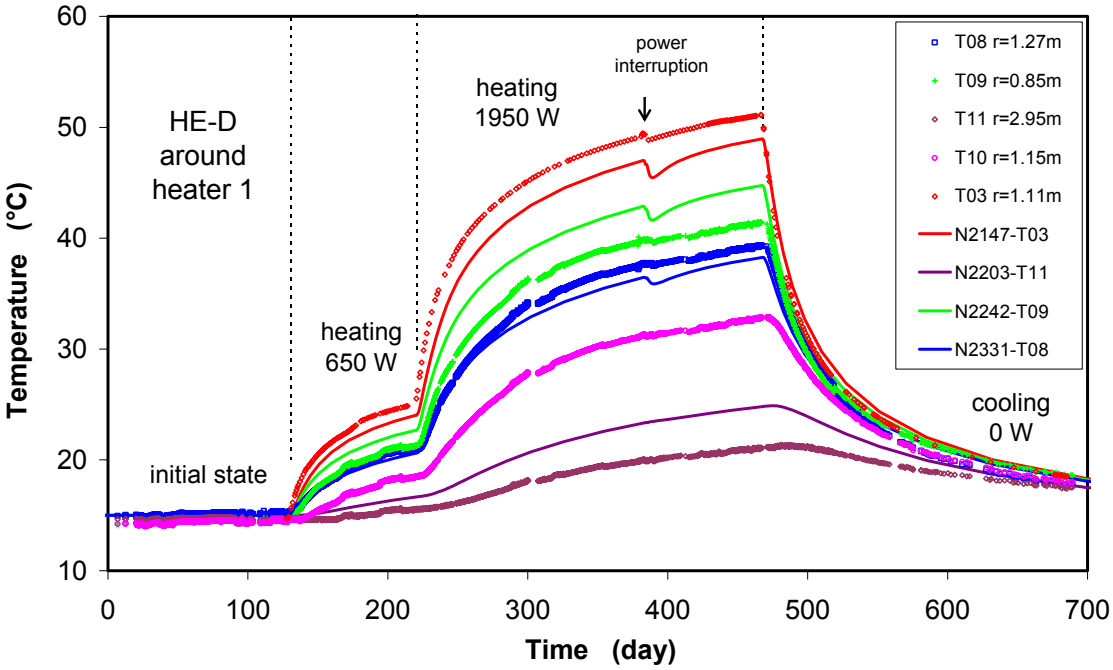

c. BHE-D03, D8 to D11

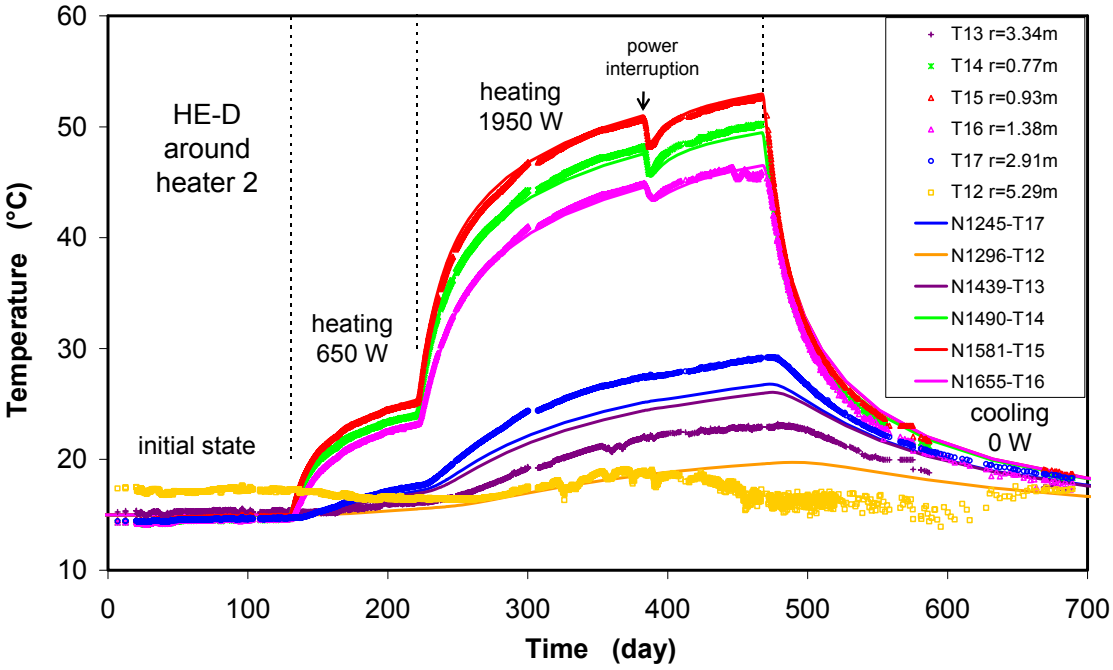

d. BHE-D12 to D17

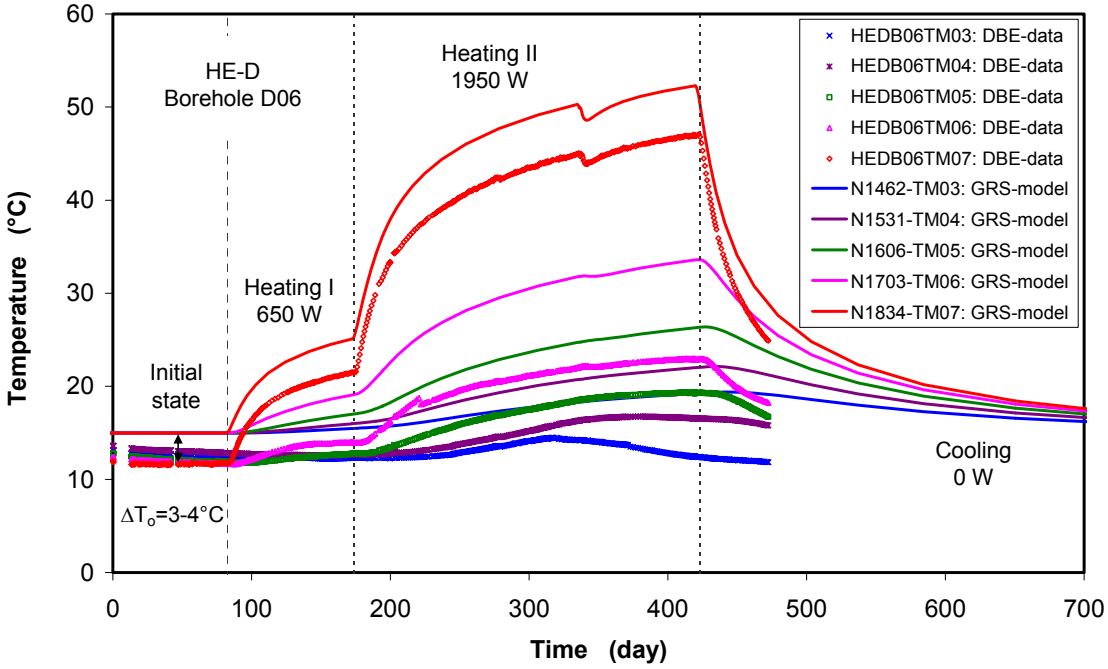

e. BHE-D06

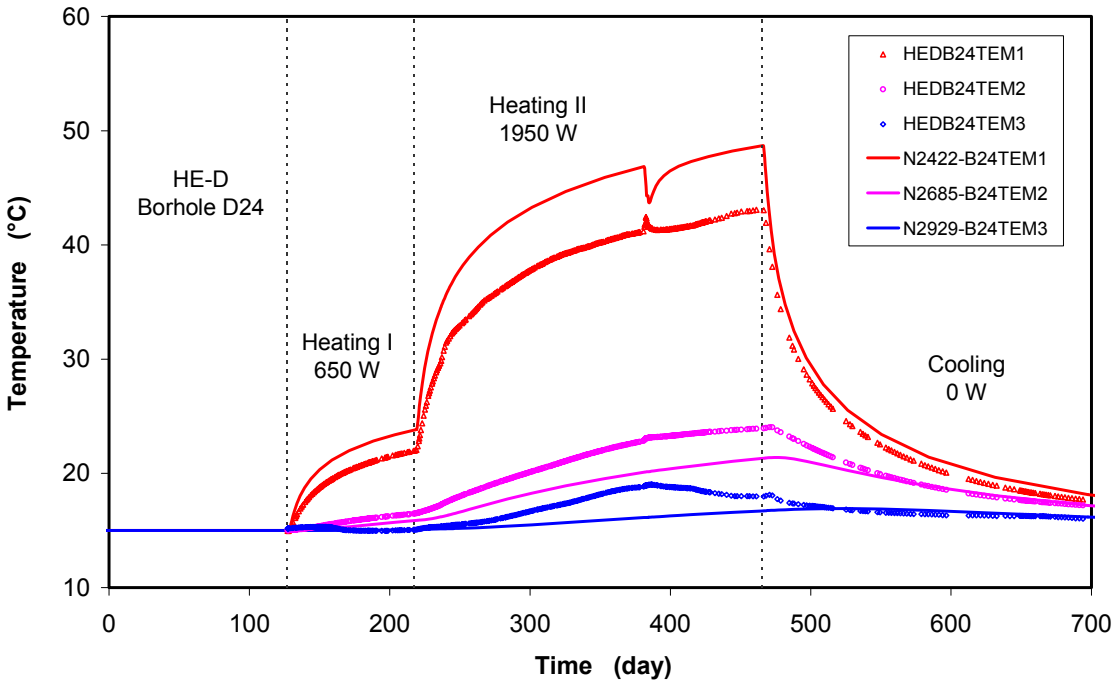

f. BHE-D24

Figure 4-23 Comparison of calculated and measured temperatures in the HE-D test field

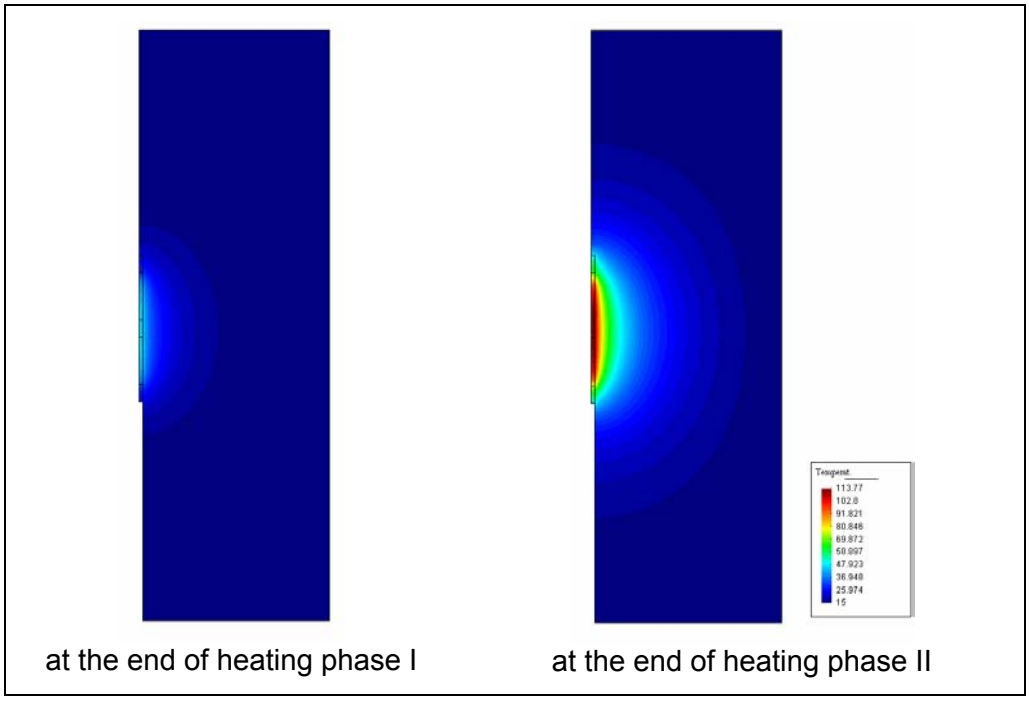

Figure 4-24 Calculated temperature distribution in the HE-D test field

Additionally, the application of the high value of thermal conductivity of λ= 2.1 W·m^{-1}·K^{-1} parallel to the bedding plane results in an underestimation of the temperatures at the heater/rock interfaces and thus also in the whole test field, as shown in Figure 4-25. So the mean value of λ = 1.7 W·m^{-1}·K^{-1} is confirmed by the in-situ measurements.

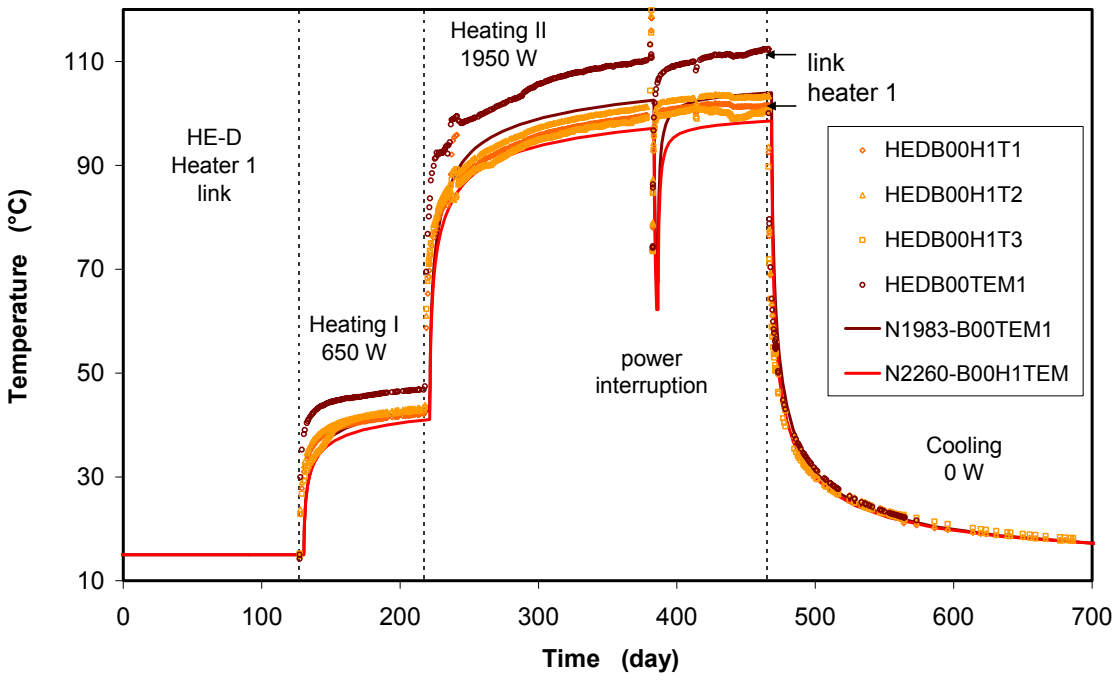

a: heater 1

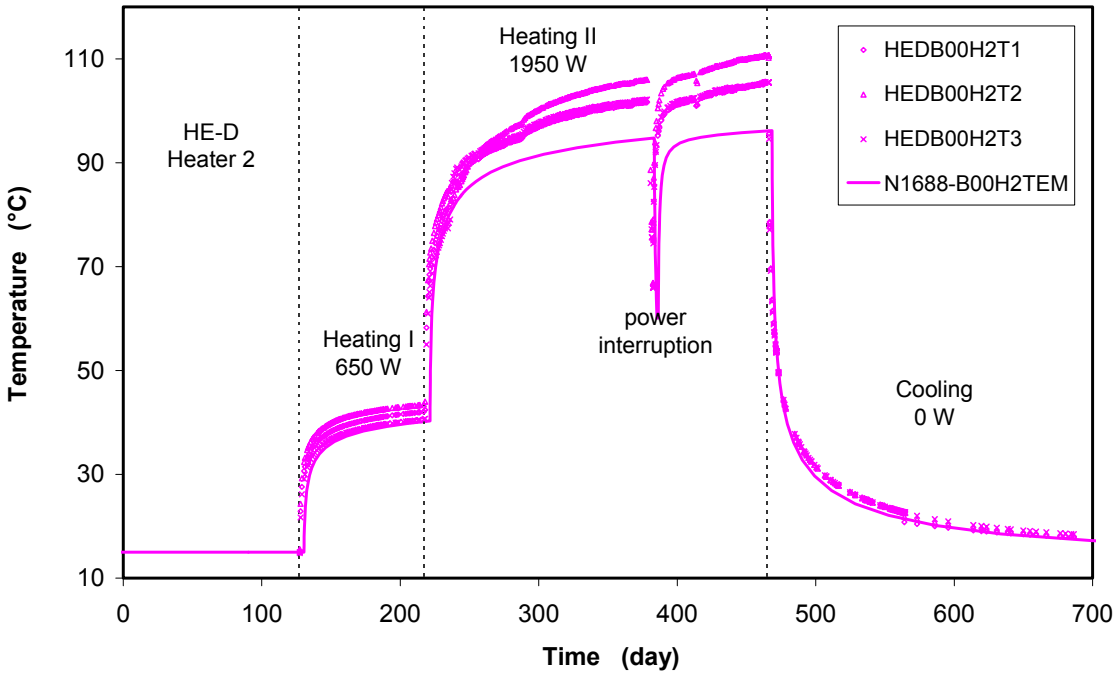

b: heater 2

Figure 4-25 Temperatures at the heater/rock interface calculated by a high thermal conductivity of λ = 2.1 $W \cdot m^{-1} \cdot K^{-1}$

4.5.4.2 Pore-Water Pressure

Generally, the thermally-induced pore-water pressure changes in the clay rock are controlled by many factors. Among of them are the rock properties of permeability, stiffness, bedding structures, degree of water saturation, thermal expansion coefficients of the solid, the liquid and the gas phase, as well as the boundary conditions. In the modelling, the intrinsic permeability, the hydraulic boundary conditions at the niche wall and at the heater/rock interface are considered as key factors and their influences are examined (Table 4-8). Model THM1 is the reference case and the modelling results for the pore-water pressures are illustrated in Figure 4-26 together with the data measured in the test intervals D3, D8, D9, D11, and D13 to D17. Sensor D10 failed, while D7 and D12 were probably located in an unsaturated zone near the MI niche. The results are interpreted as follows:

Table 4-8 Models with different boundary conditions for the calculation of the thermally-induced pore-water pressure

Model	Hydraulic conditions on the niche wall	Hydraulic conditions on the heater/rock interface	Intrinsic permeability k (m^2)
THM1	ventilation relative humidity RH=85%	drained water pressure P_l= 0.1MPa	$2 \cdot 10^{-20}$
THM2	undrained water flux Q_l= 0	drained P_l= 0.1MPa	$2 \cdot 10^{-20}$
THM3	ventilation RH = 85%	undrained water flux Q_l= 0	$2 \cdot 10^{-20}$
THM4	ventilation RH = 85%	drained P_l= 0.1MPa	$6 \cdot 10^{-20}$

- Before drilling the heater borehole, the initial pore-water pressures were measured between 0.2 and 1.2 MPa. Because of the very complicated conditions in the test field, the predicted initial pore pressures differ from the measurements at some locations (D3, D13, D14, D15, D17), but in general, they are well represented by the model. The borehole drilling led to a slight drop of the pore pressures at distances of 0.8 - 1.4 m to the heater. This effect is reasonably revealed by the model at D3, D9, D14, D15 and D16. In the far-field, no pore pressure response to the borehole drilling was observed.

- The first heating with a power supply of 650 Watts caused a rapid increase in the pore pressure of up to 2.4 MPa at a distance of 0.8 - 1.4 m to the heater (D3, D14, D15, D16). After reaching peak values the pressures remained more or less constant. Subsequently, increasing the power to 1950 Watts resulted in a further increase of the pore pressure up to 2.6 - 4.0 MPa in the near-field (D3, D14, D15, D16). Then, the pressure dropped slowly down to 1.8 - 2.5 MPa at the end of the second heating phase. However, at the far location D17 (r = 2.9 m) the pore pressure rose steadily up to a value of 3.4 MPa, which is even higher than the pressures in the more heated area close to the heater. Neglecting the initial differences, the responses of the pore-water pressures to heating are very well

represented by the model, even the effect of the power interruption is also well captured by the model.

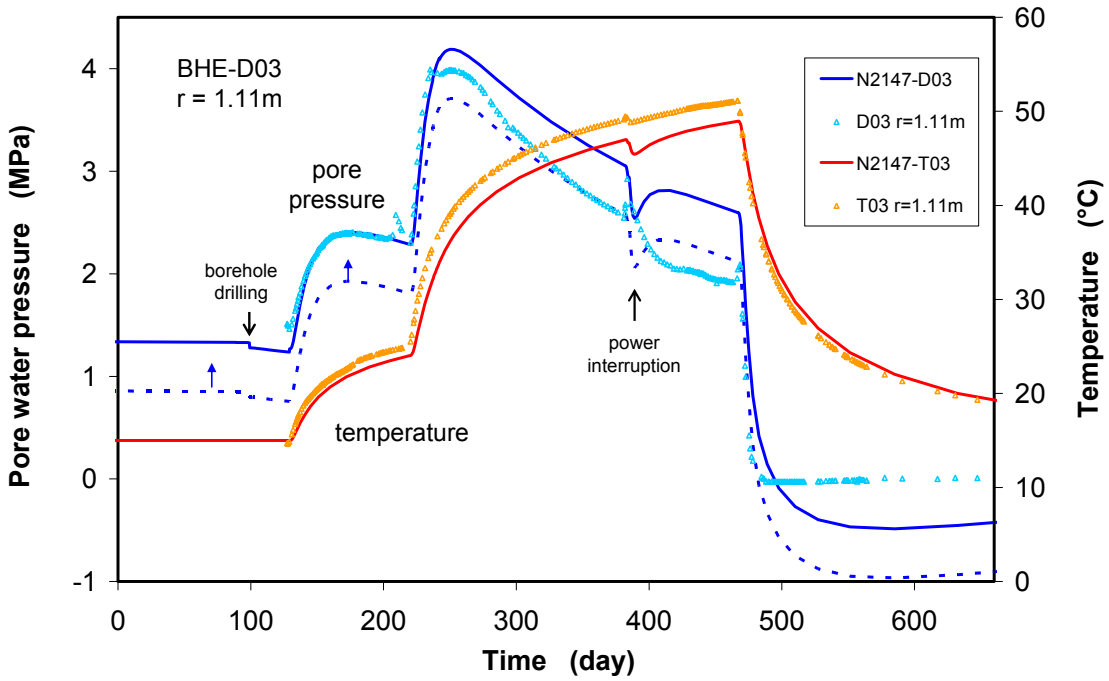

a. BHE-D03

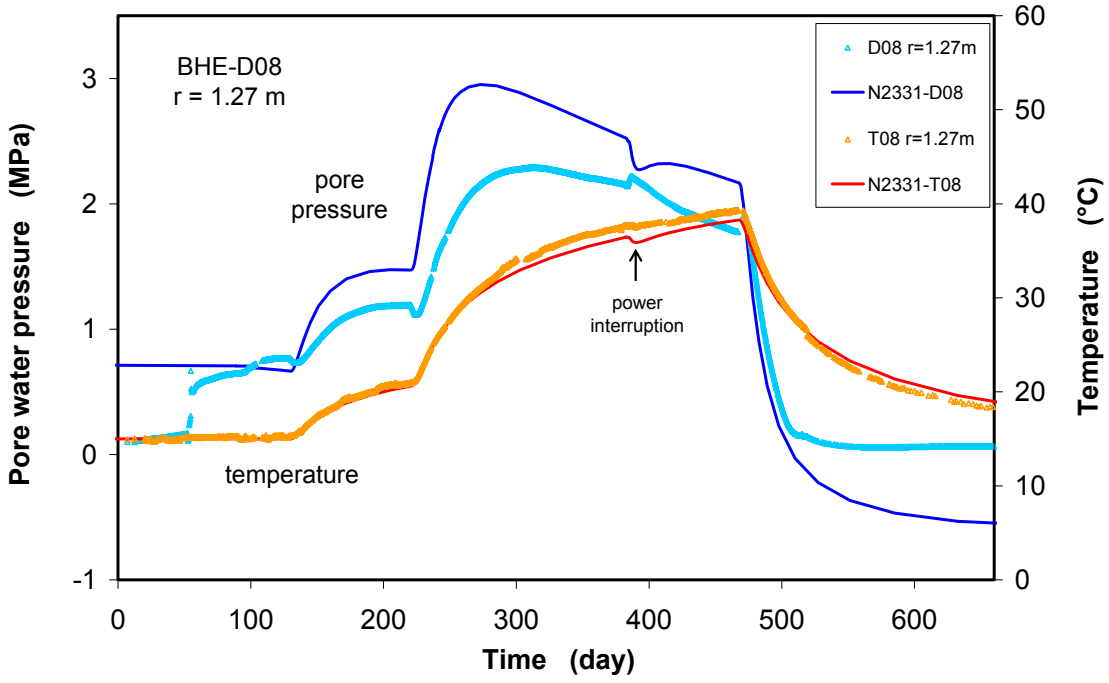

b. BHE-D08

- The cooling phase after switching off the power caused a quick reduction of the pore pressures to zero. The calculated negative pore pressures indicate de-saturation of the cooled area.

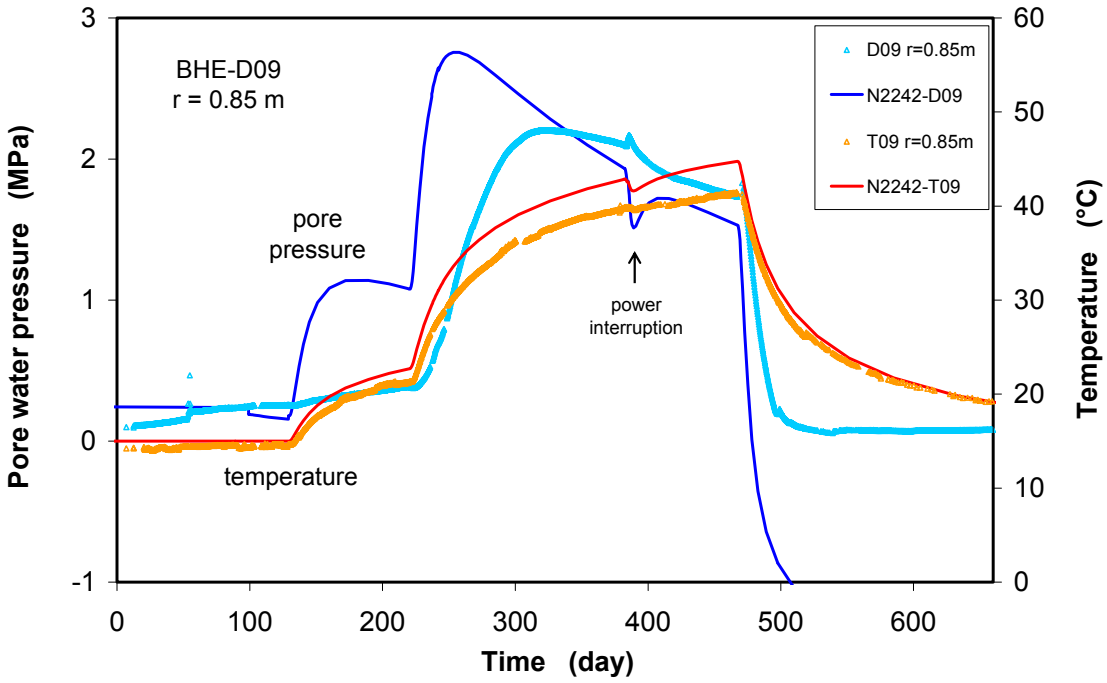

c. BHE-D09

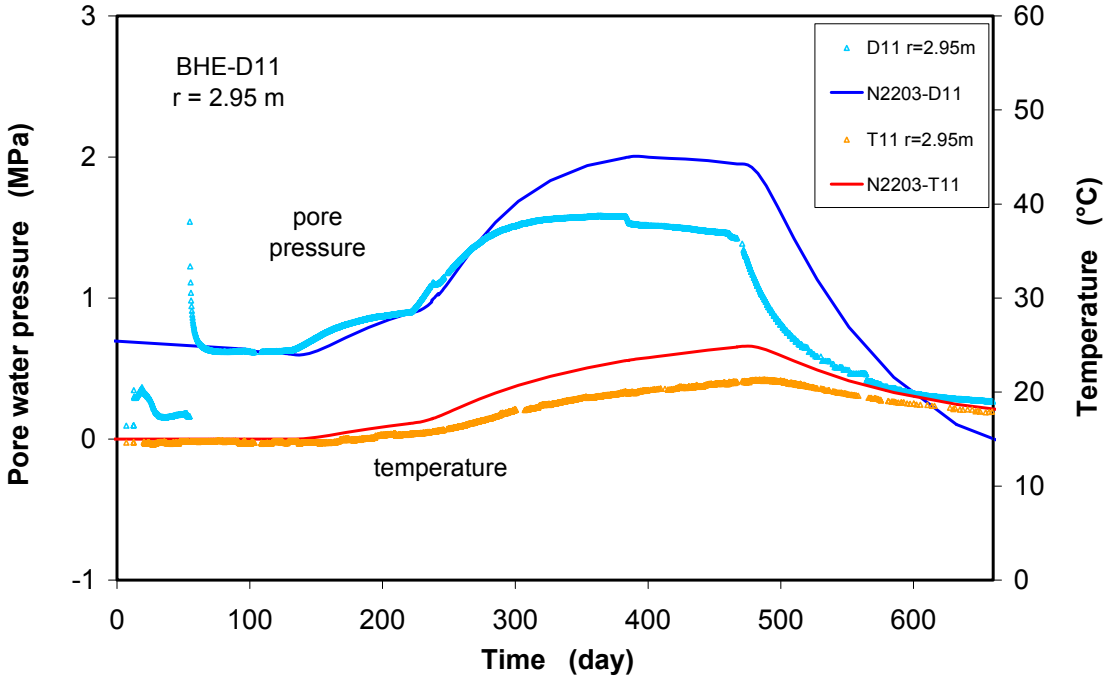

d. BHE-D11

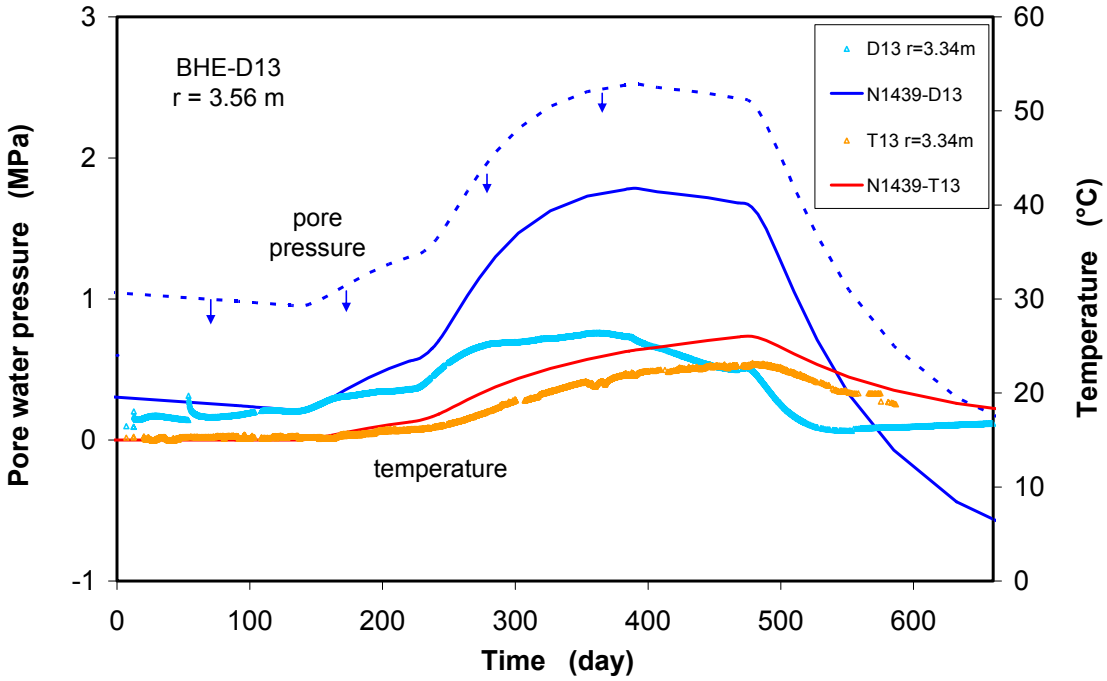

e. BHE-D13

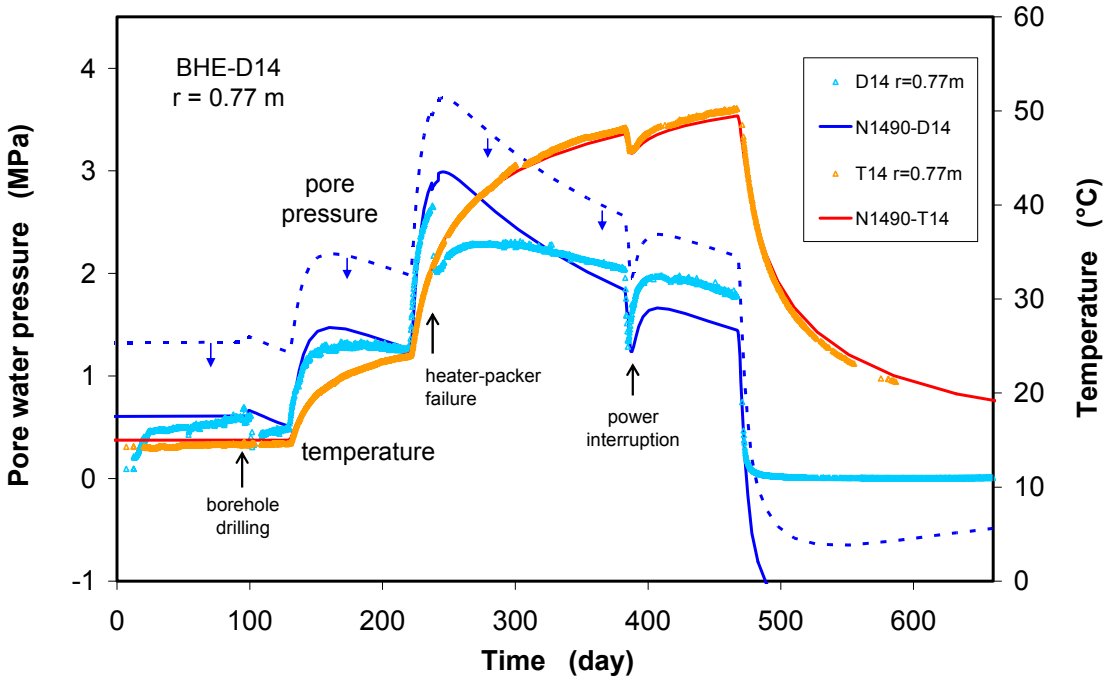

f. BHE-D14

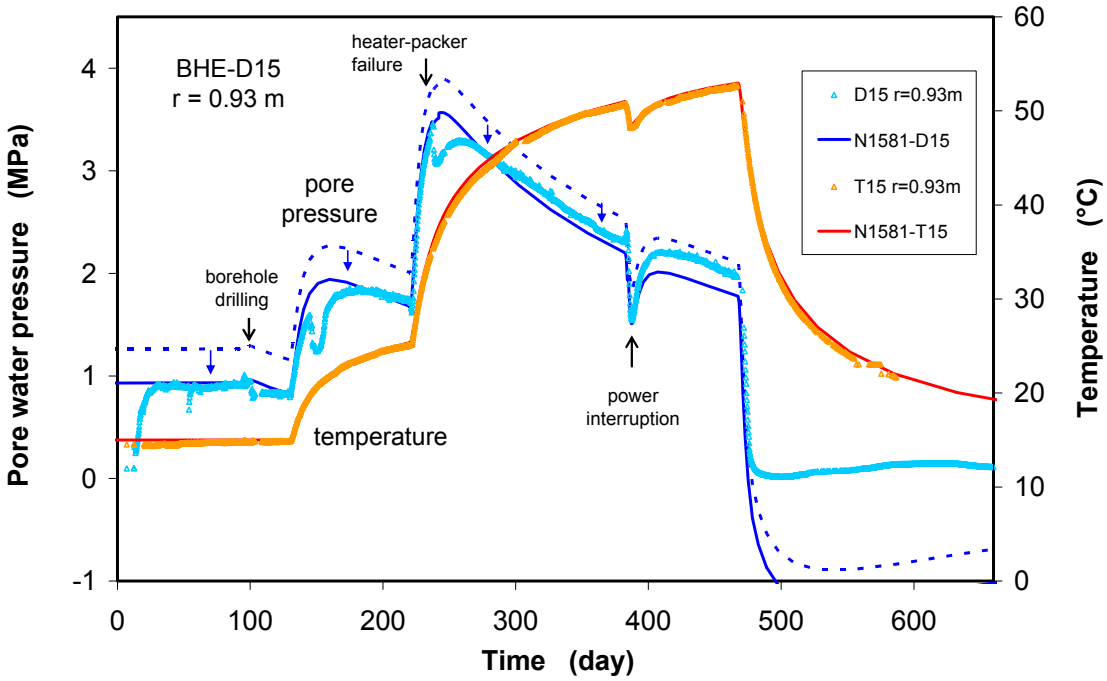

g. BHE-D15

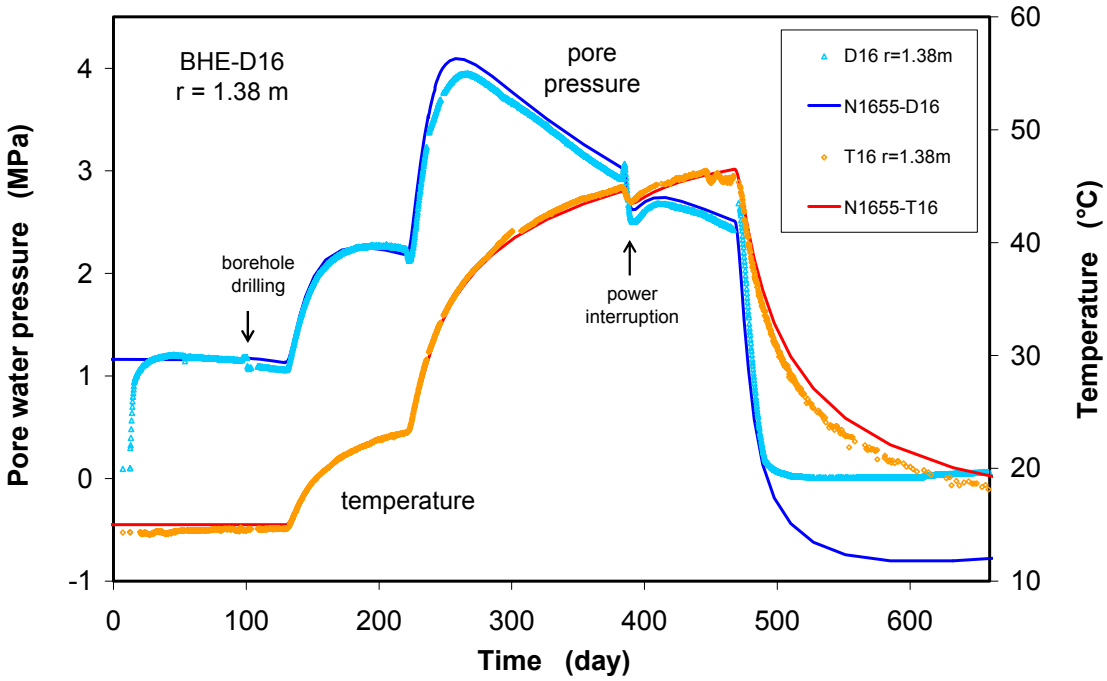

h. BHE-D16

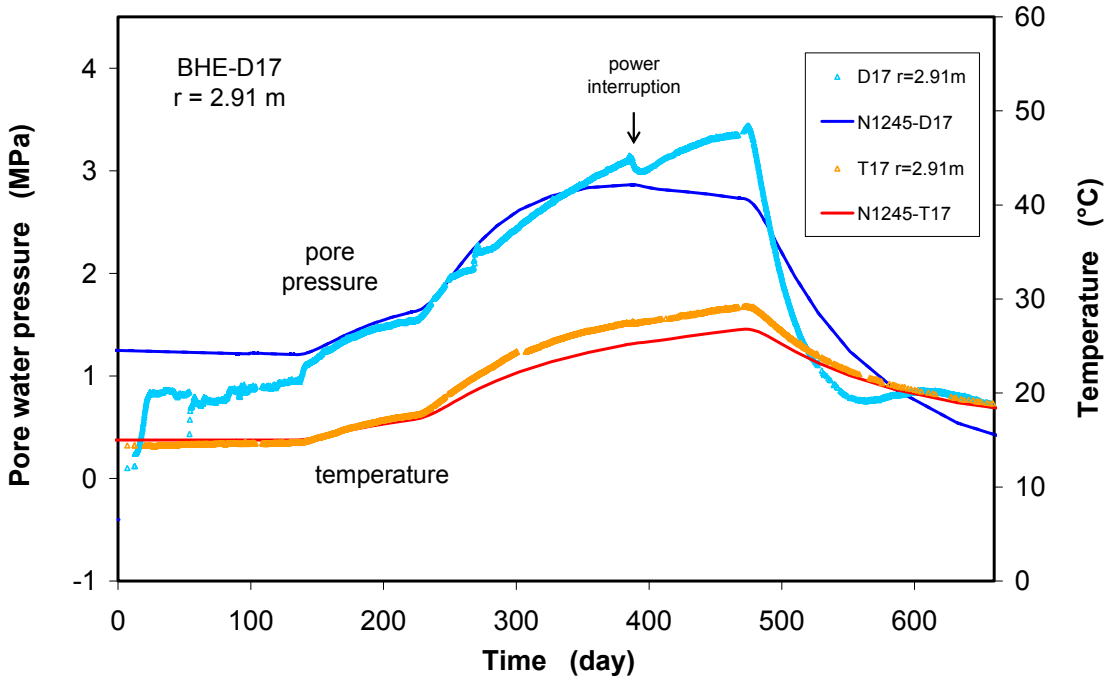

i. BHE-D17

Figure 4-26 Comparison between calculated and measured pore-water pressures in the HE-D test field

The results from the other models with different parameters and boundary conditions are compared with the measurements at the locations D3, D14, D15 and D16 in the near-field, as shown in Figure 2-27. From the comparisons one can find that

- Model THM1 under considerations of the drift ventilation, drained condition of the heater/rock interfaces at null pressure and a permeability of $2 \cdot 10^{-20}$ m^2 provides an excellent agreement with the field measurements;
- The application of undrained conditions ($Q_l = 0$) at the niche wall in model THM2 results in negligible differences compared to the pore pressures calculated under consideration of ventilation as adopted in THM1;
- The assumption of an undrained condition ($Q_l = 0$) at the heater/rock interface in model THM3 causes a large overestimation of the pore pressures;
- A high permeability of $6 \cdot 10^{-20}$ m^2 used in model THM4 allows the thermally-mobilised pore-water to escape more quickly and thus the pore pressures are underestimated.

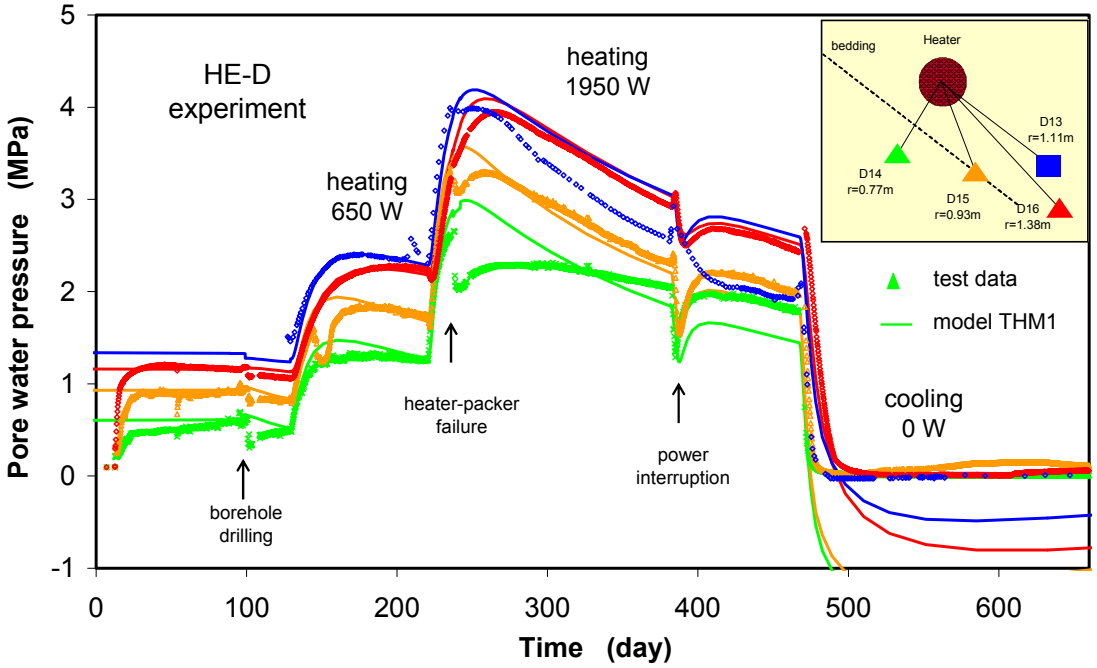

THM1: RH=85% on niche wall; P_l=0.1MPa on borehole; k=2·10^{-20} m^2

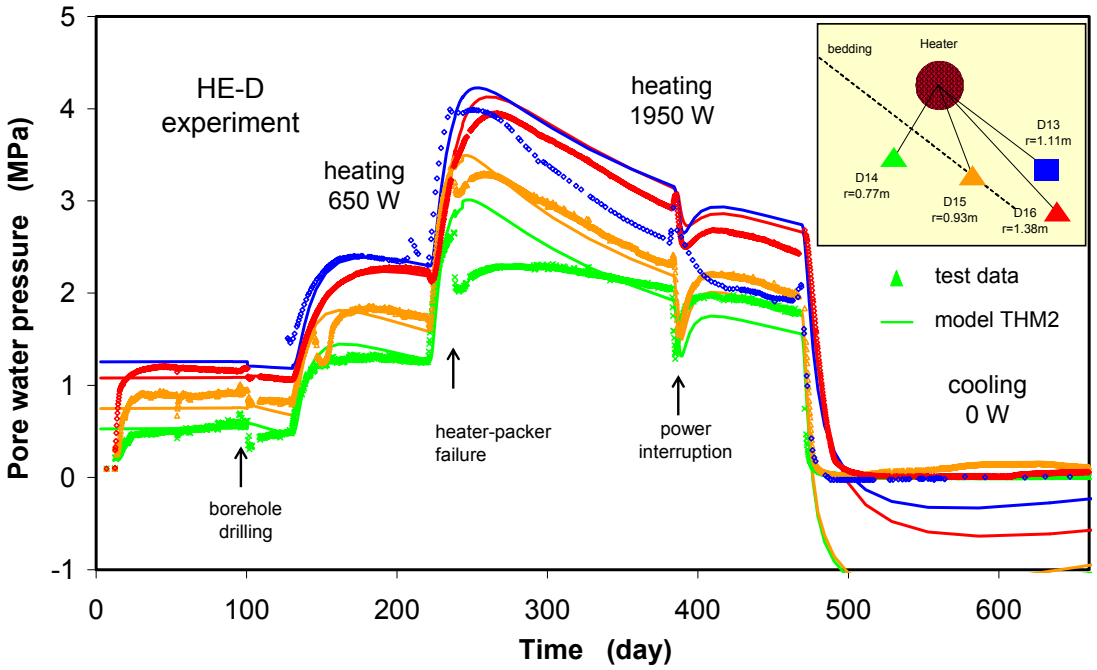

THM2: Q_l=0 on niche wall; P_l=0.1MPa on borehole; k=2·10^{-20} m^2

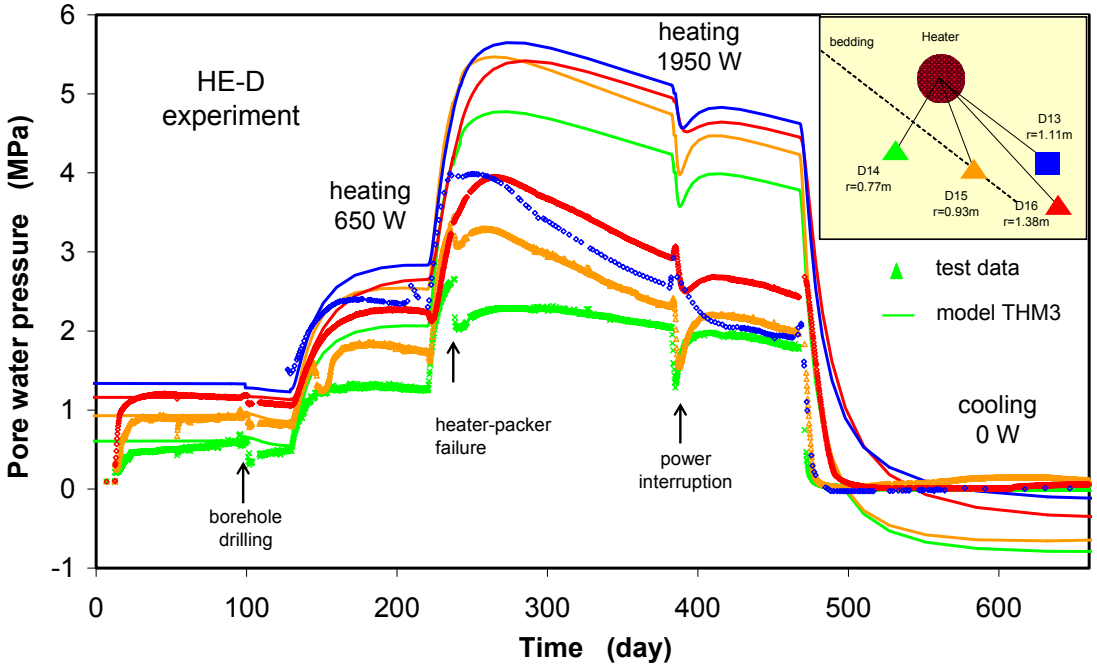

THM3: RH=85% on niche wall; Q_l=0 on borehole; k=2·10^{-20} m^2

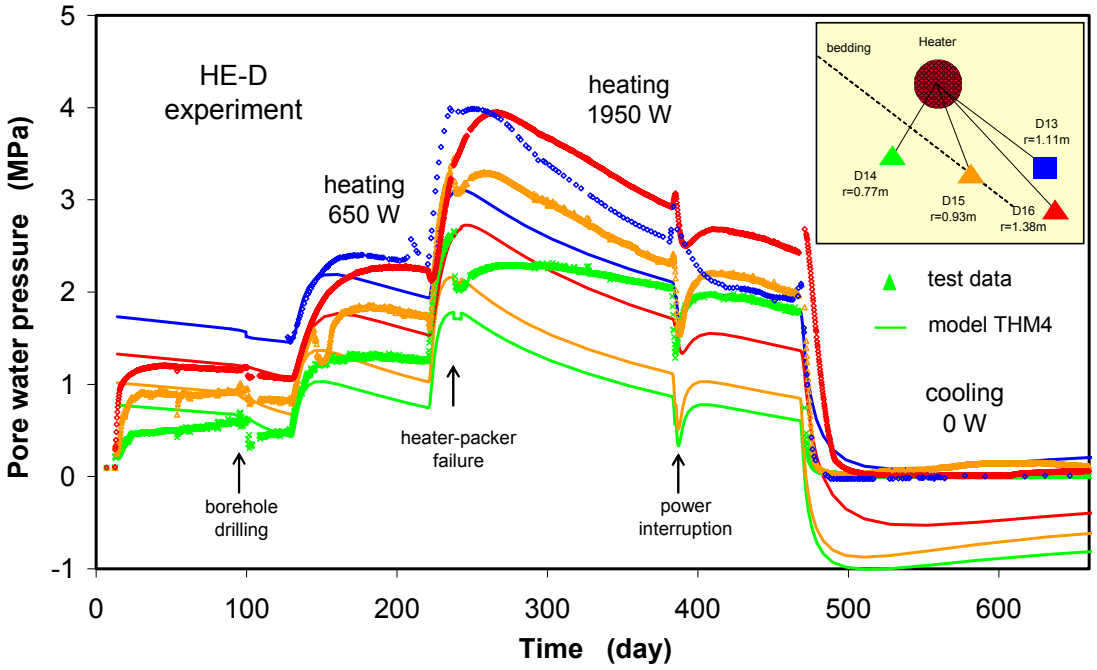

THM4: RH=85% on niche wall; P_l=0.1MPa on borehole; k=6·10^{-20} m^2

Figure 4-27 Pore-water pressures calculated for various conditions in comparison to measurement data of the in-situ heating experiment

Figure 4-28 shows an overview of the pore pressure distribution calculated (THM1) for different times before, during and after heating. The model indicates that the region

near the drift walls is de-saturated to a depth of ~1.5 m due to ventilation, as indicated by a negative pore pressure. Each heating generates a high pressure zone at a distance between 0.5 and 1.7 m from the heater, but not directly near the heater because of the drained condition at the heater/rock interface. The calculated maximum pore pressures in this zone are between 1.8 and 2.3 MPa at a time of 30 days after the first heating, 3.0 and 4.0 MPa at 17 days after the second heating, respectively. Cooling leads to a reduction of the pore pressures down to zero and even to negative values, which indicate de-saturation.

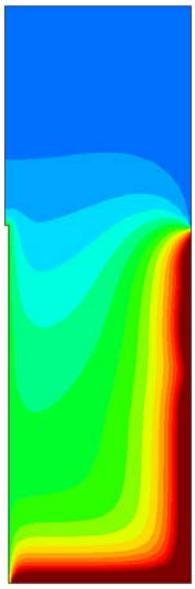

before heating

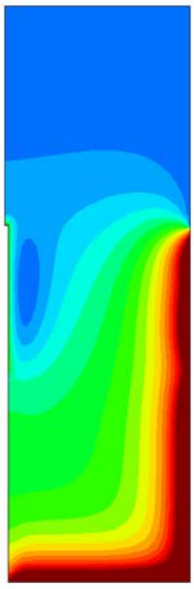

30 days after heating I

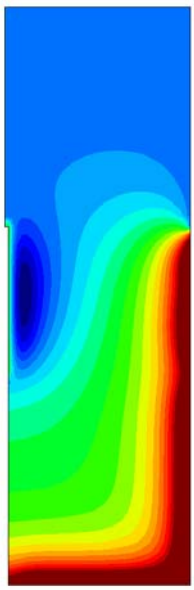

17 days after heating II

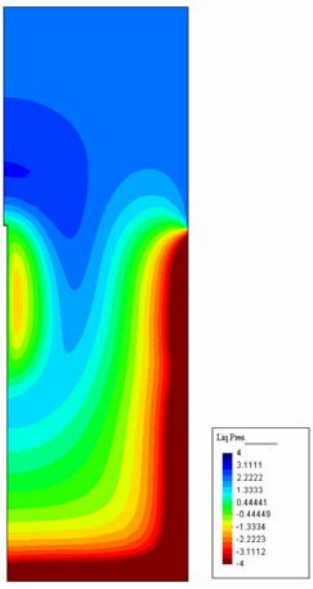

after cooling

Figure 4-28 Distribution of pore-water pressure calculated for different test stages

4.5.4.3 Deformation

Based on the extensometer measurements along boreholes D4, D5, and D6 (see section 2.7.7), the relative deformations between two neighbouring points are calculated by

$$\varepsilon_{i-j} = \frac{u_j - u_i}{d_{i-j}} \tag{4.8}$$

where u_i and u_j are the displacements of points i and j along the borehole, and d_{i-j} is the interval distance between both points. As a convention in rock mechanics, compression is signed positive and conversely extension negative.

In the modelling of thermal strains, the thermal expansion coefficient for the rock mass consisting of solid grains and pore-water, $\alpha_{mv} = 3 \cdot \alpha_m = 5.1 \cdot 10^{-5}\ K^{-1}$, is applied. Figures 4-29, 4-30 and 4-31 compare the modelling results with the measurements in boreholes D4, D5 and D6. The following conclusions can generally be drawn from this comparison:

- The drilling of the heater borehole led to more or less extensive deformations in most intervals, which is well revealed by the model.
- Each heating caused short-term compressions in most intervals due to larger deformation in the more heated area than in the less heated area. Following that, a gradual extension of the rock took place, mostly due to the relatively large thermal expansion of the pore-water. The thermally-induced deformation is very well represented by the model for most of the measuring intervals. Only for a few others, the differences between model and measurement are relatively significant. This might be due to some factors which are not considered in the model, for instance such as unsealed boreholes allowing the thermally-mobilized pore-water to escape easily and the pore pressure to be strongly reduced, which can lead to a compaction of the pores.
- During the cooling phase, the combined impacts of the pore-water contraction and the increase in effective stress result in a collapse of the de-saturated pores and thus a compaction of the rock.
- The effects of the failure of the heater-packers and the power interruption are also reasonably computed.

- In the modelling for borehole D6, the thermal expansion coefficients for the solid grains (α_{sv} = 4.5·10^{-6} K^{-1}) and for the rock mass (α_{mv} = 5.1·10^{-5} K^{-1}) are examined. The application of the coefficient for the rock mass produces an excellent agreement with the measured data, while the low value for the solid grains results in an underestimation of the thermally-induced strain increments.

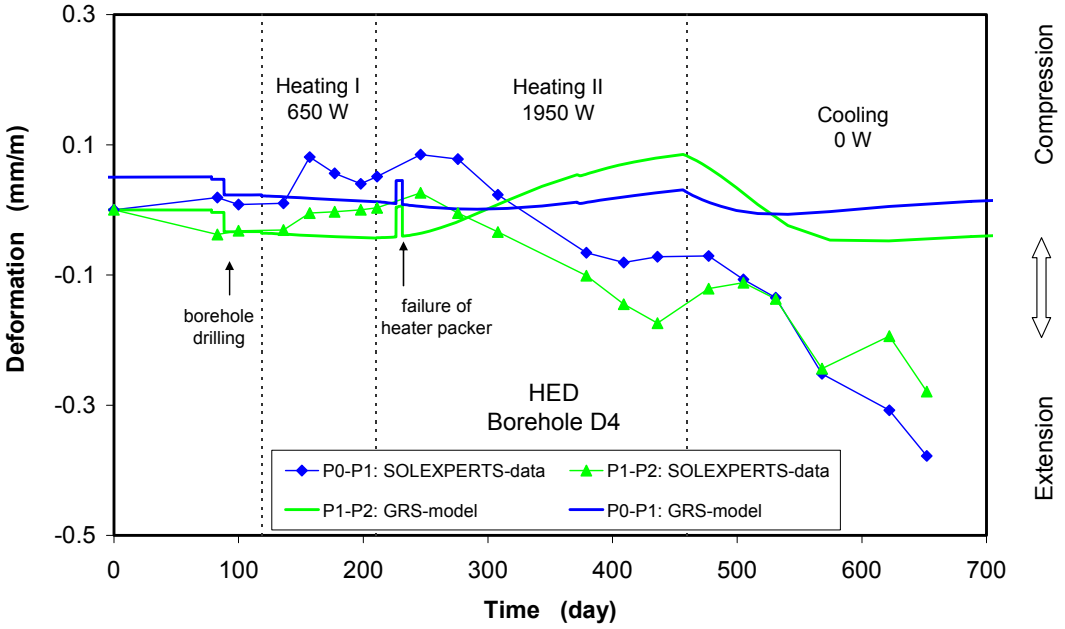

a.

P0 – P1 and P1 – P2

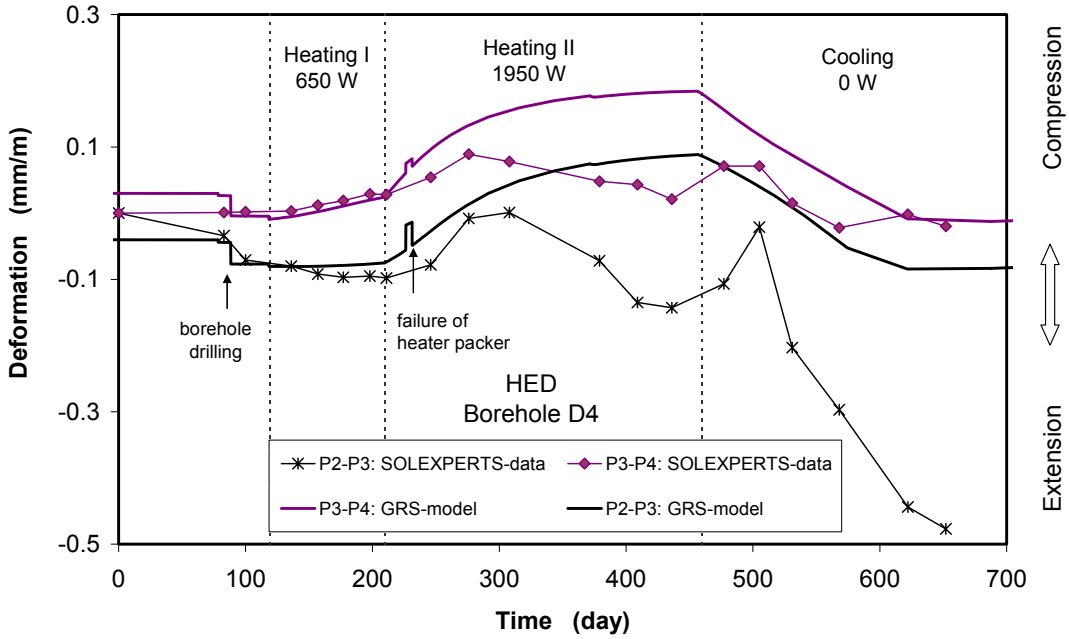

b. P2 – P3 and P3 – P4

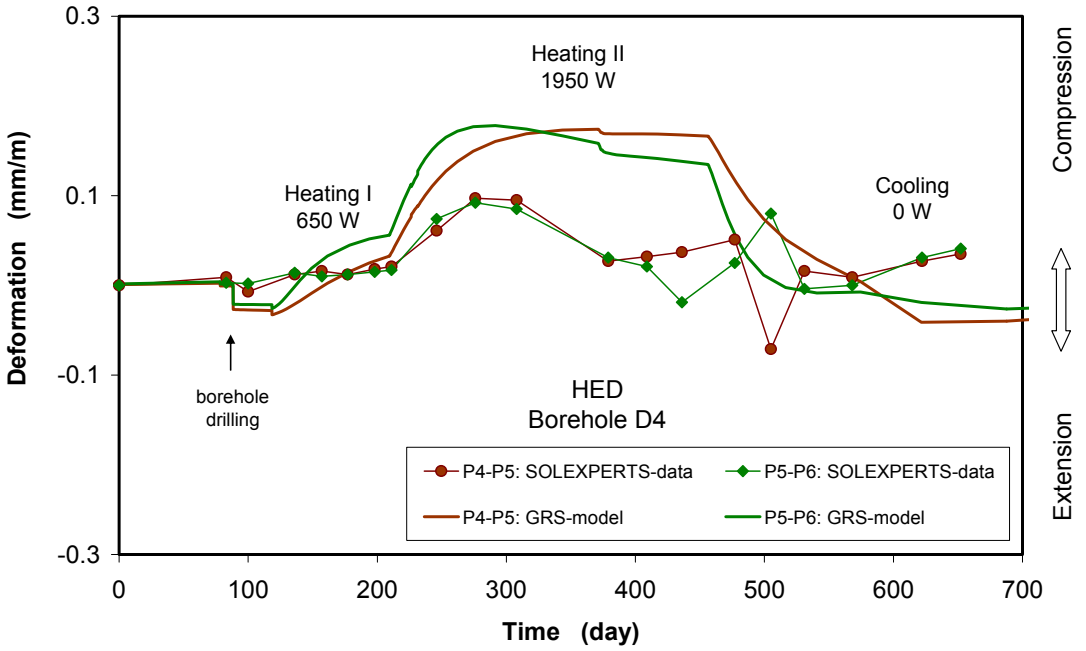

c. P4 – P5 and P5 – P6

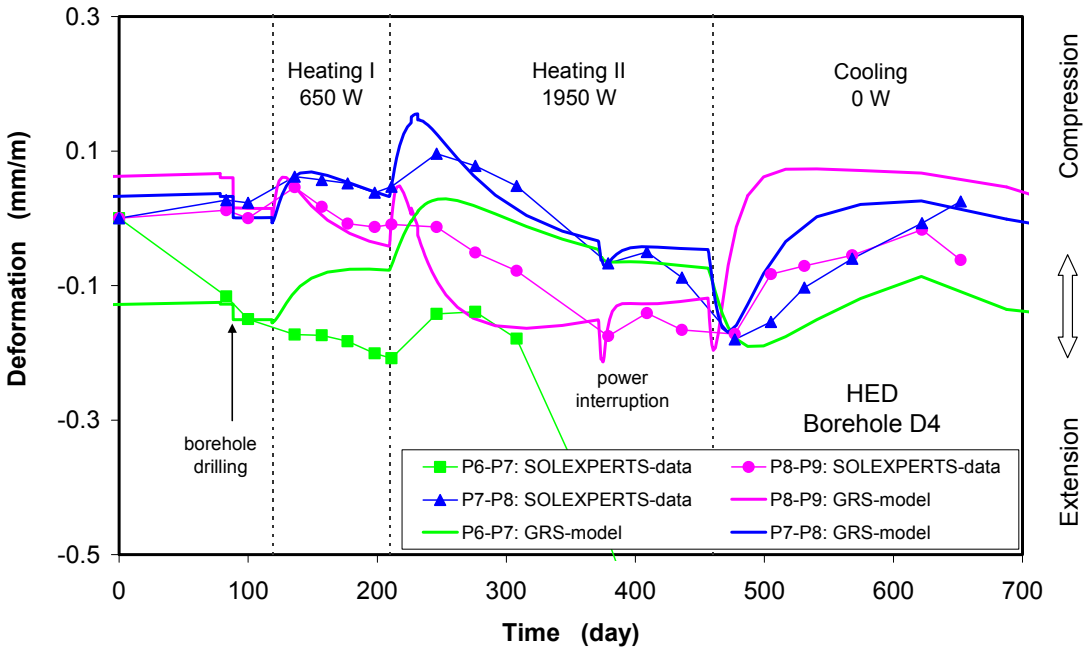

d. P6 – P7, P7 – P8 and P8 – P9

Figure 4-29 Measured and calculated deformations along borehole D4

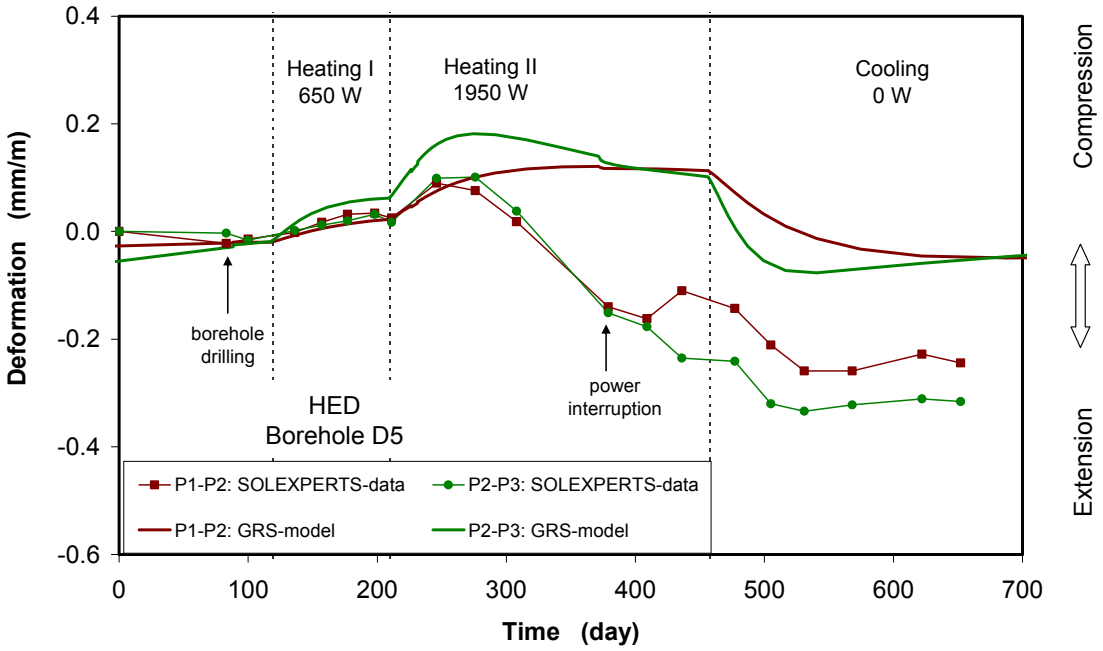

a. P1 – P2 and P2 – P3

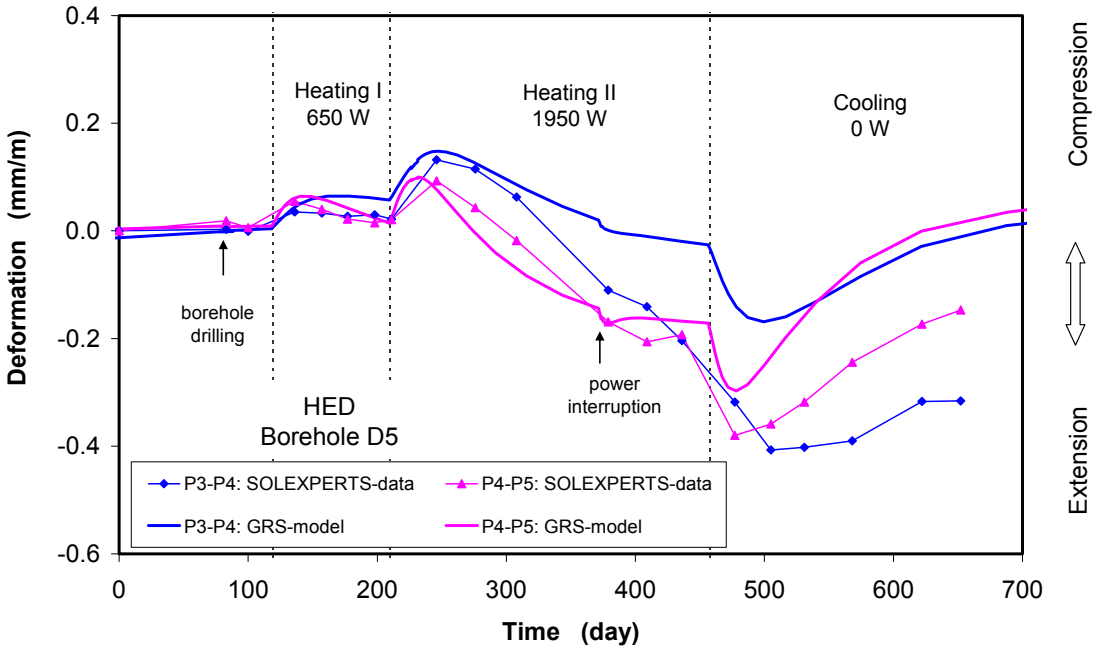

b. P3 – P4 and P4 – P5

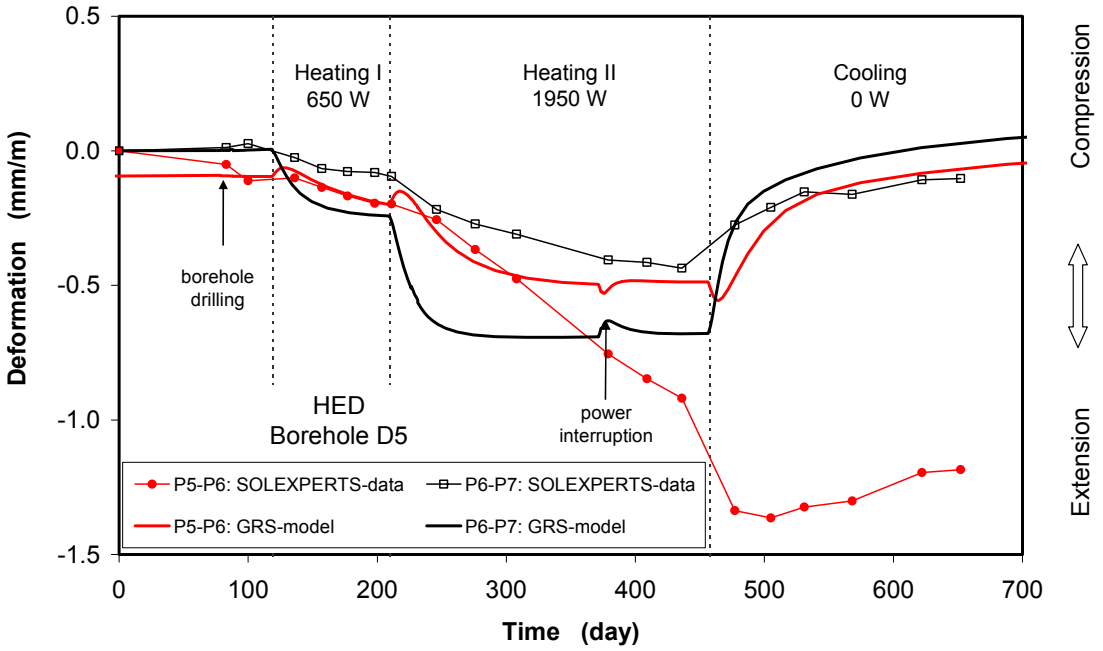

c. P5 – P6 and P6 – P7

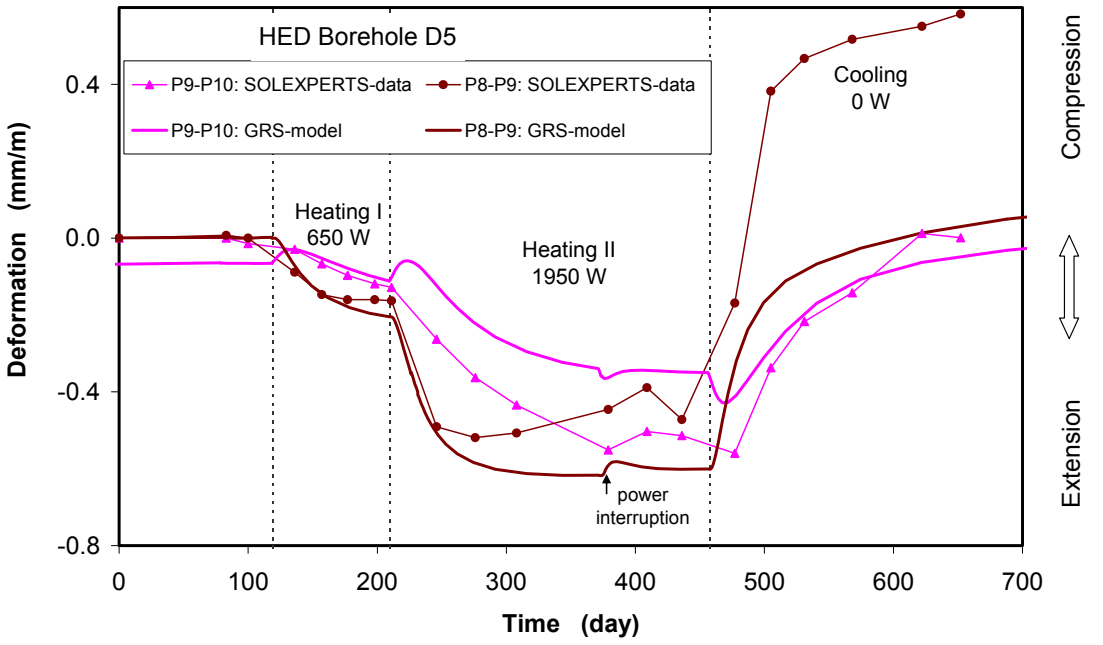

d. P8 – P9 and P9 – P10

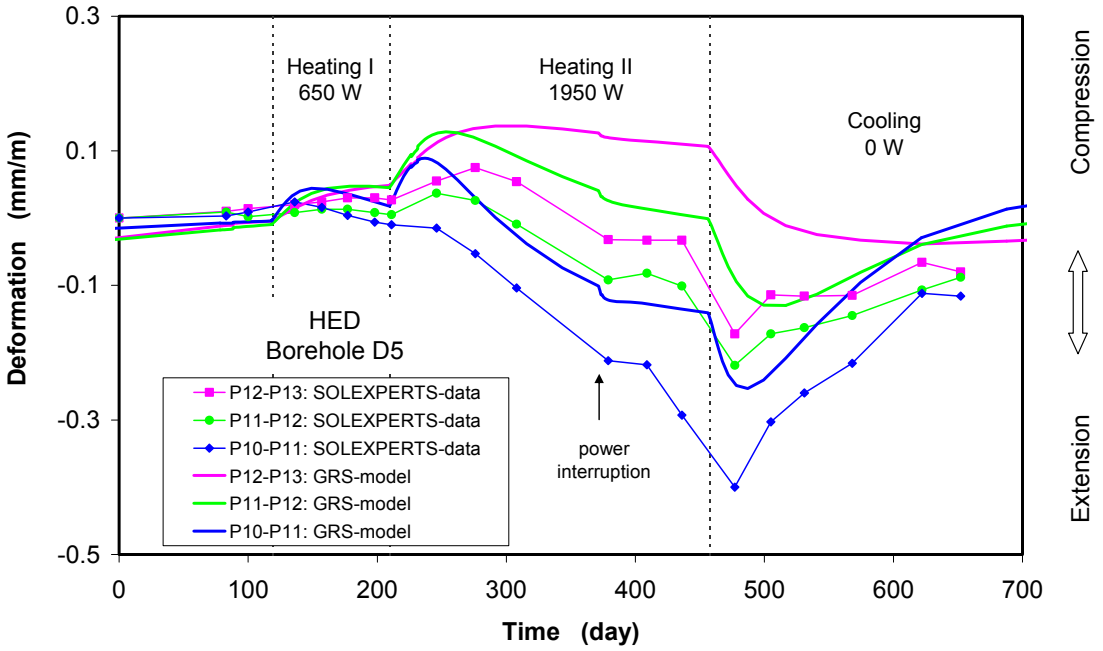

d. P10 – P11, P11 – P12 and P12 – P13

Figure 4-30 Measured and calculated deformations along borehole D5

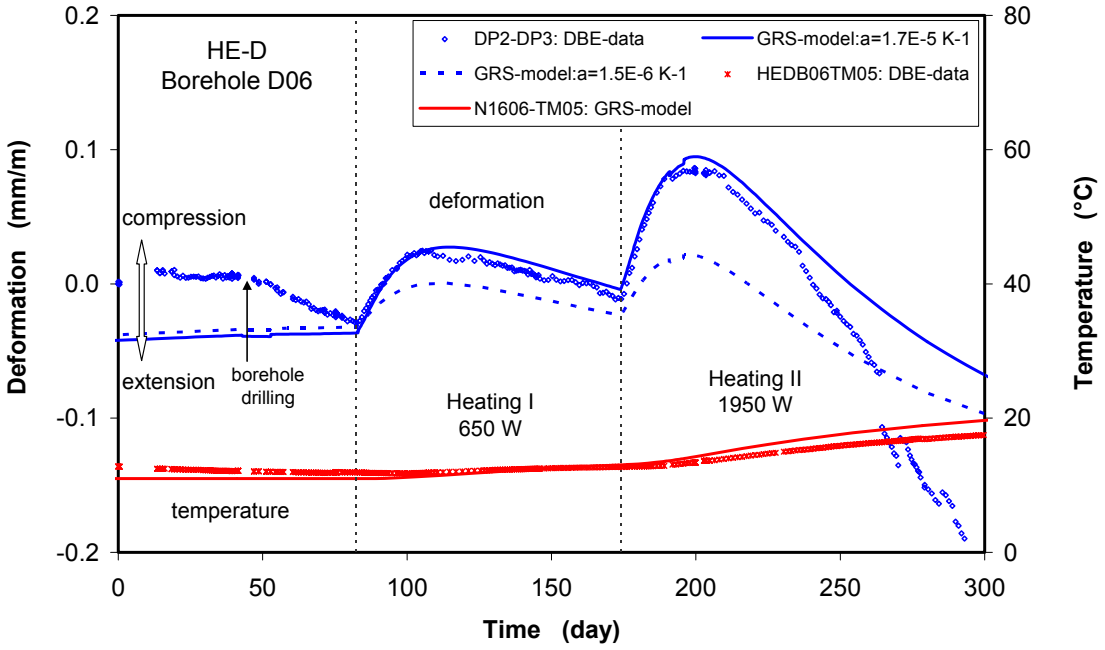

a. P2 – P3

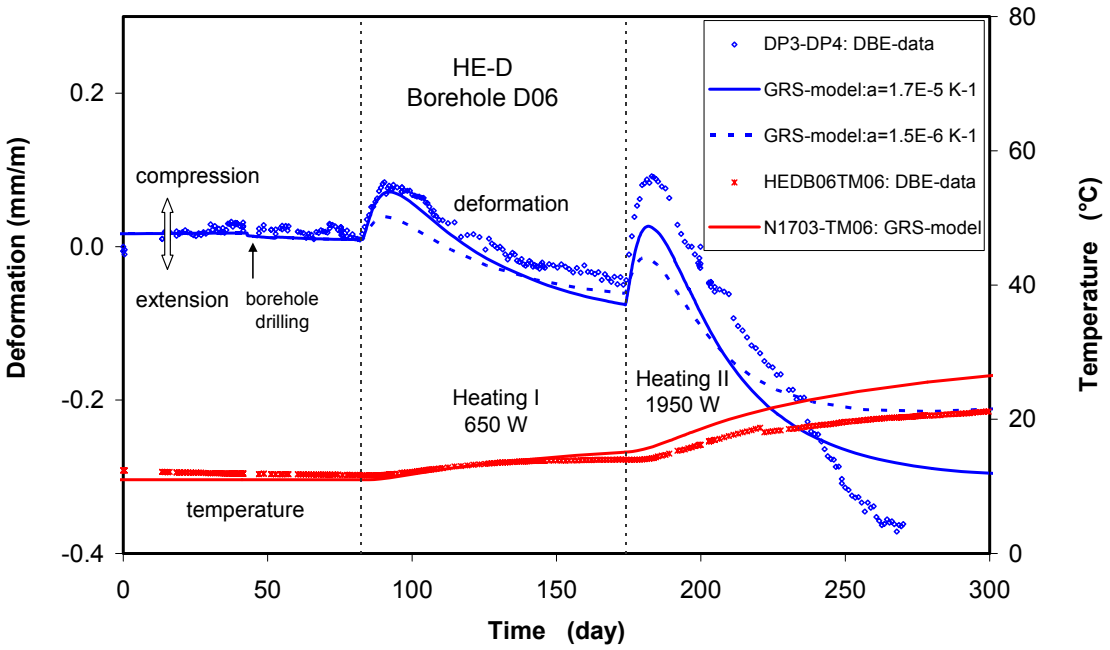

b. P3 – P4

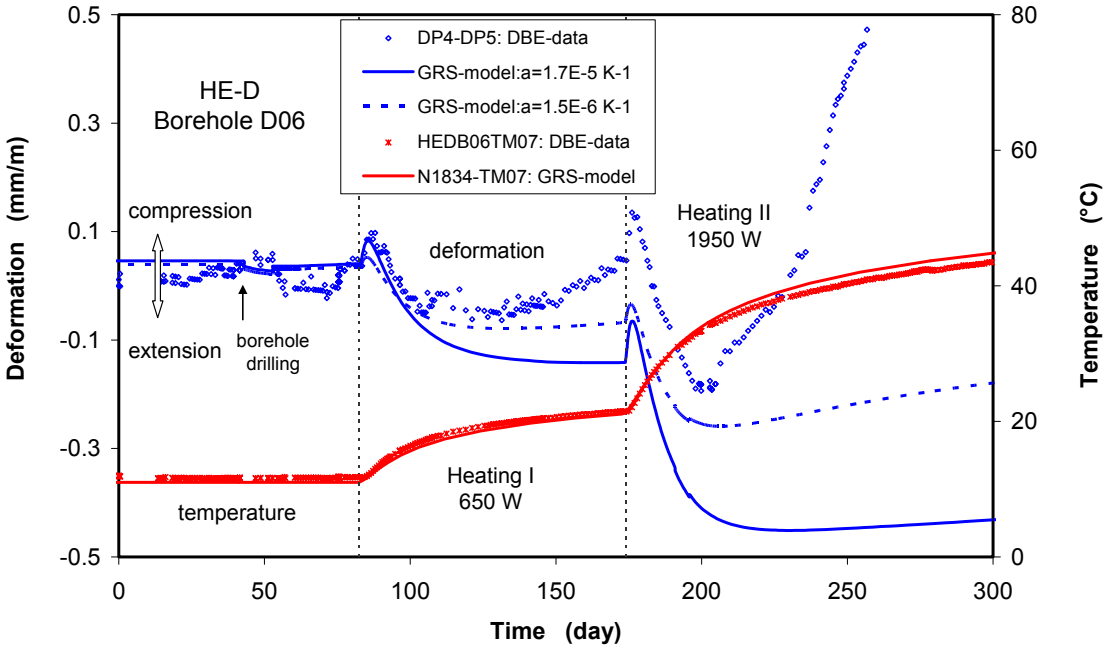

c. P4 – P5

Figure 4-31 Measured and calculated deformations along borehole D6

5 Summary and Conclusions

From October 2003 to December 2005, the HE-D heating experiment was performed at the Mont Terri Rock Laboratory by ANDRA and GRS to investigate thermal effects on clay formations hosting a repository for high level radioactive waste. GRS participated in this experiment with in-situ measurements, laboratory experiments, and numerical modelling.

In-situ Measurements

In the experiment the Opalinus clay was heated by a heater equipment of 6 m length installed in the deepest of a horizontal borehole of 300 mm diameter and 14 m length. Two heating phases were conducted with power inputs of 650 Watts over the first 3 months and 1950 Watts over the remaining 8 months. The cooling phase of 7 months followed after shut-down of the power. Temperature, pore-water pressure, gas pressure, and deformation of the surrounding rock were measured by means of 110 instruments installed in 24 boreholes.

The temperature was monitored by means of PT100 sensors at 45 positions in the rock. At the heater/rock interface, the temperature was increased from 15 to 100 °C at the end of the heating phase. Correspondingly, the temperature in the rock at distances of 0.8 - 1.4 m from the heater reached values between 45 and 55 °C. In the far-field at distances of 3.0 - 3.5 m, the maximum temperatures of 22 - 28 °C were recorded.

The pore-water pressure was measured in 11 slim boreholes equipped with GRS mini-packer-systems. The initial pore-water pressures in the test field revealed values in a range between 0.2 MPa and 1.2 MPa. Shortly after increasing the power to 1950 Watts, the pore-water pressure reached maximum values of 2.3 to 4.0 MPa in the near-field 0.8 - 1.4 m distant to the heater, afterwards gradually decreasing due to the mobilization of the pore-water at higher temperatures. During the cool-down phase the pore-water pressure dropped shortly down to zero.

After cooling, water injection tests with PEARSON water yielded rock permeability values between 10^{-20} m^2 and 10^{-19} m^2. Measurements of the gas entry pressure resulted in typical values between 0.8 MPa and 1.8 MPa.

Rock integrity was monitored throughout the entire test period in six boreholes perpendicular to the heater axis. Gas pressure measurements were performed in 24 test intervals. While the first heating produced only a slight increase of the gas pressures, the second heating phase at higher power increased the pressure up to 1.6 to 2.4 MPa. It was found out that these high pressures were mainly induced by the intrusion of the thermally-mobilized pore-water into the test intervals, whereby compressing the gas in the intervals. After switching off the heater, the gas pressure decreased to low values of less than 0.8 MPa.

Gas injection tests after termination of heating showed that the rock was impermeable below the gas entry pressure of about 1.5 MPa measured in several intervals. Even by exceeding this value, a very low gas permeability of about 10^{-22} m^2 was measured. Increasing the gas pressure up to 3 to 4 MPa led to rock fracturing oriented along the bedding plane. Re-fracture tests yielded an increased permeability of about 10^{-18} m^2.

Generally, the high pore-water and gas pressures and their gradual evolution indicate that no macro-fractures were thermally generated in the clay rock during the heating and cooling phases.

Laboratory Experiments

Various laboratory tests were carried out on normally-sized and large-scale samples taken from the HE-D test field to investigate the impact of heating on the Opalinus clay and to provide a database for identification of material parameters.

Under unloaded conditions, different thermal expansion coefficients were determined to $\alpha_{\perp}$ = $1.6 \cdot 10^{-5}$ $°C^{-1}$ perpendicular and $\alpha_{//}$ = $1.5 \cdot 10^{-6}$ $°C^{-1}$ parallel to the bedding plane. The difference indicates a significant thermal anisotropy of the rock. Under a confining stress of 3 MPa and at undrained conditions, the thermal expansion coefficient was determined to α = $1.5 \cdot 10^{-5}$ $°C^{-1}$. This value can also be calculated by $\alpha_m = \alpha_s(1-\phi)+(\alpha_w/3)\cdot\phi$ with a porosity of ϕ = 16 %, a water expansion coefficient of α_w = $3.4 \cdot 10^{-4}$ $°C^{-1}$ and a solid expansion coefficient α_s = $1.5 \cdot 10^{-6}$ $°C^{-1}$.

Undrained compression tests at high temperatures up to 115 °C showed that the clay rock behaves elasto-plastically and becomes more ductile and weaker with increasing

temperature. The initiation of damage and dilatancy took place at a stress of about 80 % of the peak strength.

Long-term uniaxial creep tests were conducted at temperatures between 24 °C and 90 °C and under axial stresses of 0.7 to 14 MPa over 1.4 to 2.7 years. Generally, the uniaxial compression is accelerated at elevating temperature.

At an axial stress of 1 MPa, one sample was dried and wetted by circulating dry air and water vapour along the sample at temperatures of 24 to 58 °C. It was found that drying led to a significant shrinkage up to 1.6 % and conversely wetting produced a large expansion up to 2.4 %. The swelling and shrinking strains are well correlated to the amount of water uptake and release, and both processes are also partly reversible.

In the THM coupling tests the following phenomena were observed:

- drained compression up to 5 MPa resulted in a consolidation of 0.3 % - 1.8 %;
- undrained compression from 5 to 15 MPa led to an increase in pore-water pressure up to 12 MPa;
- reducing the back-pressure from 12 MPa to zero caused a consolidation of 0.3 %;
- at 5 MPa confining stress and 4 MPa water back-pressure, the sample expanded significantly up to 1.1 %;
- increasing temperature from 30 to 80 °C and even higher at 15 MPa confining stress generated a significant increase in the pore pressure up to 10 - 12 MPa;
- decreasing the temperature from 120 to 30 °C led to a rapid drop of the pore pressure down to zero.

In addition to the above mentioned tests on normally-sized samples with a diameter of less than 100 mm, THM coupling tests were also performed on large samples of 260 mm diameter and 700 mm length. The large-scale consolidation tests provided similar results to those obtained on the normal samples. This indicates that the scale-effect is negligible for the clay rock within the test range.

On another big sample mock-up heating tests were performed by simulating the in-situ heating experiment in four stages: 1) re-saturation by injecting PEARSON water to the sample's top and bottom at 0 - 1 MPa; 2) re-consolidation of the sample at a confining

stress of 8 MPa; 3) heating the sample at the top to 80 °C while keeping the temperature at the other boundaries at 30 °C; and 4) cooling the sample down. Temperature, pore-water pressure and deformation were monitored by means of various instruments installed inside and outside the sample. The main observations are:

- Increase of the heater temperature from 30 to 80 °C generated a short-term thermal transient phase followed by a steady phase;
- Loading the sample up to 8 MPa caused unexpected different increases of the pore-water pressures in the test intervals between 3 and 5.5 MPa, probably due to different local disturbances more or less caused by the instrumentation;
- Heating generated insignificant pore-water over-pressures of 0.2 to 0.6 MPa due to the drained boundary conditions;
- Observed large radial deformations might be the result of the pre-existence of micro-fractures preferably oriented along the sample axis.

Modelling

The in-situ and laboratory heating experiments were simulated by use of CODE-BRIGHT under the following assumptions:

- Heat transport includes conduction (Fourier's law) through the porous medium, advection of liquid water and vapour flow;
- Water transport is controlled by liquid water advection (Darcy's law), vapour diffusion in air (Fick's law), and the liquid/gas phase changes (psychrometric law);
- Flow of dry air due to air pressure gradients (Darcy's law) and air dissolved in the liquid phase (Henry's law);
- Description of the elasto-plastic behaviour of the clay rock by the BBM model with the main features of thermal expansion / contraction, swelling / shrinking;
- The clay rock is assumed isotropic and homogeneous.

The parameters associated with the constitutive models were first estimated on basis of laboratory tests and data from literature and then calibrated by back-calculations of the lab mock-up heating tests. Finally, they are applied in the modelling of the in-situ heating experiment and confirmed by a comparison with the field measurements. By

assuming an isotropic state of the clay rock, some key parameters have been averaged as given below:

- thermal conductivity λ = 1.7 $W \cdot m^{-1} \cdot K^{-1}$
- specific heat capacity C = 800 $J \cdot kg^{-1} \cdot K^{-1}$
- linear thermal expansion coefficient of the solid grains $\alpha_s = 1.5 \cdot 10^{-6}\ K^{-1}$
- linear thermal expansion coefficient of the rock mass $\alpha_m = 1.7 \cdot 10^{-5}\ K^{-1}$
- elastic modulus E = 6680 MPa
- intrinsic permeability $k = 2 \cdot 10^{-20}\ m^2$.

From the comparison between the modelling results and the field measurements, the following conclusions can be drawn:

- The temperature evolution and distribution observed in the in-situ experiments is very well predicted. For more than 40 positions the discrepancies between model and measurement are less than 3 °C, only at 4 positions the temperatures are overestimated by 4 - 6 °C;
- The initial pore-water pressures are slightly over-predicted because of the complicated rock conditions and the simplifications of the model.
- The measured thermally-induced increase of pore-water pressures is reasonably represented by the model, especially in the near-field around heater;
- The thermal deformations are well predicted by the model with the thermal expansion coefficient of the rock mass.

Future Investigations

Although the HE-D project with its in-situ measurements, laboratory tests, and numerical simulations was successfully performed, some questions are still remaining and need to be answered. The achieved knowledge is to be verified and the certainty of the obtained data is to be enhanced. The following aspects are necessarily to be investigated further:

- thermal effects on long-term deformation and damage of clay rocks under relevant conditions in the near-field around disposed high level radioactive waste at high temperatures expected as in-situ;

- swelling behaviour (strain-pressure-suction relationship) of heated clay rocks by re-hydration under wet conditions (vapour and fluid water);
- self-sealing and healing of thermally-damaged clay rocks under the conditions prevailing in the repository post-closure period.

These investigations are to be conducted with improved methods. Because of the special features of clay rocks in comparison to other geo-materials, conventional test methods may not be sufficient in some cases. Thus special new test methods are to be developed.

The THM constitutive models and parameters used are to be validated on basis of experimental results. If necessary, improved or new models are to be developed, respectively.

6 Acknowledgements

The GRS work was funded by the German Federal Ministry of Economics and Technology (BMWi) under contract No. 02 E 9773. The authors would like to thank for this support. The supports from all the project partners are also gratefully acknowledged, and especially the coordination of the project by the French Agence Nationale Pour la Gestion de Déchets Radioactifs (ANDRA).

7 References

/ALH 04/ Alheid, H.-J.: Evolution of the Excavation Damaged Zone in Indurated Clay: Lessons Learned in the Mont Terri Underground Rock Laboratory. International conference on Radioactive Waste Disposal (DisTec2004), April 26-28, 2004, Berlin, Germany.

/ALO 02/ Alonso, E.E., Olivella, S., Delahaye, C.: Gas Migration in Clays. Environmental Geomechanics – Monte Verita 2002, 83-94.

/BOC 01/ Bock, H.: RA Experiment - Rock mechanics analyses and synthesis: Data Report on Rock Mechanics. Technical Report 2000-02.

/BOS 03/ Bossart, P., Wermeille, S.: The Stress Field in the Mont Terri Region - Data Compilation. In: Heitzmann, P. & Tripet, J.-P. (ed.): Mont Terri Project – Geology, Paeohydrology and Stress Field of the Mont Terri Region – Reports of Federal Office for Water and Geology (FOWG), Geology Series 4, 65-92.

/CRI 98/ Cristescu, N.D., Hunsche, U.: Time Effects in Rock Mechanics. John Wiley & Sons, 1998.

/FLO 02/ Floria, E., Sanz, F.J., Garcia-Sineriz, J.L.: Drying test: evaporation rate from core samples of “Opalinus clay” under controlled environmental conditions, VE-Deliverable 6, 2002.

/FRE 93/ Fredlund, D.G., Rahardjo, H.: Soil Mechanics for Unsaturated Soils. John Wiley & Sons, INC. 1993.

/GEN 98/ Gens, A.A., Garcia-Molina, A.J., Olivella, S., Alonso, E.E., Huertas, F.: Analysis of a Full Scale in-situ Test Simulating Repository Conditions. Int. J. Numer. Anal. Meth. Geomech., 22, 515-548, 1998.

/GEN 06/ Gens, A. A., Olivella, S.: Coupled Thermo-Hydro-Mechanical Analysis of Engineered Barriers for High-Level Radioactive Waste. Chinese Journal of Rock Mechanics and Engineering, 2006, 25(4), 670 -680.

/HEI 04/ Heitzmann, P.: Mont Terri Project - Hydrogeological Synthesis, Osmotic Flow, Berichte des BWG, Serie Geologie, No. 6–Bern 2004.

/HOR 96/ Horseman, S.T., Higgo, J.J.W., Alexander, J., Harrington, J.F.: Water, Gas and Solute Movement through Argillaceous Media. Report CC-96/1, 1996.

/HOT 00/ Hoteit, N., Ozanam, O., Su, K., Chiarelli, A.S.: Thermo-hydro-mechanical behaviour of deep argillaceous rocks. The 4th North American Rock Mechanics Symposium, Seattle, 31.7 –3.8, 2000.

/KUL 05/ Kull, H., Jockwer, N., Zhang, C.L., Wileveau, Y., Pepa, S.: Measurement of Thermally-Induced Pore-water Pressure and Gas Migration in the Opalinus clay at Mont Terri – HE-D heating Experiment. 2nd International Meeting of Clays in Natural and Engineered Barriers for Radioactive Waste Confinement, Tours, March 14-18, 2005.

/LEB 00/ Lebon, P., Ghoreychi, M.: French Underground Research Laboratory of Meuse/Haute-Marne: THM Aspects of Argillite Formation. EUROCK2000, Aachen, 27-31, March 2000.

/LAX 67/ Lax, E.; Synowietz, C.: Taschenbuch für Chemiker und Physiker – Band I Makroskopische physikalisch-chemische Eigenschaften, Springer-Verlag, 1967.

/MUN 03/ Munoz, J.J., Lioret, A., Alonso, E.: Laboratory Report: Characterization of hydraulic properties under saturated and non saturated conditions, VE-Deliverable 4, 2003.

/NOY 00/ Noynaert, L. et cl.: Heat and radiation effects on the near field of a HLW or spent fuel repository in a clay formation (CERBERUS Project). EUR 19125EN, Contract No F14W-CT95-0008.

/NUS 04a/ Nussbaum, C., Graf, A., Bossart, P.: Structural and geological mapping of the HE-D niche: results and discussion, HE-D Experiment, Technical Note 2004-07, August 2004.

/NUS 04b/ Nussbaum, C., Badertscher, N., Graf, A., Steiger, H., Meier, O., Bossart,P.: Drilling Campaigns of Phases 9a and 9b, Drilling and field Mapping of Drillcores including Photo Documentation – Part 2, Technical Note 2004-06, September 2004.

/OLI 94/ Olivella, S., Carrera, J., Gens, A.A., Alonso, E.E.: Nonisothermal Multiphase Flow of Brine and Gas Through Saline Media. Transport in Porous Media, 15, 271-293, 1994.

/PEA 03/ PEARSON, F.J., Arcos, D., Bath, a., Boison, J.-y., Fernández, A.M., Gäbler, H.-E., Gaucher, E., Gautschi, A., Griffault, L., Hernán, P., Waber, H.N.: Mont Terri Project – Geochemistry of Water in the Opalinus Clay Formation at the Mont Terri Rock Laboratory. No 5 – Bern 2003.

/ROD 99/ Rodwell, W.R., Harris, A.W., Horseman, S.T., Lalieux, P., Müller, W., Ortiz Amaya, L., Pruess, K.: Gas Migration and Two-Phase Flow through Engineered and Geological Barriers for a Deep Repository for Radioactive Waste. A Joint EC/NEA Status Report, European Commission, 1999, EUR 19122 EN.

/SOM 92/ Somerton, H.W.: Thermal properties and temperature-related behaviour of rock/fluid systems. 1992 ELSEVIER Science Publishers B.V. ISBN 0-444-89001-7.

/SU 03/ Su, K.: Constitutive Models of the Meuse/Haute-Marne Argillites, Project MODEX-REP – FIKW-CT2000-00029, Deliverable 2&3, 2003.

/UPC 02/ UPC: CODE-BRIGHT, A 3-D program for thermo-hydro-mechanical analysis in geological media, 2002.

/THU 99/ Thury, M., Bossart, P.: Mont Terri Rock Laboratory, Results of the Hydrogeological, Geochemical and Geotechnical Experiments performed in 1996 and 1997. Geological Report Nr. 23, 1999, Bern.

/VE 02/ VE: Ventilation Experiment in Opalinus clay – „VE“ Experiment, VE Test Plan, Deliverable 3, EC contract FIKW-CT2001-00126, 2002

/WIL 03/ Wileveau, Y., Rothfuchs, T.: HE-D Experiment: Test Plan. Mont Terri Project, Technical Note 2004-20, September 2003.

/WIL 05/ Wileveau, Y.: THM Behaviour of Host Rock – Progress Report of the HE-D Experiment, Mont Terri Project, Technical Report TR2005-03, August 2005.

/ZHA 02/ Zhang, C.L., Dittrich, J., Müller, J., Rothfuchs, T.: Experimental Study of the Hydromechanical Behaviour of the Callovo-Oxfordian Argillites – Part of the MODEX-REP Project. December 2002, GRS-187, ISBN3-931995-55-0.

/ZHA 03/ Zhang, C.L., Kröhn, K.-P., Rothfuchs, T.: Applications of CODE-BRIGHT to Thermal-Hydro-Mechanical Experiments on Clays. Proceedings of the International Conference "From Experimental Evidence towards Numerical Modelling of Unsaturated Soils," Weimar, Germany, September 18-19, 2003, Volume II, 341-357. ISSN0930-89-89.

/ZHA04a/ Zhang, C.L., Rothfuchs, T., Moog, H., Dittrich, J., Müller, J.: Thermo-Hydro-Mechanical and Geochemical Behaviour of the Callovo-Oxfordian Argillite and the Opalinus Clay. June 2004, GRS-202, ISBN3-931995-69-0.

/ZHA04b/ Zhang, C.L., Rothfuchs, T., Jockwer, N., Kröhn, K.-P., Miehe, R., Moog, H.: Results of Laboratory Investigations on Clays, Proc. International Conference on Radioactive Waste Disposal - DisTec 2004, Berlin 26-28 April 2004.

/ZHA05a/ Zhang, C.L., Rothfuchs, T., Su, K., Hoteit, N.: Experimental Study of the Thermo-Hydro-Mechanical Behaviour of Indurated Clays, 2nd International Meeting of Clays in Natural and Engineered Barriers for Radioactive Waste confinement, Tours, March 14-18, 2005.

/ZHA05b/ Zhang, C.L., Wileveau, Y., Rothfuchs, T.: A Heating Experiment in the Opalinus Clay at the Mont Terri Rock Laboratory. The 10th International Conference on Environmental Remediation and Radioactive Waste Management, September 4–8 2005, Glasgow, Scotland.

/ZHA 06/ Zhang, C.L., Rothfuchs, T., Wieczorek, K., Jockwer, N., Wileveau, Y.: Monitoring and Modelling of Responses of the Opalinus Clay to Heating. Chinese Journal of Rock Mechanics and Engineering, 2006, 25(4),659-669.

8 List of Figures

9 List of Tables

Gesellschaft für Anlagen- und Reaktorsicherheit (GRS) mbH

Schwertnergasse 1
50667 Köln
Telefon +49 221 2068-0
Telefax +49 221 2068-888

Forschungsinstitute
85748 Garching b. München
Telefon +49 89 32004-0
Telefax +49 89 32004-300

Kurfürstendamm 200
10719 Berlin
Telefon +49 30 88589-0
Telefax +49 30 88589-111

Theodor-Heuss-Straße 4
38122 Braunschweig
Telefon +49 531 8012-0
Telefax +49 531 8012-200

www.grs.de

ISBN 3-931995-98-0